



**Silesian University
of Technology**

INSA

INSTITUT NATIONAL
DES SCIENCES
APPLIQUÉES
TOULOUSE

DISCIPLINE COUNCIL FOR CHEMICAL SCIENCES

mgr inż. Agata RACZYŃSKA

**BIODEGRADATION OF SYNTHETIC
POLYMERS WITH THE USE OF ENZYMES**

**BIODEGRADACJA POLIMERÓW SYNTETYCZNYCH
Z WYKORZYSTANIEM ENZYMÓW**

**DOCTORAL THESIS
(Polish-French Joint Doctorate)**

Supervisors:

dr hab. Artur GÓRA, prof. PŚ
dr Isabelle ANDRÉ

Gliwice 2024

The future belongs to those who believe in the beauty of their dreams.

– Eleanor Roosevelt

Acknowledgement

This Polish-French double doctoral dissertation represents the fulfilment of my long-standing dream to study in France. It was made possible through the *doctorate cotutelle* programme, financed by the French Government via Campus France.

I sincerely thank the Ministry of Science and Higher Education in Poland for supporting the experimental work and materials under the “Diamond Grant” programme No. 0169/DIA/2020/49, as part of the science budget for the years 2020–2024.

I also extend my gratitude to the HPC resources of the Computing Meso-Center of the Midi-Pyrénées Region (CALMIP, Toulouse, France) and the Polish high-performance computing infrastructure PLGrid (HPC Centers: ACK Cyfronet AGH) for providing the computational facilities essential to this work.

Personal Thanks

First and foremost, I wish to express my deepest gratitude to my two exceptional supervisors, Dr. Isabelle André and Dr. Artur Góra, whose unwavering support, encouragement, and guidance have been instrumental throughout my PhD journey. I am truly fortunate to have had the opportunity to learn from them, growing both as a researcher and as an individual.

I would also like to extend my sincere thanks to Dr. Jérémy Esque and Dr. Rajendra Sharma, whose expertise in computational methodologies and scientific approaches greatly contributed to the development of the techniques and insights presented in this dissertation.

A heartfelt thank you goes to Dr. Oksana Kovalenko for her dedicated work in obtaining, purifying, and evaluating *TjCut2* and its mutants, as well as to the experimental team who supported her: Dr. Katarzyna Papaj and MSc Eng. Marzena Szawara. I deeply value our discussions on methodology and results, as well as the opportunity to assist in experiments, which allowed me to gain a deeper understanding of experimental methods.

I also want to sincerely thank Dr. Tadeusz Bieg for performing a comprehensive analysis of Impranil DLN’s structure, which gave me confidence in its modelling, and for teaching me how to interpret its NMR spectra. My gratitude extends to Dr. Katarzyna Żurawska, Dr. Anna Kasprzycka, and MSc Eng. Kinga Plasa for their invaluable assistance in these experiments.

I am also immensely thankful to my colleagues from both of my laboratories—Polish and French—for countless conversations, stimulating discussions, shared challenges, and joyous moments, including our games of Tarot. Your support and friendship have enriched my PhD journey in immeasurable ways.

Finally, I must express my heartfelt gratitude to my dearest friends for their inspiration, unwavering support, and cherished companionship throughout the countless adventures of my PhD journey.

Lastly, I owe my deepest thanks to my family, for their constant encouragement and belief in me. Their endless support has provided me with opportunities, helped me pursue my dreams, and convinced me that anything is possible.

Table of contents

Acknowledgement.....	i
Table of contents	ii
Abbreviations	v
Abstract	vii
Résumé (Abstract in French).....	viii
Streszczenie (Abstract in Polish).....	ix
Résumé détaillé (Detailed Résumé in French)	xi
Publications	xv
Introduction	1
Chapter 1: Objectives and scope of the thesis	4
Chapter 2: Literature Review on PUR and PUR-degrading Enzymes	10
2.1. Introduction	11
2.2. PUR structures and functional groups	14
2.2.1. PUR structures.....	14
2.2.2. PUR functional groups and their enzymatic hydrolysis	16
2.3. Enzymes for PUR degradation	21
2.3.1. Enzymes classification	24
2.3.2. Structures and binding sites.....	26
2.3.3. Active sites and mechanisms.....	35
2.4. Conclusions	40
2.5. Additional data and results	42
2.5.1. Cutinases	42
2.5.2. Computational studies on PUR-degrading enzymes	43
2.5.3. Engineering of PUR-degrading enzymes	45
Chapter 3: Theoretical background and methodology	46
3.1. Enzyme-catalysed reactions and kinetics	46
3.2. Investigation and analysis of protein structure, dynamics, and protein-ligand interactions	48

3.2.1. Protein structure	48
3.2.2. Source of protein structures.....	50
3.2.3. Molecular docking.....	51
3.2.4. Molecular dynamics simulations.....	52
3.2.5. MM-GBSA calculations.....	54
3.3. Enzyme engineering	55
Chapter 4: Characterisation of <i>TfCut2</i> and modelling of its interactions with Impranil DLN.....	59
4.1. Introduction	59
4.2. Methodology	64
4.2.1. Experimental methods.....	64
4.2.2. Computational methods.....	64
4.3. Results and discussion.....	70
4.3.1. Investigation of the structure of Impranil DLN.....	70
4.3.2. Sequence and structure characteristics of <i>TfCut2</i>	77
4.3.3. Investigation of the binding mode of Impranil DLN to <i>TfCut2</i>	79
4.3.4. Analysis of <i>TfCut2</i> -Impranil DLN interactions in productive poses	103
4.3.5. Estimated binding free energies via MM-GBSA approach.....	106
4.4. Conclusions	113
4.5. Supplementary materials to Chapter 4	115
Chapter 5: Description of mutational landscape and design of <i>TfCut2</i> mutants	117
5.1. Introduction	117
5.2. Methodology	120
5.3. Results and discussion.....	122
5.3.1. Assessment of mutational potential and identification of hot spots in <i>TfCut2</i>	122
5.3.2. Selection of residues for mutation.....	125
5.3.3. Computational protein design of <i>TfCut2</i> using a genetic algorithm	128

5.3.4. Rationale for proposed mutations and expected influence on TfCut2 performance.....	133
5.4. Conclusions	137
Chapter 6: Evaluation of proposed <i>TfCut2</i> mutants	138
6.1. Introduction	138
6.2. Methodology	141
6.2.1. Computational methods.....	141
6.2.2. Experimental methods.....	142
6.3. Results and discussion.....	145
6.3.1. <i>TfCut2</i> mutants structure and stability.....	145
6.3.2. Binding evaluation of <i>TfCut2</i> mutants with Impranil DLN	154
6.3.3. Degradation of Impranil DLN by <i>TfCut2</i> and mutants	156
6.3.4 Selected <i>TfCut2</i> mutants with improved properties for in-depth analysis	166
6.4. Conclusions	169
6.5. Supplementary materials to Chapter 6	171
Chapter 7: Conclusions and perspectives	174
7.1. Summary of key findings	174
7.2. Limitations of the study.....	175
7.3. Future directions.....	178
7.4. Broader impact	179
References	180
Permissions.....	195

Abbreviations

2D	Two-Dimensional
3D	Three-Dimensional
AI	Artificial Intelligence
AM1-BCC	Austin Model 1 with Bond Charge Corrections
AMBER	Assisted Model Building with Energy Refinement
AmdA	<i>Agrobacterium tumefaciens</i> d3 amidase
amdS	<i>Aspergillus oryzae</i> urethanase
BaCut1	<i>Blastobotrys</i> sp. G-9 cutinase
BALCONY	Binding Affinity and Ligand CONtributory analySis (R package)
BHET	Bis(2-Hydroxyethyl) terephthalate
CalB	<i>Candida antarctica</i> lipase B
CE_Ubrb	metagenome-derived carboxyl-ester hydrolase
CIGAR	Compressed Iterative Genetic Algorithm for Rapid
COSY	Correlation Spectroscopy spectrum
CpCut1	<i>Cladosporium</i> sp. P7 cutinase
CPUTNase	<i>Candida parapsilosis</i> NBRC 708 urethanase
Cryo-EM	Cryogenic electron microscopy
DEG	Diethylene glycol
DMSO	Dimethyl sulphoxide
DNA	Deoxyribonucleic Acid
DSF	Differential Scanning Fluorimetry
EDTA	Ethylenediaminetetraacetic acid
FTIR	Fourier-Transform Infrared Spectroscopy
GA	Genetic Algorithm
GAFF	General AMBER Force Field
<i>Hfor</i>	<i>Halopseudomonas formosensis</i> cutinase
<i>HiC</i>	<i>Humicola insolens</i> cutinase
HSQC	Heteronuclear Single Quantum Coherence spectrum
ID	Identifier
IMAC	Immobilised Metal Affinity Chromatography
IPTG	Isopropyl β -D-1-thiogalactopyranoside
K	Adsorption equilibrium constant
K_M	Michaelis constant
k_{cat}	Turnover number
k_s	Rate constant of the surface reaction
LB	Lysogeny Broth
LCC	Leaf-branch compost bacterial cutinase
M9	Minimal Salts Medium
MD	Molecular Dynamics
MM-GBSA	Molecular Mechanics - Generalised Born Surface Area
MM-PBSA	Molecular Mechanics Poisson-Boltzmann Surface Area
MSA	Multiple Sequence Alignment
NMR	Nuclear Magnetic Resonance
P1	Binding pose 1 of Impranil DLN with <i>TfCut2</i> in computational studies

P2	Binding pose 2 of Impranil DLN with <i>TjCut2</i> in computational studies
PA	Polyamide
PBAT	Poly(butylene adipate-co-terephthalate)
PBS	Polybutylene succinate
PCR	Polymerase Chain Reaction
PDB	Protein Data Bank
pelB	Signal sequence, derived from the <i>pelB</i> gene encoding pectate lyase B in <i>Erwinia carotovora</i>
PET	Polyethylene terephthalate
<i>pNP</i>	<i>para</i> -nitrophenol
<i>pNPB</i>	<i>para</i> -nitrophenyl-butyrate
<i>pNPC</i>	<i>para</i> -nitrophenyl-N-benzylcarbamate
<i>pNPBC</i>	butyl-N(<i>para</i> -nitrophenyl)carbamate
<i>pNPA</i>	<i>para</i> -nitrobutyranilide
pueA	Polyurethanase A from <i>Pseudomonas chlororaphis</i> or <i>Pseudomonas protegens</i> strain Pf-5
pueB	Polyurethanase B from <i>Pseudomonas chlororaphis</i> or <i>Pseudomonas protegens</i> strain Pf-5
PudA	<i>Comamonas (Delftia) acidovorans</i> TB-35 lipase
Pu1A	<i>Pseudomonas fluorescens</i> esterase
PUR	Polyurethane
PVC	Polyvinyl chloride
RC1	Binding pose 1 of Impranil DLN with PueA in computational studies
RC2	Binding pose 2 of Impranil DLN with PueA in computational studies
RMS	Root Mean Square
RMSD	Root Mean Square Deviation
RMSF	Root Mean Square Fluctuation
RNA	Ribonucleic Acid
RU	Rosetta units
SDS-PAGE	Sodium Dodecyl Sulphate–Polyacrylamide Gel Electrophoresis
<i>Tcur1278</i>	<i>Thermomonospora curvata</i> DSM43183 cutinase
<i>Tcur0390</i>	<i>Thermomonospora curvata</i> DSM43183 cutinase
TEV	Tobacco Etch Virus Protease
<i>TjCut2</i>	<i>Thermobifida fusca</i> cutinase
TIP3P	Transferable Intermolecular Potential with 3 Points
<i>T_m</i>	Thermal unfolding transition midpoint
UMG-SP-1	metagenome-derived urethanase 1
UMG-SP-2	metagenome-derived urethanase 2
UMG-SP-3	metagenome-derived urethanase 3
<i>v₀</i>	Initial degradation rate
WT	Wild-type
X-ray	X-ray Crystallography

Abstract

Plastic waste, including polyurethane (PUR), represents a significant environmental challenge due to its widespread use in various industries and its resistance to natural degradation. As traditional recycling methods for plastics remain inefficient, alternative approaches, such as enzymatic degradation, offer a promising, eco-friendly solution. However, research on enzymes capable of degrading PUR is still limited. This dissertation focuses on investigating the cutinase enzyme from *Thermobifida fusca* (*TfCut2*) and its potential for PUR degradation, with Impranil DLN used as a model substrate to explore the enzyme's catalytic activity.

The study employs a combination of computational and experimental methods to identify the molecular determinants involved in substrate binding and catalysis. Molecular docking and molecular dynamics simulations were performed to study the interactions between *TfCut2* and Impranil DLN, identifying key residues that play a role in the enzyme's ability to bind to the PUR substrate. In addition, computational protein design tools were used to engineer mutations aimed at enhancing protein-ligand binding and enzyme's catalytic performance.

Experimental validation of the designed mutants showed that three single-point variants, namely G62A, T61V and T207D, demonstrated significantly increased degradation rates, with G62A achieving more than a twofold improvement in activity over the wild-type enzyme. T207D also showed a marked increase in production yield, further underscoring the potential of rational enzyme engineering. These results suggest that engineering mutations can substantially enhance the catalytic efficiency of *TfCut2* for PUR degradation.

The study highlights the complexities of modelling and experimentally assessing PUR degradation, given the heterogeneity of PUR structures and their degradation products. Despite these challenges, this work establishes a framework for tailoring cutinases for synthetic polymer degradation, providing insights into substrate binding modes, and potential rate-limiting steps. The findings contribute to the broader goal of developing efficient, sustainable solutions for polymer recycling and plastic waste remediation.

Keywords

Plastic biodegradation, Enzymatic degradation, Polyurethane, Cutinase, Enzyme engineering, Molecular modelling, Molecular dynamics, Protein design

Résumé (Abstract in French)

Les déchets plastiques, y compris le polyuréthane (PUR), représentent un défi environnemental majeur en raison de leur utilisation répandue dans diverses industries et de leur résistance à la dégradation naturelle. Alors que les méthodes traditionnelles de recyclage des plastiques restent inefficaces, des approches alternatives, telles que la dégradation enzymatique, offrent une solution prometteuse et écologique. Cependant, les recherches sur les enzymes capables de dégrader le PUR demeurent limitées. Cette thèse se concentre sur l'étude de l'enzyme cutinase de *Thermobifida fusca* (*TfCut2*) et de son potentiel pour la dégradation du PUR, en utilisant l'Impranil DLN comme substrat modèle pour explorer l'activité catalytique de l'enzyme.

L'étude combine des méthodes computationnelles et expérimentales pour identifier les déterminants moléculaires impliqués dans la liaison au substrat et la catalyse. Des simulations de docking moléculaire et de dynamique moléculaire ont été réalisées pour étudier les interactions entre *TfCut2* et l'Impranil DLN, permettant d'identifier des résidus clés jouant un rôle dans la capacité de l'enzyme à se lier au substrat PUR. De plus, des outils de conception computationnelle de protéines ont été utilisés pour prédire des mutations visant à améliorer la liaison protéine-ligand et les performances catalytiques de l'enzyme.

La validation expérimentale des mutants prédits a révélé que trois mutants ponctuels, à savoir G62A, T61V et T207D, présentent des taux de dégradation significativement accrus, avec G62A affichant une amélioration de l'activité de plus du double par rapport à l'enzyme sauvage. T207D a également montré une augmentation marquée du rendement de production, mettant ainsi en évidence le potentiel de l'ingénierie rationnelle des enzymes. Ces résultats suggèrent que les mutations ingénierées peuvent améliorer de manière substantielle l'efficacité catalytique de *TfCut2* pour la dégradation du PUR.

L'étude met en lumière les complexités de la modélisation et de l'évaluation expérimentale de la dégradation du PUR, étant donné l'hétérogénéité des structures du PUR et des produits de dégradation associés. Malgré ces défis, ce travail établit un cadre pour l'adaptation des cutinases à la dégradation des polymères synthétiques, offrant des éclairages sur les modes de liaison au substrat et les étapes potentiellement limitantes. Les résultats contribuent à l'objectif plus large de développer des solutions efficaces et durables pour le recyclage des polymères et la gestion des déchets plastiques.

Mots-clés

Biodégradation des plastiques, Dégradation enzymatique, Polyuréthane, Cutinase, Ingénierie des enzymes, Modélisation moléculaire, Dynamique moléculaire, Conception protéique

Streszczenie (Abstract in Polish)

Odpady plastikowe, w tym poliuretany (PUR), stanowią poważne wyzwanie środowiskowe z powodu odporności na naturalną degradację. Mimo że tworzywa sztuczne odgrywają kluczową rolę w wielu branżach, ich nadmierna produkcja i trudności w recyklingu prowadzą do nagromadzenia odpadów, które zanieczyszczają ekosystemy lądowe i wodne. W tradycyjnych metodach recyklingu plastiku, takich jak recykling chemiczny, stosunkowo niska efektywność procesów sprawia, że stają się one niewystarczające do rozwiązania problemu. Metody, takie jak degradacja enzymatyczna, mogą stanowić ekologiczną i efektywną alternatywę, umożliwiającą rozkład odpadów w sposób zrównoważony. Jednak badania nad enzymami zdolnymi do degradacji PUR wciąż pozostają w fazie początkowej.

Celem niniejszej pracy było zbadanie aktywności enzymu kutynazy bakteryjnej pochodzącej z *Thermobifida fusca* (*TfCut2*) wobec PUR, przy użyciu modelowego substratu Impranilu DLN, aby zrozumieć mechanizm degradacji oraz możliwości inżynierii tego enzymu w celu zwiększenia jego wydajności katalitycznej. Praca łączy podejścia obliczeniowe oraz eksperymentalne, aby zidentyfikować molekularne aspekty odpowiedzialne za wiązanie substratu oraz katalizę reakcji degradacji. Symulacje dokowania molekularnego oraz dynamiki molekularnej pozwoliły na zbadanie interakcji między *TfCut2* a Impranilem DLN, identyfikując kluczowe aminokwasy na powierzchni enzymu, które odgrywają rolę w wiązaniu PUR. Zastosowano również narzędzia do projektowania białek, które umożliwiły opracowanie mutacji w celu zwiększenia powinowactwa enzymu do substratu oraz poprawy jego wydajności katalitycznej.

Walidacja eksperymentalna zaprojektowanych mutantów wykazała, że trzy warianty punktowe enzymu *TfCut2* – G62A, T61V i T207D – wykazały zwiększenie szybkości degradacji Impranilu DLN, przy czym G62A uzyskał ponad dwukrotną poprawę aktywności w porównaniu do enzymu typu dzikiego. Mutant T207D wykazał również wyraźny wzrost wydajności produkcji, co podkreśla potencjał racjonalnej inżynierii enzymów w kontekście degradacji PUR. Zgodnie z wynikami eksperymentalnymi, inżynieria mutacji może znacząco zwiększyć efektywność katalityczną *TfCut2*, co otwiera nowe możliwości w zakresie inżynierii enzymów do degradacji polimerów syntetycznych.

Przeprowadzone badania uwydatniają złożoność modelowania oraz eksperymentalnego oceniania degradacji PUR, biorąc pod uwagę heterogeniczność ich struktur oraz produktów ich degradacji. Pomimo tych wyzwań, wyniki tej pracy stanowią

istotny krok w kierunku opracowania ram do dostosowania kutyńaz do degradacji polimerów syntetycznych, umożliwiając lepsze zrozumienie sposobów wiązania substratu, a także identyfikację potencjalnych etapów ograniczających szybkość reakcji. Ponadto, badania te dostarczają cennych informacji dotyczących znaczenia kontekstu strukturalnego i funkcjonalnego enzymu przy projektowaniu nowych mutantów do degradacji polimerów syntetycznych.

W kontekście szeroko pojętej gospodarki o obiegu zamkniętym, wyniki niniejszej pracy przyczyniają się do rozwoju metod recyklingu polimerów syntetycznych, proponując rozwiązania oparte na enzymach, które mogłyby znaleźć zastosowanie w odzyskiwaniu materiałów z odpadów plastikowych. Badania nad enzymatyczną degradacją PUR mogą mieć kluczowe znaczenie w poszukiwaniach bardziej zrównoważonych metod recyklingu, które pozwolą na skuteczniejsze przetwarzanie odpadów plastikowych. W przyszłości możliwe jest dalsze doskonalenie tego procesu poprzez iteracyjną inżynierię enzymów, a także dostosowanie warunków eksperymentalnych, takich jak optymalizacja temperatury, aby uzyskać większą wydajność katalityczną w warunkach przemysłowych.

Wnioski z pracy stanowią istotny wkład w globalną walkę z problemem odpadów plastikowych, zwłaszcza w kontekście recyklingu PUR, i otwierają drogę do rozwoju nowych, efektywnych i zrównoważonych rozwiązań w zakresie ochrony środowiska.

Résumé détaillé (Detailed Résumé in French)

Contexte

Les plastiques, matériaux polyvalents et durables, figurent parmi les avancées technologiques les plus marquantes du XX^e siècle, transformant des secteurs tels que l'emballage, la santé et l'électronique. Cependant, leur résistance chimique les ont rendus symboliques de la consommation non durable. La majorité des déchets plastiques, en raison d'un recyclage insuffisant, finit dans des décharges, polluant les écosystèmes terrestres et aquatiques [1,2].

Face à cette crise, les procédés enzymatiques offrent une alternative prometteuse au recyclage chimique. Certains plastiques, tels que les polyuréthanes (PUR), possédant des liaisons hydrolysables, peuvent être dégradés. Les enzymes, comme les cutinases, permettent une dégradation spécifique et respectueuse de l'environnement, mais leur application aux PUR reste peu étudiée.

Objectifs

La thèse vise à explorer et optimiser les mécanismes enzymatiques de dégradation des PUR via l'étude de la cutinase bactérienne de *Thermobifida fusca* (*TfCut2*) et son interaction avec le substrat modèle polyester PUR Impranal DLN. L'objectif principal est de caractériser les déterminants moléculaires impliqués dans la dégradation enzymatique des polymères synthétiques de la famille des PUR et d'améliorer la performance de *TfCut2* à l'aide d'approches computationnelles combinées à des évaluations expérimentales.

Les objectifs spécifiques de cette thèse incluent :

1. Caractérisation de la *TfCut2* sauvage et identification des déterminants moléculaires clés impliqués dans la liaison du substrat, notamment l'élucidation structurale de l'Impranal DLN et son interaction avec *TfCut2* dans le cadre du mécanisme d'hydrolyse enzymatique.
2. Re-design du site de liaison du substrat pour proposer une librairie de mutants de *TfCut2* permettant d'explorer les rôles spécifiques des résidus dans la liaison.
3. Évaluation computationnelle et expérimentale des mutants de *TfCut2* pour étudier les effets des mutations sur la liaison et l'efficacité catalytique.

Méthodes

Pour caractériser les interactions moléculaires entre *TfCut2* et l'Impranal DLN et identifier les déterminants critiques de la liaison, des approches computationnelles ont été

utilisées : Rosetta docking, simulations de dynamique moléculaire, analyses ProLIF, calculs MM-GBSA ; et vérification expérimentale de structure de l'Impranil DLN par RMN.

Pour concevoir des mutations visant à renforcer les interactions enzyme-substrat tout en maintenant la stabilité de l'enzyme, des outils de re-design des protéines et d'analyse évolutive ont été appliqués : Rosetta design, FoldX, HotSpotWizard, et analyse MSA.

Les performances des mutants ont été évaluées par des tests expérimentaux (analyses d'activité enzymatique et mesures de thermostabilité) et des simulations computationnelles (dynamique moléculaire et analyses visuelles).

Resultats

Structure de l'Impranil DLN et hydrolyse de ses liaisons

La structure propriétaire de l'Impranil DLN a présenté des défis pour la modélisation moléculaire, avec des descriptions variables dans la littérature [3,4]. Pour surmonter ces incertitudes, des analyses approfondies par RMN ont permis de caractériser sa composition chimique, comprenant : 1,6-hexanediol, acide adipique, glycol néopentyl, et 1,6-hexaméthylène diisocyanate.

L'analyse des échantillons hydrolysés par *TfCut2* a révélé une préférence pour l'hydrolyse des liaisons ester adjacentes au 1,6-hexanediol, acide adipique et glycol néopentyl.

Modélisation des interactions enzyme-polymère

Des études computationnelles ont été menées pour modéliser les interactions entre *TfCut2* et l'Impranil DLN. Huit modes de liaison ont été explorés à l'aide de docking moléculaire et de simulations de MD, en considérant les liaisons ester et uréthane comme susceptibles d'être clivées. Une méthodologie a été développée pour sélectionner des conformations "productives" en fonction des distances catalytiques clés (attaque nucléophile et transfert de proton).

Les résultats montrent que *TfCut2* reconnaît globalement la chaîne de polymère. Des résidus clés, tels que Y60, M131 et W155, stabilisent la polymère chaîne, d'autres résidus hydrophobes contribuant également à la liaison mais étant moins critiques. Les interactions hydrophobes dans le sillon de *TfCut2* offrent une flexibilité dans la liaison à la chaîne polymère, expliquant la large promiscuité de substrat des cutinases.

Ingénierie rationnelle de l'enzyme

Des outils computationnels ont été utilisés pour prédire des mutations destinées à améliorer l'affinité et l'efficacité catalytique. Une analyse de mutabilité a permis de prioriser neuf positions clés : T61, G62, A65, S66, Q92, I178, T207, F209 et N212. Ces résidus ont été

ciblés pour optimiser les interactions hydrophobes, la complémentarité stérique, ou l'efficacité catalytique.

Une librairie de mutants a été proposée en combinant re-design computationnel à l'aide de Rosetta et d'algorithmes génétiques, tout en validant les propositions par inspection visuelle.

Évaluation expérimentale des mutants

Parmi 24 mutants simples et 5 mutants multiples proposés, 20 mutants simples et 5 combinés ont été produits et testés. Trois mutations simples (G62A, T61V et T207D) ont montré des taux de dégradation accrus, G62A présentant une amélioration de plus de deux fois par rapport au type sauvage. Les autres mutations ont eu peu ou pas d'effet, et plusieurs ont réduit l'activité catalytique, notamment pour les mutants combinés. Les résultats suggèrent que la liaison du substrat n'est pas nécessairement l'étape limitante de la dégradation de l'Impranil DLN. D'autres facteurs, tels que la stabilité structurale, les propriétés de surface ou la dynamique du site actif, peuvent jouer un rôle plus important dans la détermination de l'efficacité enzymatique. Ces résultats soulignent l'importance de prendre en compte le contexte plus large de la fonction enzymatique lors de l'interprétation des prédictions informatiques et de la conception des expériences futures.

Apports de la thèse et perspectives

Cette thèse représente une étude complète, alliant à la fois une analyse bioinformatique et une validation expérimentale, visant à explorer le processus de dégradation enzymatique du PUR. Elle constitue également la première étude systématique sur l'ingénierie des cutinases pour la dégradation du PUR, offrant un aperçu des déterminants moléculaires impliqués dans la liaison du PUR au site de liaison de *TfCut2*.

L'intégration des approches bioinformatiques et expérimentales a permis d'identifier des déterminants critiques pour la liaison et la catalyse, ainsi que des mutations prometteuses susceptibles d'améliorer les performances de *TfCut2*. Cette thèse démontre que bien que la liaison au substrat soit cruciale, elle n'est pas l'étape limitante de la vitesse de dégradation du PUR.

Les travaux futurs pourraient se concentrer sur l'amélioration des enzymes en recombinant les mutations bénéfiques identifiées dans cette étude, afin de guider des cycles itératifs d'ingénierie enzymatique. Par ailleurs, l'exploration de nouvelles conditions expérimentales, telles que l'augmentation de la température, pourrait offrir des pistes pour optimiser les performances catalytiques dans des contextes industriels.

Cette recherche s'inscrit également dans une perspective plus large, visant à favoriser une économie circulaire. Elle ouvre la voie au développement de filières intégrées combinant prétraitements efficaces, conditions optimisées de réaction et formulations enzymatiques adaptées aux défis spécifiques de la dégradation des polymères synthétiques. Une meilleure compréhension des mécanismes moléculaires sous-jacents pourrait également guider la conception de matériaux polymériques plus biodégradables, répondant ainsi aux enjeux environnementaux.

Enfin, cette thèse contribue significativement à l'enjeu mondial du recyclage des plastiques, en particulier des PUR. En proposant des solutions enzymatiques durables et innovantes, elle s'inscrit dans une démarche visant à réduire les déchets plastiques et à promouvoir une économie circulaire, offrant ainsi une approche résiliente et respectueuse de l'environnement pour le traitement des polymères synthétiques.

Publications

Raczyńska A., Góra A., André I.: An overview on polyurethane-degrading enzymes, *Biotechnology Advances*, vol. 77, 2024, 1-19, DOI: 10.1016/j.biotechadv.2024.108439

Raczyńska A.: Highlights from the Biocatalysis Faraday Discussion, May 2024, London, United Kingdom, Chemical Communications, RSC Publications, vol. 60, nr 76, 2024, 10431-10438, DOI:10.1039/d4cc90306d

Indexed conference proceedings

Acevedo-Rocha C., Berlicki L., Bornscheuer U., Campopiano D., Chaiyen P., Čivić J., Cong Z., Ehinger F., Flitsch S., Góra A., Hanzevacki M., Harvey J., Hilvert D., Hollfelder F., Jarvis A., Lichtenstein B., Lutz S., Malcomson T., Marsh E., McFarlane N., McKenzie A., Mulholland A., Osuna S., Pelletier J., **Raczyńska A.**, Roelfes G., Rulišek L., Stockinger P., Turner N., Valetti F., Van der Kamp M., Widersten M., Zeymer C.: Enzyme evolution, engineering and design: mechanism and dynamics: general discussion, *Faraday Discussions, ROYAL SOC CHEMISTRY*, vol. 252, 2024, s. 127-156, DOI:10.1039/d4fd90022g

Alogaidi A., Armstrong F., Bakshi A., Bornscheuer U., Brown G., Bruton I., Campopiano D., Dourado D., Ehinger F., Flitsch S., Góra A., Green A., Hilvert D., Honda S., Huang M., Jones R., King T., Lichtenstein B., Lihan M., Luk L., Lurshay T., Lutz S., Marsh E., McKenzie A., Orton B., Pelletier J., **Raczyńska A.**, Rulišek L., Stockinger P., Syrén P., Turner N., Valetti F., Van der Kamp M., Wong L.: Biocatalysis for industry, medicine and the circular economy: general discussion, *Faraday Discussions, ROYAL SOC CHEMISTRY*, vol. 252, 2024, s. 480-506, DOI:10.1039/d4fd90025a

Abramiuk M., Acevedo-Rocha C., Alogaidi A., Armstrong F., Bakshi A., Bornscheuer U., Campopiano D., Chaiyen P., Ehinger F., Flitsch S., Harvey J., Hilvert D., Jarvis A., Jones R., Lichtenstein B., Luk L., Lurshay T., Malcomson T., Marsh E., McFarlane N., McKenzie A., Megarity C., Moliner V., Mulholland A., Orton B., Pelletier J., **Raczyńska A.**, Syrén P., Thompson S., Turner N., Valetti F., Wong L., Zeymer C.: Biocatalytic pathways, cascades, cells and systems: general discussion, *Faraday Discussions*, vol. 252, 2024, s. 241-261, DOI:10.1039/d4fd90023e

Acevedo-Rocha C., Bakshi A., Bornscheuer U., Campopiano D., Čivić J., Drienovská I., Ehinger F., Gomm A., Góra A., Green A., Hanzevacki M., Harvey J., Hilvert D., Huang M., Jarvis A., Kamerlin S., Lichtenstein B., Luk L., Lutz S., Marsh E., McKenzie A., Moliner V., Mulholland A., Osuna S., Pelletier J., **Raczyńska A.**, Rao A., Rhys G., Roelfes G., Rulišek L., Stockinger P., Szleper K., Thompson S., Turner N., Van der Kamp M., Xu G., Zeymer C.: Artificial, biomimetic and hybrid enzymes: general discussion, *Faraday Discussions*, vol. 252, 2024, s. 354-386, DOI:10.1039/d4fd90024c

Poster presentations

Raczyńska A., Sharma R., Esque J., Góra A., André I., Computational study towards enzymatic degradation of synthetic polymers, *European Rosetta Con 2023, September 25-27 2023, Leipzig, Germany*;

Raczyńska A., Sharma R., Esque J., Góra A., André I., Computational studies towards enzymatic degradation of polyurethane, *Groupe de Graphisme et Modélisation Moléculaire- May 15-17 2023, Toulouse, France*.

Introduction

Plastics, versatile and durable as they are, rank among the 20th century's most impactful technological advancements, revolutionising industries such as packaging, healthcare, and electronics. However, these same properties—once celebrated—have now rendered plastic a symbol of unsustainable consumption and environmental peril. As we navigate the Anthropocene, the geological epoch defined by the human influence on the planet, widespread pollution caused by plastic waste stands as a clear indicator of our environmental impact.

At present, plastics are not only ubiquitous materials but they are also an enduring marker of the human presence. From the depths of the oceans to the summit of Mount Everest, plastics have become a permanent fixture in every corner of the Earth, even in the most isolated places. Sadly, future archaeologists will not uncover relics of pottery or ancient tools; instead, they will unearth plastic bags, candy wrappers, and discarded packaging. Plastic waste has become an ecological footprint that, as noted by Estelle Praet, embeds human impact permanently into the planet's geological record [5].

The high chemical and thermal resistance of synthetic polymers, as well as their low weight and high strength are the reasons for their continuing popularity [2]. The challenge of managing vast amounts of plastic waste has led to the development of various chemical recycling processes. However, these methods require high temperatures and often produce byproducts that contribute to environmental pollution. More primitive disposal methods, such as combustion, release highly toxic organic compounds; for instance, burning polyvinyl chloride (PVC) generates carcinogenic furans and dioxins [6]. According to the Environmental Protection Agency, only 7% of the plastic waste generated is recycled annually, with an additional 8% incinerated [7].

Due to insufficient recycling, the majority of plastic waste is sent to landfills, where millions of tons accumulate each year, polluting land and aquatic environments, causing harmful effects on these ecosystems [1,2]. The decomposition of plastic is a very slow process, taking hundreds of years, which is why this type of waste remains, disturbing the balance of the ecosystem. In addition, plastic stored on land is exposed to oxygen and strong sunlight, which causes it to partially disintegrate and crack, resulting in the formation of microplastics. Microplastics, now pervasive in the water, soil, and even the air we breathe, present an increasing danger which is difficult to eliminate. As is lamented by Treebeard in 'The Lord

of the Rings' [8], "For the world is changing: I feel it in the water, I feel it in the earth, and I smell it in the air"; plastic pollution, much like the creeping evil in Tolkien's world, now threatens the very fabric of our environment. Microplastics can enter the upper respiratory tract with air, penetrate the digestive system with food and contaminated water, and penetrate the skin. Once in the body, they can cause cytotoxic effects, inflammation, and even lead to the production of reactive oxygen species [9].

In the face of this challenge, biotechnology offers a compelling answer through the power of enzymes. Plastics that have a hydrolysable bond in their structure may undergo degradation. Enzymes stand out compared to other biotechnological approaches due to their specificity, mild operational conditions, and potential for scaling. Enzymatic biocatalysis, an alternative and environmentally friendly approach to plastic degradation, involves replacing chemically catalysed processes with enzyme-driven ones.

While synthetic chemistry has catalysed the rise of plastics, enzymes—nature's own catalysts—may now play a pivotal role in their degradation. Ironically, we now turn to natural processes to break down materials once engineered to resist them. Inspired by the fictional idea of plastic-eating organisms in *Mutant 59: The Plastic-Eaters* [10], today's science is bringing this vision to life through enzyme-based degradation, a prime example of green chemistry's potential to eliminate hazardous waste sustainably.

This environmental era compels us to rethink our responsibility towards the planet and our place within it, as emphasised by Bruno Latour [11] in his concept of "earthbound"—a reminder that our environmental disruptions directly affect our own well-being. Driven by concern for the environment and a fascination for enzymatic potential, this dissertation investigates enzyme-based solutions to plastic pollution. By studying how enzymes recognise and degrade synthetic polymers, this work aims to contribute to a new wave of sustainable waste management practices. As Carl Sagan reflected in *Pale Blue Dot* [12], the Earth is the only home we have ever known, and it is up to us to protect it. Through this research, I hope to advance both science and environmental stewardship, addressing one of our most pressing global challenges.

This dissertation is organised as follows: Chapter 1 introduces the motivation, objectives and scope of this dissertation. Chapter 2 provides a comprehensive literature review on PUR and enzymes involved in its biodegradation, that led to a publication of a review article in *Biotechnology Advances* in 2024 [13]. This chapter also includes additional sections

detailing literature data on cutinases, as well as information on computational studies related to PUR degradation and mutational data on PUR-degrading enzymes.

Chapter 3 outlines the theoretical background of the computational methods applied in this study. Chapters 4-6 present and discuss the results for each of the three main objectives: investigating the binding of a PUR model to *TjCut2*, conducting computational protein design and mutational analysis of *TjCut2*, and validating the proposed *TjCut2* mutants. Finally, the last Chapter 7 summarises the main conclusions and outlines perspectives for future research.

Chapter 1: Objectives and scope of the thesis

The main objective of my thesis is to investigate the molecular determinants involved in enzyme-based degradation of synthetic polymers from the polyurethane family (PUR) and further optimise the degradation performances of a targeted enzyme using a combination of computational and experimental methods.

While most of the current research on plastic degradation focuses on polyethylene terephthalate (PET), PUR presents unique advantages and challenges for studying substrate recognition. PET is often considered a model system for biodegradation research due to its uniform bond types and consistent chemical environment, which simplifies the study of enzymatic cleavage. PUR, in contrast, features a variety of bonds and chemical contexts within a single polymer chain, making it an ideal candidate for investigating enzyme-mediated polymer recognition.

Beyond its structural complexity, PUR's widespread production also underscores the need for effective degradation methods. As the sixth most-produced plastic globally, PUR accumulates significantly in the environment. Its complex structure, which includes both C–O and C–N bonds, often leads to lower reaction barriers and nearly neutral reaction free energies, properties that can theoretically facilitate degradation [14,15]. However, PUR's structural diversity complicates the development of a unified enzymatic degradation strategy, posing unique challenges compared to more uniform plastics [16–18].

A review of current literature reveals that enzymatic PUR degradation research is still in its early stages. To date, only a few hydrolytic enzymes have been identified with the ability to depolymerise PUR [19–25]. The field is gradually expanding, with recent discoveries of novel fungal cutinases, such as CpCut1, which has shown enhanced activity relative to other fungal and bacterial cutinases [24], and urethanases [19,26], which target PUR degradation through urethane bond cleavage. These advancements highlight the potential for enzymatic degradation of PUR, but critical research gaps remain unaddressed.

Foremost among these gaps is the scarcity of computational studies on PUR enzymatic degradation processes. Experimental studies have also been limited, partly due to the proprietary and complex nature of many PUR compounds, such as the commonly used model substrate, Impranil DLN. Most research has focused on isolated PUR components, like carbamates or dicarbamates, rather than on the complete polymer structures. Monitoring degradation progress presents further challenges: many PUR polymers lack well-defined

structures, making it difficult to quantify the exact number of cleaved bonds or identify degradation intermediates. For instance, while turbidity reduction is often used as a measure of polyester PUR degradation, it remains unclear which bonds are being cleaved or what fraction must be hydrolysed to achieve transparency, commonly interpreted as "complete degradation" [24].

Key mechanistic questions also persist, including the exact nature of PUR binding to enzyme surfaces and whether binding constitutes the rate-limiting step in degradation. A study involving enzyme fused with binding module suggests that initial adsorption could play a crucial role in the degradation process [27].

Critically, no mutational data or computational protein engineering studies have been published on PUR-degrading enzymes. This dissertation addresses this gap by focusing on the mechanisms of binding between *TfCut2* and a model PUR substrate, Impranil DLN, and by investigating whether binding is the rate-limiting step in degradation. Through this research, mutations to *TfCut2* are proposed to enhance its activity and affinity for PUR substrates, marking the first computational protein redesign attempt for a PUR-degrading enzyme. By deepening the understanding of the enzymatic process involved in PUR depolymerisation, this study aims to use the acquired insights to enhance the stability, affinity and activity of the selected PUR-degrading enzyme, as well as to verify the hypothesis whether binding is the rate limiting step of the enzymatic PUR degradation process. The knowledge gained in this process is expected to advance both fundamental knowledge and practical applications, potentially enabling engineering of improved enzymes for more efficient PUR degradation.

To fulfill the objectives of my dissertation, I had to select both model PUR substrate and enzyme for its degradation. Impranil DLN, a polyester PUR model molecule containing ester and urethane linkages, was selected as a model substrate to provide insight into the recognition and binding of these functional groups by the enzyme. Impranil DLN, produced by Covestro (Germany), was previously used in many studies identifying PUR-degrading enzymes [20,28,37–39,29–36]. Based on my literature review of reported PUR-degrading enzymes, conducted in mid-2020/2021, I identified a cutinase from the bacteria *Thermobifida fusca* (*TfCut2*), whose PUR-degrading activity—tested on substrates including Impranil DLN—was examined by Schmidt et al. [20], as the most promising enzyme at that time for further study and redesign.

To investigate at molecular level, how this enzyme can degrade the PUR model and provide insights to guide the engineering of *TfCut2* to improve the performance of the enzyme to degrade PUR, I have developed a strategy that combines both modern computational techniques with experimental evaluation. Integrating *in silico* and experimental methods to ensure comparable results is often challenging, as simulations typically simplify complex biological systems and may not fully capture actual conditions. Moreover, computational studies typically examine single-molecule interactions in isolation, while experimental results represent an averaged view of numerous molecules in various conformational states. Experimental evaluation is therefore essential to assess whether computational predictions—such as binding affinities or structural stability of enzyme variants—accurately reflect the enzyme’s behaviour in realistic settings. After experimental evaluation, the next step would involve analysing the results to confirm whether the experimental data align with the computational predictions.

This work was thus divided into three main objectives that will be described in the results section:

1. *Characterisation of wild-type TfCut2 and identification of key molecular determinants involved in substrate binding* – characterising the *TfCut2* enzyme and analysing critical aspects of PUR recognition and binding, including structural elucidation of the model PUR, Impranil DLN, to understand its interaction with *TfCut2* in line with the enzyme's hydrolysis mechanism.
2. *Re-designing the substrate binding site of TfCut2* – suggesting a library of mutants of *TfCut2* to investigate the specific roles of residues in *TfCut2*'s binding site.
3. *Computational and experimental evaluation of TfCut2 mutants* – assessing the effects of the proposed mutations on binding and catalytic efficiency.

To fulfil the first objective— *Characterisation of wild-type TfCut2 and identification of key molecular determinants involved in substrate binding*, which involves characterising *TfCut2* and resolving structure of the model substrate, Impranil DLN, several *in silico* methods were applied to analyse critical aspects of PUR recognition and binding to *TfCut2* consistent with its hydrolysis mechanism. They included Rosetta molecular docking, MD simulations, and enzyme-ligand interaction analyses using ProLIF and MM-GBSA. The goal was to develop structural models for Impranil DLN and *TfCut2*, characterise *TfCut2*, and model its interactions with the substrate. This included ensuring that enzyme-ligand complexes adopted a 'productive pose,' aligning catalytic distances to facilitate the initial hydrolysis step. To achieve this,

a pipeline was developed to select frames from MD simulations in a productive configuration, which were then analysed to identify key residues in the binding site. The enzyme-ligand interactions, as well as individual amino acid contributions to Impranil DLN binding, were examined to characterise the molecular interactions critical for effective binding. Due to Impranil DLN's proprietary nature and structural inconsistencies in literature, it became evident during the research that the initially proposed and utilised structure might not be correct. As a result, NMR studies were carried out to verify the structure and provide a reliable model for all analyses (Fig. 0).

The second objective—*Re-designing the substrate binding site of TfCut2*, involving the selection of amino acid mutations to investigate specific residue roles in *TfCut2*'s binding site—was achieved by analysing data from the first objective, combined with an assessment of the mutability of *TfCut2* and the feasibility of introducing mutations that enhance enzyme-ligand interactions while preserving protein stability. Since Impranil DLN is not a native substrate of *TfCut*, I hypothesised that substrate recognition and binding affinity may be key determinants in facilitating catalysis, and that enhancing enzyme-ligand interactions could be beneficial to activity. For this, mutations were proposed to *TfCut2*-Impranil DLN complexes using Rosetta protein design. Moreover, sequence, structure, evolutionary variability of positions in sequence, and overall mutability of *TfCut2* were analysed using tools and webservers such as: FoldX, HotSpotWizard and BALCONY. This way, a library of *TfCut2* mutants was proposed (Fig. 0).

The third objective—*Computational and experimental evaluation of TfCut2 mutants*—was addressed using both experimental and computational approaches. Experimental tools, such as activity analysis and thermostability measurements, directly assessed the activity of *TfCut2* and its mutants on Impranil DLN degradation and the enzymes' thermostability. These methods, however, when applied to analysis of degradation of a PUR substrate, do not reveal the exact impact of each substitution or its influence on specific degradation aspects (e.g., catalytic efficiency, binding). To address this, additional computational and visualisation techniques were applied to develop a rationale behind the mutations in *TfCut2* and their potential influence on activity (Fig. 0).

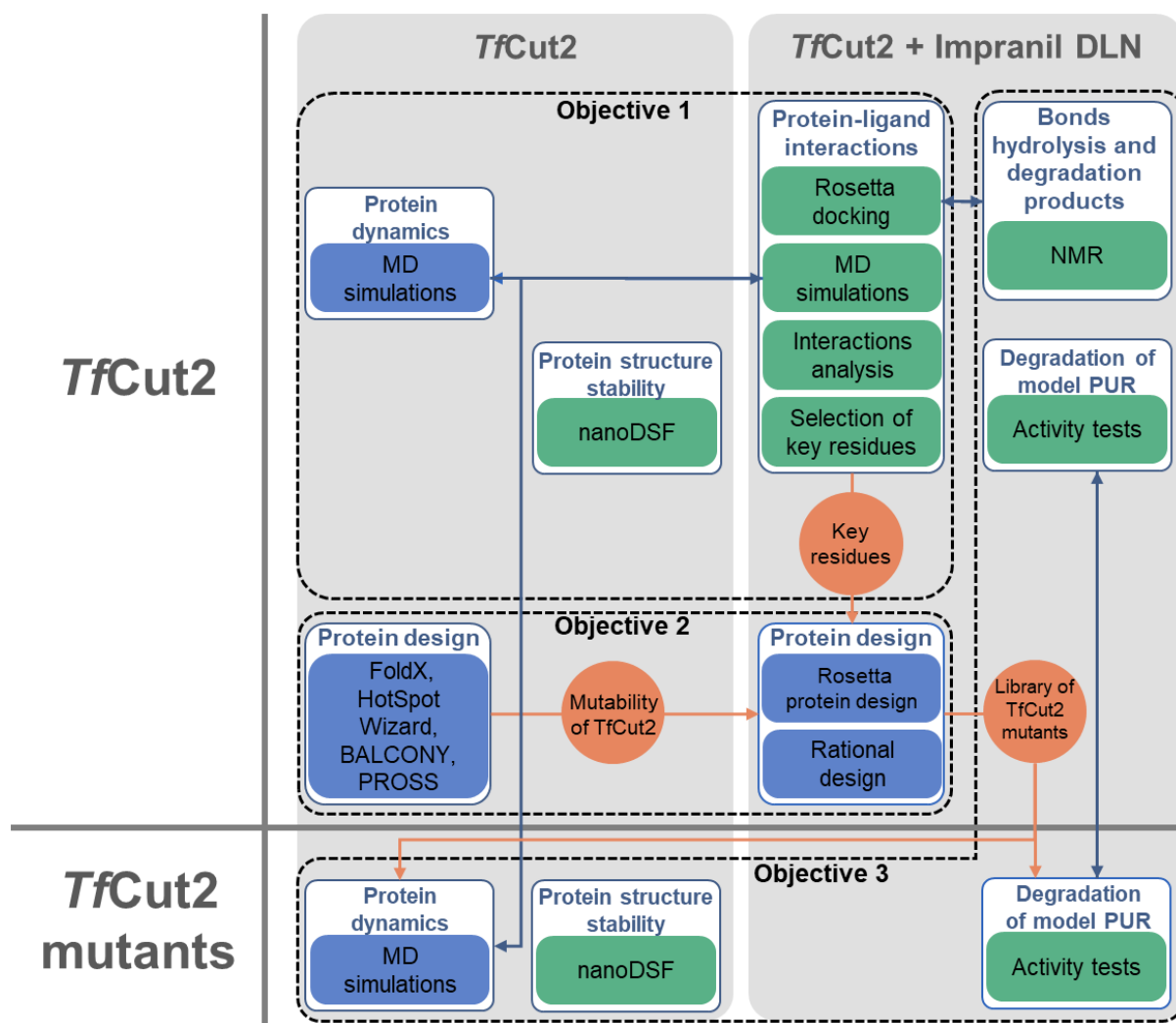


Fig. 0. Schematic overview of the computational and experimental methods design and integration with respect to objectives of this dissertation. Computational methods are represented in blue, and experimental methods in green, with comparable and corresponding results highlighted by blue connections. The specific objectives for each method are indicated in orange.

Author's Statement

This dissertation was completed as a doctorate cotutelle between Poland and France through a Campus France scholarship of the French Government. In particular, I benefited from the guidance of my French supervisor and the expertise of the French research team, specialising in enzyme and polymer degradation modelling, which enriched the computational aspects of this work.

Additionally, this dissertation was conducted as part of the 9th edition of the Diamond Grant national project, titled "Surface modifications of hydrolases degrading synthetic polymers directed towards increasing the spectrum of degradable plastics - theoretical and experimental study". The project (number: 0169/DIA/2020/49, value: PLN 220,000)

was managed by me, Agata Raczyńska, under funding from the Ministry of Science and Higher Education and implemented at the Faculty of Chemistry, Silesian University of Technology, Gliwice.

As the project manager and primary researcher, I led the design, planning, and execution of computational studies central to this research, benefiting from guidance from my supervisors and mentors throughout the project. In the context of the Diamond Grant, I also coordinated a collaborative team for the experimental components, contributing to the design and planning of experimental protocols and overseeing the execution of key experiments conducted by colleagues at the Silesian University of Technology. Specifically, the following individuals carried out the experimental work:

Production, purification, and activity testing on *TfCut2* and its mutants: Dr. Oksana Kovalenko and MSc Eng. Marzena Szawara.

Thermostability tests on *TfCut2* and its mutants: Dr. Katarzyna Papaj and Dr. Oksana Kovalenko.

NMR Analysis of Impranil DLN and its hydrolysis by *TfCut2*: Dr. Tadeusz Bieg, Dr. Katarzyna Żurawska, MSc Eng. Eng. Kinga Plasa, Dr. Anna Kasprzycka.

Chapter 2: Literature Review on PUR and PUR-degrading Enzymes

PUR are durable synthetic polymers widely utilised across numerous industries, contributing substantially to global plastic consumption. Despite their broad applicability, PUR pose significant challenges in terms of degradability and recyclability, mainly due to their intricate compositions and diverse formulations. The proprietary additives and structural variations found in commercial PUR formulations further complicate recycling efforts, making effective PUR waste management an urgent environmental priority. Although PUR incorporate hydrolysable bonds, primarily urethane and ester linkages, their depolymerisation requires the action of esterolytic and urethanolytic enzymes capable of cleaving these bonds. The structural diversity, binding site architecture, and active site composition of these enzymes are crucial factors influencing their specificity for different bond types and their efficiency in degrading complex, bulky substrates like PUR.

Parts of this chapter (specifically subsections 2.1–2.4) are based on a review article published in *Biotechnology Advances*, Volume 77, December 2024 [13]:

Raczyńska A., Góra A., André I.

An overview on polyurethane-degrading enzymes

Biotechnology Advances (2024) 77, 108439

This manuscript was authored primarily by Agata Raczyńska, who was involved in all steps of the article creation, whereas Dr. Artur Góra and Dr. Isabelle André were responsible for guidance, supervision and Review & Editing of the original manuscript and served as corresponding authors. No other researchers contributed to the manuscript.

Since this dissertation is prepared in accordance with both Polish and French university requirements as part of a dual doctorate cotutelle, reproducing the full text of the manuscript, rather than paraphrasing, was necessary to meet French institutional standards that regard rephrasing published content as potential plagiarism. While Polish guidelines typically favour rephrasing, the unaltered inclusion of the manuscript ensures compliance with both institutions.

The manuscript is a result of the initial literature review performed at the beginning of this dissertation, on the reported PUR-degrading enzymes in order to carefully select a model

enzyme, in this case *TfCut2*, for the studies. This analysis later expanded, resulting in the publication. The manuscript explores the enzymatic degradation of PUR, detailing the structural and functional characteristics of both enzymes and PUR substrates. It examines native enzymes reported to hydrolyse specific PUR bonds, discussing their structural configurations, reaction mechanisms, substrate specificity, and binding site architecture. Additionally, it highlights features necessary for enzyme redesign to enhance the efficiency of PUR biodegradation. Together, these insights provide a comprehensive foundation for readers, orienting them to the challenges of enzymatic PUR degradation and informing the objectives of this dissertation.

Chapter 2.1 constitutes an introduction to the problem of PUR waste and explains the need for research towards its sustainable management. Chapter 2.2 “PUR structures and functional groups” explains the structure and functional groups of PUR, challenges with managing its degradation, and introduces possibility of application of enzymes for its degradation. Chapter 2.3 “Enzymes for PUR degradation” constitutes an overview of reported enzymes that degrade PUR, together with information about their classification, activity, structure, architecture of the binding site and catalytic mechanism. Lastly, in chapter 2.4, conclusions and future perspectives on research on PUR enzymatic degradations are discussed.

Additionally, subsection 2.5 presents further findings and identifies research gaps uncovered through an extended literature review, that were not included in the published manuscript, which guide this study’s aims of contributing to sustainable PUR waste management and pollution reduction.

2.1. Introduction

Synthetic polymers, commonly known as plastics, are durable materials that possess many desirable features, but their high resistance to biodegradability, once considered an advantage, is now one of the main causes of pollution in terrestrial and aquatic environments. Production of plastics has outgrown most man-made materials, however, the management of their end-of-life remains very limited.

Polyurethanes (PUR) represent a prevalent and economically significant class of plastics, primarily derived from fossil-based resources, constituting 5.3% of the global plastics production, accounting for 21.2 Mt in 2022 [40]. Current trends in polymer research

show an increasing focus on developing PUR from natural and renewable raw materials, with the aim of proposing more sustainable and degradable alternatives [41,42]. The global market for PUR has witnessed substantial growth, with a valuation of USD 75.8 billion in 2022, projected to reach USD 108.8 billion by 2031, exhibiting a Compound Annual Growth Rate (CAGR) of 4.1% during the forecast period (2023-2031) [43]. Widely used across industries, PUR finds applications in coatings, elastomers (thermoplastics), and flexible and rigid foams (thermosets). Thermoset PUR, characterised by their chemically cross-linked nature, represent the most commercially prevalent form, albeit posing significant recycling challenges due to their complex composition and varied formulations. Combined with the diverse composition of PUR encountered during waste disposal, the effective management of PUR waste is a significant challenge.

Given the significant challenges associated with managing PUR waste, alternative solutions are being explored. Enzymatic polymer recycling has emerged as a promising solution, offering lower supply chain energy requirements and reduced greenhouse gas emissions [14,24,44–47]. However, scaling up enzymatic degradation on an industrial level presents a complex challenge that necessitates the development of specialised enzymes. Synthetic polymers, introduced on a large scale only in the 1960s, have not been subjected to the evolutionary pressures that would have fostered the emergence of effective polymer-degrading enzymes [2]. To address this challenge, three avenues are usually explored to identify novel enzyme catalysts: i) by searching novel adapted enzymes in environments with accumulated synthetic polymer waste, ii) by using promiscuous enzymes with potential polymer-degrading activity, and iii) by engineering existing enzymes towards enhanced polymer degradation. In particular, the discovery and engineering of efficient enzymes capable of degrading synthetic polymers have been reported with notable success. For instance, the enzymatic depolymerisation of polyethylene terephthalate (PET) into its constituent monomers has been achieved, allowing for the subsequent production of PET without any loss of properties [48–51].

While extensive work has been conducted on PET-degrading enzymes [52–55], research on enzymatic degradation of PUR, polyamides (PA) and other recalcitrant synthetic polymers remain in the lag phase. PUR and PA are structurally related through their nitrogen-containing backbones and liberate primary amines upon hydrolysis. Polymers with backbones composed of C-O and C-N bonds inherently have lower reaction barriers and nearly neutral reaction free energies. These structural features favourably contribute

to the degradation process of plastics. [14,15]. However, unlike PET and PA, which are composed of uniform monomers and feature exclusively either C-O or C-N bonds (ester and amide, respectively), PUR may contain many different bonds: urethane, ester, urea, amide and ether [16–18]. PUR presents a significant challenge for degradability and recyclability due to its intricate chemical composition and the steric effects associated with its supramolecular structures, which include soft and hard segments [24,56–58]. Moreover, commercial PUR structures are often proprietary, what prevents the development of a universal recycling method for all PUR families [15,59,68,69,60–67]. In some studies, however, PUR-based molecules were purposely synthesised by the authors and were thus rather well characterised [22,24,77,27,70–76]. Given the complexity and diversity of structural facets in PUR, coupled with the presence of additives, real-world pre- and post-consumer PUR products exhibit high recalcitrance and limited susceptibility to microbial and enzymatic degradation [24,56–58,78]. Most reported PUR-degrading enzymes, including urethanases, amidases, and esterases, primarily target soluble carbamates or polyester PUR, such as Impranil DLN, but not polycarbamates [3,14,81–83,20,31–33,37,38,79,80].

Within the scope of this review, we aim to address the inherent challenges posed by the complex and often unspecified composition of PUR structures, particularly in the context of enzymatic hydrolysis. These challenges significantly impact the study of enzymes involved in PUR degradation, leading to uncertainties in substrate specificity determination, limitations in accurately measuring enzymatic activity, and deficiencies in establishing standardised analytical methodologies. Furthermore, these obstacles hinder the scalability of enzymatic processes, impeding efforts to effectively translate laboratory findings into industrial applications. By examining these challenges, we aim to provide insights into the complexities of enzymatic PUR degradation and offer avenues for future research to overcome these hurdles effectively. Our focus aims at exploring the structural and functional characteristics of PUR and how they influence enzymatic degradation mechanisms. Subsequently, we survey documented native enzymes with reported efficacy in degrading various bonds within PUR. Our analysis encompasses a thorough examination of enzyme structures, reaction mechanisms, substrate preference, and the architecture of substrate binding and catalytic sites. Moreover, we propose essential features for the future redesign of enzymes to optimise PUR degradation efficiency. Finally, we outline prospective research directions aimed at advancing the field of enzyme-based degradation of PUR.

2.2. PUR structures and functional groups

The potential for enzymatic degradation of PUR (and other synthetic polymers) is significantly constrained by factors related to 1) the supramolecular structure of PUR, including the 3D polymer structure, hydrophobicity, crystallinity, and the availability of hydrolysable groups for enzymes, and 2) the conditions required for PUR enzymatic hydrolysis, such as the energy needed to hydrolyse bonds and the characteristics of specialised enzymes capable of binding to synthetic polymers and cleaving these bonds. Addressing these limitations involves two primary approaches: overcoming challenges related to PUR's structural properties, which may require pretreatment, and optimising enzymatic hydrolysis through the selection and redesign of appropriate enzymes. Subsections 1.1 and 1.2 of this review will respectively delve into these factors, focusing specifically on the information relevant to the enzymatic hydrolysis of PUR while directing readers to additional literature for comprehensive insights into PUR synthesis, structure, function, and applications [16,84–89].

2.2.1. PUR structures

PUR is a highly diverse group of synthetic polymers characterised by the presence of urethane bonds in their chain. These bonds are formed through a reaction between alcohols ($-\text{OH}$) and isocyanates ($-\text{NCO}$) (Fig. 1A) [16,88,90], constituting the core structure of PUR. Despite PUR's nomenclature, pure PUR are infrequently encountered in practical applications. Additionally, chain extenders and cross-linkers, carrying various functional groups, can be used to produce more rigid or mechanistically stronger PUR structures, respectively [85].

By combining structural units containing two functionalities, long linear polymers are formed, which are referred to as thermoplastic PUR (TPU). TPU are commonly described by two types of segments: hard and soft (Fig. 1A). Generally, the soft segments, made from high molecular weight polyols, are flexible and can even form foil-like structures. In contrast, the hard segments, composed of isocyanates and chain extenders, are rigid and immobile [57,91,92]. TPU are often semi-crystalline structures, as the segments are generally organised with a specific micro-segregation. The urethane linkages located near the isocyanate segments, have the possibility to be associated by hydrogen bonds to generate the hard segments of a PUR elastomer (Fig. 1B). The strong hydrogen bonding interactions between groups of the hard segments cause the chains to align in a very orderly fashion (Fig. 1C).

The percentage of NH groups forming hydrogen bonding interactions with carbonyl (-C=O) groups of the hard segment is large (> 45%). The network of strong hydrogen bonds present in the hard segment groups is sensitive to the solvent environment, in particular the presence of water molecules [93]. Segments content and properties can influence the biodegradation susceptibility of a given PUR [94,95], as mobile soft PUR segments are more easily recognised by enzymes than hard PUR segments. Consequently, the higher the content of hard segments, the lower the susceptibility to biological degradation [57].

Structural units with more than two functionalities enable polymer crosslinking, allowing the synthesis of branched three-dimensional PUR structures known as thermosets (Fig. 1D). As crosslinks are made up of covalent bonds, thermosets are thermally, mechanically, and chemically resistant and therefore their recycling is currently very difficult and energy intensive [96]. As opposed to thermoplastics, thermosets remain hard even when heated. Thermoset polyurethanes typically do not have significant crystalline regions due to their highly crosslinked structure, which restricts the movement and alignment of polymer chains necessary for crystallisation. However, localised or partial crystallinity can occur in certain formulations, especially in the hard segments of the polymer [97]. The reported PUR-degrading enzymes have been mainly tested on TPU and only few were reported to degrade thermoset PUR foams [58,70,77].

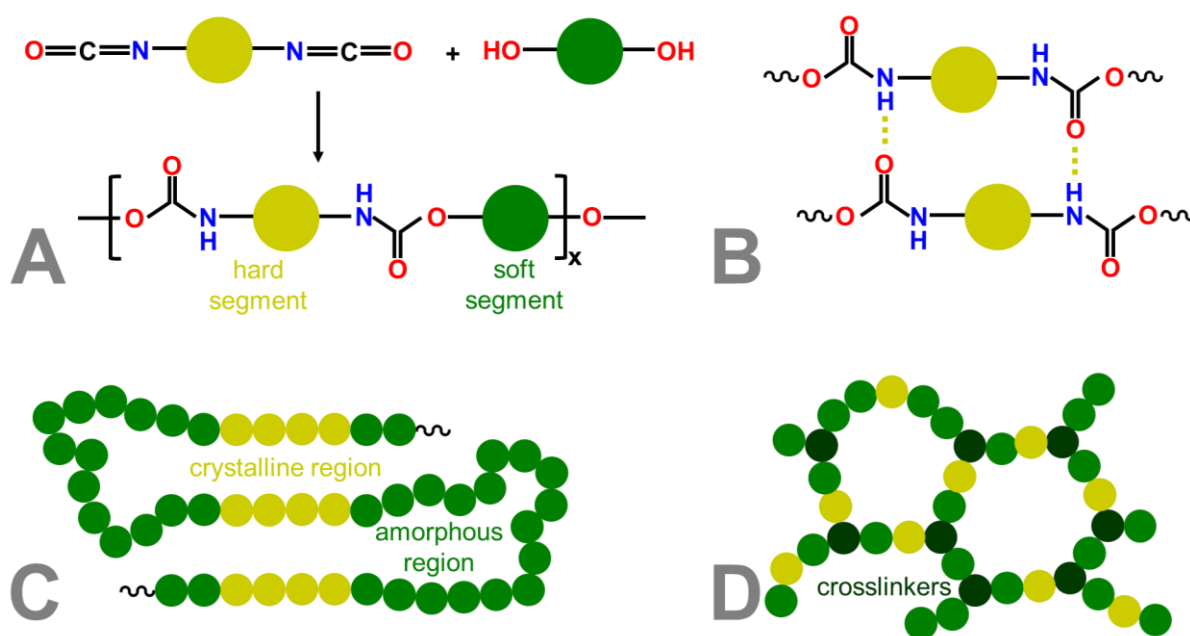


Fig. 1. PUR synthesis and structure. The polyol structural units are represented by green circles and isocyanate structural units as yellow circles. Isocyanate fragment can contain chain extenders and soft polyol fragment can additionally contain ether or ester bonds. **A)** Common route for the synthesis of PUR. **B)** Hydrogen bonds forming between urethane linkages in PUR.

C) Linear TPU structure. TPUs are often semi-crystalline structures. The hard segment is a block segment with low mobility mainly formed by the isocyanate and the short-chain extender. By contrast, the soft segment is mainly based on the long polyol part. D) Simplified structure of a thermoset. The linear polymer chains are covalently connected by crosslinking compounds indicated by dark green circles that can be e.g. trifunctional crosslinking hydroxyl compound.

2.2.2. PUR functional groups and their enzymatic hydrolysis

The incorporation of various structural units, including isocyanates, polyols, cross-linkers, and chain extenders, not only alters the properties of PUR but also introduces different functional groups beyond urethane bonds into their structure. In the case of polyols, they are most often either based on polyethers, especially in thermosets, which is the main application of PUR; or on polyesters, particularly in TPUs. Corresponding polymers are thus often referred to as polyether PUR and polyester PUR, respectively. Overall, PUR may contain urethane, ester, ether, amide and urea functional groups, characterised by either C-N or C-O links in their backbone [98]. Enzymes with specific activities can target these bonds for hydrolytic cleavage, however, ether bonds demonstrate exceptional hydrolytic stability, rendering polyether PUR more suitable for applications in moist environments compared to polyester PUR [84].

Functional groups containing carbonyl groups facilitate the nucleophilic attack on their carbonyl carbon, leading to the cleavage of neighbouring C-N or C-O bonds. The C-N link is present in urethane, amide and urea bonds in PUR and can be hydrolysed by enzymes such as: urethanases, amidases and ureases that belong to EC 3.5.1 (3. Hydrolases; 5. Acting on carbon-nitrogen bonds other than peptide bonds; 1. In linear amides) (Fig. 2A-C). The C-O links are located in urethane and ester functional groups. The ester and urethane bonds can be hydrolysed by enzymes: esterases, cutinases and lipases that are categorised under EC 3.1.1 (3. Hydrolases, 1. Acting on ester bonds, 1. Carboxylic ester hydrolases) [57,99,100] (Fig.2D-E). Throughout this review, we will denote these enzyme groups as "urethanolytic" and "esterolytic," as their activities predominantly involve the hydrolysis of urethane and ester bonds in PUR or analogous compounds.

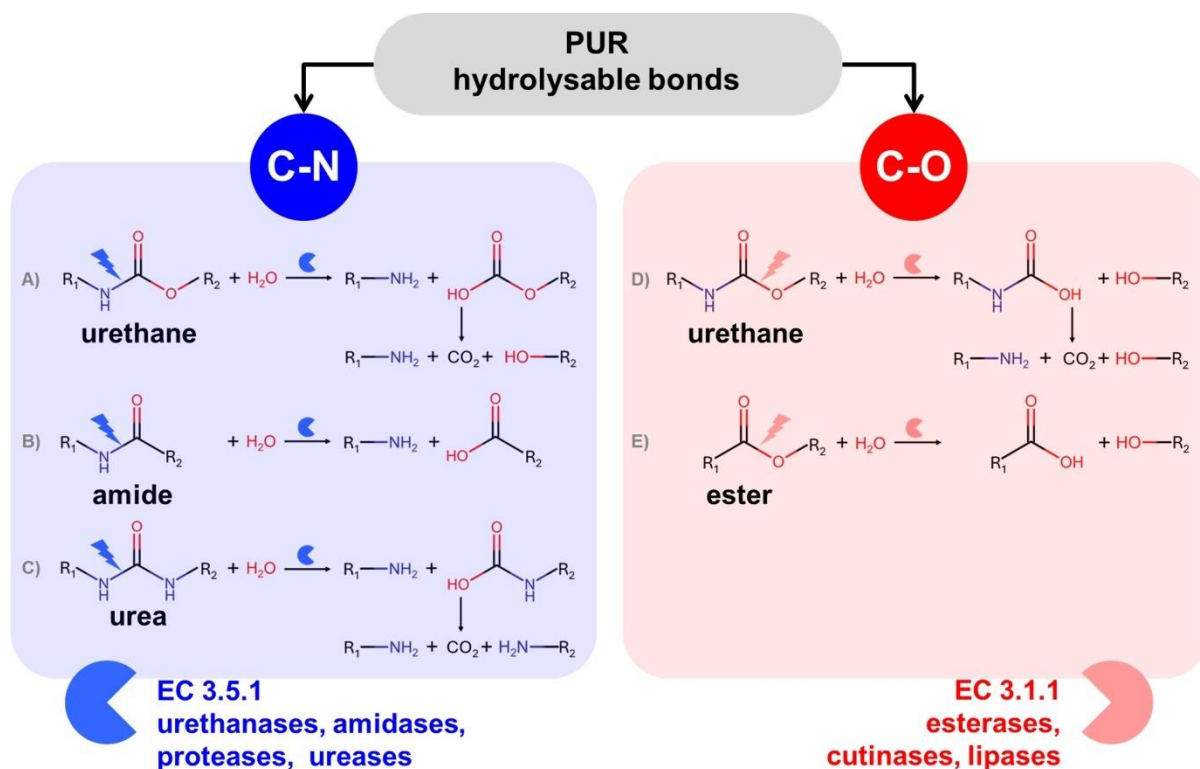


Fig. 2 Two types of hydrolysable bonds in PUR: C-N (A-C) and C-O (D-E). Functional groups containing C-N bonds (on blue background) include **A)** urethane, **B)** amide, and **C)** urea; and those containing C-O bonds (on red background) include **D)** urethane and **E)** ester. The hydrolysis reaction pathways by urethanolytic enzymes (urethanases/amidases/ureases) and esterolytic enzymes (esterases/lipases/cutinases) are depicted. Following enzymatic cleavage, the subsequent reactions are characterised by spontaneous decomposition, leading to further breakdown of the polymer. The chemical structures were drawn using ChemSpaceE [101].

The primary bonds within PUR, namely urethane bonds, comprise both C-N and C-O bonds, suggesting the potential for hydrolysis by enzymes possessing either urethanolytic or esterolytic activities. Urethanolytic enzymes, acting on the C-N bond, catalyse the hydrolysis of urethane bonds into an amine and an alkyl carbonate, which subsequently decomposes into an alcohol and carbon dioxide. Conversely, esterolytic enzymes, targeting the C-O bond, hydrolyse urethane bonds into an alcohol and a carbamic acid group, with the latter decomposing into an amine, releasing carbon dioxide [77,84,99]. Despite the different pathways, the products of urethane bond hydrolysis remain consistent, regardless of the cleaved bond: an amine, an alcohol, and carbon dioxide (Fig. 2A, 2D).

In terms of energy considerations, ester bonds generally exhibit lower resistance to hydrolysis compared to urethane bonds [102]. Several factors influence the hydrolysis resistance of these bonds, including temperature, steric hindrance, and pH. Steric hindrance not only impacts the accessibility of the bond to water but also affects the hydrophobicity

of the polymer. pH plays a significant role in hydrolysis reactions, particularly in acidic conditions where the reaction is catalysed. Esters undergo hydrolysis to form acid and alcohol groups (Fig. 2E), potentially leading to an autocatalytic reaction when additional acid functionality is introduced [84].

So far, mainly enzymes degrading polyester PUR have been reported. It is not surprising, as easily-hydrolysable ester linkages in polyester PUR are often found in the soft fragments constituted of polyols, which represent vulnerable points in the polymer structure. Polyester PUR are more prone to rapid degradation, especially in high humidity or when exposed to water, leading to faster disintegration due to volume swell and property reduction. Water infiltration between molecules acts as a plasticizer, forming hydrogen bonds with polar urethanes and disrupting internal hydrogen bonds between polymer chains. In contrast, polyether PUR exhibits low water absorption rates and minimal volume swell, rendering them water-repellent and resistant to disruption by water interacting with urethane bonds. Additionally, ether bonds are highly resistant to hydrolysis [47,84], making them less susceptible to be degraded by hydrolases.

Most PUR-degrading enzymes were identified using a model PUR molecule, Impranil DLN, which is in fact a 40% water dispersion of polyester PUR. As Impranil DLN becomes translucent when the hydrolysis of ester bonds occurs in its structure, it is possible to develop activity assays based on visual inspection of Impranil DLN plates [20,80,103–106]. Consequently, the majority of identified polyurethanases are, in fact, polyesterases capable of degrading ester bonds in polyester PUR. Impranil DLN chemical structure is proprietary, although its chemical structure was proposed in two studies, first in 2015 by Biffinger et al. [3] and then in 2022 by Fuentes-Jaime et al. [4]. While Biffinger et al. describe the synthesis of Impranil DLN from hexamethylene diisocyanate and polyhexane neopentyl adipate polyester, Fuentes-Jaime et al. suggest that Impranil DLN is derived from hexamethylene diisocyanate, neopentyl glycol, adipic acid, and 1,6-hexanediol, along with certain plasticizers and chain extenders. The lack of clarity regarding the composition of Impranil DLN utilised in PUR hydrolysis studies poses numerous obstacles [107]. These include the identification of the precise bonds whose cleavage triggers translucency, quantifying the proportion of bonds that must be cleaved to induce this effect, understanding the resulting products of hydrolysis, determining the extent of substrate degradation, and evaluating the possibility to recover PUR building blocks from the hydrolysed substrate. These uncertainties introduce complexity into the comparison of enzymatic activities across various research endeavours.

Recently, a novel polyester PUR, poly(1,4-butylene adipate)-based PUR (PBA-PUR), was synthesised and proposed as a model TPU to replace Impranil DLN. PBA-PUR was synthesised from 4,4'-methylene diphenyl isocyanate and PBA. The authors suggest that it more closely resembles commercial bulk PUR materials compared to Impranil DLN, which is primarily utilised in textile coatings [76]. Similar to Impranil DLN, PBA-PUR can be employed for screening microorganisms and enzymes for polyester PUR-degrading activity, as it becomes translucent upon degradation [23,24,76]. Furthermore, due to its well-defined structure, the metabolites resulting from its degradation, which include adipic acid, 1,4-butanediol, and 4,4'-methylenedianiline, can be readily analysed.

In summary, enzymatic degradation of PUR faces significant challenges due to their complex structure and limitations in enzymatic hydrolysis. These limitations are attributed to factors such as the three-dimensional organisation of PUR, its hydrophobicity, crystallinity, and the presence of various hydrolysable bonds. While enzymatic hydrolysis can target these bonds, its efficacy is influenced by bond energy and enzyme specificity. Polyester PUR is more susceptible to hydrolysis than polyether PUR due to its easily hydrolysable ester functional groups and reduced hydrophobicity, allowing easier permeation of water molecules and enzymes. Pretreatment methods are often necessary for enhanced enzymatic degradation of synthetic polymers. Types of pretreatments applied for synthetic polymers include thermal and thermochemical, oxidative, chemical, and mechanical methods [108,109]. For PUR, primarily thermochemical and mechanical methods of degradation have been proposed, such as hydrolysis [110], glycolysis [26,111,112], phosphorolysis [113], hydroglycolysis [41,114], and subcritical hydrothermal liquefaction [115]; these processes could serve as effective pretreatment techniques. Such approaches may be instrumental in overcoming the challenges of PUR biological degradation by making the polymer more accessible to enzymatic action and thus enhancing degradation efficiency.

Another important factor is the effect of natural aging, which refers to the physical and chemical changes that materials undergo over time due to environmental factors such as exposure to light, oxygen, humidity, and temperature fluctuations. For PUR, natural aging can significantly impact biodegradability, particularly when it comes to enzymatic degradation. While aged PUR might be more susceptible to enzymatic degradation due to increased surface area, lower molecular weight, and the introduction of new functional groups, the effects of aging can also make the material more resistant if cross-linking and crystallinity increase [116–118]. Despite the recognised impact of natural aging on PUR properties, there is limited

research specifically exploring how these aging-induced changes influence subsequent enzymatic degradation. Understanding these interactions could be crucial for developing more effective recycling and biodegradation strategies for PUR waste.

A comprehensive approach to PUR depolymerisation may entail employing a diverse array of enzymes that target specific types of chemical bonds, which could enhance the efficiency and effectiveness of the recycling process. Such a concerted strategy has already been proposed as a means to completely degrade PUR into recoverable building blocks, highlighting the importance of enzyme cooperation in the development of efficient biotechnological strategies for PUR waste management and recycling [4,119,120]. Applying an esterolytic enzyme to initiate the depolymerisation process of polyester PUR, succeeded by the enzymatic cleavage of urethane bonds within the fragmented PUR via an urethanolytic enzyme, offers a promising strategy to circumvent structural limitations arising from the restricted accessibility to urethane bonds in PUR. This dual-enzyme approach holds potential for facilitating the regeneration of PUR building blocks (Fig. 3). However, to date, comprehensive life cycle assessments (LCAs) of PUR derived from structural units obtained through biological recycling remain absent from the literature. Existing LCAs have primarily focused on PUR production from polyols regenerated via chemical recycling pathways [15,121], or from bio-based sources [122].

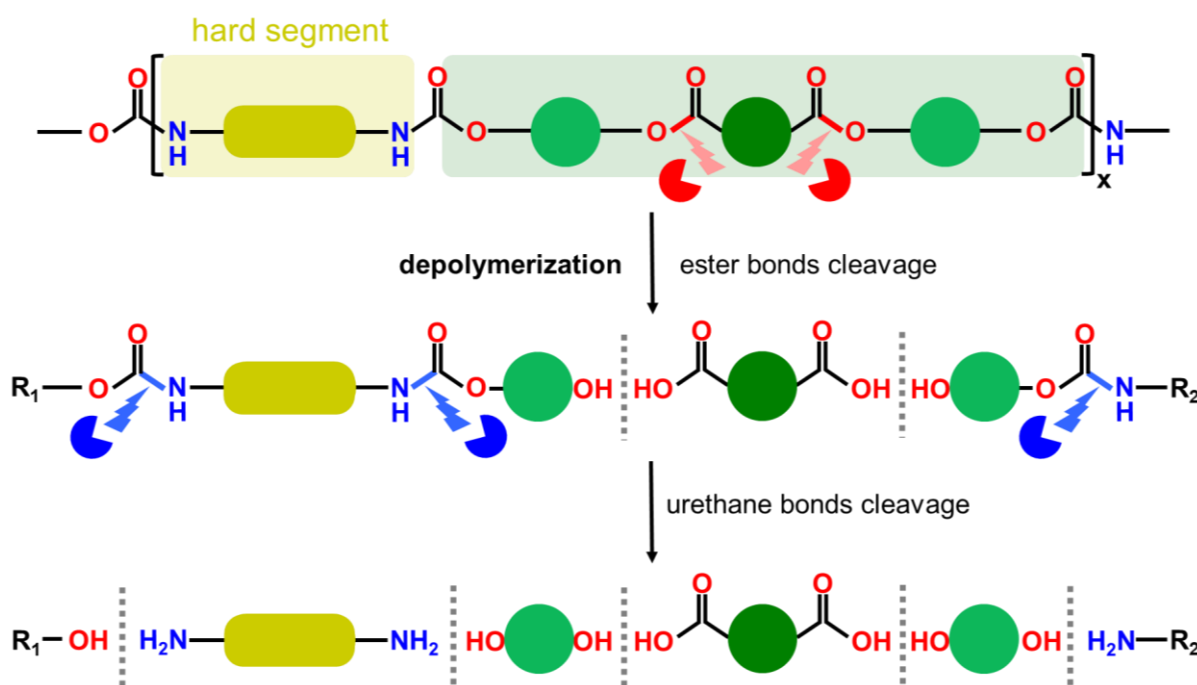


Fig. 3. A proposed holistic enzymatic degradation pipeline for polyester PUR, based on literature [4,119,120], entails the sequential utilisation of two classes of enzymes: esterolytic enzymes for initial depolymerisation through the cleavage of ester bonds in soft

PUR segments, followed by urethanolytic enzymes for the degradation of urethane bonds in exposed PUR fragments post-depolymerisation. This concerted enzymatic action aims to facilitate the retrieval of structural units inherent in PUR, namely diols and diisocyanates, thereby enabling their potential reuse in subsequent manufacturing processes. Through this systematic approach, the enzymatic breakdown of polyester PUR can be optimised, offering a sustainable solution for PUR recycling and resource recovery.

2.3. Enzymes for PUR degradation

The enzymes reported to have PUR-degrading activity are mainly hydrolases and oxido-reductases [70]. Oxido-reductases, however, can only catalyse non-specific oxidations under certain conditions and their degradation performance on PUR is often low. These enzymes typically release small quantities of undefined degradation products, which cannot be recovered in large quantities and may have other environmental toxicity [70,123]. As a result, oxido-reductases are unsuitable for the development of plastic degradation and recycling techniques.

Instead, a more viable option is the use of hydrolases, which constitute a broad class of enzymes that catalyse bond cleavage by reaction with water. The natural function of most hydrolases is to breakdown nutrients into smaller units for digestion. Hydrolases are ideal catalysts, as they display a broad substrate specificity, do not require cofactors, are usually stable and can be easily purified, as they are generally extracellular enzymes [124]. However, enzymes that degrade insoluble or large molecules, such as those in PUR, can also be cell-associated. These cell-associated enzymes, often linked to biofilm formation on insoluble substrates like PUR, tend to have higher specificity against high molecular weight substrates [72,125,126]. Hydrolases, including esterases, lipases, cutinases, amidases, proteases, and urethanases, have been reported to degrade certain PUR [57,58].

Given the limited information available on PUR-degrading enzymes in the literature, our aim is to systematise the current knowledge and offer classification and characteristics of native enzymes known to degrade PUR. For this purpose, in this review, we focus on describing PUR-degrading hydrolases that are included in the PAZY database (<https://pazy.eu>) [127] (as of August 2024) with reported degradation activity towards various PUR.

The PAZY database gathers 31 hydrolases with verified activity on PUR. We discarded from the analyses two enzymes that did not have properly reported sequences or translated

genes (*Pestalotiopsis microspora* lipase, *Rhodococcus equi* TB-60). We also discarded five putative urethanases (*Klebsiella oxytoca* 1686, *Burkholderia phytofirmans* DSM17436, *Microbacterium hydrocarbonoxydans*, *Sporosarcina ureae* P17a, *Rhodococcus erythropolis* CCM2595) which were not confirmed in urethanase activity screening on ethyl carbamate as reported by the authors [83]. Additionally, one recently described fungal cutinases, *Humicola insolens* (HiC), not available in the PAZY database, was included in our analysis as this enzyme has a well documented PUR-degrading activity on several PUR [22]. Altogether, 25 enzymes were analysed in more detail (Table. 1).

Table 1. Details of selected PUR-degrading enzymes reported in the PAZY database. Columns: Enzyme type - enzyme classification based on the dendrogram in Fig. 4A; Enzyme – general name of the presented enzyme, usually containing name of the host organism; Accession – Uniprot or NCBI id to the enzyme sequence; PDB - if available, PDB id of the crystal structure is provided; Catalytic triad – residue ids of amino acids constituting catalytic triad of a given enzyme; the numbering is according to the first reference in the Accession table; Oxyanion hole - residue ids of amino acids constituting oxyanion hole of a given enzyme; Size [kDa] - size of a given enzyme in kDa; Cleavage site – the type of bond(s) in PUR that were cleaved by a given enzyme in the literature; Substrate for activity test and reference - PUR substrate, on which a given enzyme’s activity was tested.

Enzyme type	Enzyme and origin	Accession	PDB	Catalytic triad	Oxyanion hole	Size [kDa]	Cleaved bond	Substrate for activity test and references
Bacterial cutinases	<i>TfCut2</i> <i>Thermobifida</i> (<i>Thermomonospora fusca</i> , (Cut2-kw3)	E5BBQ3_TH EFU	4CG1, 4CG2, 4CG3	S130 D176 H208	Y60 M131	28.4	ester	Impranil DLN; Elastollan B85A-10 and C85A-10 (supplied by BASF) [20]
	<i>Tcur0390</i> <i>Thermobifida</i> (<i>Thermomonospora curvata</i> DSM43183	ACY95991.1 D1A2H1		S161 D207 H239	F93 M162	31.3	ester	
	<i>Tcur1278</i> <i>Thermobifida</i> (<i>Thermomonospora curvata</i> DSM43183	D1A9G5, ACY96861.1	7YKO, 7YKP, 8GZD	S159 D205 H237	F91 M160	31.2	ester	
	LCC leaf compost metagenome	G9BY57	4EBO and others	S165 D210 H242	Y95 M166	27.8	ester	
	<i>Hfor_PE-H</i> <i>Halopseudomonas formosensis</i>	WP_0905386 41.1		S171 D217 H249	G97 M172	32.3	ester	Impranil DLN-SD; solid commercial bio-based polyester PUR coatings: ICO-THANE and ICO-FIX (I-COATS N.V (Antwerp, Belgium)) [128]
Fungal cutinases	<i>HiC</i> <i>Humicola insolens</i>	ASK40094.1 A0A075B5G4	4OYY, 4OYL	S105 D160 H173	S28 Q106	19.9	ester, urethane, amide	Polyurethane-polyester copolymer; <i>p</i> BPB, <i>p</i> NPC, <i>p</i> NPBS and <i>p</i> NPA [22]
	<i>CpCut1</i> <i>Cladosporium</i> sp. P7	PRJNA99275 7 OR245267		S129 D184 H197	S50 Q130	22.5	ester	Impranil DLN-SD; TPU film PBA-PUR;

								post-consumer polyester PUR foam [24]
	BaCut1 <i>Blastobotrys</i> sp. G-9	XAQ58225		S107 D184 H199	G38 Y106	23.4	ester	PBA-PUR, polyester PUR foam [23]
Esterases	PudA <i>Comamonas (Delftia) acidovorans</i> TB-35	BAA76305.1 Q9WX47		S225 E350 H459	H140 G141 G142 A143	57.8	ester	Impranil DLN [28–30]; Polyester PUR synthesised from: poly(diethylene glycol adipate) and 2,4-tolulene diisocyanate [72]; poly(diethylene glycol adipate) [125]
	<i>Diutina (Candida) rugosa</i>	20261 P20261	1CRL, 1LPM, 1LPN, 1LPO, 1LPP, 1LPS, 1TRH, 3RAR	S224 E356 H464	F136 G137 G138 G139	58.6	ester	Impranil DLN [31]
	CE_Urb metagenome-derived	A0A2I2K6T5 SIP63154.1		S127 D230 H262	S56 S128	32.5	ester	Impranil DLN; pNP chromogenic esters of various chain lengths (C2, C4 and C16) [32]
Lipases	PueA <i>Pseudomonas chlororaphis</i>	AAD22743.1 A0A0D5XYX 5		S207 D255 H313	T143 L208	64.8	ester	Impranil DLN [33–36]
	PueB <i>Pseudomonas chlororaphis</i>	AAF01331.1 Q9R9H2		S152 ? ?	? L153	60.1	ester	
	PueA <i>Pseudomonas protegens</i> strain Pf-5	AA92471.1 A0A2C9EMV 6		S207 D255 H313	T143 L208	65.0	ester	Impranil DLN [37]
	PueB <i>Pseudomonas protegens</i> strain Pf-5	AA92474.2		S149 D198 H256	L150 T95	59.1	ester	
	PulA <i>Pseudomonas fluorescens</i> , esterase	AAF66684.1 Q9LAB9		S184 D232 H290	L185 ?	48.2	ester	Impranil DLN [38,39]
	CalB <i>Candida antarctica</i>	P41365	ITCA and others	S105 D187 H224	Q106 T40	33.0	ester	TDI- and MDI-PCL based polyester PUR foams and polyester TPU coatings [77]
Urethanas es	<i>Lysinibacillus fusiformis</i>	KU353448 A0A4Y5NHK 8		K81 S156 S180	T177 A178 G179	51.5	urethane	Ethyl carbamate [82]
	amdS <i>Aspergillus oryzae</i>	Q12559		K130 S205 S229	I226 G227 G228	60.1	Urethane, amide	Ethyl carbamate; methyl carbamate, n-butyl carbamate, acetamide, propionamide, butyramide, acrylamide, meth-acrylamide, benzamide, thioacetamide, and nicotinamide [81]

CPUTNase <i>Candida parapsilosis</i> NBRC 708	P20261 A0A679EIJ6		K149 S224 S248	I245 G246 G247	61.8	Urethane, amide	Ethyl carbamate, methyl carbamate, n-butyl carbamate, acetamide, propionamide, butyramide, acrylamide [129]
AmdA <i>Agrobacterium tumefaciens</i> d3	AAK28498.1 Q9AHE8		K98 S147 S197	Q194 G195 G196	55.9	Urethane, amide	Ethyl carbamate [83]; racemic 2-phenylpropionamide (amine) [130]
<i>Rhodococcus erythropolis</i> MP50	AY026386		K105 S179 S203	E200 A201 G202	55.6	urethane	Ethyl carbamate [83]
UMG-SP-1 metagenome-derived	WBR49956.1		K77 S152 S176	I173 G174 G175	45.4	urethane	Low molecular weight dicarbamates: Methylenedianiline (MDA)-methanol, MDA-ethanol, MDA-benzyl alcohol, Toluenediamine (TDA)-ethoxyethanol, 2,4-TDA-diethylene glycol, and 2,6-TDA-diethylene glycol [26]; additionally UMG-SP-1: thermoplastic polyester PUR [19]; additionally UMG-SP-2: low molecular weight dicarbamates after glycolysis of TDI-based polyether PUR fragments [26]
UMG-SP-2 metagenome-derived	WBR49957.1		K76 S151 S175	I172 G173 G174	45.7	urethane	
UMG-SP-3 metagenome-derived	WBR49958.1		K76 S151 S175	I172 G173 G174	45.6	urethane	

2.3.1. Enzymes classification

All 25 selected enzymes were further analysed by computing a Multiple Sequence Alignment (MSA) and a phylogenetic tree (Fig. 4A). Overall, five clusters of homologous enzymes emerged and two outliers, CE-Ubrb and CalB, were found (Fig. 4A). These groups were classified based on their: 1) sequence and MSA analysis, 2) classification in Uniprot [131] and NCBI [132] databases, and 3) hydrolytic selectivity of PUR bonds (as reported in published studies listed in Table 1). The esterolytic enzymes were found in four distinct groups (referred to as “Bacterial cutinases”, “Fungal cutinases”, “Esterases” and “Lipases”). All the esterolytic enzymes belong to the alpha/beta-hydrolase fold superfamily and they display the classical Ser-His-Asp/Glu catalytic triads. Urethanolytic enzymes, on the other hand, are found in a single group, referred to as “Urethanases” that all have Ser-(cis)Ser-Lys catalytic triad (Fig. 4A; Table 1). The “Urethanases” group exhibits the most variation among its enzyme members in terms of sequence identity (Fig. 4B).

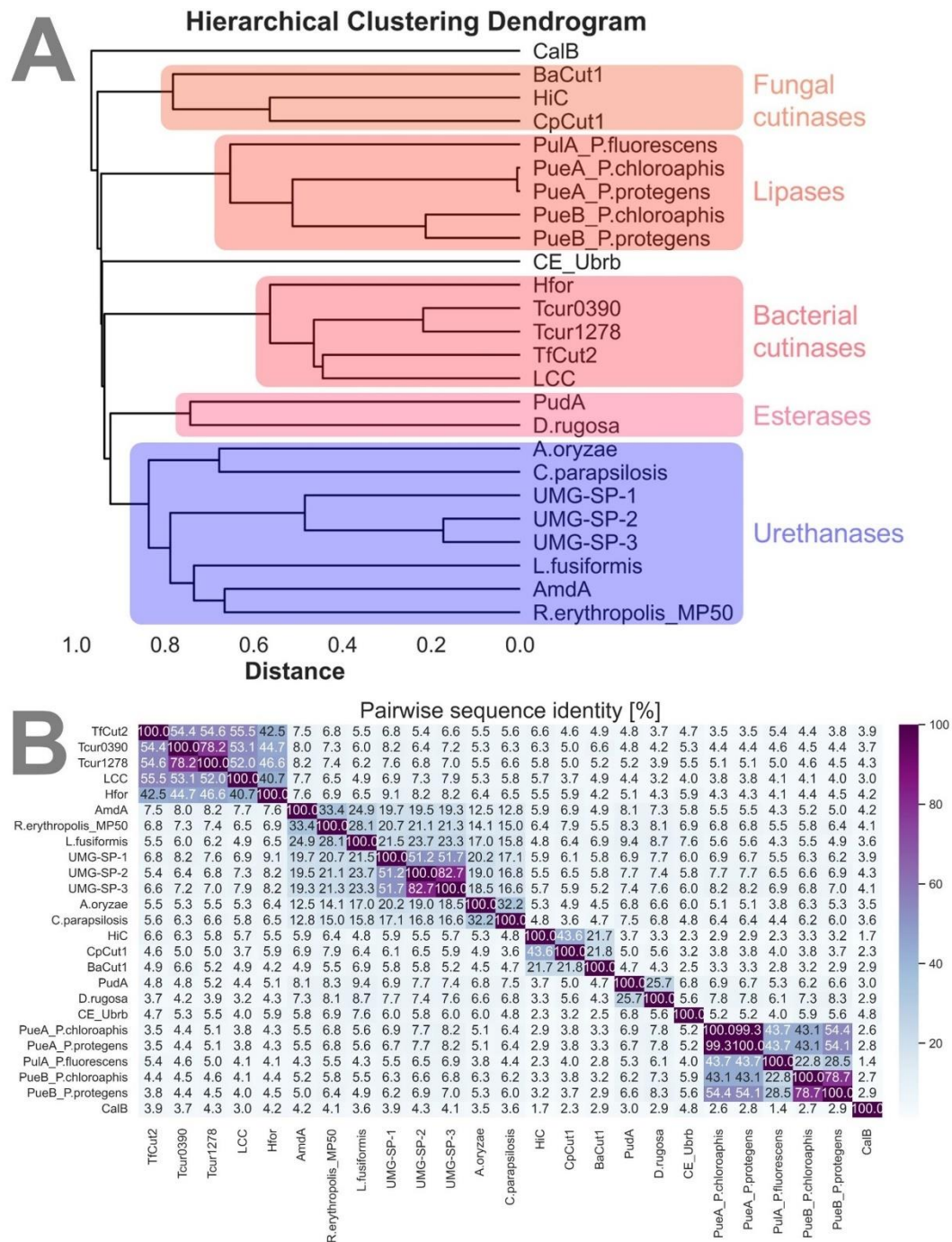


Fig. 4. **A)** Dendrogram of 25 enzyme sequences showing similarity relationships between PUR-degrading enzymes included in the PAZY database. Esterolytic enzymes marked in red and urethanolytic enzymes in blue. Additionally, one fungal cutinase, *HiC*, identified from the literature as having a PUR-degrading activity was added to the dendrogram. MSA and phylogenetic tree were prepared using the MAFFT webserver [133] with the G-INS-1 progressive method. The enzymes were grouped based on pairwise sequence alignment using Ident and Sim suite [134], with a threshold of sequence identity >10%. Group classification was determined according to the classification of individual enzymes in the Uniprot [131] and NCBI [132] databases. **B)** Heatmap of pairwise sequence identity [%] of all the 25 selected enzymes. Pairwise sequence alignment was calculated using Ident and Sim [134] based

on the MSA computed by MAFFT [133]. The data was curated and visualised using Pandas [135] and Seaborn [136] Python libraries.

While this review initially categorises enzymes based on their primary activity—amidases/urethanases and esterases/lipases/cutinases—it is important to acknowledge that these enzymes often exhibit substrate promiscuity, meaning they can act on both ester and amide/urethane bonds. This promiscuity is particularly relevant for the degradation of polyester PUR, which contains both types of bonds.

Recent studies have highlighted the dual activity of certain hydrolases, where enzymes traditionally classified as esterases also exhibit amidase activity, and vice versa. For instance, it was demonstrated through computational approaches that the substrate promiscuity of *Candida antarctica* lipase B (CalB) extends to amidase activity, a finding that has been supported by experimental data [137,138]. Similarly, esterases were engineered to enhance its activity on amide bonds, effectively switching its specificity [139,140].

This promiscuity not only expands the potential applications of these enzymes in biocatalysis but also suggests that the enzymatic degradation of PUR might involve a more complex interplay of activities than previously assumed. The implications for PUR recycling are significant, as a single enzyme or a consortium of enzymes with overlapping specificities could potentially streamline the degradation process by targeting both ester and amide bonds within the polymer matrix.





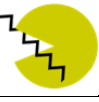

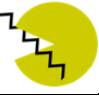


Given the growing body of research in this area [141–144], it is clear that understanding and leveraging enzyme promiscuity will be critical for the development of more efficient and versatile enzymatic systems for PUR degradation.



2.3.2. Structures and binding sites

For each enzyme, we curated 3D crystal structures or AlphaFold 2 models of enzymes, to examine and elucidate the shared structural motifs characteristic of the respective group. For the enzymes that do not have a crystallographic structure available in the Protein Data Bank (PDB) [145], or a 3D model in the AlphaFold2 Protein Structure Database (AlphaFold DB) [146–148], three-dimensional organisations were derived through computational modeling using AlphaFold 2 [146]. The details of the structure's origin are listed in Table 2.

Table 2. The binding and active site characteristics of the selected PUR-degrading enzymes. Columns: **Group** - enzyme classification as in the dendrogram in Fig. 4A; **Enzyme** – shortened

name of the presented enzyme; **Structure** – the origin of a given enzyme’s 3D structure; “PDB” if a crystal structure is available in the PDB database, “AF DB” if a model was downloaded from AlphaFold DB, or “AF2” if a structure was modelled using AlphaFold 2; **Binding site** – given enzyme’s binding site architecture based on the models presented in Fig. 5; **Catalytic triad** – amino acids forming the catalytic triad of a given enzyme, amino acids coloured according to Clustal Omega; **Oxyanion hole** – amino acids forming the oxyanion hole of a given enzyme, amino acids coloured according to Clustal Omega; **Fold** – the fold of an enzyme structure.

Group	Enzyme	Structure	Binding site architecture	Catalytic triad	Oxyanion hole	Fold
Bacterial cutinases	<i>TjCut2</i>	PDB		S H D	Y M	α/β
	<i>Tcur0390</i>	AF DB			F M	
	<i>Tcur1278</i>	PDB			Y M	
	LCC	PDB			G M	
	<i>Hfor</i>	AF2				
Fungal cutinases	<i>HiC</i>	PDB		S H D	S Q	
	<i>CpCut1</i>	AF2			G Y	
	<i>BaCut1</i>	AF2				
Esterases	PudA	AF DB		S H E	H G G A	
	from <i>D.rugosa</i>	PDB				
Outlier	CE-Ubrb	AF DB		S H D	S S	
Lipases	PueA <i>P. chlororaphis</i>	AF DB		S H D	Y K	
	PueA <i>P. protegens</i>	AF DB				
	Pu1A <i>P. fluorescens</i>	AF DB			L ?	
	PueB <i>P. protegens</i>	AF2			L T	
	PueB <i>P. chlororaphis</i>	AF DB			? L	
Outlier	CalB	PDB		S H D	Q T	
Urethanases	AmdA	AF DB			Q G G	?
	from <i>L. fusiformis</i>	AF DB			T A G	
	UMG-SP-1	AF2		S _c S K		
	UMG-SP-2	AF2				
	UMG-SP-3	AF2			I G G	
	amdS	AF DB				
	CPUTNase	AF DB				

	from <i>R. erythropolis</i>	AF2				
--	-----------------------------	-----	---	--	---	--

Overall, the binding site architectures of the selected enzymes can be conceptualised into three distinct topologies (Fig. 5). Cutinases exhibit a highly exposed binding site located on the surface (Fig. 5A), reflecting their natural affinity for polymer chains. This configuration facilitates enzyme association with polymer substrates, thereby promoting enzymatic degradation. In contrast, some enzymes feature a more buried binding site that remains relatively wide and capable of tightly associating with polymer chains. However, in such a case, binding to a polymer may necessitate the enzyme to adopt a more open conformation, potentially slowing down the catalytic rate (Fig. 5B). The third type of binding site enables hydrolysis primarily of terminal or near-end groups of degraded compounds. Such a binding site is likely unsuitable for the depolymerisation of high molar mass PUR (Fig. 5C). This classification underscores the diverse strategies employed by enzymes for substrate recognition and catalytic activity, highlighting the importance of understanding binding site architectures in the context of enzymatic degradation pathways.

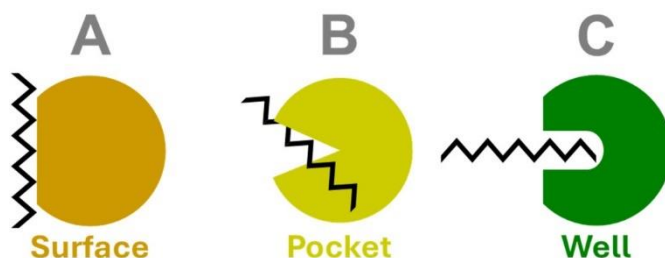


Fig. 5. Schematic representation of different binding site topologies encountered in PUR-degrading hydrolytic enzymes.

For visualisation purposes, a single representative enzyme was chosen for each enzyme group (Fig. 6), except for the outliers, CE-Urb and CalB. However, in the case of "Urethanases," two representative enzyme structures were selected instead of one. This decision was driven by the bifurcation observed within this group: one subset displaying catalytic activity exclusively on short carbamates, while the other subset demonstrates activity towards short segments of polyether PUR. The selected enzymes representing each group are as follows:

1. "Bacterial cutinases": *TfCut2* (PDB id: 4CG1 [149])
2. "Fungal cutinases": *HiC* (PDB id: 4OYY [150])
3. "Esterases": *Diutina (Candida) rugosa* (PDB id: 1CRL [151])

4. “Lipases”: PueA, *Pseudomonas chlororaphis* (AlphaFold DB model, Uniprot id: A0A0D5XYX5)
5. “Urethanases”: CPUTNase, *Candida parapsilosis* NBRC 708 (AlphaFold DB model, Uniprot id: A0A679EIJ6) and UMG-SP-2 (AlphaFold2 model)

In the next subsections, we discuss the groups of enzymes in more detail focusing on their structure, binding site and reported activity. However, comparing the efficiency of PUR degradation among the selected enzymes is not feasible due to the lack of standardised PUR-degrading assays. Various studies have employed diverse high molar mass PUR substrates and carbamates under differing conditions, including variations in time, pH, and temperature. Liu et al. [24] attempted to summarise the degradation efficiency of some reported PUR-degrading microorganisms, ranging from kinetic analyses to mere indications of clear zone formation on agar plates with Impranil DLN, underscoring the inherent variability in experimental approaches.

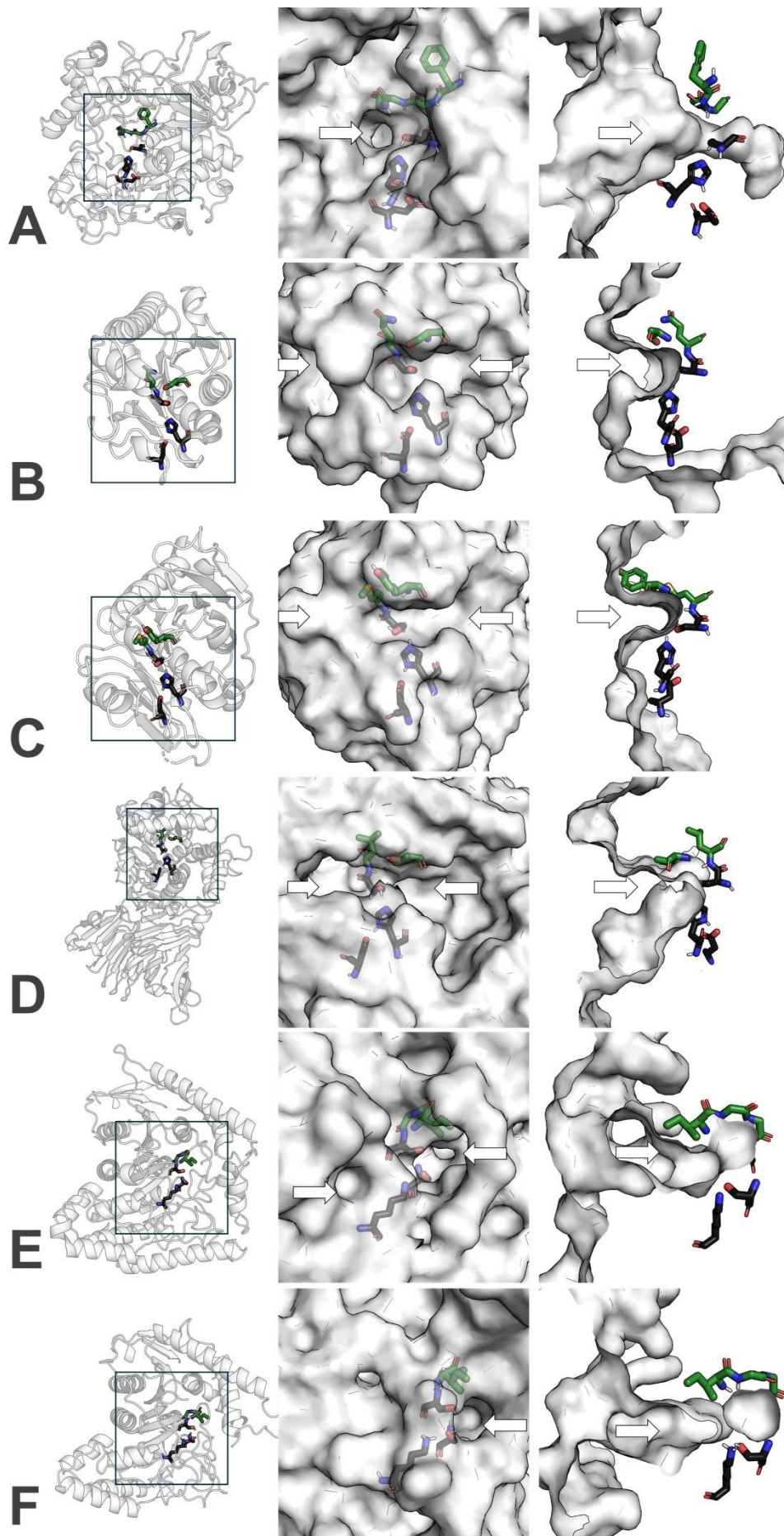


Fig. 6. Binding site architectures of representative enzymes from all homologous groups. Graphics were created using PyMOL [152]. Catalytic triads are depicted as black sticks, while oxyanion hole amino acids are shown as green sticks. The first column displays each enzyme in cartoon form. In the second column, a close-up of the binding site is presented, with the enzyme shown as a surface and the active site displayed transparently. The third column provides a side view of the active site, allowing its shape and depth to be observed. Arrows indicates entry to the binding site visible at the surface (middle column) or cross-section (right column). **A.** “Bacterial cutinases”: *TfCut2* (PDB id: 4OYY); **B.** “Fungal cutinases”: *HiC* (PDB id: 4CG1); **C.** “Esterases”: *Diutina (Candida) rugosa* (PDB id: 1CRL); **D.** “Lipases”: *PueA, Pseudomonas chlororaphis* (AlphaFold DB model, Uniprot id: A0A0D5XYX5); **E.** “Urethanases”: *CPUTNase, Candida parapsilosis* NBRC 708 (AlphaFold DB model, Uniprot id: A0A679EIJ6); **F.** UMG-SP-2 (AlphaFold 2 model).

Esterolytic enzymes

The first group, “Bacterial cutinases” is formed by five bacterial cutinases (EC 3.1.1.74): one from leaf compost metagenome: Leaf-branch compost bacterial cutinase (LCC); and three from Actinobacteriota: *Thermobifida (Thermomonospora) fusca (TfCut2)*, *Thermobifida (Thermomonospora) curvata* DSM43183 (*Tcur1278*), *Thermobifida (Thermomonospora) curvata* DSM43183 (*Tcur0390*) [20] and and one from Proteobacteria, *Halopseudomonas formosensis (Hfor)* [128]. All of the bacterial cutinases were reported to cleave ester bonds in Impranil DLN and other polyester PUR [20,128]. LCC and *TfCut2* caused a weight loss in Elastollan B85A-10 and C85A-10 of 0.9-3.7% in 60-70°C after 100h of incubation [20]. *Hfor* activity towards degradation of Impranil DLN, ICO-THANE and ICO-FIX , was measured by the consumption of ammonium (NH⁺₄).

The second group of enzymes, “Fungal cutinases” includes three cutinases (EC 3.1.1.74), one from *Humicola insolens (HiC)* [22], another from *Cladosporium* sp. P7 (CpCut1) [24,76], and a recently characterised enzyme from *Blastobotrys* sp. G-9 (BaCut1) isolated from a 20-year landfill [23]. CpCut1 remarkable polyester PUR-degrading activity was recently shown on three polyester PUR (including a thermoset PUR), exceeding performance of some bacterial cutinases. CpCut1 exhibited superiority, completely degrading 1.0% (vol/vol) of Impranil DLN-SD particle dispersion within 30 minutes, as evidenced by the gradual decrease in turbidity over time. In contrast, LCC, *TfCut2*, and *HiC* achieved comparable degradation levels of 1.0% Impranil DLN-SD dispersion after 3 hours of reaction, with extents of degradation at 23.5%, 5.3%, and 10.7%, respectively, significantly lower than CpCut1. Moreover, while differences in degradation efficiency among the cutinases were smaller for the other two PUR substrates, CpCut1 notably outperformed its counterparts, resulting in the highest weight loss in both the synthesised TPU film PBA-PUR

and post-consumer PUR foam after 12 hours of treatment, 40.5% and 20.6%, respectively. In comparison, the weight loss for the PBA-PUR treated with the LCC, *TjCut2* and *HiC* ranged from 20.8% to 13.7%, and for post-consumer PUR foam, it ranged from 9.5% to 5.8% [24]. BaCut1 was also reported to degrade PBA-PUR, releasing adipic acid as major product, and degraded 50% of commercial polyester PUR foam within 48 h at 37 °C [23]. All three fungal cutinases were reported to degrade ester bonds in polyester PUR. Additionally, *HiC* is the only polyester PUR degrading enzyme with confirmed uretanolytic and amidolytic activity [22].

For the group of "Bacterial cutinases," we present the crystal structure of *TjCut2* cutinase (PDB id: 4CG1) (Fig. 6A), while for "Fungal cutinases," the selected structure is *HiC* cutinase (PDB id: 4OYY) (Fig. 6B). Interestingly, sequences of fungal cutinases are not very similar to bacterial cutinases (only 3.7-6.6% sequence identity), hence fungal and bacterial cutinases were grouped separately. However, structurally they partly align; fungal cutinases are smaller, as the bacterial cutinases structure is formed by central nine-stranded β -sheet flanked by 11 α -helices on both sides [149], whereas fungal cutinases contain only five β -sheet surrounded by α -helices [150] (Fig. 6A-B). Both fungal and bacterial cutinases feature an active site situated at the enzyme's surface, incorporating the classical Ser-His-Asp catalytic triad and an oxyanion hole formed by backbone amine groups of two amino acids (Table 1, Table 2). Notably, within the binding site, a hydrophobic groove facilitates polymer binding. Given the surface localisation of the active site, no tunnel leads to it, rendering it highly accessible and capable of binding bulky polymer chains, including their natural substrate, cutin, as well as synthetic polymers (Fig. 6A-B). The binding site of cutinases is illustrated in the model depicted in Fig. 5A. Overall, fungal and bacterial cutinases are a very promising group of enzymes for PUR depolymerisation, as they are serine hydrolases that naturally catalyse the breakdown of polyesters that form the cuticle that protects plants. The main component of cuticle is cutin, a waxy water-repellent lipid polyester, which is the natural substrate of cutinases [153]. As cutin resembles structurally synthetic polyesters that contain hydrolysable ester bonds, native cutinases have been shown to be able to degrade ester bonds in PET [154–157] and polyester PUR [20,22,24].

The third group of enzymes, "Esterases", is constituted of two quite distant (sequence identity of 25.7%) esterolytic (EC 3.1.2.-) alpha-beta hydrolases: *Comamonas (Delftia) acidovorans* TB-35 (PudA) carboxylic ester hydrolase from Proteobacteria [28–30,72,125] and *Diutina (Candida) rugosa* lipase 1 from Eukaryotic host [31]. After a period of seven days,

PudA enzyme achieved complete degradation of $10 \text{ g}\cdot\text{L}^{-1}$ of cube-shaped polyester PUR using it as a sole substrate, characterised by long-chain polyester segments synthesised from poly(diethylene glycol adipate and 2,4-tolylene diisocyanate), converting it into diethylene glycol (DEG) and a small amount of trimethylolpropane (TMP) [28]. *Diutina (Candida) rugosa* lipase 1 degraded Impranil DLN, yielding diethylene glycol (DEG) as a byproduct, at a generation rate of 0.12 mg/L/min [31] (Table 1).

Our selection for structural representation focused on *Diutina (Candida) rugosa* (PDB id: 1CRL [151]), the sole protein within this group with available crystal 3D structures in the PDB database. Specifically, we opted to showcase the structure with the highest resolution. Notably, an alternate structure (PDB id: 1LPP) within the database features a ligand comprising a molecule of 1-hexadecanesulfonic acid which contains hydrophobic hydrocarbon tail. Although not depicted, it is worth noting that a PUR chain binding to *Diutina (Candida) rugosa* could mimic the conformation observed with this ligand. This enzyme is distinguished by its unique Ser-His-Glu catalytic triad, augmented by an oxyanion hole formed by HGG motif [158–160] that is substituted to FGG in *Diutina (Candida) rugosa* (Table 1, Table 2). Furthermore, *Diutina (Candida) rugosa* showcases a notable structural feature—a lengthy and slender tunnel extending from the active site amino acids deep into the protein core (Fig. 6A), whose shape corresponds to the model on Fig. 5C.

The fourth group, “Lipases” consists of five PUR-degrading lipases (EC 3.1.1.3) from *Pseudomonas* strains that belong to Proteobacteria: PUR esterases A (PueA) and B (PueB) from *Pseudomonas chlororaphis* [33–36], PUR lipase (PulA) from *Pseudomonas fluorescens* [38,39] and lipases A (PueA) and B (PueB) from *Pseudomonas protegens* strain Pf-5 [37]. Although they are often referred to as “polyurethanases,” these enzymes are more accurately classified as extracellular lipases and esterases [37]. All the discussed enzymes were proved to hydrolyse ester bonds in Impranil DLN, indicated by a change in relative absorbance [37] or a halo formation on Impranil DLN agar plates [25,33–35,37,38]. In the case of *Pseudomonas chlororaphis* and *Pseudomonas fluorescens*, two-enzyme systems were assigned to hydrolyse PUR: PueA with higher and PueB with lower activity.

For the group of “Lipases”, we present the structure of PueA from *Pseudomonas chlororaphis*, for which an AlphaFold2 model is available (Uniprot id: A0A0D5XYX5). These lipases are relatively large enzymes (~60 kDa) stabilised by calcium ions. Their active site, comprising the classical catalytic triad and two residues forming an oxyanion hole (Table 1, Table 2), is situated within a spacious pocket, albeit more solvent-exposed compared

to cutinases. However, this pocket is still notably more buried than in the case of cutinases and represents the model on Fig. 5B. The depth of the active binding site in lipases may impose constraints on their ability to efficiently bind PUR polymer chains, potentially leading to lower efficiency of PueA [161] in comparison to cutinases. This distinction underscores the nuanced interplay between enzyme structure and substrate specificity, shedding light on potential differences in catalytic efficiency among enzyme classes (Fig. 6D).

The outliers that were found, a metagenome-derived carboxyl-ester hydrolase belonging to the lipolytic family IV (CE_Ubrb) [32] and *Candida antarctica* lipase B (CalB) both show less than 10% sequence identity with any other enzyme (Fig. 4B). CE_Ubrb was reported to degrade ester bonds in Impranil DLN (Table 1) shown by its clearing [32]. CalB was reported to depolymerise polycaprolactone-based polyester PUR foams and TPU coatings due to ester bonds cleavage [77].

Urethanolytic enzymes

The fifth group, “Urethanases” is formed by eight enzymes with reported urethanolytic activity (EC 3.5.1.75) from Actinobacteriota: *Lysinibacillus fusiformis* [82]; Eucaryotic hosts: *Aspergillus oryzae* (amdS) [81], *Candida parapsilosis* NBRC 708 (CPUTNase) [129]; Proteobacteria: *Agrobacterium tumefaciens* d3 (AmdA) [83,130], *Rhodococcus erythropolis* MP50 [83] and from metagenomes isolated from an enriched site containing perennial PUR waste (UMG-SP-1, UMG-SP-2, UMG-SP-3) [26]. These urethane bond-degrading enzymes were tested either on carbamates [82,83,129,130], prior-depolymerised PUR fragments [26] or polyether PUR [19]. In fact, most of the urethanases included in the PAZY database were identified as potential enzymes able to degrade ethyl carbamate with application in food industry, especially alcohol beverages [81–83,129]. Such urethanases usually naturally catalyse the hydrolysis of terminal urethane releasing alcohol, CO₂, and NH₃ [83,162], hence they might not be able to hydrolyse urethane bonds in PUR, as in such a case these bonds are incorporated inside a bulky polymer chain.

In early 2023, Branson et al. reported three novel urethanases capable of degrading urethane bonds within low molecular weight dicarbamates [26]. These urethanases, namely UMG-SP-1, UMG-SP-2, and UMG-SP-3, were isolated from a metagenome library derived from soil exposed to PUR waste over an extended period. In their study, Branson et al. synthesised a TDI-based polyether PUR foam, which was subsequently depolymerised via glycolysis into low molecular weight dicarbamates. The resulting dicarbamates underwent

degradation facilitated by UMG-SP-2, releasing glycol, carbon dioxide, and aromatic diamine. UMG-SP-2 was able to convert approximately 65 % of glycolysedPUR fragments to aromatic diamine within 24 h. Adding more enzyme led to complete conversion after 48 h. This integrated approach proposed by Branson et al. effectively enabled the comprehensive degradation of polyether PUR foam through combined chemical and biological recycling methods [26]. In a recent study, the hydrolysis profile of UMG-SP-1 was expanded beyond the reported low-molecular-weight dicarbamates, demonstrating its ability to degrade urethane bonds in thermoplastic polyester PUR [19].

For the group of "Urethanases", two representative structures were chosen, CPUTNase and UMG-SP-2. CPUTNase exhibits urethanase activity limited to small carbamates, such as ethyl carbamate, methyl carbamate, n-butyl carbamate, acetamide, propionamide, butyramide, and acrylamide [129] (Fig. 6E). In contrast, UMG-SP-2 demonstrates activity on glycolysed PUR fragments [26] (Fig. 6F). Both urethanasases feature an active site comprised of a Ser-(cis)Ser-Lys catalytic triad, along with an oxyanion hole formed by three backbone amino acids: Ile, Gly, and Gly (Table 1, Table 2). The active sites of both enzymes are nestled within the protein structure, with CPUTNase exhibiting one tunnel and UMG-SP-2 displaying two tunnels. Notably, the binding cavity of UMG-SP-2 appears more capacious than that of CPUTNase, suggesting a potential for UMG-SP-2 to accommodate bulkier substrates. CPUTNase is likely specialised in cleaving terminal amine groups from substrates, whereas UMG-SP-2, isolated from an enriched site containing perennial PUR waste, is indicative of an enzyme evolved to degrade urethane bonds within PUR. This observation underscores the adaptive nature of UMG-SP-2, potentially tailored for the degradation of PUR (Fig. 6E-F). The configuration of the CPUTNase active site groove aligns with the binding site model depicted in Fig. 5C, while the binding site of UMG-SP-2 could potentially be represented by the model in Fig. 5B. However, it is challenging to ascertain definitively for these enzymes.

2.3.3. Active sites and mechanisms

The PUR-degrading hydrolases selected in our study encompass one of two catalytic triads: the "classical" catalytic triad Ser-His-Asp (or its variant with Glu substituting Asp) (Fig. 7A-B), or the Ser-(cis)Ser-Lys catalytic triad (Fig. 7C-D). Notably, esterolytic enzymes exclusively feature the classical Ser-His-Asp/Glu catalytic triad, while urethanolytic enzymes possess the Ser-(cis)Ser-Lys catalytic triad (Table 2). Both types of catalytic triads facilitate

nucleophilic attack by an activated seryl residue onto the carbonyl carbon of the scissile bond (Fig. 7A, C), resulting in the formation of a tetrahedral intermediate. The substrate specificity of these catalytic triads primarily revolves around their ability to stabilise this tetrahedral intermediate [163,164]. Furthermore, both catalytic triads are accompanied by an oxyanion hole, typically formed from backbone amine groups. Among the selected enzymes, three types of oxyanion holes were observed. Interestingly, enzymes within the described groups share a common type of oxyanion hole: composed of backbone amine groups of four amino acids in "Esterases" [158], three amino acids forming a XGG or XAG motif in "Urethanases," and those created by only two amino acids in cutinases and lipases. Theoretical and computational findings by Cerqueira et al. (2017) [164] suggest remarkable similarities between the catalytic mechanisms of enzymes employing the Ser-(cis)Ser-Lys catalytic triad and the classical Ser-His-Asp catalytic triad. Specifically, the role of the unconventional (cis)Ser alongside the catalytic Lys appears to replace the functional role of His-Asp. The (cis)Ser, positioned in an unusual cis orientation, facilitates precise contacts with the other two residues of the catalytic triad and stabilises the amine group of the tetrahedral intermediate. In esterolytic enzymes, however, it is the catalytic histidine that stabilises the ester bond's alkoxy oxygen in the tetrahedral intermediate. A notable distinction lies in the arrangement of the catalytic triad within the active site. While the Asp in the classical triad does not directly interact with the substrate, the catalytic Lys in the Ser-(cis)Ser-Lys triad can engage directly with the substrate, influencing its orientation within the active site. Energy calculations suggest that the unique alignment of the Ser-(cis)Ser-Lys catalytic triad relative to the classical Ser-His-Asp triad may enhance the stabilisation of tetrahedral reaction intermediates, thereby lowering the activation energies required for catalysis and potentially rendering these enzymes more catalytically efficient [107].

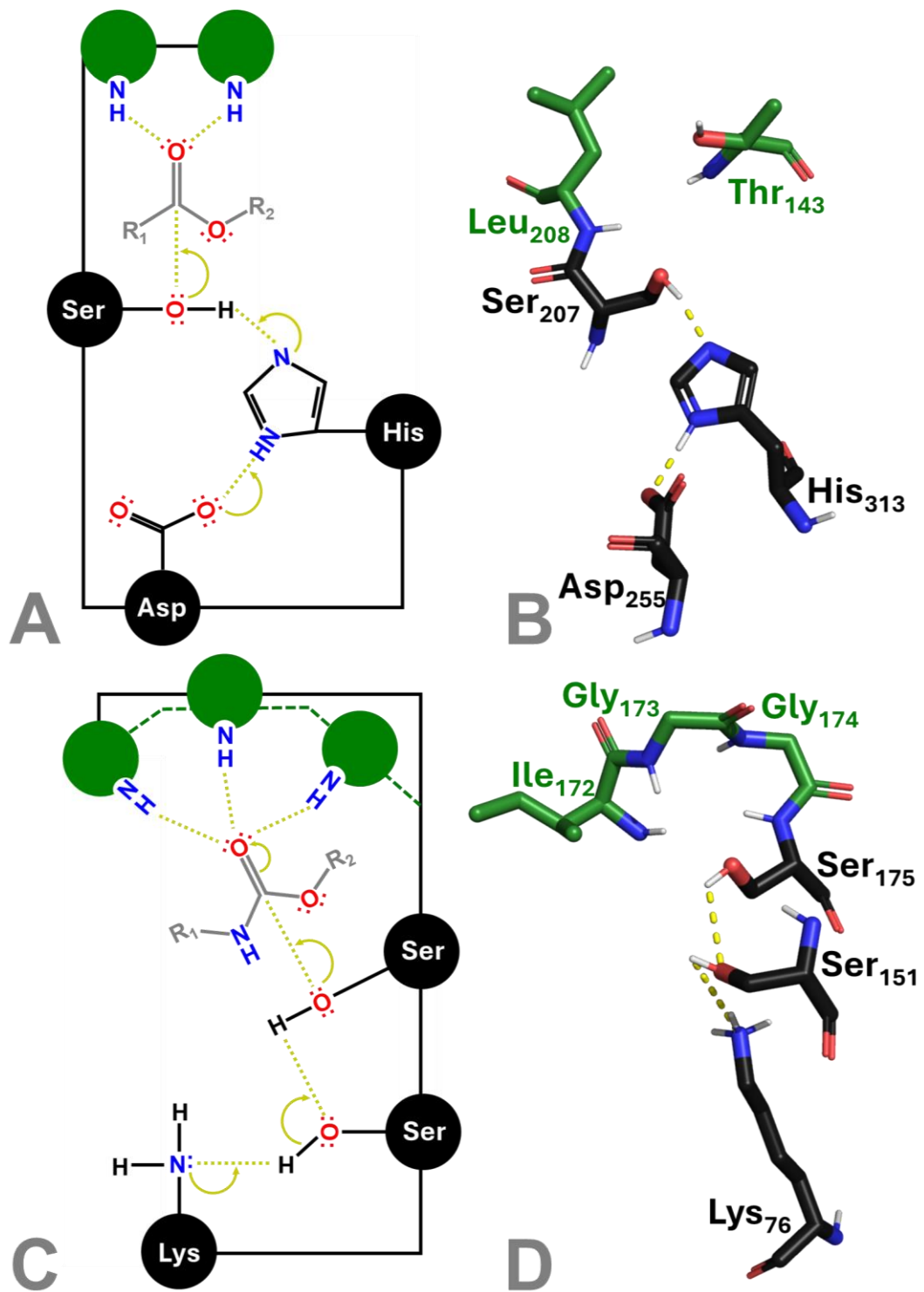


Fig. 7. A) Active site residues: classical Ser-His-Asp catalytic triad (black) with oxyanion hole (green) of esterase/lipase/cutinases during the first step of enzymatic catalysis on an ester bond. Catalytic histidine acts as a general base activating the catalytic serine hydroxyl group for nucleophilic attack on the carbonyl carbon of the ligand. The third component of this catalytic triad, aspartic acid, acts to increase the basicity of the catalytic histidine. The oxyanion intermediate formed is stabilised by the backbone amide groups of two residues (green). B) Active site of *Pseudomonas chlororaphis* lipase PueA modelled with AF2. The catalytic triad residues are shown as black sticks. The oxyanion forming residues shown as green sticks. C) Active site residues: Ser-(cis)Ser-Lys catalytic triad (black) and oxyanion pocket (green)

of amidases/urethanases during the first step of enzymatic catalysis on an urethane bond. Ser is ionised through proton transfer to (cis)Ser. In the same step, the proton bonded to (cis)Ser migrates to Lys. Ser performs nucleophilic attacks towards the carbonyl carbon of the substrate (grey), leading to formation of a tetrahedral adduct. The negatively charged carbonyl group of the amide of the substrate is stabilised by hydrogen bonding provided by the NH groups of the oxyanion pocket. **D)** Active site of UMG-SP-2 urethanase modelled with AlphaFold 2. The catalytic triad residues are shown as black sticks. The oxyanion forming residues shown as green sticks.

Recently, a novel computational study has been published on the mechanism of ester bond cleavage in Impranil DLN repeating unit by PueA from *Pseudomonas chlororaphis* [161]. The proposed mechanism aligns with that suggested for other esterolytic serine hydrolases [165–169]. Additionally, computational studies on peptide amidases with Ser-(cis)Ser-Lys catalytic triads have also been explored [164,170]. The degradation mechanisms of both enzyme types, facilitated by their distinct catalytic triads acting on parallel C-N/C-O amide/ester bonds, exhibit parallel pathways and were divided by the authors into mechanisms consisting of either 4 or 5 steps. The degradation mechanisms mediated by both catalytic triads on parallel C-N/C-O amide/ester bonds can be outlined as follows:

1. **Nucleophilic Attack by catalytic serine:** The catalytic serine residue undergoes nucleophilic attack on the carbonyl group of the substrate, resulting in the formation of the first tetrahedral intermediate.
2. **Formation of the Acyl-Enzyme Complex:** The nucleophilic attack leads to the formation of an acyl-enzyme complex, wherein the substrate becomes covalently bound to the enzyme via an ester or amide linkage.
3. **Release of Ammonia/Alcohol Product:** During this step, an ammonia or alcohol molecule, depending on the nature of the substrate, is released as a product of the reaction.
4. **Nucleophilic Attack by a Water Molecule:** A water molecule then acts as a nucleophile, attacking the acyl-enzyme complex, leading to the formation of the second tetrahedral intermediate.
5. **Release of the Carboxylic Acid Product:** Finally, the product of the reaction, typically a carboxylic acid, is released from the enzyme, completing the catalytic cycle.

The divergence in substrate specificity among enzymes hydrolysing C-O and C-N bonds, despite their mechanistic similarities, is intriguing [171,172]. Particularly noteworthy is the prevalence of the classical Ser-His-Asp catalytic triad across diverse enzyme groups, including some amidases, similarly to the esterolytic PUR-degrading enzymes discussed in this review. As previously noted, the substrate specificity of hydrolases is primarily determined

by their ability to stabilise the tetrahedral intermediate formed during nucleophilic attack by an activated serine residue onto the carbonyl carbon of the scissile bond. Despite this shared mechanistic feature, the precise factors contributing to the observed differences in substrate specificity remain elusive.

When considering parallel C-N/C-O amide/ester bonds, it is crucial to acknowledge the distinct characteristics of amides compared to esters. Amides exhibit partial C-N double bond character and feature an additional hydrogen atom bound to the amide nitrogen, a feature absent in esters [163]. Esterases typically lack the capability to form a hydrogen bond with the scissile NH group of the substrate during the transition state. This interaction, crucial for amidase/protease-catalysed hydrolysis, affects the energy landscape of the reaction. In amidases, the transition state for nitrogen inversion corresponds to the highest energy point along the reaction coordinates for the acylation step of amide-bond hydrolysis [173]. This is attributed to the energetic cost of nitrogen inversion being added to the high energy of the tetrahedral intermediates formed during the reaction. The ability of an enzyme to accommodate such a hydrogen bond distinguishes amidases/proteases from esterases/lipases. Moreover, this hydrogen bond acceptor could reside either in the enzyme [140] or in the substrate, facilitating substrate-assisted catalysis [163,174]. Leveraging interactions with this hydrogen bond during the transition state can significantly reduce the activation energy of hydrolysis, equivalent to the energy of a hydrogen bond [163]. The importance of stabilising the tetrahedral intermediate in hydrolysed PUR was also confirmed in the previously mentioned computational study, which investigated the cleavage of ester bonds in Impranil DLN by PueA from *Pseudomonas chlororaphis*. While it was established that PueA can degrade ester bonds in Impranil DLN, the substrate's binding mode was previously unknown. Consequently, the authors explored two possible opposing orientations of the Impranil DLN repeating unit in the binding site, referred to as RC1 and RC2. Their findings demonstrate that pose RC2 exhibits superior protein-ligand interactions decomposed by ligand and activation free energy of the acylation step, which is 10 kcal/mol lower than for RC1 starting structure. Interestingly, while the kinetics of activation of the catalytic serine is basically equivalent in the two reactions, a notable difference arises in the second step of the acylation. This step involves the proton transfer from the protonated catalytic histidine to the carbonyl oxygen of the Impranil, which is necessary to release the first product of the reaction, the alcohol [161]. Notably, in the favourable orientation RC2,

the interactions of the leaving group oxygen with the N ϵ atom of catalytic histidine are more feasible, facilitating stabilisation of tetrahedral intermediate.

Introducing mutations to known esterolytic enzymes to create a hydrogen bond acceptor for the scissile NH group of the substrate could be a promising strategy for designing polyurethanases. These engineered enzymes could then be capable of degrading urethane, urea, and amide bonds in PUR. An example of such an approach is the re-engineering of *HiC* cutinase with altered substrate specificity towards amide hydrolysis through the introduction of single-point mutations acting as scissile NH hydrogen bond acceptors [140], or the development of a *HiC* variants with lost polyesterase activity (verified on PET) in favour of amidase activity, confirmed on the insoluble substrate 3PA 6,6 [139]. In the second study, however, no depolymerising activity on nylon 6,6 of these *HiC* variants was confirmed. Although the activity of these mutants has not been specifically verified on PUR depolymerisation, their potential as candidates for novel polyurethanases is promising, particularly given *HiC* cutinase's demonstrated ability to hydrolyse ester bonds, and, albeit less efficiently, urethane bonds in PUR [22].

These insights into the mechanistic underpinnings of substrate specificity not only reinforce the potential of such engineered enzymes but also suggest that exploiting or enhancing enzyme promiscuity could be a viable strategy for broadening their catalytic scope. For instance, by introducing mutations that enable esterases to form hydrogen bonds with the scissile NH group of amide bonds, these enzymes could potentially acquire or enhance amidase activity. This concept is exemplified by the aforementioned studies in which *HiC* cutinase variants were engineered for altered specificity towards amide hydrolysis [139,140], underscoring the potential for tailoring enzyme activity to target both ester and urethane bonds in complex polymers like PUR.

2.4. Conclusions

Enzyme-based degradation of PUR presents both promise and challenge as an alternative to traditional recycling methods. The complexity arises from the crosslinked structure of certain PUR types, particularly thermosets, and the diverse formulations encountered in PUR waste. This diversity complicates the development of a universal recycling method. Previous efforts in enzymatic depolymerisation have primarily focused on polyester PUR, targeting ester bonds using esterolytic enzymes. Recently, enzymatic

hydrolysis of urethane bonds in polyester PUR was demonstrated, marking a significant advancement [19]. However, depolymerisation via urethane bond cleavage remains largely unexplored. This gap can be attributed to several factors, including the inherent susceptibility of ester bonds to cleavage, their predominant localisation within accessible soft amorphous PUR segments, and the availability of specialised esterolytic enzymes such as cutinases in natural systems.

The limited accessibility of urethane bonds may necessitate pre-treatment steps of PUR to render the urethane bonds accessible. In particular, polyether PUR present additional challenges due to their higher resistance to degradation. The stable ether bonds and reduced water absorption capacity of polyether PUR hinder enzymatic hydrolysis, highlighting the complex interplay between polymer structure and enzymatic activity in PUR biodegradation.

The diverse array of functional groups in PUR, such as urethane, ester, urea, amide, and ether, synthesised from various structural units, prevents the existence of a generalised PUR structure. Consequently, using a single enzyme for the degradation of all PUR types may not be feasible. Instead, it is important to investigate various enzyme groups and consider combining them with optimised mechanical and chemical recycling techniques to address the diverse nature of PUR. A holistic approach to biological recycling could involve the application of various enzymes targeting specific bond types, either as a mixture or in a systematic pipeline process. Alternatively, PUR may need to be categorised into distinct groups, each requiring a tailored degradation pipeline. This modular approach offers a promising avenue for the comprehensive and efficient biological recycling of PUR.

The emerging understanding of enzyme promiscuity offers a promising avenue for tackling the challenges associated with PUR biodegradation. As the diversity of functional groups in PUR complicates the development of a universal enzymatic approach, leveraging the inherent promiscuity of certain hydrolases could be key to devising more versatile and effective degradation strategies. The ability of some esterases to also hydrolyse amide and urethane bonds suggests that a tailored combination of such promiscuous enzymes could significantly enhance the efficiency of PUR recycling processes. Furthermore, enzyme engineering efforts aimed at enhancing promiscuity or specificity could yield biocatalysts capable of addressing the structural heterogeneity of PUR materials.

The effectiveness of serine hydrolases in PUR degradation depends on their ability to stabilise tetrahedral intermediates formed after the acylation step involving nucleophilic

attack of the catalytic serine on the carbonyl carbon of the cleaved group. The ability to stabilise -O or -NH groups may dictate substrate specificity and the type of bonds hydrolysed (C-N or C-O). Developing cutinases with urethanolytic activity holds thus promise as a strategy for hydrolysing urethane bonds in PUR.

The field of PUR enzymatic degradation awaits redefinition [175]. Thus far, enzyme selection for PUR depolymerisation has predominantly been based on the ability to degrade the aqueous dispersion of polyester PUR using PUR model substrates, such as Impranil DLN. However, there is a growing recognition of the need to reconsider this approach and select new model PUR that more closely mimic the structures of commercially used PUR [76,88,176]. Each PUR variant may require specific hydrolysing enzymes, which could be sourced from nature or engineered through mutagenesis techniques. The redesign of PUR-degrading enzymes should ideally focus on enhancing several key properties: activity, thermostability, and binding affinity. Increasing the catalytic efficiency of enzymes can lead to more rapid breakdown of PUR materials. Improved thermostability enables enzymes to remain functional under harsh industrial conditions, which often involves elevated temperatures to increase reaction rates. Enhanced binding affinity ensures that the enzymes can effectively recognise and interact with PUR molecules. Tailoring enzymes for industrial applications necessitates thorough optimisation, but the initial step involves identifying promising candidates. This review aims to illuminate the structural and functional characteristics of enzymes reported thus far, laying the groundwork for future advancements in the enzyme-based degradation of PUR.

2.5. Additional data and results

In this chapter, additional information from literature is presented in order to provide the reader with more insight into specific problems and research gaps that dissertation aims to bridge.

2.5.1. Cutinases

Cutinases (EC 3.1.1.74) are enzymes distributed across fungi, bacteria, and plants, each exhibiting unique structures and properties (Liang et al., 2023). Traditionally, cutinases are recognised for degrading cutin, an aliphatic polyester that forms a protective barrier on plant

surfaces [177]. For plant pathogens, cutinases are crucial, as they enable the degradation of cutin, thereby accessing carbon sources within host tissues [178–180].

In recent years, cutinases have gained attention for their ability to hydrolyse synthetic polyesters, particularly in plastic degradation. The discovery of *IsPETase*, a PET-hydrolysing enzyme from *Ideonella sakaiensis*, marked a major breakthrough. *IsPETase*, discovered at a Japanese waste site, has evolved to metabolise PET as a carbon source [49]. Although structurally related to other bacterial cutinases, *IsPETase*, classified already as EC 3.1.1.101 (PET hydrolase), possesses a highly flexible structure and a wider binding pocket, allowing it to accommodate synthetic substrates like PET (Yoshida et al., 2016).

In contrast to lipases, which act at lipid-water interfaces with a mobile lid domain covering the active site [181], cutinases lack this structural feature. Instead, they possess an exposed active site, enhancing their capacity to catalyse diverse substrates effectively [182]. Cutinases exhibit significant degradation activity toward synthetic polyesters, including PET [48,49], poly(butylene succinate) (PBS) [183], and poly(butylene adipate-co-terephthalate) (PBAT)) [182], making them promising candidates for PUR biodegradation.

Several cutinases, both bacterial and fungal, have been identified for their potential in degrading ester bonds in PUR, including *Thielavia terrestris* cutinase A (*TtcutA*) [184], Leaf-branch compost cutinase (LCC), *Thermobifida fusca* cutinase 2 (*TfCut2*) [20], *Thermomonospora curvata* cutinase (*Tcur1278*) [154], *Humicola insolens* cutinase (*HiC*) [22], *Cladosporium sp. P7* cutinase (*CpCut1*) [24], and *Blastobotrys sp. G-9* cutinase (*BaCut1*) (Jiang et al., 2024). However, due to evolutionary adaptation focused on natural substrates, these enzymes typically exhibit higher activity on PUR oligomers than on solid, complex PUR forms wastes [23,119,185].

While bacterial cutinases have been widely studied, recent discoveries of novel fungal cutinases, *BaCut1* and *CpCut1*, have shown that these enzymes also possess polyester PUR-degrading abilities. In a 2024 study, *CpCut1* outperformed previously characterised PUR-degrading cutinases, making it a promising option for industrial applications [24].

2.5.2. Computational studies on PUR-degrading enzymes

To date, few computational studies have thoroughly explored the degradation of PUR by microbial enzymes. One such study by Petry do Canto et al. [186] enhances our understanding of PUR degradation by modelling three-dimensional (3D) structures of lipases

from *Pseudomonas* species (specifically pueA, pueB, and pulA), known to experimentally degrade PUR. Using homology modelling, the study generated computational structures for these lipases for the first time. Molecular dynamics simulations were employed to assess structural stability, revealing stable configurations for pueA and pueB, while some flexibility was noted in the C-terminal region of pulA. Further docking studies identified favourable interactions between PUR monomers and key residues within the catalytic pockets, with consistent binding regions across the models.

Another study by Flores-Castañón et al. [187] provides insights into the structural characteristics and potential activity of microbial cutinases, particularly *TfCut2* and *HiC*, against PUR monomers. This study integrates structural and physiochemical analyses with molecular docking to evaluate the enzymes' binding affinities for PUR monomers. Key findings suggest that these cutinases, noted for their thermostability and hydrophilicity, bind PUR monomers in hydrophobic grooves near the catalytic triad. The docking results indicate stable binding poses with an average binding energy around -6 kJ/mol, suggesting that microbial cutinases could play a role in PUR degradation, presenting a promising avenue for future bioremediation applications targeting synthetic plastic waste.

However, neither of these studies verified that the docked poses they analysed were productive or confirmed that catalytic distances were optimised for effective catalysis. This lack of specificity in binding analyses limits the mechanistic insights provided.

Recently, a novel computational study by Świderek et al. [161] has investigated the specific mechanism of ester bond cleavage in the Impranil DLN repeating unit by PueA from *Pseudomonas chlororaphis*. While PueA's capacity to degrade ester bonds in Impranil DLN was known, the binding mode of the substrate had not been previously characterised. To address this, the authors examined two potential orientations of the Impranil DLN unit within the binding site, termed RC1 and RC2. Their findings reveal that the RC2 orientation offers stronger protein-ligand interactions and has an activation free energy for the acylation step that is 10 kcal/mol lower than that of the RC1 configuration. Although the activation kinetics of the catalytic serine were similar between the two reactions, a significant difference arose in the second step of acylation. This step involves proton transfer from the protonated catalytic histidine to the carbonyl oxygen of Impranil DLN, facilitating the release of the reaction's first product, the alcohol. In the favourable RC2 orientation, interactions between the leaving group oxygen and the N ϵ atom of the catalytic histidine are more stabilised, which promotes the formation of the tetrahedral intermediate [107].

This study is particularly relevant to this dissertation as it aligns with the hydrolysis mechanism proposed for *TfCut2* cutinase, offering insight into the preferential binding pose of Impranil DLN and the energetics of each reaction step. Apart from this recent contribution by Świderek et al. [161], there remains a significant research gap in the computational understanding of enzymatic PUR degradation, which this dissertation aims to help bridge.

2.5.3. Engineering of PUR-degrading enzymes

To date, only a few studies have explored protein engineering specifically for PUR degradation. Although the PUR-degrading enzymes discussed in earlier chapters—primarily cutinases—have been engineered, these efforts were largely directed at other substrates such as PET [48,188–191], tomato cutin [192] or small esters such as *p*NPB [192,193].

For PUR degradation specifically, only limited engineering studies have been reported, mainly involving the fusion of enzymes with polymer-binding modules. For instance, a polyamidase from *Nocardia farcinica* was fused to a polymer-binding module derived from a polyhydroxyalkanoate depolymerase from *Alcaligenes faecalis*. This fusion enzyme demonstrated up to four times greater activity on PUR than the native enzyme, indicating the significant role of enzyme adsorption to facilitate efficient hydrolysis [27]. These findings highlight the importance of the initial enzyme adsorption process in PUR degradation [176].

Chapter 3: Theoretical background and methodology

This chapter provides an overview of the computational and experimental methodologies applied in this dissertation, to provide the basic principles of the theoretical approaches. Details about the used methods will be provided within the results Chapters 4-6, in the methods sections.

3.1. Enzyme-catalysed reactions and kinetics

Enzymes catalyse reactions by lowering the activation energy required for the conversion of substrates into products. The general reaction mechanism can be described by the Michaelis-Menten model [194]:



Where:

- E – enzyme
- S – substrate
- ES – enzyme-substrate complex
- P – product

This mechanism includes three individual reactions with three different rate constants:

- $E + S \rightarrow ES$, formation of the enzyme-substrate complex, with the rate constant k_1 ,
- $ES \rightarrow E + S$, dissociation of the enzyme and the substrate, with the rate constant k_{-1} ,
- $ES \rightarrow E + P$, dissociation of the enzyme and the product, with the rate constant k_2 .

The reaction rate, v , represents the change in concentration over time and can be expressed as either the rate of product formation or substrate consumption:

$$v = \frac{d[P]}{dt} = -\frac{d[S]}{dt}$$

The catalytic efficiency of an enzyme is characterised by two key parameters:

- k_{cat} (turnover number): The number of substrate molecules converted to product by a single enzyme molecule per unit of time under saturating substrate conditions.
- K_m (Michaelis constant): The substrate concentration at which the reaction rate is half of v_{max} , reflecting the enzyme's substrate affinity.

The Michaelis-Menten equation describes the relationship between the reaction rate and the substrate concentration:

$$v = \frac{v_{\max}[S]}{K_m + [S]}$$

Where v_{\max} is the maximum reaction rate at saturating substrate concentration.

In the classical Michaelis-Menten model, it is assumed that the third reaction $ES \rightarrow E + P$ is the rate-limiting step. In this case, k_2 , also referred to as k_{cat} , defines the overall turnover number. However, for more complex reaction mechanisms, k_{cat} may depend on multiple rate constants.

Heterogenous substrates and enzymatic kinetics

Michaelis-Menten kinetics is not directly applicable to enzymatic reactions involving heterogeneous substrates [195]. Such reactions, including the enzymatic hydrolysis of synthetic and natural polymers, present unique challenges due to factors like substrate surface heterogeneity and complex structural compositions.

In a study by Schmidt et al. [20], the degradation rates of Impranil DLN by cutinases *TfCut2*, *LCC*, *Tcur1278*, and *Tcur0390* were analysed using a kinetic model proposed by Mukai et al. [195]. Schmidt et al. determined two key parameters for these enzymes: the rate constant of the surface reaction k_s and the adsorption equilibrium constant K . The Mukai model, originally developed for poly[(R)-3-hydroxybutyrate] (P[(R)-3HB]) films, provides a framework for understanding enzymatic hydrolysis of polymer substrates.

In Mukai's study, the water-soluble degradation products of P[(R)-3HB] were quantified spectrophotometrically by monitoring the absorbance at 210 nm, corresponding to the carbonyl groups. Using the absorption coefficient of 3-hydroxybutyric acid, the authors estimated the amount of degradation products, assuming the absorption coefficient was independent of chain length. The kinetic model proposed for heterogeneous enzymatic hydrolysis is as follows:

$$R = \frac{k_s K [E]}{(1 + K [E])^2}$$

Where:

- R – hydrolysis rate
- $[E]$ – enzyme concentration
- k_s – rate constant of the surface reaction
- K – adsorption equilibrium constant

This model indicates that at low enzyme concentrations $K[E] \ll 1$, the hydrolysis rate increases proportionally with enzyme concentration. At higher concentrations $K[E] \gg 1$, the rate becomes inversely proportional to $[E]$, eventually approaching zero due to enzyme crowding, which can block access to cleavable bonds on the substrate surface.

To estimate k_s and K , the equation can be linearised as:

$$\left(\frac{[E]}{R}\right)^{\frac{1}{2}} = \frac{K[E]}{\alpha} + \frac{1}{\alpha}, \quad \text{where } \alpha = (k_s K)^{\frac{1}{2}}$$

Plotting $\left(\frac{[E]}{R}\right)^{\frac{1}{2}}$ versus $[E]$ enables determination of the k_s and K constants through linear regression.

3.2. Investigation and analysis of protein structure, dynamics, and protein-ligand interactions

3.2.1. Protein structure

Proteins are fundamental macromolecules in living organisms, encoded by genes and assembled through translation of messenger RNA. These complex molecules are composed of amino acid residues linked by peptide bonds, and their function is intrinsically linked to their structure, which is organised into four hierarchical levels: primary, secondary, tertiary, and quaternary structures.

Primary Structure

The primary structure of a protein is its linear sequence of amino acids, joined by peptide bonds. This sequence is determined by the genetic code and dictates the protein's higher-order structures and function. Amino acids vary in their side chains, which exhibit different chemical properties—hydrophobic, polar, or charged—that influence how the protein folds and interacts with its environment.

Secondary Structure

The secondary structure of a protein refers to the regular, repeating patterns of hydrogen bonding between the backbone amide and carbonyl groups of the polypeptide chain. These interactions create distinct structural motifs, which serve as the foundation for further folding:

- **Alpha helices:** Right-handed coils stabilised by intra-chain hydrogen bonds, often providing flexibility and structural support.
- **Beta sheets:** Extended polypeptide strands linked laterally by hydrogen bonds, forming stable, pleated sheet-like structures.

In addition to these regular elements, **loops** are regions of the polypeptide chain that connect secondary structural elements. Unlike alpha helices and beta sheets, loops do not adopt regular patterns of hydrogen bonding and are therefore highly variable in structure. Despite their irregularity, loops often play critical roles in protein function. For example, in enzymes such as *TfCut2*, loops frequently form part of the active or binding site, influencing substrate specificity and catalytic efficiency. However, the structural variability of loops makes their prediction challenging, even with advanced computational methods.

Tertiary Structure

The tertiary structure describes the 3D conformation of a single polypeptide chain, encompassing the spatial arrangement of alpha helices, beta sheets, and other elements. This structure is stabilised by various interactions, including:

- Hydrophobic interactions, which drive nonpolar side chains toward the protein interior.
- Hydrogen bonds and ionic interactions, which stabilise polar and charged residues.
- Covalent disulfide bonds formed between cysteine residues.

The tertiary structure determines the functional regions of the protein, such as active sites, and allows for specific interactions with substrates or other biomolecules.

Quaternary Structure

Proteins that consist of more than one polypeptide chain exhibit a quaternary structure. This level of organisation describes how multiple subunits interact and assemble into functional complexes. Subunits may be identical (homomeric) or distinct (heteromeric), and their interactions are stabilised by similar forces as those in tertiary structure.

Protein Folding

Proteins fold into their native conformations based on the principle of energetic favourability, with the folded state being the most stable. This folding process is influenced by the sequence of amino acids, the aqueous cellular environment, and interactions with molecular chaperones. Fully folded proteins remain dynamic, allowing for conformational

changes critical to their function. Hydrophilic residues are often exposed to the solvent, while hydrophobic residues are buried in the protein core, stabilising the overall structure.

3.2.2. Source of protein structures

The 3D structure of a protein can be obtained either through experimental data or computational modelling techniques.

Experimental Data

The Protein Data Bank (PDB) is the primary repository for experimentally determined macromolecular structures, including proteins, nucleic acids, and their complexes [145]. Structures in the PDB are derived using techniques such as X-ray crystallography, nuclear magnetic resonance (NMR) spectroscopy, and cryo-electron microscopy (cryo-EM). Each PDB entry includes detailed atomic coordinates, secondary structure information, and bibliographic references. This database is continually updated, making it an invaluable resource for structural biology research.

Protein structure prediction

Homology modelling is a widely used computational method for predicting protein structures by leveraging sequence similarity with known structures. The process typically involves target-template identification, sequence alignment, model building, and refinement [196,197]. Tools such as Modeller [198], SWISS-MODEL [199], and I-TASSER [200] provide robust platforms for homology modelling and analysis.

A major breakthrough in protein structure prediction came with the development of AlphaFold by DeepMind, introduced in 2021 [146]. AlphaFold employs artificial intelligence (AI) to predict protein structures from amino acid sequences, achieving accuracy comparable to experimental methods like X-ray crystallography. By 2022, AlphaFold had predicted structures for nearly all catalogued proteins, covering over 200 million entries in its AlphaFold Protein Structure Database (AlphaFold DB), created in collaboration with the European Molecular Biology Laboratory (EMBL).

In 2024, the Nobel Prize in Chemistry was awarded to Demis Hassabis and John Jumper for their work on AlphaFold, recognising its transformative impact on biology, particularly in areas like drug discovery and disease research. David Baker also received a share of the

prize for his contributions to computational protein design, underscoring the growing importance of computational tools in structural biology.

3.2.3. Molecular docking

Molecular docking is a computational approach used to predict the binding interactions and conformations of two molecules, which may include small ligands and receptors, as well as larger biomolecular complexes such as protein-protein, protein-DNA, or protein-RNA interactions. This technique plays a critical role in various scientific fields, including structure-based drug design, molecular biology, and biophysics, offering insights into the atomic-level interactions that govern binding specificity and affinity [197,201].

The primary goal of molecular docking is to model the optimal binding arrangement between two molecules and estimate the strength of their interactions using computer-based methods [202]. While it is frequently employed to model small-molecule ligands with macromolecular targets, the versatility of molecular docking extends to studying complex biological interactions, such as protein assemblies or nucleic acid recognition [203–205]. Docking results often serve as a preliminary step for more detailed analyses, such as molecular dynamics simulations, which provide additional information on the stability and dynamics of the docked complexes.

The docking process involves two main steps: sampling of the ligand and application of a scoring function. Sampling algorithms identify energetically favourable ligand conformations within the receptor's active site, considering the binding mode. These conformations are then ranked using a scoring function [206,207]. Various scoring functions are employed, including force field-based, empirical functions (e.g., linear regression), knowledge-based, and consensus methods [201].

Molecular docking can be classified into two types: 1) rigid-body docking, where both the receptor and ligand are treated as rigid entities, or 2) flexible-body docking, where the receptor is rigid, but the ligand is flexible [197].

The search algorithm aims to explore all possible orientations and conformations of the ligand within the receptor. These algorithms can be classified into: 1) systematic or direct methods, such as conformational searches and fragmentation approaches, 2) stochastic or random methods, including Monte Carlo simulations, genetic algorithms, and Tabu searches [201].

In this study, a flexible docking approach was employed due to the size and complexity of the modelled ligand, Impranil DLN, which has a high number of rotatable bonds and degrees of freedom. This approach allowed fragments of the ligand to be docked sequentially, starting with an anchor fragment and building outward. The flexible docking protocol in Rosetta [208] was used to model the binding of a single structural unit of Impranil DLN to *Tf*Cut2, providing initial binding poses and interactions that guided subsequent molecular dynamics simulations.

Rosetta is a suite of tools widely used in protein modelling [209], including applications for protein structure prediction [210], protein-protein docking [211], protein design [212], and protein-ligand docking. Specifically, RosettaLigand, a tool within the Rosetta framework, was utilised to model protein-ligand interactions. It samples the rigid-body position and orientation of the ligand as well as side-chain conformations using Monte Carlo minimisation. To account for conformational flexibility, ensembles of ligand conformations and protein backbones were used. The models generated by RosettaLigand were evaluated with a scoring function that incorporates an electrostatics model, an orientation-dependent hydrogen bonding potential, an implicit solvation model and van der Waals interactions. This flexible docking approach provided crucial hypotheses for understanding the binding mechanisms of Impranil DLN to *Tf*Cut2 and guided further computational studies [208].

3.2.4. Molecular dynamics simulations

Static models, such as those obtained from docking studies, often fall short in capturing the dynamic behaviour of molecular systems, particularly when flexibility plays a significant role, as in polymer chains or macromolecular interactions. Molecular dynamics (MD) simulations provide a powerful computational approach to address this limitation. By simulating the time-dependent movements and interactions of atoms over time, MD allows for the exploration of structural changes and dynamic processes in a wide range of systems, including isolated proteins, protein-ligand complexes, and other biomolecular assemblies. This technique provides valuable insights into molecular flexibility, stability, and interactions at an atomic level, revealing details that are often inaccessible through experimental methods alone [213,214].

MD simulations are based on classical mechanics, where atoms are treated as spheres connected by springs (representing covalent bonds). The motion of atoms is governed by Newton's second law [215]:

$$F = ma$$

Here, F represents the force acting on an atom, m its mass, and a its acceleration. Forces are derived from the potential energy V of the system, calculated using a chosen force field. For a system of N atoms, the force on each atom is:

$$F_i = -\frac{\partial V_{tot}(r_1, r_2, \dots, r_N)}{\partial r_i} \quad (i = 1, 2, \dots, N)$$

where V_{tot} encompasses bonding potentials (bond lengths, angles, dihedrals) and non-bonding interactions (van der Waals and electrostatic forces).

To simulate atomic movements, numerical integration methods (e.g., Verlet or leapfrog algorithms) calculate new positions and velocities at discrete time steps (Δt). The simulation time step is constrained by the highest vibrational frequency in the system, typically around 1-2 femtoseconds.

The accuracy of MD simulations depends heavily on the force field, which defines the interaction potentials. Commonly used force fields include AMBER and CHARMM for biological systems (proteins, nucleic acids, membranes) [216–218]; GAFF (General AMBER Force Field) for organic molecules [219]; and MMFF for small molecules and hydrocarbons [220,221].

Force field parameters, such as atomic radii, bond lengths, and angle values, are derived from experimental data and quantum mechanical calculations. To model realistic environments, MD simulations employ simplifications:

- **Periodic Boundary Conditions:** To mimic an infinite system, the simulation box is surrounded by identical copies of itself, avoiding edge effects.
- **Cutoff Radii:** Long-range non-bonding interactions are truncated beyond a set distance to reduce computational costs.
- **Exclusion of Quantum Effects:** While MD captures atomic motion, it cannot simulate bond breaking or formation. Quantum mechanics-based methods are required for such studies.

MD simulations provide dynamic insights into enzyme-ligand interactions. For example, they allow exploration of: 1) binding stability by monitoring the stability of a protein-ligand complex over time, 2) interaction patterns by identifying key residues involved in ligand binding, and 3) protein and ligand flexibility by assessing how conformational changes impact function.

In this study, MD simulations refined the docking results of *Tf*Cut2 bound to Impranil DLN. Simulations were conducted using AMBER, with ligand parameterisation performed via

the Antechamber [222] module and GAFF [219]. The AM1-BCC charge model [223] was used for partial charge assignment, balancing computational efficiency with accuracy. MD simulations represent single-molecule behaviour, contrasting with experimental methods that capture ensemble averages. Additionally, simplifications like cutoff radii and classical mechanics can limit the accuracy of certain interactions.

3.2.5. MM-GBSA calculations

The Molecular Mechanics energies combined with Poisson–Boltzmann or Generalised Born and Surface Area continuum solvation (MM-PBSA and MM-GBSA) methods are widely used to estimate the free energy of ligand binding to biological macromolecules. These methods, based on molecular dynamics MD simulations, balance accuracy and computational efficiency, making them valuable for explaining experimental findings, improving virtual screening, and refining docking predictions [224].

The primary difference between MM-PBSA and MM-GBSA lies in the solvation model used for calculating polar solvation energy. MM-PBSA employs the Poisson–Boltzmann equation, which provides higher accuracy but is computationally intensive. MM-GBSA, on the other hand, uses the Generalised Born approximation, offering faster calculations suitable for large systems or high-throughput studies. Although MM-GBSA is slightly less precise than MM-PBSA, it remains highly effective for many applications such as to estimate protein–ligand binding affinities [225,226], to find important residues for protein–protein interactions [227,228], and to study macromolecular stability [229,230]

In this study, the MM-GBSA method was employed to estimate the contributions of individual residues to the binding of the polymer chain. The free energy of binding was calculated as [224,231]:

$$\Delta G_{bind} = \Delta G_{complex} - (\Delta G_{protein} + \Delta G_{ligand})$$

where the free energy of each component is computed as:

$$G = E_{int} + E_{ele} + E_{vdW} + G_{pol} + G_{np} - TS$$

Here, E_{int} , E_{ele} , and E_{vdW} represent the internal, electrostatic, and van der Waals energies, respectively; G_{pol} and G_{np} are the polar and non-polar solvation energies; and TS is the entropy term.

3.3. Enzyme engineering

Enzyme engineering offers promising solutions by enabling modifications to enhance the ability of enzymes to degrade non-natural substrates like plastics. This involves altering amino acid sequences to improve catalytic efficiency, substrate specificity, thermostability, and tolerance to environmental stresses [232–234]. Stability is a particularly critical aspect, as natural proteins are often marginally stable, making them susceptible to unfolding under environmental conditions such as increased temperature [235]. Since enzyme stability can directly impact catalytic performance, it is a key target in protein engineering. Thermal stability can be addressed through strategies such as rigidifying flexible protein regions, particularly loops, which are often implicated in thermal fluctuations [236]. However, this approach is complex for enzymes like cutinases, including *TfCut2*, which rely on the flexibility of their loop regions to accommodate large substrates [149]. Modifications to improve stability in these enzymes must balance rigidity with the functional dynamics essential for activity.

Advances in enzyme engineering technologies have expanded their applications across diverse fields, driven by key approaches like directed evolution, rational design, and semi-rational design. Mimicking natural selection in a laboratory setting, directed evolution involves iterative rounds of mutagenesis and screening to optimise enzyme functions. This method has revolutionised protein engineering by focusing on small, functionally enriched libraries rather than large, random ones, supported by computational tools for analysing protein datasets and conformational variations [237,238].

Rational design involves targeted mutations based on detailed knowledge of enzyme structure and mechanism, often aided by computational modeling to predict structure-function relationships. Despite its precision, rational design relies heavily on available data, limiting its application to well-characterised systems [239,240].

Semi-Rational Design combines aspects of rational design and directed evolution. Semi-rational approaches use structural insights to create ‘smart’ libraries of mutations. These strategies effectively address limitations of both methods, enabling efficient exploration of beneficial mutations for enhanced enzyme performance [237,241].

Computational methods to guide (semi-)rational enzyme engineering

Computational methods are central to guide rational enzyme engineering, particularly in designing enzymes for non-natural substrates like synthetic polymers. These approaches

provide detailed molecular-level insights into enzyme-substrate interactions, identify key residues, and predict binding poses and reaction mechanisms. Additionally, computational tools play a crucial role in constructing semi-rational libraries by guiding the design of small, focused libraries of mutants. Diversification or randomisation is introduced at targeted regions, often informed by computational analysis, to balance thorough exploration with experimental feasibility. By complementing experimental methods, computational tools significantly enhance the development of synthetic polymer-degrading enzymes, guiding and rationalising experiments while improving their success rates [242–245]. The computational approaches can be broadly classified into structure-based, sequence-based, and data-driven machine learning computational design [246].

Structure-based computational design requires accurate enzyme structures to identify critical residues in the active site, understand the chemical mechanism, and tailor interactions between amino acids and substrates. These methods allow precise adjustments to catalytic pockets and have even enabled *de novo* enzyme design. However, their effectiveness depends on the availability of high-quality structural data, which may not always be accessible, as obtaining crystal structures can be laborious and time-consuming [246]. Recently, an escalating number of researchers have recognised the significant implications of conformational dynamics for the catalytic promiscuity and evolution of enzymes [247–255].

Sequence-based design addresses some of these limitations by directly using protein sequences to infer evolutionary principles. With the growing availability of sequence data through next-generation sequencing, researchers can conduct phylogenetic analyses to understand enzyme evolution and identify key functional residues. These insights can be used to engineer enzymes without needing explicit structural information, thereby providing an alternative when structural data is incomplete or unavailable [256].

Data-driven methods, particularly those involving machine learning, are becoming increasingly influential in enzyme engineering. Machine learning algorithms such as random forests, support vector machines, and neural networks can model complex sequence-function and structure-function relationships. These methods have been applied to predict enzyme stability, solubility, and catalytic mechanisms after mutations [257–259]. Machine learning accelerates enzyme design by generating rapid predictions once trained on appropriate datasets, but its success depends on the quality of the training data and algorithmic efficiency. Limitations such as data standardisation issues, small homogeneous datasets, and the diversity of catalytic mechanisms still present challenges to its widespread adoption [260–263].

An illustrative computational enzyme engineering pipeline, proposed by Scherer et al. [264], begins with structure-function analysis to identify target residues. Subsequent steps include building enzyme-substrate complexes, analysing interactions, and performing evolutionary conservation studies to pinpoint design positions. Enzyme sequence space is then modified for desired traits such as stability or substrate specificity. Finally, computational screening evaluates stability, affinity, and activity to identify promising variants for experimental validation. This workflow highlights the synergy between computational tools and experimental efforts.

From the computational tools instrumental in advancing enzyme design, Rosetta [265,266] stands out as a foundational platform, offering physics-based energy functions and advanced sampling algorithms to model protein-ligand interactions and structural changes upon mutation. Its ability to predict the most energetically favourable protein conformations based on primary amino acid sequences makes it especially valuable in rational and semi-rational enzyme engineering. Rosetta's precision in guiding the generation and ranking of small, focused mutant libraries is pivotal, allowing for targeted modifications that balance experimental feasibility with functional improvement.

Emerging techniques like RFdiffusion [267] and ProteinMPNN [268] have significantly expanded the possibilities of de novo protein design. RFdiffusion employs diffusion models to generate novel protein sequences by exploring sequence space with minimal reliance on pre-existing structural templates. ProteinMPNN, on the other hand, uses message-passing neural networks to predict amino acid sequences that will fold into a desired structure. Both methods improve predictions related to enzyme stability, function, and substrate specificity, enabling more precise enzyme designs.

Moreover, AlphaFold [146], renowned for its high-accuracy protein structure predictions, complements these advanced tools by providing reliable structural models even in the absence of experimental data. AlphaFold's integration of evolutionary information and its capacity to model complex biomolecular systems further enhance the accuracy of computational designs.

The continued development of these AI-driven tools, coupled with traditional computational methods, has established a robust foundation for the rational design of enzymes with specific functions, sizes, and binding characteristics, propelling the field towards the creation of tailored enzymes [269].

Results and discussion

Chapter 4: Characterisation of *TfCut2* and modelling of its interactions with Impranil DLN

4.1. Introduction

In this chapter are described results obtained on the *Characterisation of wild-type TfCut2 and identification of key molecular determinants involved in substrate binding* using computational methods. More particularly, this chapter investigates the binding recognition of a model PUR substrate, Impranil DLN, by the *TfCut2* enzyme.

TfCut2 cutinase is a thermophilic enzyme originally produced by *Thermobifida fusca*, a bacterium that harbours two open reading frames for cutinases, namely Tfu_0882 (*TfCut1*) and Tfu_0883 (*TfCut2*) [270]. *TfCut2* was isolated from *Thermobifida fusca* KW3 for its high hydrolytic activity towards PET plastic [271]. Interestingly, despite the high sequence identity of approximately 93% between *TfCut1* and *TfCut2*, the latter exhibits roughly twice the activity towards PET compared to *TfCut1* [272,273]. *TfCut2* also demonstrates remarkable tolerance to various organic solvents, making it well-suited for industrial applications [272,273]. Its apparent melting temperature has been determined to be 70°C, however, activity measurements indicate a loss of function at temperatures as low as 61°C [149].

As a cutinase, *TfCut2* naturally catalyses cutin hydrolysis [149,189,274] and also exhibits esterase activity towards p-nitrophenol-linked aliphatic esters (*p*NP-aliphatic esters) [149,188,189,274,275]. In addition, it hydrolyses triglycerides, including triacetin, tributyrin, tricaprin, and trilaurin, showing a preference for short-chain substrates [275]. *TfCut2* also degrades the hemicellulose xylan [276] and several synthetic polyester polymers beyond PUR, such as poly(ethylene terephthalate) (PET), the most prevalent polyester plastic [48,188,189], poly(ϵ -caprolactone) (PCL), a synthetic aliphatic biodegradable polyester [275], and polyoxyethylenesorbate esters, with a preference for shorter chain lengths [276]. *TfCut2* also exhibited hydrolysis activity on a recently proposed model polyester PUR, the PBA-PUR, as indicated by transparent clear zones formation on agar plates [277].

The broad substrate range of *TfCut2* highlights its notable substrate promiscuity, largely attributed to a hydrophobic binding site exposed on the enzyme's surface [48,149,278]. Unlike enzymes with buried active sites, which constrain substrate size, shape, and volume, *TfCut2*'s accessible binding site allows it to interact with a variety of substrates, including bulky polymer

chains. *TfCut2*, classified as EC 3.1.1.74 (cutinase) within the carboxylic-ester hydrolases, can be activated by divalent metal ions such as Ca^{2+} and Mg^{2+} [188].

In computational studies, especially prior to advancements such as AlphaFold in 2021 [146], obtaining a high-quality experimental structure was crucial. *TfCut2* is well-characterised by multiple X-ray crystal structures available in the PDB database [145], with the structure deposited under the PDB code 4CG1 providing the highest resolution of 1.4 Å [149]. This structure reveals the classic catalytic triad of serine (S130), histidine (H208), and aspartic acid (D176), where serine serves as the nucleophile and histidine and aspartic acid form a charge relay system. The oxyanion hole, essential for stabilising transition states, is formed by the backbone nitrogens of M131 and Y60. The binding site also features an aromatic clamp formed by Y60 and W155, with I178 stabilising substrates *via* hydrophobic interactions [149].

TfCut2 has a highly flexible region around residues 245-247, which required the fitting of multiple conformations during ensemble refinement. Due to this flexibility, D246 was not resolved [149]. A disulfide bridge between C241 and C259, located near this flexible region, is believed to stabilise the structure and prevent denaturation at higher temperatures. The enzyme adopts a classical α/β -hydrolase fold, with a central nine-stranded β -sheet flanked by 11 α -helices on either side [149].

This dissertation focuses on *Thermobifida fusca* cutinase (*TfCut2*), a bacterial cutinase. At the time this dissertation began in October 2020, *TfCut2* appeared to be the most promising enzyme for studying polyester PUR biodegradation. Schmidt et al. [20] tested *TfCut2* along with three other bacterial cutinases—Leaf-branch compost cutinase (LCC), *Thermomonospora curvata* DSM43183 *Tcur1278*, and *Tcur0390*—on the hydrolysis of Impranil DLN and two other polyester PURs, Elastollan B85A-10 and C85A.

In the study by Schmidt et al., the degradation kinetics of Impranil DLN (0.1%) was analysed using a turbidimetric assay, revealing a linear decrease in OD_{400} during the initial reaction phase. From this linear region, initial hydrolysis rates were calculated and used to determine kinetic parameters, such as the rate constant of the surface reaction k^s and the adsorption equilibrium constant K , following the kinetic model by Mukai et al. [195]. *TfCut2* and *Tcur0390* exhibited the highest hydrolysis rate constants for Impranil DLN (0.026 s^{-1}), with *TfCut2* also requiring the lowest enzyme concentration to achieve maximum initial hydrolysis rate. Notably, *TfCut2* displayed the highest adsorption constant K , indicating a strong affinity for Impranil DLN [20]. These findings positioned *TfCut2* as a promising candidate for further exploration.

In tests on other polyester PURs, *TfCut2* and LCC achieved about 1% weight loss for Elastollan B85A-10 and C85A at 60 °C. At 70 °C, LCC demonstrated increased degradation, attributed to its higher thermostability [278]. FTIR analysis of the *TfCut2* and Elastollan samples indicated ester bond cleavage, confirmed by shifts in carbonyl and C–O stretching peaks, verifying PUR degradation. [20].

The model PUR substrate, Impranil DLN (produced by Covestro, Germany), has been used in many experimental studies to screen for PUR-degrading activity [20,80,103–106]. It was thus decided to be used in the studies within this dissertation. However, although widely regarded as a PUR model substrate, its exact structure is proprietary. Initially, Biffinger et al. [3] proposed a structure for Impranil DLN (Fig. 8A), suggesting it comprised hexamethylene diisocyanate and polyhexane neopentyl adipate polyester (Fig. 8B). This model was subsequently adopted in several studies [58,161] and also served as the basis for the initial modelling work in this dissertation.

However, in 2022 Fuentes-Jaime et al. [4] suggested that Impranil DLN is derived from hexamethylene diisocyanate, neopentyl glycol, adipic acid, and 1,6-hexanediol (Fig. 8 C-D), with added plasticizers and chain extenders.

Overall, the two proposed structures of Impranil DLN single repeating unit are rather similar. They both contain ester and urethane bonds and are derived from hexamethylene diisocyanate. However, the structure proposed by Biffinger has longer carbon chains, and hydrolysable ester bonds are located further from each other. This property can cause this model to primarily interact *via* hydrophobic interactions, whereas in the case of Fuentes-Jaime et al.'s model, the more concentrated ester bonds may form hydrogen bonds with the surface of the receptor, and solvent. Also, Fuentes-Jaime et al.'s model features two types of alcohols in the soft polyol segment: neopentyl glycol and 1,6-hexanediol, which complicates the structure of a single repeating unit of Impranil DLN.

Given the ambiguity regarding the Impranil DLN structure, together with NMR specialists, we have performed analysis of the Impranil DLN structure and products of its hydrolysis which will be described in details in the results section. The results were in agreement with findings and Impranil DLN structure proposed by Fuentes-Jaime et al [4]. As a result, the computational studies for modelling Impranil DLN with *TfCut2* had to be restarted using the newly verified structure. The results presented in this chapter are based on Impranil DLN structure proposed by Fuentes-Jaime et al.; the initial results obtained using the structure of Impranil DLN proposed by Biffinger et al. are not included in this manuscript.

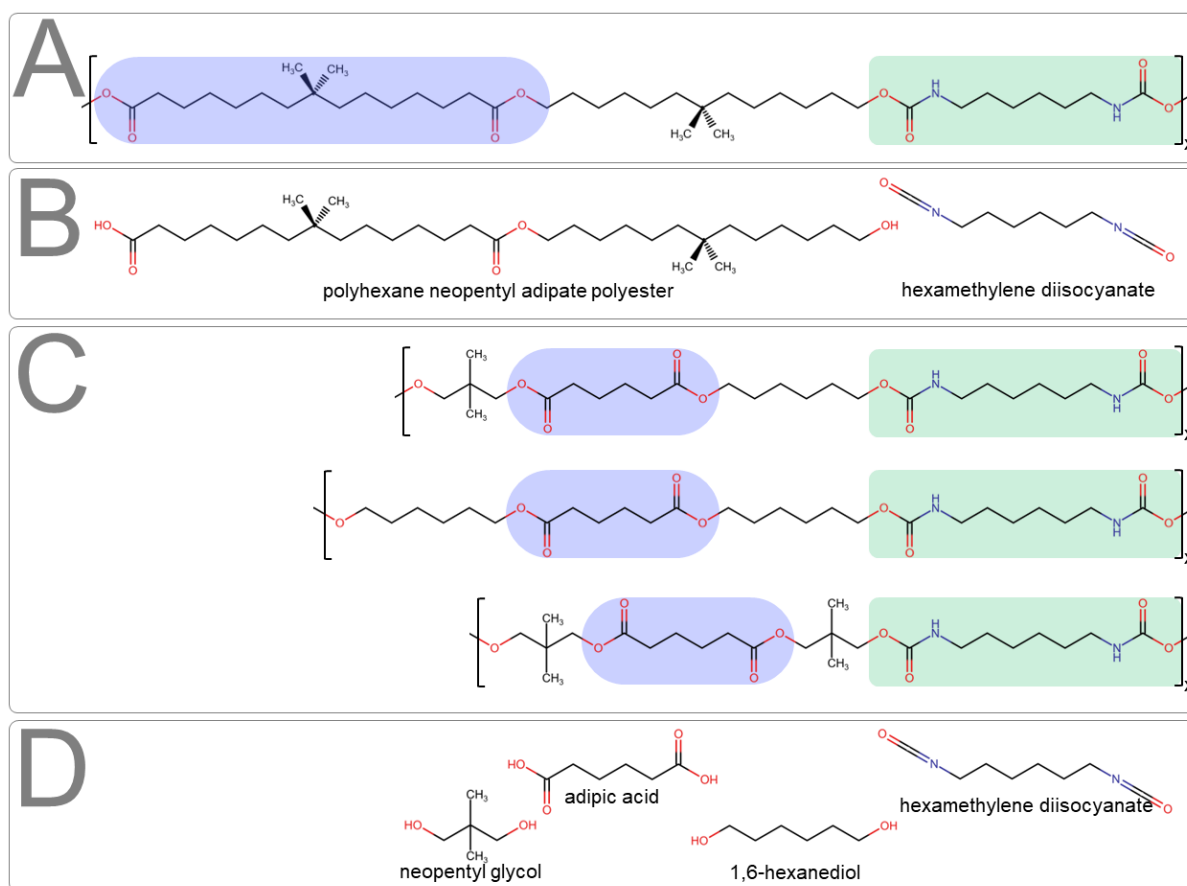


Fig. 8. Proposed structures of Impranil DLN single repeating unit. “X”-number of repeating units not known. The purple oval indicates the ester part of the repeating unit, formed by an acid substrate, and green rectangle informs about hard urethane segment formed by isocyanate substrate. **A)** Structure proposed by Biffinger et al. [3]. **B)** Substrates of Impranil DLN synthesis according to Biffinger et al. [3]. **C)** Structures proposed by Fuentes-Jaime et al. [4]. Due to multiple building blocks, several combinations exist. **D)** Substrates of Impranil DLN synthesis according to Fuentes-Jaime et al. [4].

To date, computational studies involving non-homogeneous polymers are limited, with most research focusing on small polymer fragments or homogeneous polymers, due to the structural complexity of the entire polymer chains. The presented study applies and adapts existing computational techniques to explore *TfCut2* interactions with models built-in to describe in a simplified way the complexity of surroundings of hydrolysable bonds which can be attacked by the enzyme. The primary objective is to identify key molecular determinants in *TfCut2* that contribute to PUR recognition and binding, consistent with its hydrolysis mechanism. To achieve this, a range of computational methods were employed, while characterising *TfCut2* and its interactions with the selected regions of the model substrate, Impranil DLN, ensuring enzyme-ligand complexes adopted a “productive pose” where catalytic distances were favourable for the initial hydrolysis step. To achieve this, a specific

pipeline was developed to select MD simulation frames that capture productive configurations. These frames were then further analysed to identify key molecular interactions and amino acid residues within the *Tf*Cut2 binding site, focusing on their individual contributions to Impranil DLN binding. This analysis guided the selection of residues for mutation, providing grounds to guide the re-design of the active site to improve PUR degradation, which will be presented in Chapter 5. Schematic of computational studies performed on *Tf*Cut2 in interaction with Impranil DLN is presented in Figure 9.

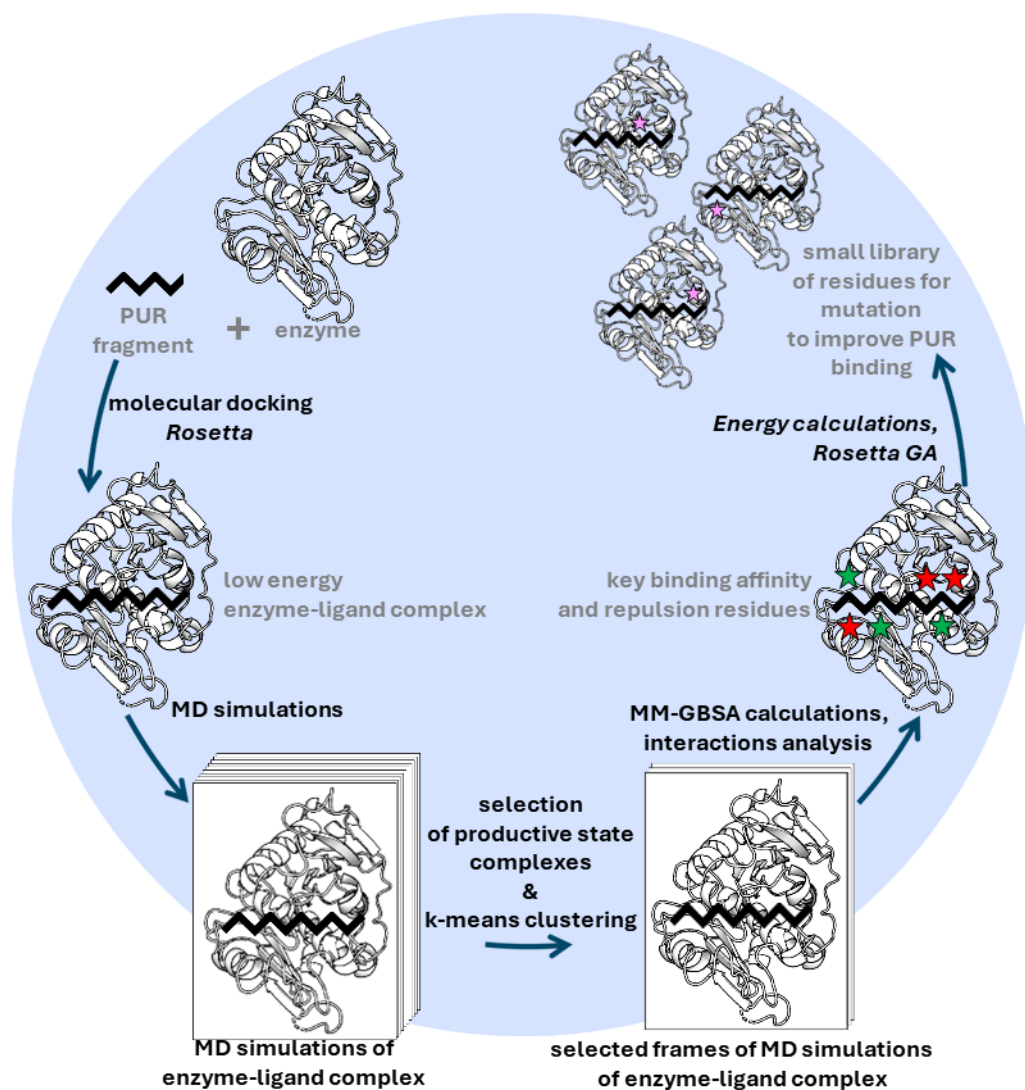


Fig. 9. Schematic of computational studies performed on *Tf*Cut2 in interaction with Impranil DLN, detailing the process of analysing enzyme-ligand interactions in productive poses to identify key amino acid residues that could be targeted by mutagenesis.

4.2. Methodology

4.2.1. Experimental methods

Preparation of Impranil DLN for NMR structural analysis

Impranil DLN, a 40% aqueous dispersion of polyester PUR, was supplied by Covestro (Germany). The Impranil DLN sample was lyophilised and then dissolved in chloroform or DMSO.

NMR spectra

To confirm the structure of the Impranil DLN, NMR spectroscopy was used: ^1H and ^{13}C NMR. ^1H and ^{13}C NMR spectra were recorded on a Varian 600 MHz spectrometer, using the following deuterated solvents: DMSO and CDCl_3 .

4.2.2. Computational methods

Sequence analysis

A Multiple Sequence Alignment (MSA) of four cutinases: *TfCut2*, LCC, *Tcur1278* and *Tcur0390* was prepared to assess information about sequence identity between these enzymes, their conserved and variable regions and relations and to check how distant or similar *TfCut2* is to them.

The MAFFT webserver [133] was used with G-INS-1 progressive method. The alignment was visualised using the EsPript webserver [279] to highlight conserved and variable regions, accompanied by annotation of *TfCut2*'s secondary structure based on the 3D structure deposited in PDB under PDB ID: 4CG1 [149]. Pairwise sequence identity was calculated from this MSA using the Ident and Sim webserver [134] to assess the degree of similarity between each enzyme.

Protein 3D models preparation

The X-ray crystallographic structure of *TfCut2* (PDB ID: 4CG1) [149] and LCC (PDB ID: 4EB0) [280] were downloaded from the Protein Data Bank [145]. All ligands were manually removed from the structure, while the crystallographic water molecules were

retained. The missing residue D246 in *TfCut2* was added by performing homology modelling using SWISS-MODEL [281,282].

The 3D structures of Tcur1278 and Tcur0390 were modelled using I-TASSER [200,283,284] based on the deposited amino acid sequences with Gene IDs HG939554 and HG939555, respectively.

The protonation states of titratable residues were determined using the H++ Server [285] at pH 8.0, ensuring that the catalytic residue H208 was correctly protonated as HIS- ϵ to correspond to the protonation state in the first stage of the hydrolysis mechanism of *TfCut2* [165,166].

Search for Ca²⁺ ion binding sites in TfCut2

The PDB database was searched for protein structures homologous to *TfCut2*, that contain divalent metals (Ca²⁺ or Mg²⁺) bound to their structure. The following structures were retrieved for further analysis: 3WYN, 5LUI, 4WFJ, 5ZNO, 5LUK, 6AID. The protein structures were downloaded and aligned in PyMOL [152]. After alignment, four divalent metal-binding sites could be observed indicated by presence of at least one divalent metal ions from the crystal structures. One Ca²⁺ ion from each of the four divalent-metal binding sites was copied to the 4CG1 structure. The crystal water was added to the system. LeaP from AmberTools18 suite [286] was used to add counterions and immerse all models in a TIP3P water molecules octahedral box of the size 12 Å.

Molecular docking of model PUR fragments

The molecular docking protocol was adapted from a previously published method [287] using Rosetta 3.13 [266] using *ref2015* all-atom energy scoring function [288]. The ester and urethane moieties were constructed and minimised using Avogadro 1.2.0 [289]. These fragments, which include two ester or urethane groups each, were adjusted with terminal methylene groups to stabilise chemical charges. Ligand parameterisation was performed using the Antechamber module in Amber18 [222].

To explore diverse binding poses of the ligand, conformational sampling was carried out using the Confab package within Open Babel (1.1.0) [290]. In this study, 14 conformers of the ester moiety and 20 conformers of the urethane moiety were generated, with RMSD and energy cutoffs set at 1.3 Å and 50 kcal/mol, respectively, and a maximum limit of 10,000

conformers. The initial placement of the ligand in the complex was performed manually, ensuring that catalytic distances were maintained to facilitate accurate docking.

To ensure the correct orientation of the docked ligand poses, the carbonyl oxygen of the ligand's ester/urethane group was restrained to the catalytic S130 hydroxyl group γ -oxygen. Simultaneously, the catalytic H208 ϵ -nitrogen was restrained to the S130 hydroxyl group γ -hydrogen, using a flat harmonic potential with distances set to 1.5–3.5 Å and 1.5–2.5 Å, respectively. Additionally, a flat harmonic potential was set to 100–110° for angle between S130 O γ , the carbonyl carbon, and the carbonyl oxygen.

Overall, four initial complexes were generated: ester P1, ester P2, urethane P1 and urethane P2. Each of the complex was then relaxed using Rosetta 3.13 [291,292] using different standard deviation values and the lowest interface score relaxed complex was then used for flexible ligand docking. The docking calculations were run using a custom Rosetta3 XML script enabling backbone and side-chain flexibility as previously described [208,293] including added Backrub module for backbone flexibility in the binding site region. In the calculations, 10 000 enzyme-ligand complex structures were generated. The lowest 10% interface scored complexes were clustered according to total score, interface score and ligand rms without superposition, and the lowest interface scored enzyme-ligand complex from the most populated cluster was further used.

Preparation of TfCut2-Impranil DLN complexes for MD simulations

The procedure of constructing the Impranil DLN unit on a docked ester/urethane moiety was as follows:

1. Save the docked ligand (ester/urethane P1/P2 moiety) as a MOL2 file.
2. Open the ligand pose in Avogadro 1.2.0 [289], attach the missing atoms of an Impranil DLN repeating unit, and save the structure;
3. Align the constructed Impranil DLN repeating unit to the bound ligand moiety in the initial complex using atom pair fitting in PyMOL [152], and save the enzyme with the Impranil DLN repeating unit.
4. Run the Rosetta relax module [291,292] to minimise the energy of the complex and remove atom clashes. The constructed repeating units of Impranil DLN were parameterised using the Antechamber module of Amber18 [222] along with the General AMBER force field [219] and the AM1-BCC charge model [223].

Crystallographic water molecules present in the 4CG1 structure were retained. Additionally, two Ca^{2+} ions were added to each divalent-metal binding site within the structure. To prepare the system for simulation, the LeaP tool from AmberTools18 [286] was employed. LeaP was used to add the necessary counterions to neutralise the system and immerse the model in a 20 Å octahedral box of TIP3P water molecules. The topology of the model and coordinates of atoms in space were generated using the LeaP tool.

MD simulations

Within the methods presented in this chapter, two types of MD simulations were carried out: 1) analysis of *TfCut2* in the presence of four bound Ca^{2+} ions to identify potential divalent metal binding sites, and 2) analysis of *TfCut2* in complex with Impranil DLN single repeating unit, in different poses, 8 systems overall. The procedures were the same for both systems and are described below.

MD simulations were conducted using the AMBER 18 software package for the system, using the *ff14SB* protein force field [216]. For each simulated system, ten repetitions of 50 ns were performed, totalling 500 ns of MD simulations. The protocol consisted of three main stages: minimisation, equilibration, and production.

Minimisation

The minimisation procedure consisted of five steps, each with progressively decreasing constraints on the protein backbone. Initially, 1000 steps were performed with a restraint weight of $500 \text{ kcal/mol} \times \text{Å}^2$, consisting of 500 steepest descent steps followed by 500 conjugate gradient steps. This was repeated for the second stage, focusing on the backbone atoms. In the third stage, the restraint weight was reduced to $125 \text{ kcal/mol} \times \text{Å}^2$, and the same minimisation steps were applied. The fourth stage used a restraint weight of $25 \text{ kcal/mol} \times \text{Å}^2$, again focusing on the backbone atoms. Finally, a minimisation was performed without any restraints.

Additionally, for the systems of *TfCut2* with Impranil DLN, during minimisation, distance constraints were applied to ensure the correct binding of the ligand to the enzyme. Specifically, the carbonyl oxygen of the ester group was restrained to the S130 hydroxyl group γ -oxygen, and the H208 ϵ -nitrogen was restrained to the S130 hydroxyl group hydrogen, using a flat harmonic potential with distance ranges of 1.0-3.0 Å and 2.0-5.5 Å, respectively.

Equilibration

Gradual heating from 0 K to 298 K was performed over 20 ps using a Langevin thermostat with a temperature coupling constant of 1 ps in a constant volume periodic box. This was followed by equilibration under constant pressure periodic boundary conditions for 2 ns with a 2 fs time step. Additionally, for the systems of *Tf*Cut2 with Impranil DLN, distance constraints applied during minimisation were maintained during equilibration to ensure correct ligand binding.

Production

Production MD simulations were conducted for 50 ns with a 2 fs time step under constant temperature conditions, maintained using the weak-coupling algorithm. A temperature coupling constant of 1.0 ps was used. Long-range electrostatic interactions were modelled using the Particle Mesh Ewald method [294] with a non-bonded cut-off of 10 Å. The SHAKE algorithm [295] was employed to maintain geometric constraints. Coordinates were saved at intervals of 2 ps. No distance constraints were applied during the production phase.

Trajectories analysis

The trajectories obtained from MD simulations were analysed using *Cpptraj*, a tool within the AMBER software suite [296,297]. *Cpptraj* was employed to perform a variety of post-simulation analyses, enabling the assessment of system stability and the preparation of data for subsequent analyses. *Cpptraj* was used for the calculation of the Root-Mean-Square Deviation (RMSD), Root-Mean-Square Fluctuation (RMSF), and calculating distances and contact numbers between specific atoms or residues within the system.

Selection of productive MD simulations frames

For each ligand pose, only frames where the ligand was productively bound within the hydrophobic groove of *Tf*Cut2 were selected for interaction analysis. To ensure accurate representation of the system's conformational diversity, ten representative snapshots were selected from the MD simulations using a pipeline of productive frames selection, followed by clustering technique.

Filtering Based on Distance and Angle Criteria

Frames were selected if they met the following criteria:

- Distance between the γ -oxygen of S130 and the carbonyl carbon of the cleaved group ≤ 3.5 Å.

- Distance between the γ -hydrogen of S130 and the ϵ -nitrogen of H208 ≤ 2.5 Å.
- Angle for the nucleophilic attack between S130 O γ – carbonyl carbon – carbonyl oxygen of the cleaved bond between 60° and 120°.

Filtering Based on Ligand Pose Shape

Frames were further filtered to ensure the ligand was in an extended pose along the *TfCut2* binding groove. This involved:

- Measuring the distance between the carbonyl carbons on both sides of the Impranil DLN repeating unit chain.
- Assessing the angles between the carbonyl carbons.
- Counting the number of residues within 6 Å of the ligand.
- Maximising these values for each pose separately to ensure at least 15 frames were selected.

Clustering to Ensure Diversification

The remaining frames were clustered using the k-means method ($n_clust = 10$) in AMBER 18 [286] without ligand superimposition. This produced an artificial trajectory of ten frames for each binding pose, with the ligand bound in a nucleophilic attack position in an extended pose.

MM-GBSA calculations

Short ten-frame MD snapshots acquired in the previous step were used to calculate binding free energies using the MM-GBSA method as implemented in AMBER 18 [286]. This method combines molecular mechanics energies with generalised Born solvation energies to estimate binding affinities [224,298]. The Generalised Born (GB) model was utilised for its computational efficiency and ability to handle large systems.

The calculations were performed using the *Cpptraj* module for trajectory analysis and the *MMPBSA.py* script for binding free energy calculations [297]. Using selected ten MD snapshots instead of single ones allowed to capture the conformational diversity of the system.

ProLIF

To analyse the interactions between *TfCut2* and the ligand Impranil DLN, the ProLIF (Protein-Ligand Interaction Fingerprints) Python library, version 2.0.0 [299], was employed.

Visualisation

This subsection describes the tools utilised to visualise the quantitative results as plots or visualise molecules in 3D. The techniques described here were used in the next Chapters 5 and 6 as well.

For data analysis and visualisation in a form of plots, Python 3.9.5 [300] programming language was used together with libraries: Pandas 1.5.3 [301], Numpy 1.26.2 [302], Matplotlib 3.8.2 [303], Seaborn 0.13.2 [304], Biopython 1.81 [305], Scipy 1.11.4 [306].

For 3D visualisation of proteins, PyMOL 2.5.4 software was used [152]. Additionally, python scripting language with library cmd (Support for line-oriented command interpreters.

The chemical structures were drawn the author using Microsoft PowerPoint, or using ChemSpace [101].

4.3. Results and discussion

4.3.1. Investigation of the structure of Impranil DLN

To characterise the structure and composition of Impranil DLN, nuclear magnetic resonance (NMR) spectroscopy was employed. Impranil DLN, a 40% aqueous dispersion of polyester PUR, was generously provided by Covestro (Germany). The NMR spectra were acquired in a solvent that prevents the exchange of labile protons, enabling the observation of functional groups such as carboxyl, hydroxyl, and amino groups formed during hydrolysis, therefore, deuterated dimethyl sulfoxide (DMSO) was used. Prior to analysis, the sample was lyophilised and subsequently dissolved. Comprehensive structural analysis of Impranil DLN requires advanced NMR techniques, particularly 2D NMR methods, including both homonuclear and heteronuclear approaches, to resolve its complex molecular features fully.

To confirm the structure of Impranil DLN, a ^{13}C NMR spectrum and a set of two-dimensional (2D) NMR spectra (COSY, HSQC, and CIGAR) were recorded. The 2D spectra provided detailed insights: the COSY spectrum revealed directly coupled protons, the phase-sensitive HSQC spectrum allowed the assignment of carbons directly bonded to hydrogen atoms and distinguished carbon multiplicity, while the CIGAR spectrum enabled the identification of the carbon chain backbone by analysing proton-carbon couplings over two and three bonds, which helped locate quaternary carbon atoms.

The comprehensive information obtained from NMR spectroscopy enabled the proposal of Impranil DLN's chemical structure, shown in Fig. 10. Its composition includes the following components: 1,6-hexanediol, adipic acid, neopentyl glycol, and hexamethylene diisocyanate.

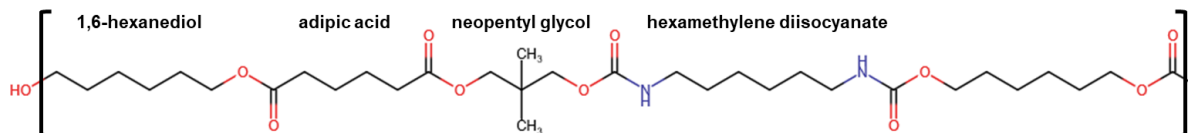


Fig. 10. Proposed chemical structure of Impranil DLN based on NMR data.

Figure 11 presents the NMR spectrum of Impranil DLN in deuterated DMSO. The following figures present the interpreted ^{13}C NMR spectra with assigned carbon signals (Figs. 12-13). Significant fragments of 2D spectra, which enabled a complete characterisation of the structure of Impranil DLN are provided in Supplementary figures 4.1-4.4 at the end of Chapter 4.

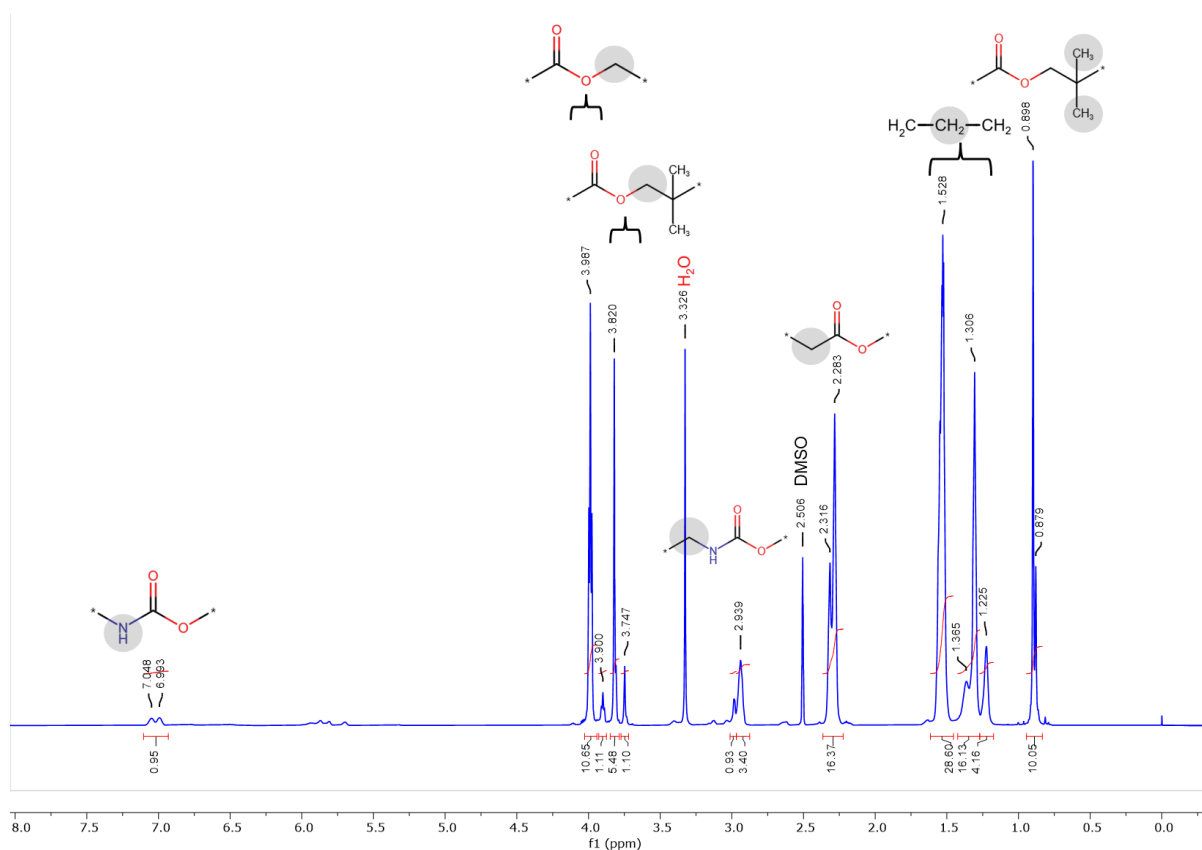


Fig. 11. ^1H NMR spectrum of Impranil DLN in DMSO- d_6 (600MHz), range 0-8.0 ppm. Above the picks, chemical structures containing proton groups responsible for signals are proposed (in green).

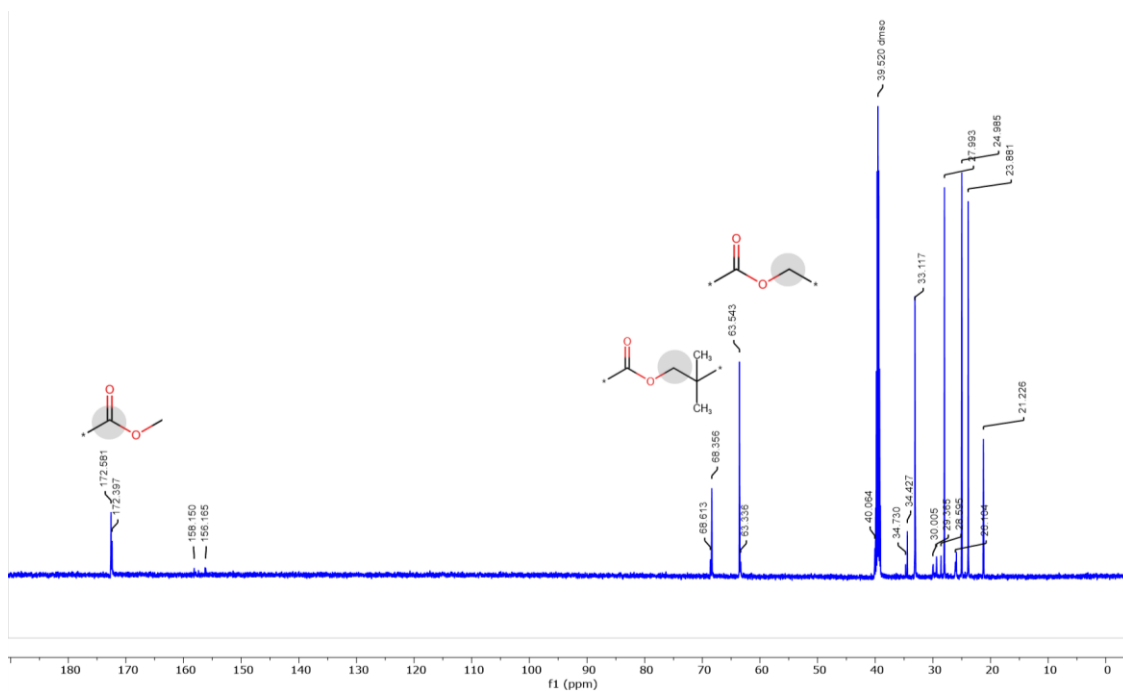


Fig. 12. ^{13}C -NMR spectrum of Impranil DLN in DMSO-d_6 (Varian 600MHz).

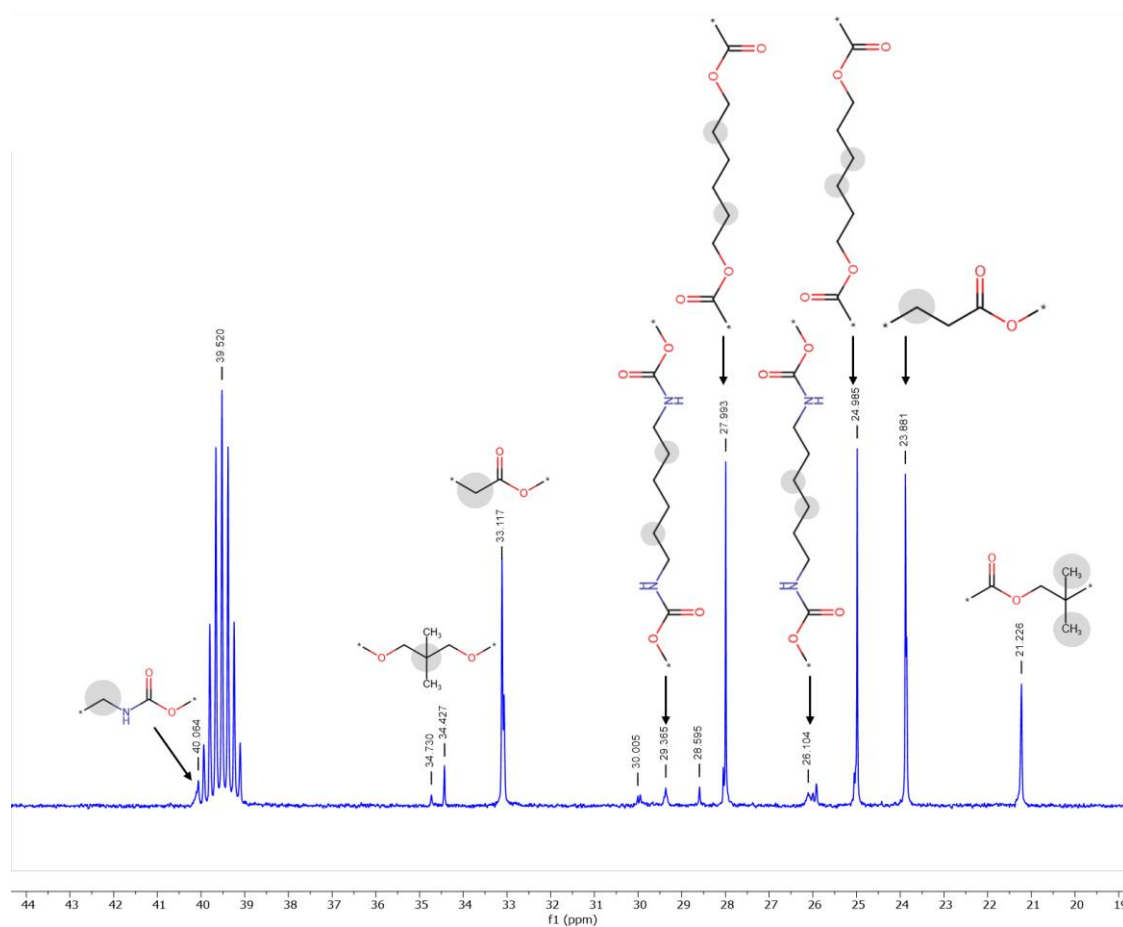


Fig. 13. Fragment of the ^{13}C -NMR spectrum of Impranil DLN (aliphatic carbon range) in DMSO-d_6 (600MHz).

Quantitative analysis of the ¹H NMR spectrum of Impranil DLN in deuterated chloroform

As mentioned before, deuterated DMSO was chosen as a primary solvent because it prevents the exchange of labile protons, enabling the observation of functional groups such as carboxyl, hydroxyl, and amino groups formed during hydrolysis. However, since on ¹H NMR spectrum of Impranil DLN in deuterated DMSO, the signals from ester groups in 1,6-hexanediol and neopentyl glycol are bifurcated, for the quantitative analysis, the ¹H NMR spectrum of Impranil DLN recorded in deuterated chloroform was used, to minimise bias.

The ¹H NMR spectrum of Impranil DLN (Fig. 14), recorded in deuterated chloroform, reveals characteristic signals corresponding to fragments present in its structure. At a chemical shift of 4.8 ppm, the spectrum shows a signal attributed to NH protons from the urethane group. In the range of 3.8–4.2 ppm, signals from ester fragments are observed: a triplet at 4.1 ppm corresponding to the CH₂ group of the ester's alcohol residue, and a singlet at 3.9 ppm attributed to the isolated CH₂ group of neopentyl glycol.

The signal at 3.2 ppm is characteristic of CH₂ groups adjacent to nitrogen in the urethane system, while a multiplet at 2.3 ppm corresponds to CH₂ protons in the α-position relative to the ester carbonyl group. Signals in the 1.2–1.8 ppm range originate from CH₂ groups in the β- and γ-positions of the 1,6-hexanediol chain and the β-position of adipic acid. The most shielded signal in the spectrum, a singlet at 1.0 ppm, corresponds to isolated CH₃ groups in the aliphatic structure of neopentyl glycol.

A summary of the characteristic structures identified in Impranil DLN, based on the ¹H NMR spectrum, is presented in Table 3.

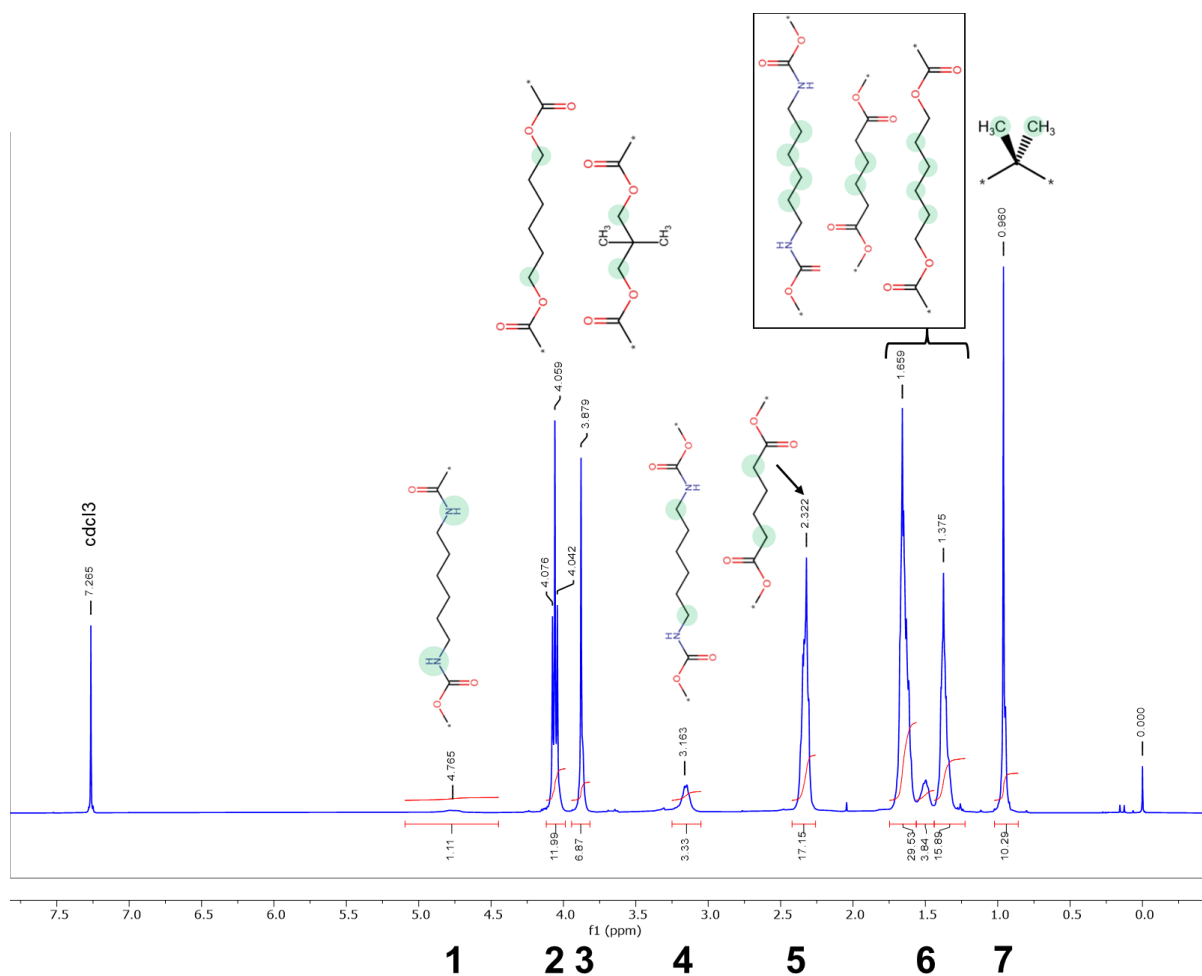


Fig. 14. ^1H NMR spectrum of Impranal DLN in chloroform, range 0-4.2 ppm. Above the picks, chemical structures containing proton groups responsible for signals are proposed (in green). The numbers in below correspond to rows in Table 3.

Table 3. Summary of characteristic structures found in Impranal DLN. Detailed NMR results, specifying the range of chemical shifts (ppm), name of the found compound, its chemical structure and marked groups of protons giving the signals, signal types, integral values (signal intensities), the number of protons, and the integral-to-proton ratio.

	Chemical shifts (ppm)	Name of compound	Chemical structure	Signal types	Integral value	Number of protons	integral-to-proton ratio
1	4.8	NH group in hexamethylene diisocyanate		multiplet	1.11	2	0.56
2	4.1	Ester from 1,6-hexanediol		triplet	11.99	4	3.00
3	3.9	Ester From neopentyl glycol		singlet	6.87	4	1.72

4	3.2	Urethane hexamethylene diisocyanate		multiplet	3.33	4	0.83
5	2.3	Adipic acid		multiplet	17.15	4	4.29
6	1.2-1.8	-CH2- In chain		multiplet	29.53 3.84 15.89 Sum: 49.26		
7	1.0	Methyl group In neopentyl glycol		singlet	10.29	6	1.72

The correctness of the proposed structure of Impranil DLN can be checked by checking the value of the integrals and the number of protons for the peaks representing the same group:

Protons in Neopentyl Glycol

- Signal at **3.9 ppm**: corresponds to CH₂ groups in the ester system (C=O)-O-CH₂-. The total integral is 6.87, with four protons in two CH₂ groups. The integral-to-proton ratio is 1.72.
- Signal at **1.0 ppm**: corresponds to CH₃ groups in neopentyl glycol. The integral is 10.29, with six protons in two CH₃ groups. The integral-to-proton ratio is also 1.72.

-CH₂- Groups in the Polymer Chain

Repeating -CH₂- groups originate from:

- **1,6-Hexanediol**: 8 protons from CH₂ groups.
- **Adipic Acid**: 4 protons from CH₂ groups.
- **Hexamethylene Diisocyanate**: 8 protons from CH₂ groups.

Expected sum of integrals:

- 1,6-Hexanediol: $3.00 \times 8 = 2.00$
- **Adipic Acid**: $4.29 \times 4 = 1.44$
- Hexamethylene Diisocyanate: $0.83 \times 8 = 0.56$

The cumulative integral for signals in the 1.7-1.3 ppm range is 49.26, aligning with the expected sum of 47.8. Slight deviations may indicate the presence of additional minor chain-extending groups.

The values that do not correspond are the integral-to-proton ratio of NH group in hexamethylene diisocyanate (0.56) versus integral-to-proton ratio of CH₂ groups adjacent to nitrogen in the urethane system of hexamethylene diisocyanate (0.83). However, the signal from of NH group in hexamethylene diisocyanate is weak and wide, therefore its integral value can have more bias.

Molar ratio of structural units in Impranil DLN

By assessing the value of the integral for one proton (Integral / no. of protons) for the specific structural units, their molar ratio can be estimated:

- 1,6-Hexanediol: 30.5%
- neopentyl glycol: 17.5%
- Adipic acid: 43.6%
- Hexamethylene diisocyanate: 8.4%

These results are rational, as adipic acid should be present in the largest amounts, given its role in forming ester bonds with diols, while isocyanate is present in the smallest amounts, consistent with the structure of polyester PUR, which predominantly consists of long, soft polyol segments with relatively few hard segments. From the molar ratio of structural units in Impranil DLN, the ratio of urethane to ester bonds can be estimated. Taking into account that each mole of adipic acid reacts with diols to form ester bonds (43.60%), and each mole of diisocyanate hexamethylene diisocyanate reacts with diols to form urethane bonds (8.44%), the ratio of urethane to ester bonds is $\frac{8.4}{43.6}$. Therefore, the ratio is approximately 1:5.2.

Through detailed analysis of ¹H and ¹³C NMR spectra, along with two-dimensional (2D) NMR spectra (COSY, HSQC, and CIGAR), it was possible to propose a composition for Impranil DLN, produced by Covestro. These findings are consistent with the structure of Impranil DLN proposed by Fuentes-Jaime et al. [4]. However, the precise composition, such as the lengths of individual polymer chains, incorporation of chain extenders, or plasticisers, remains unresolved. Further analysis could provide these insights, since the molar ratio of the structural units has been estimated.

4.3.2. Sequence and structure characteristics of *TfCut2*

The enzyme selected for these studies, bacterial cutinase *TfCut2* from *Thermobifida fusca*, shares 54.7-55.7% pairwise sequence identity with three other cutinases—LCC, *Tcur0390*, and *Tcur1278* (Fig. 15A), which were experimentally analysed by Schmidt et al. and reported to degrade Impranil DLN and two other polyester PURs [20]. Structurally, all four cutinases are very similar. The structures feature nine beta-sheets surrounded by alpha helices [149]. All examined cutinases share the α/β -hydrolase fold, which includes the well-known GX SXG motif characteristic of the serine hydrolase family [307]. In *TfCut2*, this motif appears at positions 128-132 as GHSMG, featuring the catalytic serine (S130) within the sequence (Fig. 15C). Sequence alignment of these cutinases reveals that the many residues are indeed conserved (Fig. 15C). The catalytic triad is conserved, with a serine at position 130, an aspartic acid at 176, and a histidine at position 208 in *TfCut2*. Notably, one of the oxyanion hole residues varies at position 60, where *TfCut2* and LCC have a tyrosine, while *Tcur0390* and *Tcur1278* contain phenylalanine; the other oxyanion hole residue is conserved as methionine at position 131. The oxyanion hole of cutinases is formed by the backbone amide groups of these residues, therefore variability is tolerated in these positions.

Calcium ions are known to stabilise the structure of many cutinases [188,308–310]. To identify potential divalent metal-binding sites in *TfCut2*, 10 repetitions of 50 ns MD simulations at 298 K were conducted with a Ca^{2+} ion positioned in each of four putative sites identified in crystallographic data from homologous proteins (Fig. 16). One of these sites in *TfCut2* contained three negatively charged amino acids: D174, D204, and E253, another site one only one: E72, and the last two (located near residues G38 and N160) did not contain any negative amino acids. Only one site—located near residues D174, D204, and E253—retained the Ca^{2+} ion consistently across all ten simulation replicates. The negatively charged environment created by D174, D204, and E253 effectively maintained the Ca^{2+} ion, forming a stable divalent metal-binding site. This site aligns with previously described metal binding sites in the literature, and studies have shown that substituting these residues with arginine in related enzymes increases thermal stability, underscoring its functional importance [188]. This divalent metal binding site is also conserved in other cutinases, such as LCC [48].

In the two other putative metal binding sites lacking negatively charged residues, the Ca^{2+} ions were found to dissociate into the solvent within the first ns of simulations.

An additional site near residue E72 retained the Ca²⁺ ion in only three out of the ten simulation replicates.

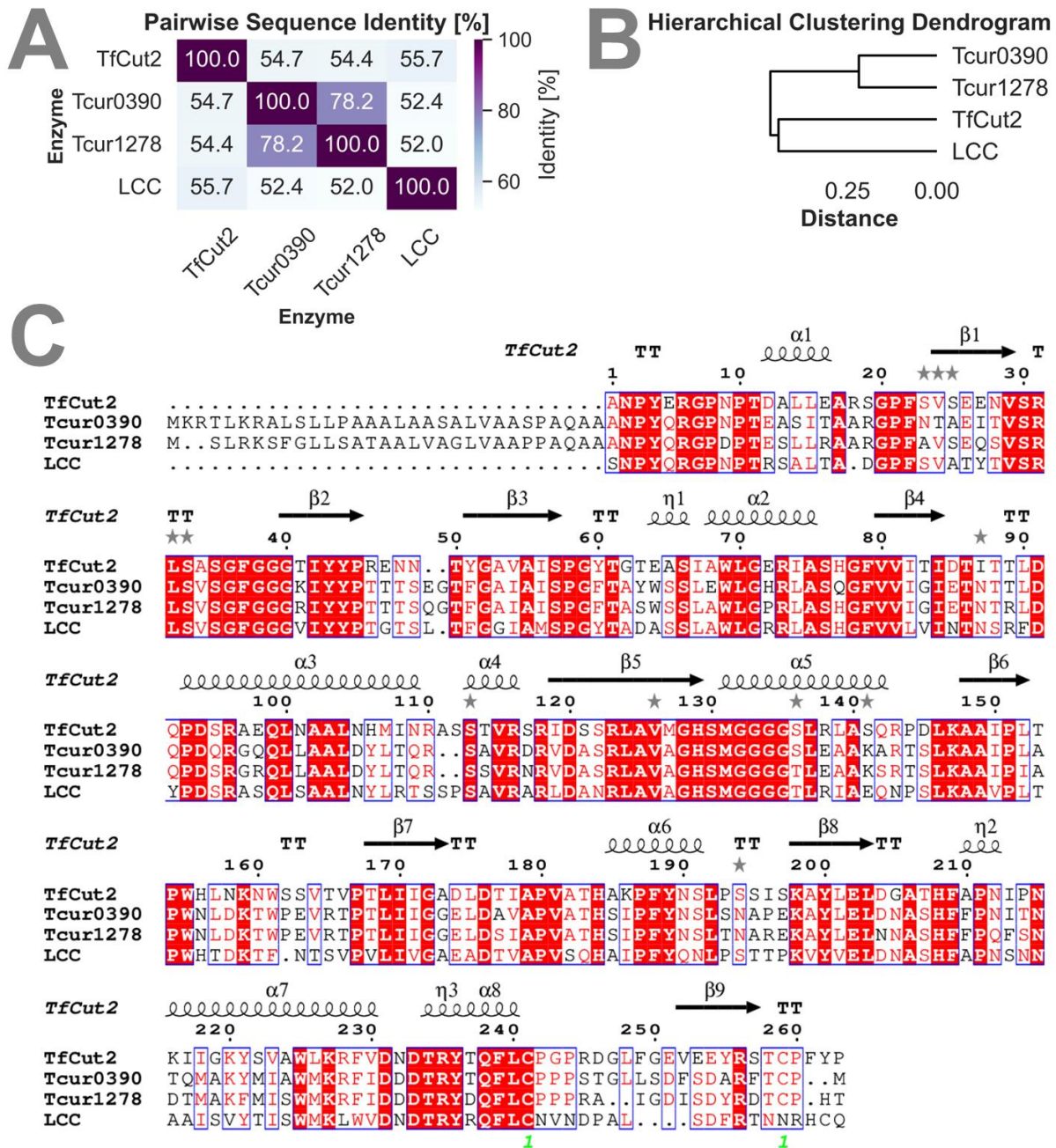


Fig. 15. Sequence analysis of four cutinases: *TfCut2*, LCC, *Tcur0390*, and *Tcur1278*
 A) Pairwise sequence identity matrix. B) Hierarchical clustering dendrogram. C) MSA.

Despite presented computational results showing a clear divalent metal binding site composed of D174, D204 and D253, it was reported, that no sign for a metal dependence was found for *TfCut2*, as shown on a comparative activity assay against *p*NPB with metal chelator EDTA or various metal ions [272]. In the 4CG1 X-ray structure of *TfCut2* [149], the divalent metal ion is also absent. The likely explanations for this observation is that the predicted metal-

binding site is an ancestral feature that has become non-essential due to evolutionary adaptations, allowing *TfCut2* to function independently of divalent metal ions. Another possibility includes that the assay substrate, *p*NPB, may not require the functionality associated with the metal-binding site, as its role could be substrate-specific.

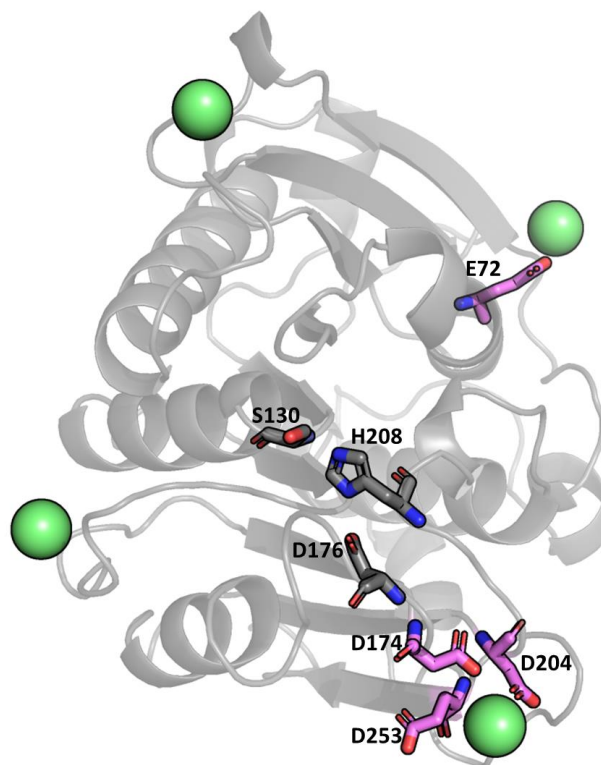


Fig. 16. Structure of *TfCut2* shown as a grey cartoon, with four Ca^{2+} ions. Negatively charged residues (glutamates and aspartates) within 5 Å of the ions are displayed as pink sticks, while the catalytic triad is shown as grey sticks.

4.3.3. Investigation of the binding mode of Impranil DLN to *TfCut2*

As shown on NMR analysis presented in Chapter 4.3.1 and also in a study by Fuentes-Jaime et al. [4] Impranil's structure is complex, with two types of bonds: urethane and ester, in different chemical environments. Therefore, in order to investigate the different possibilities of substrate to bind enzyme (or enzyme to substrate), it was necessary to build a series of 3D models representing each bond type within distinct chemical contexts. Given the various building blocks constituting the soft segment—neopentyl glycol, adipic acid, and 1,6-hexanediol—different configurations of a single repeating unit of Impranil DLN are possible.

To reduce the number of structures for modelling, Impranil DLN model structure was simplified to consist of hexamethylene diisocyanate (urethane moiety) and adipic acid (ester moiety), connected by either neopentyl glycol or 1,6-hexanediol (Fig. 17A). This approach lowered to some extent the complexity of the Impranil DLN structure while retaining both hydrolysable bonds—ester and urethane (Fig. 17A, C).

Previous research has demonstrated that *TfCut2* can degrade Impranil DLN by cleaving ester bonds, while urethane bonds remain resistant to enzymatic hydrolysis, as observed through FTIR spectroscopy [20]. However, *TfCut2* belongs to serine hydrolase family, a highly promiscuous class of enzymes [311]. As the example of cutinase *HiC*, which was reported to degrade mainly ester bonds in PUR, and urethane bonds with low activity, it was shown in another study on *HiC*, that even a single mutation near the active site could shift enzyme activity from esterolytic (C-O bond hydrolysis) to amidolytic (C-N bond hydrolysis)) [140]. This shift in activity is thought to result from the stabilisation of the leaving amine group in the tetrahedral intermediate formed during hydrolysis.

Given the potential to alter an enzyme's activity from esterase to amidase or urethanase, interactions with Impranil DLN were modelled with both ester and urethane bonds positioned in the active site, resulting in four potential binding modes (Fig. 17B). Consequently, four distinct models of the Impranil DLN moiety in complex with *TfCut2* were built: 'ester P1' and 'ester P2' for poses where the ester bond is situated in the active site, and 'urethane P1' and 'urethane P2' for poses where the urethane bond is located in the active site (Fig. 17B). With two models of the Impranil DLN repeating unit, a total of eight possible poses of Impranil DLN bound to *TfCut2* were modelled.

Due to the large number of rotatable bonds in the single repeating units of Impranil DLN, generating diverse and computationally manageable conformers for the docking procedure proved challenging. Therefore, it was decided to focus the docking studies on specific fragments of the Impranil DLN repeating units, specifically the ester and urethane moieties, corresponding to the building blocks adipic acid and hexamethylene diisocyanate, respectively. These fragments are common to both the hexanediol and neopentyl repeating units of Impranil DLN and contain the cleaved ester or urethane bond, which is crucial for accurate positioning during nucleophilic attack. To ensure stability and neutralise terminal charges, -CH₃ (methyl) groups were added as capping groups on these fragments (Fig. 17C).

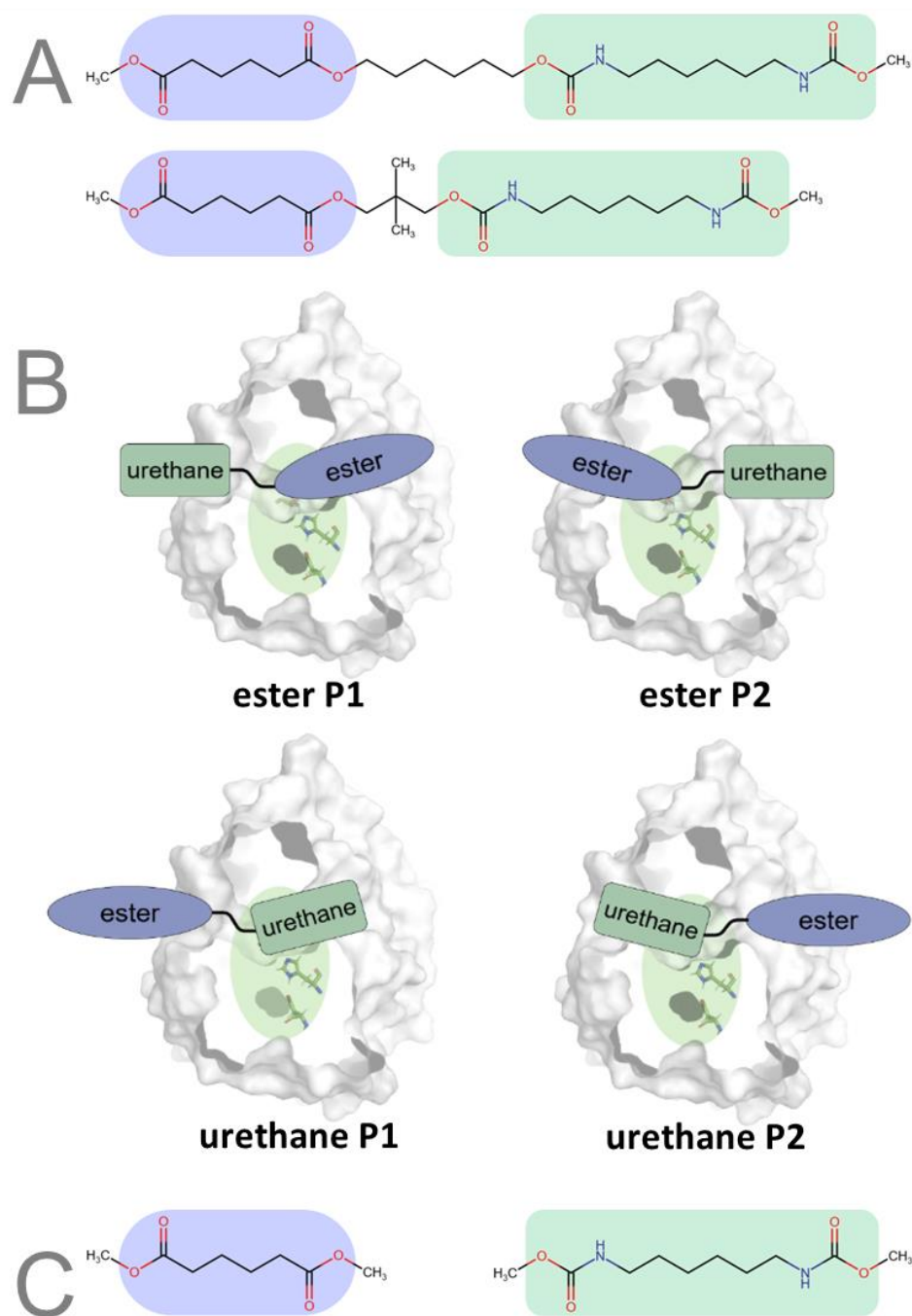


Fig. 17. Impranil DLN structures and poses for modelling studies. **A)** Structures of the Impranil DLN moiety used for modelling. **B)** Possible poses of Impranil DLN moiety bound to *TjCut2*. **C)** Ester (adipic acid) and urethane (hexamethylene diisocyanate) moieties used later for docking studies.

Starting from these four poses (ester P1, ester P2, urethane P2 and urethane P2), conformational sampling of impranil DLN bound to *TjCut2* was further investigated using the Rosetta software suite [266] with a flexible XML docking protocol [208,293]. The docking approach was adapted from a previously published study about molecular docking of PET dimers to binding site of the crystal structures of *TjCut2*, LCC, and *IsPETase* [287].

The approach enabled to explore optimal binding poses for the ester and urethane moieties of Impranil DLN within the flexible active site of *TfCut2*. For each ligand, ester and urethane moieties, and each orientation (P1 and P2), 10,000 docking complexes were generated, resulting in a total of 40,000 potential enzyme-ligand complexes. The docking results were analysed by plotting interface score against total score, and interface score against ligand RMS. The poses were evaluated using the *ref2015* all-atom energy scoring function [288] with scores expressed in Rosetta units (RU). For each ligand, one pose from a set of 10,000 complexes was selected for further analysis. Selected were the complexes with the lowest interface score among the complexes found within a ligand RMS cluster representing extended ligand poses. This way, the four complexes that were further selected (ester P1, ester P2, urethane P1, urethane P2) were characterised by low interface energies, and the ligands in these complexes adopted an extended conformation. Such extended conformation of a ligand facilitates the subsequent construction of the Impranil DLN repeating unit, ensuring proper positioning within the *TfCut2* active site. The details of the selection of the complexes for further studies, together with their characteristics are described below.

Plots of interface score vs. total score (Fig. 18) were used to identify poses with both low interface and total score, indicating stable and energetically favourable binding configurations. The selected complexes correspond to the lowest (Fig. 18B, “ester P1” and “urethane P2”) or near-lowest (Fig. 18B, “ester P2” and “urethane P1”) interface scores. Additionally, the generated docking complexes were distributed around the energy landscape of the initial *TfCut2*-ester/urethane moiety complexes used in the docking studies, as indicated by the central location of yellow dots in Figure 18A, which represent the initial complexes of *TfCut2* and ligands placed manually that were used for the docking studies.

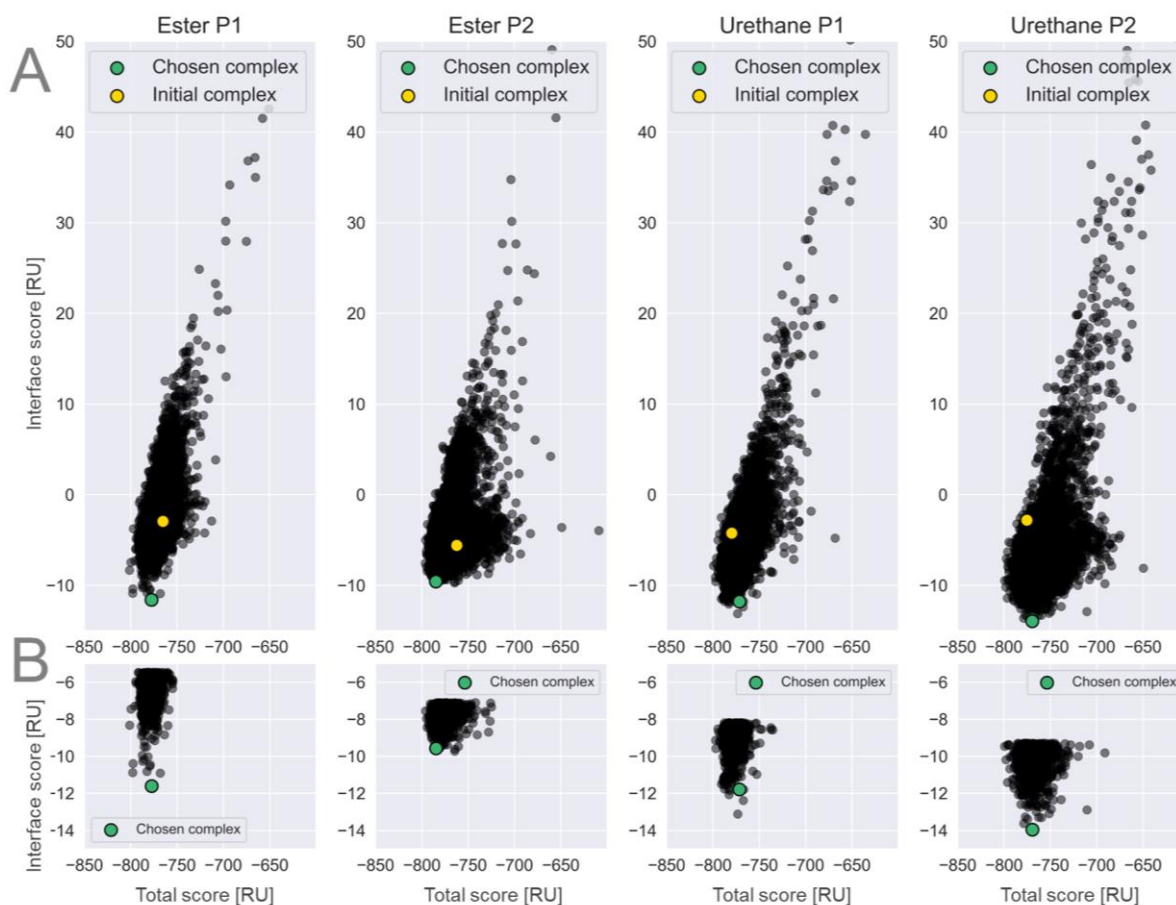


Fig. 18. Interface score vs. Total score for all complexes of ester and urethane moieties docked in *TfCut2*, in Rosetta units (RU). Selected complexes are marked with coloured green dots. The initial starting geometries are shown with yellow dots. **A)** All 10,000 docked complexes. **B)** 1,000 complexes with the lowest interface energies.

The interface score vs. ligand RMS plots (Fig. 19) were used to assess the conformational variability of the ligand in the binding site and to distinguish energetically favourable conformations. In this context, RMS refers to the root mean square of the deviation in ligand position within the binding site, without superimposing the structure (Fig. 19B). Unlike RMSD, which is typically used for measuring the deviation of superimposed structures (Fig. 19A), RMS here provides insight into how the ligand conformation varies in terms of position within the binding site.

The poses within the selected complexes had extended conformations, coinciding with the lowest interface energies (Fig. 19A, “ester P1” and “urethane P2”) or near-lowest (Fig. 19A, “ester P2” and “urethane P1”). Plots of ligand RMS without superimposition (Fig. 19B) confirmed that the chosen ligand pose within the *TfCut2* active site corresponds to low-energy configurations, especially for ester P1.

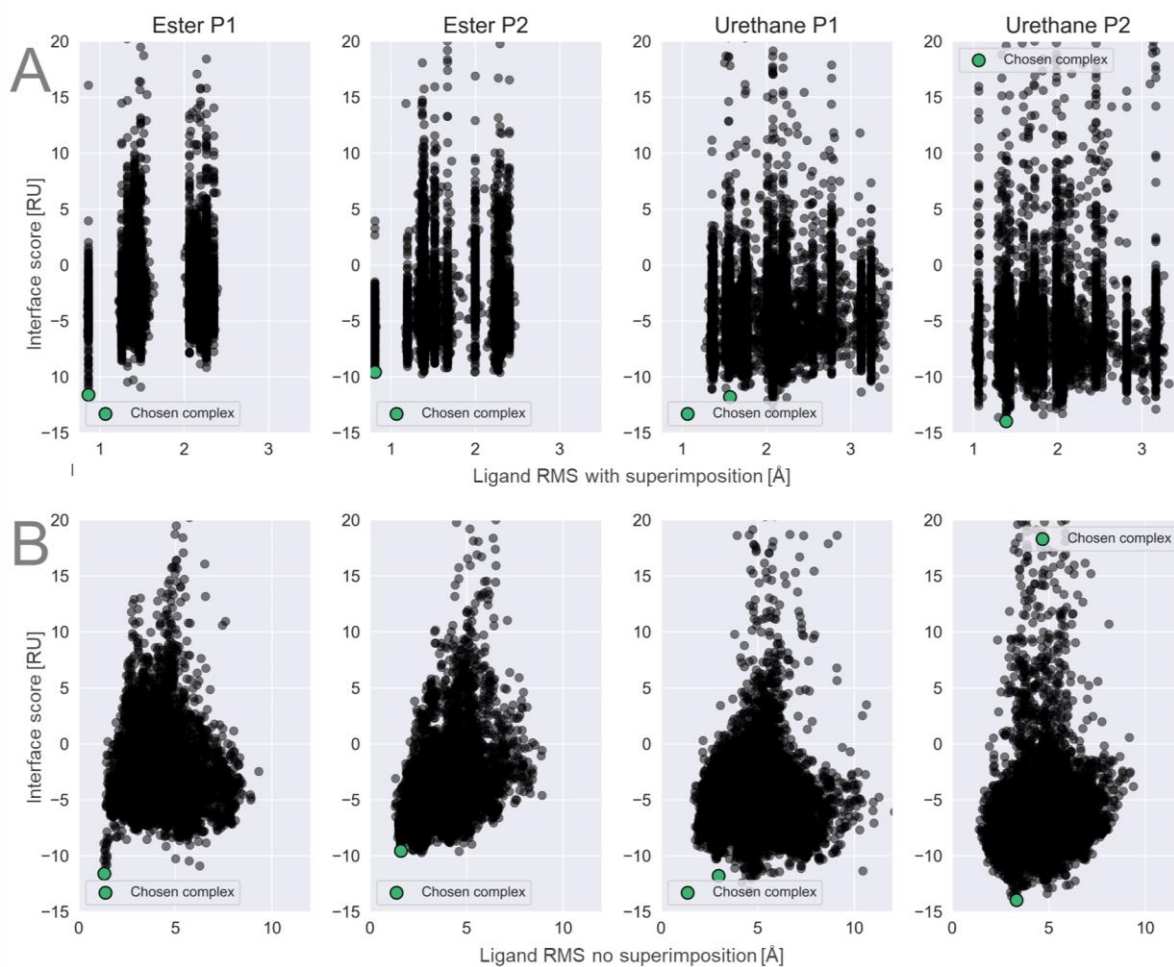


Fig. 19. Interface score vs. Ligand RMS for all docking poses. Selected complexes are highlighted as in Fig. 18. **A)** Superimposed ligand RMS. **B)** Ligand RMS without superimposition.

The selected complexes display favourable catalytic distances (Fig. 20, Table 4). However, the distances required for nucleophilic attack were initially quite large in some complexes (Table 4) but decreased during MD simulations, as discussed in later sections.

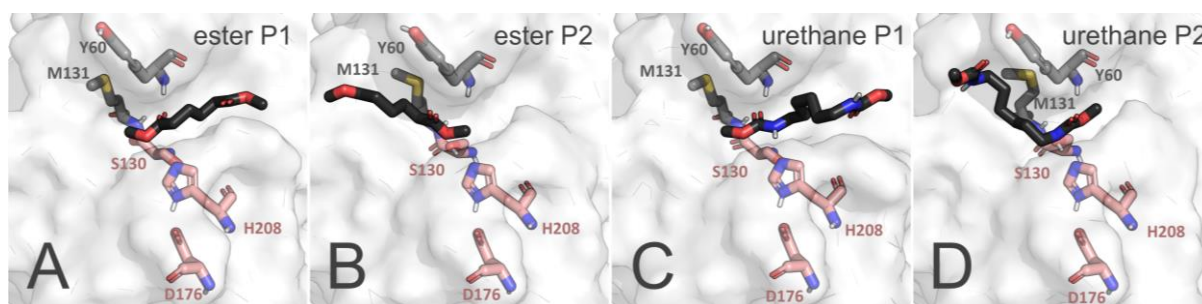


Fig. 20. Snapshots of the selected docking poses for each ligand type: **A)** ester P1, **B)** ester P2, **C)** urethane P1, **D)** urethane P2, bound to *TfCut2*. Ligand shown as black sticks, catalytic triad as salmon sticks, and oxyanion hole residues as grey sticks, *TfCut2* shown as white surface.

Among the complexes, *TfCut2* with urethane P2 displayed the lowest interface score, while the complex with ester P2 showed the lowest total score (Table 4). Despite these findings, identifying a clearly preferred pose solely based on these docking studies remains challenging, as the ligand sizes differ between ester and urethane moieties, and the initial complex energies vary (Table 4).

The distance flat harmonic potential constraints applied between the γ -oxygen of S130 and the carbonyl carbon of the cleaved bond, set to 1.5–3.5 Å, were met only in the urethane P2 pose. The constraints between the γ -hydrogen of S130 and the ϵ -nitrogen of H208, set to 1.5–2.5 Å for proton transfer, were fulfilled in all selected poses except ester P1. However, the nucleophilic attack angle constraint between S130 O γ , the carbonyl carbon, and the carbonyl oxygen, set to 100–110°, was unmet in any of the selected poses (Table 4). These results suggest that despite employing a flexible docking protocol in Rosetta and working with relatively small ligands, the sidechains and backbone of *TfCut2* may not have adjusted sufficiently to position the ligand within the optimal range for nucleophilic attack (≤ 3.5 Å).

Table 4. Calculated interface and total energies of selected poses for further studies.

Pose	Interface score [RU]	Total score [RU]	Distance for nucleophilic attack (Å)	Distance for S130-H208 proton transfer (Å)	Angle for nucleophilic attack (°)
Ester P1	-11.6	-777.4	4.4	2.9	77.9
Ester P2	-9.6	-784.7	4.6	1.9	163.4
Urethane P1	-11.8	-771.3	4.5	1.7	86.7
Urethane P2	-14.0	-769.432	3.3	2.0	171.8

MD simulation of TfCut2 and Impranil DLN complexes

In the next step, for each of the four enzyme-ligand complexes, the full Impranil DLN repeating unit was constructed based on the ester or urethane moiety bound in the P1/P2 pose. Two types of Impranil DLN units were created to account for variability in building blocks, as shown previously in Figure 17:

1. adipic acid (ester moiety), 1,6-hexanediol (chain extender), and hexamethylene diisocyanate (urethane moiety),
2. adipic acid (ester moiety), neopentyl glycol (chain extender), and hexamethylene diisocyanate (urethane moiety).

These units are designated as “hexamethylene” and “neopentyl,” respectively, based on the chain extender used. Each constructed Impranil DLN unit includes two ester bonds, two urethane bonds, and terminal methyl groups.

Before initiating MD simulations, proper solvation of the well-protonated system is a critical step. For the present study, crystallographic water molecules present in the 4CG1 structure were kept. Additionally, two Ca^{2+} ions were added to each divalent-metal binding site within the structure. To prepare the system for simulation, necessary counterions to neutralise were added and the system was immersed in a 20 Å octahedral box of TIP3P water molecules. This solvation approach ensures that the system is fully solvated and capable of maintaining its structural integrity during subsequent MD simulations. The relatively large size of the water box was chosen to ensure proper periodic box conditions for the large ligand, such as Impranil DLN single repeating unit.

MD simulations were performed using the AMBER 18 software package for the system, using the *ff14SB* protein force field [216]. AMBER 18 was selected due to its robustness and reliability in biomolecular simulations, providing accurate and reproducible results. The *ff14SB* force field was chosen for its validated parameters that are well-suited for proteins and peptides. For each simulated system, ten repetitions of 50 ns were performed, totalling 500 ns of MD simulations.

RMSD and RMSF analysis

RMSD measures the average deviation of the atomic positions in the simulated structure from a reference structure, typically the initial crystal structure. By tracking RMSD over the course of the simulation, the stability of the system can be assessed. A stable RMSD plot indicates that the system has equilibrated and remained structurally consistent throughout the simulation. In addition to RMSD, Root-Mean-Square Fluctuation (RMSF) enables analysis of the flexibility of individual residues within the protein. RMSF measures the average deviation of each residue's position from its average position over time. High RMSF values indicate regions of the protein that are more flexible, while low RMSF values suggest more rigid, stable regions. This analysis is particularly useful for identifying flexible loops, binding sites, or regions involved in significant conformational changes during the simulation.

RMSD and RMSF of the *TfCut2* throughout the MD simulations of the protein-ligand complexes were calculated using *Cpptraj*, to analyse respectively the average deviations and the flexibility of individual residues within the protein. The RMSD analysis of the MD simulations indicated that the *TfCut2* protein in complex with Impranil DLN repeating units remains stable across most simulations, with deviations consistently below 2 Å (Fig. 21). Of note, only the 9th replica of the MD simulation involving Neopentyl Impranil DLN

in the urethane P1 pose, showed a notable instability during the second half of the simulation (last 25 ns). This instability was further monitored using an RMSF (Root Mean Square Fluctuation) plot, which revealed that the elevated RMSD values were mainly due to significant fluctuations in the N-terminal region (residues 1-10) (Fig. 22B).

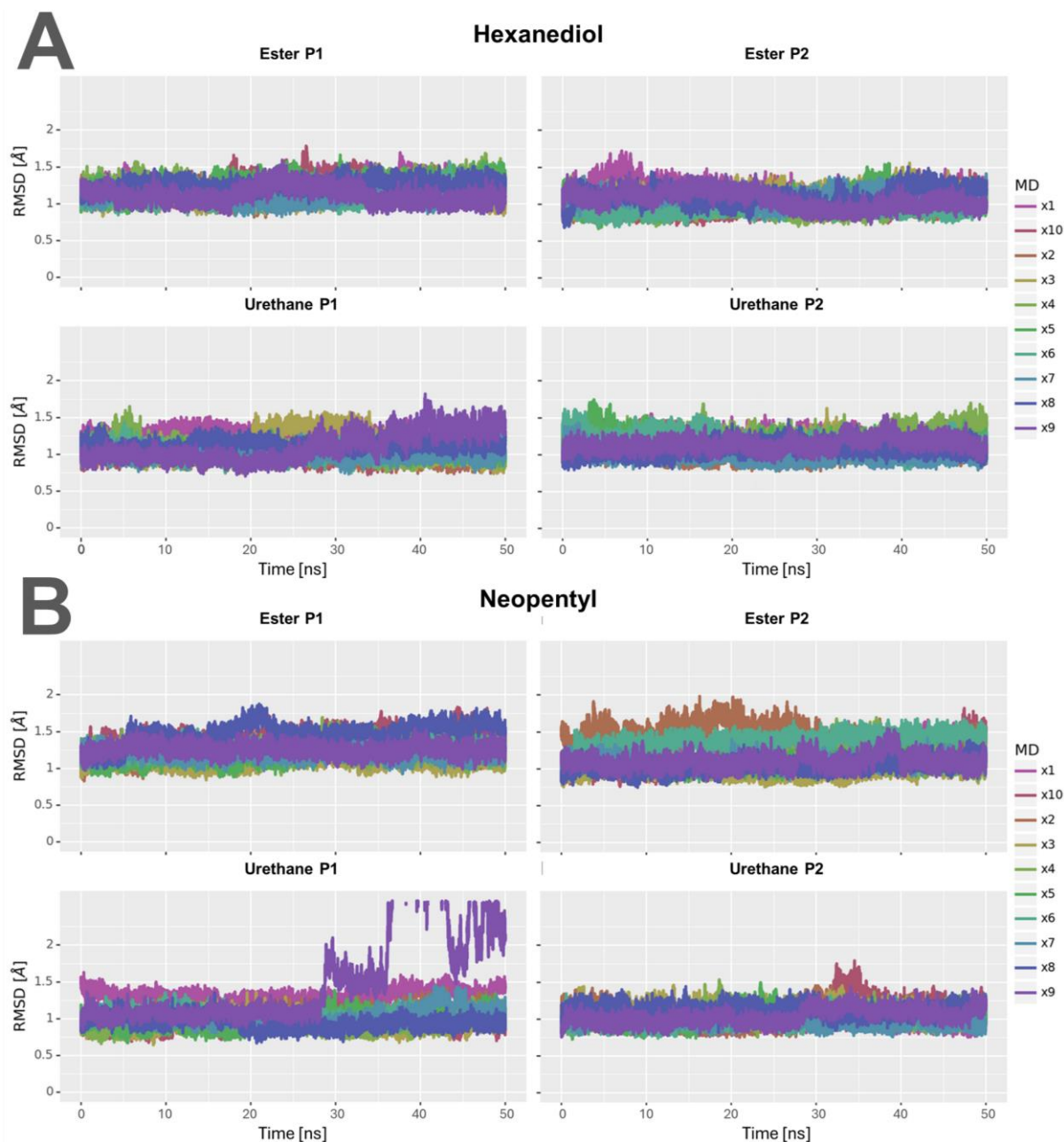


Fig. 21. RMSD calculated for the C-alpha, C, and N atoms of *Tj*Cut2 during MD simulations of *Tj*Cut2 in complex with Impranil DLN repeating units. Different colors represent datasets from various MD simulation replicas 1-10. **A)** Hexanediol Impranil DLN; **B)** Neopentyl Impranil DLN.

In addition to the N-terminal region, the RMSF analysis enabled to identify another highly fluctuating region, specifically the loop encompassing residues 241-251. This loop contains D246, a residue that was not resolved in the original crystal structure of *Tj*Cut2

(PDB ID: 4CG1) and its high flexibility was already reported before [149]. The flexibility of this loop may suggest a structural adaptability in this region that could be functionally relevant.

Furthermore, the RMSF plots indicated that the binding region, highlighted in blue in Fig. 22, exhibits higher RMSF values, suggesting a degree of flexibility. This flexibility likely facilitates the enzyme's ability to accommodate large ligands, such as synthetic polymer chains, within its active site.

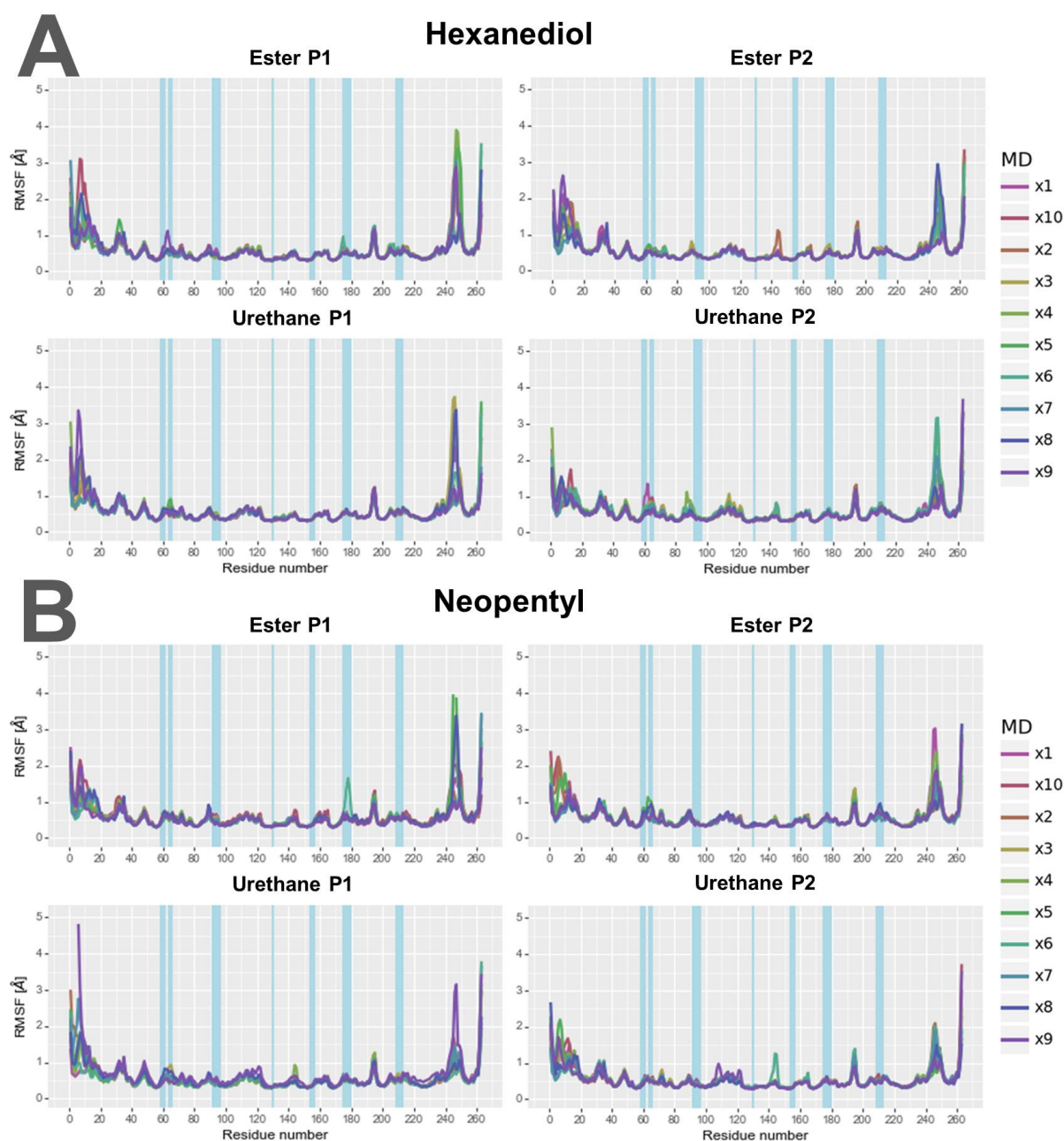


Fig. 22. RMSF calculated for the C-alpha, C, and N atoms of *TjCut2* during MD simulations of *TjCut2* in complex with Impranil DLN repeating units. Different colors represent datasets from various MD simulation replicas 1-10. Blue regions indicate the binding site of the enzyme. The RMSF plots suggest that the binding region is flexible, which likely allows

the enzyme to incorporate large ligands such as synthetic polymer chains. **A)** Hexanediol Impranil DLN; **B)** Neopentyl Impranil DLN.

Catalytic distances

In the classical Ser-His-Asp catalytic triad of *Tf*Cut2, the catalytic serine (S130) is activated by proton transfer of its γ -hydrogen to the catalytic histidine's (H208) ϵ -nitrogen, which acts as a general base. This activation allows the serine to perform a nucleophilic attack on the carbonyl carbon of the substrate's cleaved bond, representing the first step of the catalytic mechanism. The role of the catalytic aspartic acid (D176) is crucial in this process. Aspartic acid stabilises the protonated form of histidine by forming a hydrogen bond with it, between δ -nitrogen of histidine and carboxylate oxygen of aspartic acid, ensuring that histidine can effectively act as a proton acceptor (Fig. 23).

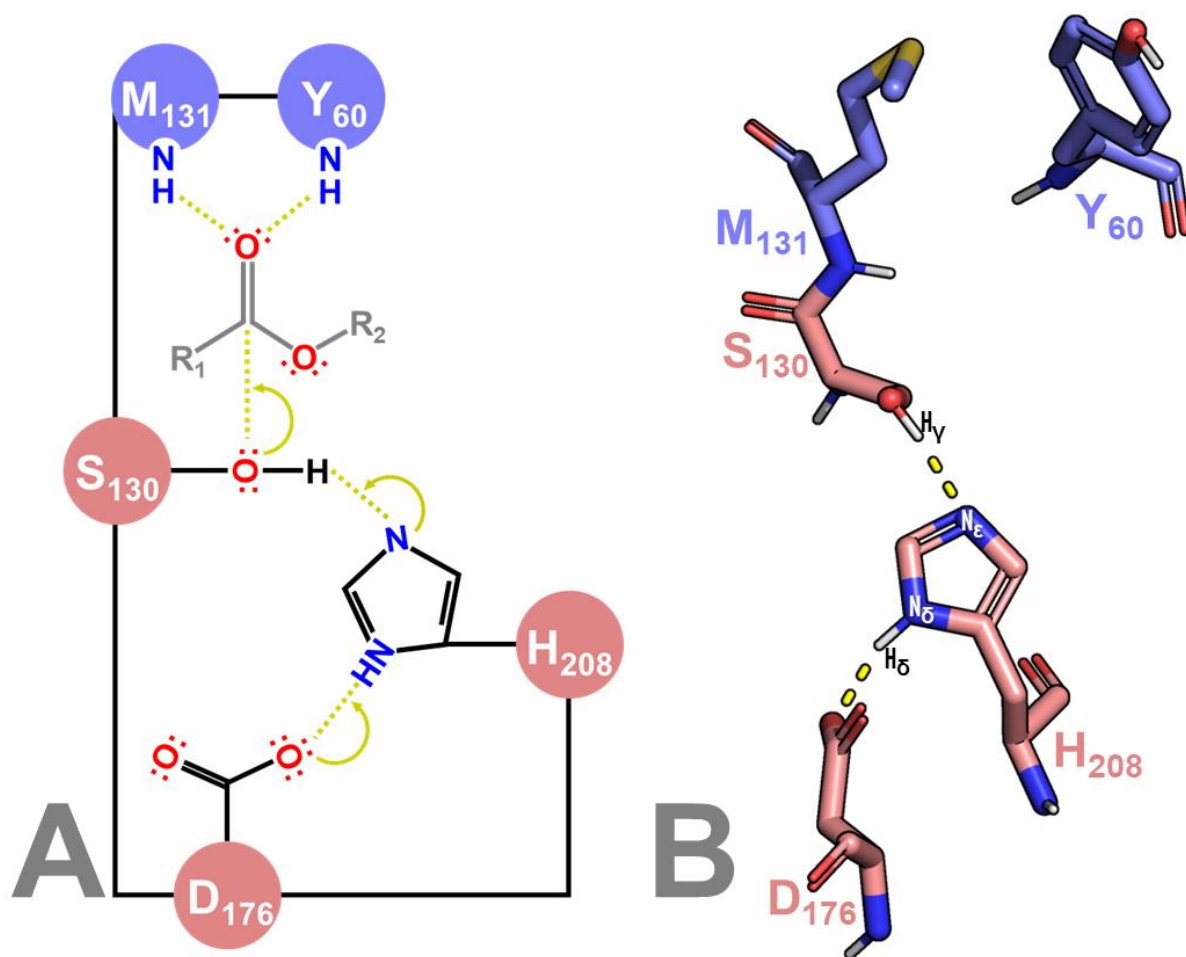


Fig. 23. Figure adapted from Raczyńska et al. [13] **A)** Schematic of first step of catalytic mechanism of ester bond hydrolysis by *Tf*Cut2: active site residues: S130-H208-D176 catalytic triad (salmon) with the oxyanion hole comprised of Y60 and M131 (purple). H208 acts as a general base, activating the S130's hydroxyl group for nucleophilic attack on the carbonyl carbon of the ligand. D176 enhances the basicity of the H208. The oxyanion intermediate formed is stabilised by the backbone amide groups of the two oxyanion hole residues Y60

and M131. **B)** Active site of *TfCut2* cutinase (productive frame exported from MD simulations). The catalytic triad residues S130-H208-D176 are shown as salmon sticks. The oxyanion hole forming residues Y60 and M131 shown as purple sticks.

In this study, key distances that are critical for catalysis of Impranil DLN by *TfCut2* were measured. Specifically, two distances were monitored:

1. The distance between the γ -oxygen of the catalytic serine (S130) and the carbonyl carbon of the cleaved group of the Impranil DLN repeating unit, which is crucial for nucleophilic attack.
2. The distance between the γ -hydrogen of S130 and the ϵ -nitrogen of the catalytic histidine (H208), which is essential for proton transfer and activation of the serine.

The *Cpptraj* tool from AMBER 18 [286] as used to measure these distances, enabling insights into dynamic interactions between *TfCut2* and Impranil DLN. Additionally, *Cpptraj* calculated contact numbers, which reflect the extent of specific interactions, such as hydrogen bonding and van der Waals contacts, providing a clearer picture of ligand stability and the enzyme's conformational behavior.

These distance measurements allowed to determine whether the ligand was bound in a productive pose conducive to catalysis. The following results were obtained from multiple MD simulation replicas, indicating how many times the Impranil DLN repeating unit remained bound in a productive pose (Fig. 24):

- Hexanediol Impranil DLN Single Repeating Unit:
 - **Ester P1:** 7/10 replicas
 - **Ester P2:** 1/10 replicas
 - **Urethane P1:** 2/10 replicas
 - **Urethane P2:** 4/10 replicas
- Neopentyl Impranil DLN Single Repeating Unit:
 - **Ester P1:** 1/10 replicas
 - **Ester P2:** 1/10 replicas
 - **Urethane P1:** 6/10 replicas
 - **Urethane P2:** 8/10 replicas

In several cases, the ligand remained bound to *TfCut2* in a productive pose throughout the simulation, with the cleaved bond maintained within catalytic distance of the serine. In other cases, the ligand fluctuated, and the cleaved bond drifted away from the catalytic serine, although the ligand did not completely exit the active site and remained bound. When

the ligand did not remain bound in the simulations, it either dissociated early, potentially reflecting inherent instability in the initial binding pose, or it gradually left the binding site of *Tf*Cut2 during the MD simulation. In some cases, the ligand could be seen to bind again in the productive pose (Fig. 24).

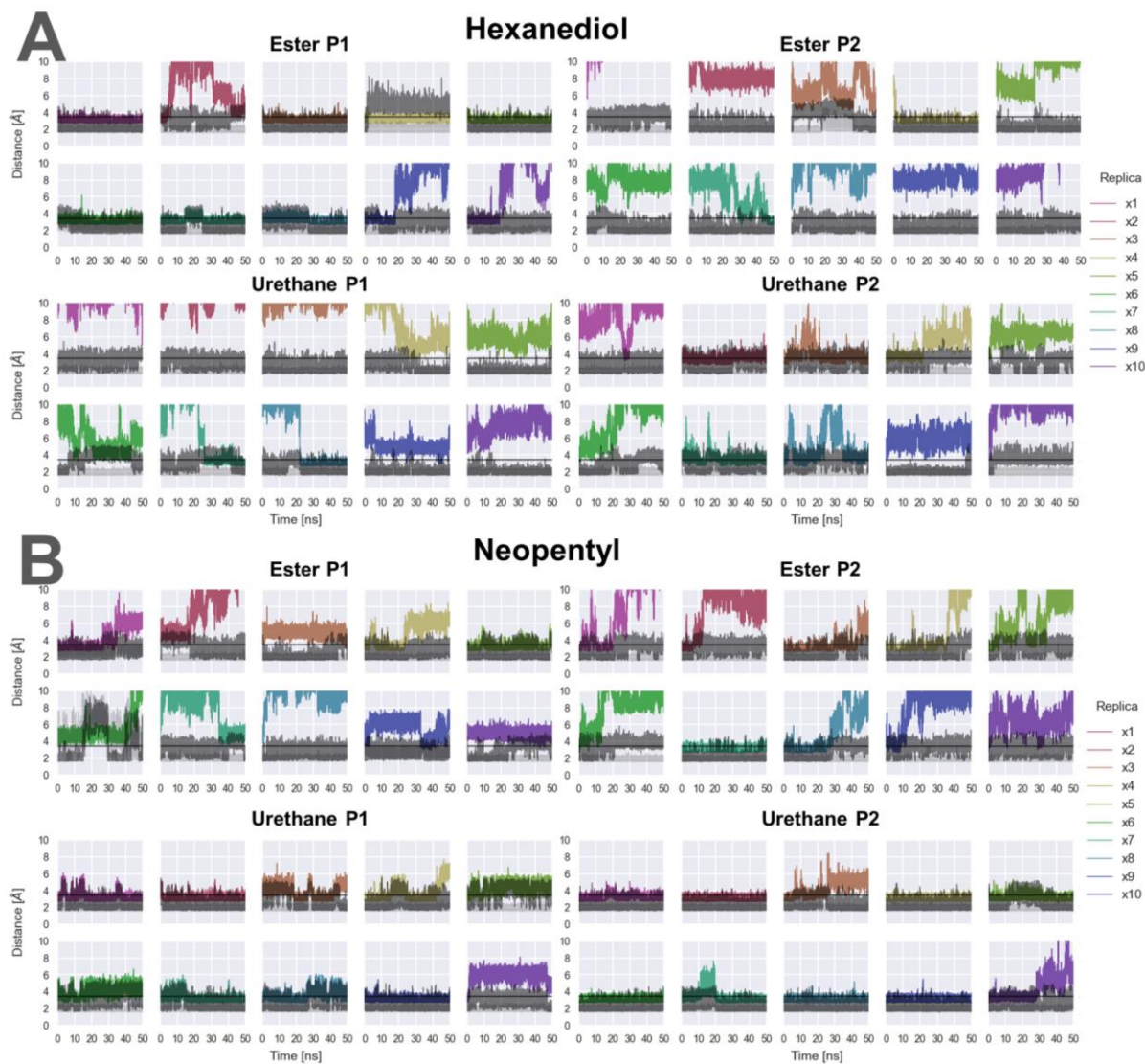


Fig 24. Measured distances throughout the MD simulations of *Tf*Cut2 in complex with Impranil DLN repeating units. The colored datasets indicate the distance for nucleophilic attack between the γ -oxygen of catalytic S130 and the carbonyl carbon of the cleaved group in the ligand, while the grey datasets represent the distance between the γ -hydrogen of catalytic S130 and the ϵ -nitrogen of H208; and the lightgrey the distance between the δ -nitrogen of H208 and catalytic D176. The black horizontal line at $y=3.5$ Å indicates the cutoff for the nucleophilic attack distance to be considered "productive". Different colors correspond to various MD simulation replicas (1-10). **A)** Hexanediol Impranil DLN; **B)** Neopentyl Impranil DLN.

If the distances are too large for proton transfer via S130-H208-D176, such a situation might restrict its catalytic efficiency. It was observed that during the MD simulations,

the catalytic triad residues do not always maintain these hydrogen bond distances, and there are, in fact, four configurations by which their contacts can be described (Fig. 25):

- **S-H-D:** All three residues are in hydrogen bond contact (Fig. 25A).
- **S-H:** Only catalytic serine and histidine are interacting via hydrogen bonds (Fig. 25B).
- **H-D:** Only catalytic histidine and aspartic acid are interacting via hydrogen bonds (Fig. 25C).
- **None:** None of the catalytic residues are interacting, and H208 is "flipped" (Fig. 25D).

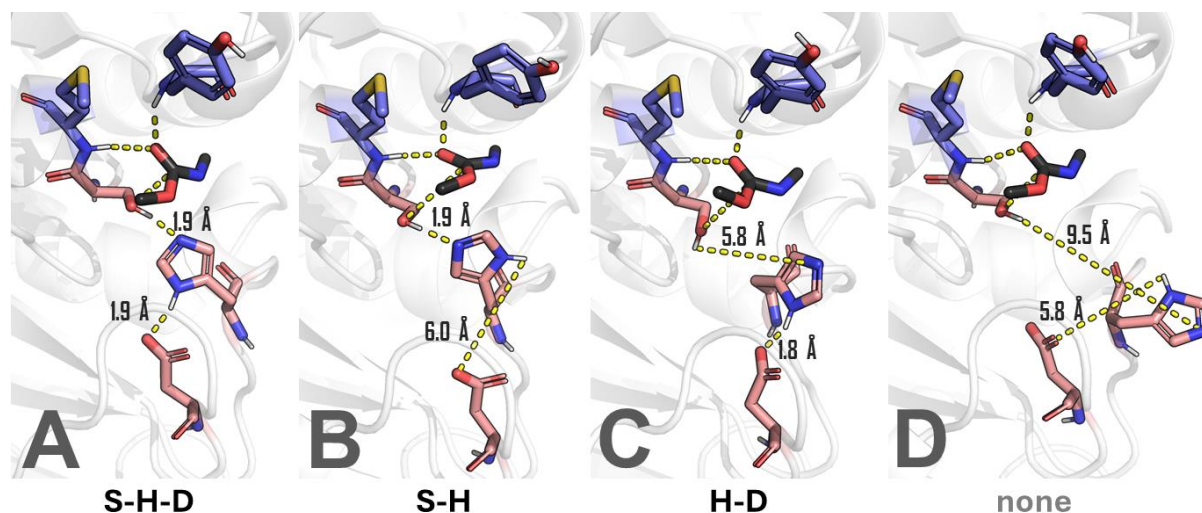


Fig. 25. The possible configurations of catalytic triad residues with a fragment of Impranil DLN urethane bond (shown as black sticks) in distance for the nucleophilic attack by S130 (≤ 4.0 Å). The figures were prepared by visualising selected frames of MD simulations of *TjCut2* with hexanediol Impranil DLN repeating unit in pose urethane P1. The catalytic triad residues (S130, D176, H208) are shown as salmon sticks, and the oxyanion hole residues (Y60, M131) are shown as purple sticks. The measured distances between the catalytic triad residues are shown as yellow dashed lines with values (in Å) printed in black. **A)** "S-H-D" – all three residues are involved in hydrogen bond contacts; **B)** S-H – only catalytic serine and histidine are interacting via hydrogen bonds; **C)** H-D – only catalytic histidine and aspartic acid are interacting via hydrogen bonds; **D)** None of the catalytic residues are interacting, and H208 is "flipped."

The occurrences of these poses were investigated and compared to the occurrences in the MD simulations of the free enzyme as well (Fig. 26). In frames where the ligand was in a productive pose, with a distance for the nucleophilic attack ≤ 3.5 Å, most frames adopted the S-H-D configuration (Fig. 26A). A smaller proportion of frames represented the H-D configuration, and very few represented S-H and "None" (Fig. 26A).

It appears that when the ligand was not in a productive pose, a greater proportion of frames represented the "H-D" configuration rather than "S-H-D," both in the case of unbound *TjCut2* and *TjCut2* in complex with the Impranil DLN repeating unit in any

of the poses (Fig. 26B). These findings suggest that either the bound ligand helps maintain the configuration of catalytic triad residues for effective proton transfer between all three catalytic triad residues, or fluctuations of H208 and its shift toward D176 may cause the ligand to destabilise and dissociate. In Figure 24, it is also visible how if ligand dissociates, the S-H distance (shown in grey) fluctuates strongly, indicating lack of stabilised interactions between S130 and H208.

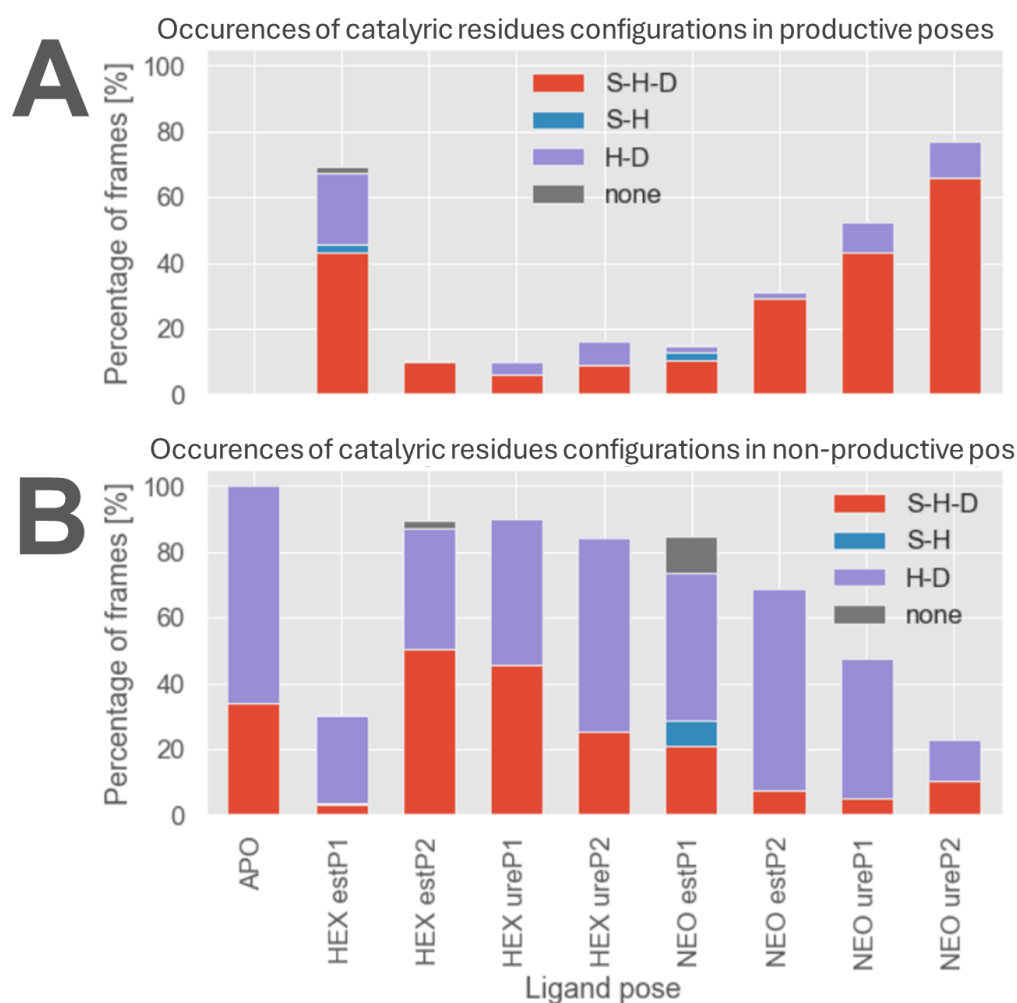


Fig. 26. Percentage of frames in which a given catalytic triad configuration is observed. The interaction between two catalytic triad residues is confirmed when the distance between the specific atoms for proton transfer is ≤ 2.5 Å. **A)** Frames in productive form, indicated by a distance for nucleophilic attack ≤ 3.5 Å. **B)** Frames in non-productive form, indicated by a distance for nucleophilic attack > 3.5 Å.

Selection of MD simulation frames

A previous study has shown that the active site residues exhibit greater deal of mobility when the hydrogen bonds connecting them in the starting conformation of MD simulations are broken [312]. In the presented case, when all the hydrogen bonds are disrupted, the catalytic

residues fluctuate to form hydrogen bonding interactions with other neighbouring atoms. Especially H208, which is a long amino acid side chain, can flip and adopt an altered conformation [313], and distance itself from S130 and D176, which could potentially inhibit catalysis (Fig. 25D).

Interestingly, 'S-H' configuration in productive poses of Impranil DLN can be observed only for the ester P1, both hexanediol and neopentyl (Fig. 26A). The fact that in unproductive poses (Fig. 26B), the ratio of 'H-D' and 'none' occurrences is much higher, may suggest that a bound ligand stabilises hydrogen bond between S130 and H208, probably by stabilising S130 via interactions of its O_{γ} with ligands carbonyl carbon.

In the analysis of interactions between *TfCut2* and a single Impranil DLN repeating unit, the focus was placed on identifying configurations where the ligand was bound in a productive conformation—corresponding to the first step of *TfCut2*'s catalytic mechanism—and tightly associated along the binding groove of *TfCut2*. A workflow consisting of three steps was developed (Fig. 27) to extract frames from the MD simulations where the ligand exhibited such productive conformation.

Firstly, only frames where the ligand was productively bound within the *TfCut2* hydrophobic groove were selected, based on specific distance and angle criteria in accordance with the catalytic mechanism. Secondly, additional filtering was applied to ensure that the Impranil DLN ligand was in an extended pose along the binding groove by maximising distances and angles between the carbonyl carbons on either side of the repeating unit and maximising residue contacts. Finally, k-means clustering (n=10) in AMBER 18 [286] was applied to produce a trajectory of ten frames per binding pose, each reflecting the ligand bound in a catalytically productive position (Fig. 27).

In the first step of the selection, a "productive" pose was defined based on specific geometric criteria:

1. The distance between the γ -oxygen of S130 and the carbonyl carbon of the cleaved bond (either ester or urethane) should be ≤ 3.5 Å to allow for nucleophilic attack.
2. The distance between the γ -hydrogen of S130 and the ϵ -nitrogen of H208 should be ≤ 2.5 Å to facilitate proton transfer for catalytic serine activation.
3. The angle between S130 O_{γ} , the carbonyl carbon, and the carbonyl oxygen should range between 60° and 120° , ensuring proper alignment for stabilisation by the oxyanion hole.

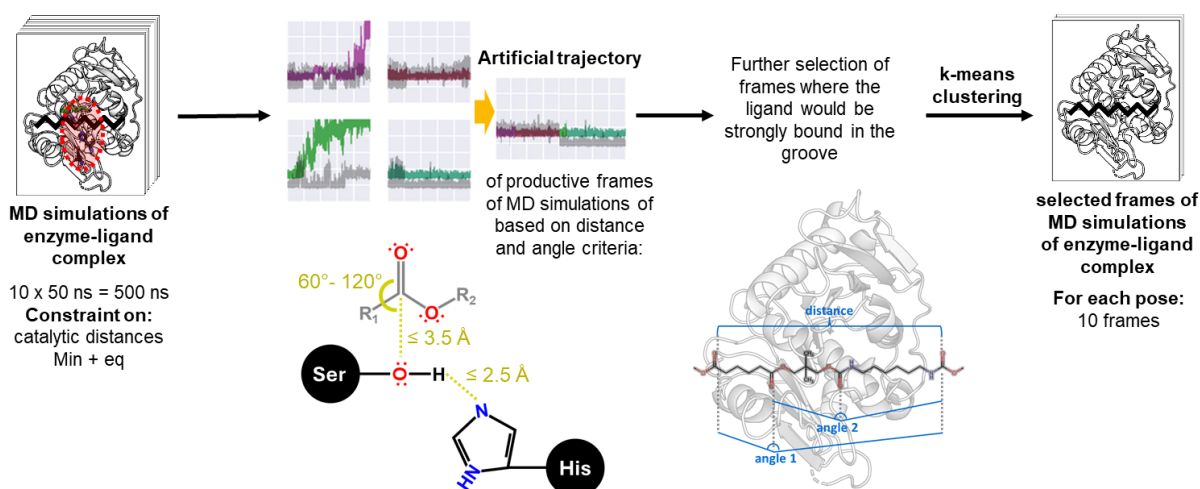


Fig. 27. Overview of the workflow for selecting productive frames from MD simulations of *Tj*Cut2 in complex with an Impranil DLN repeating unit. From MD simulations, “productive” frames are selected based on the distances and angle constraints for the nucleophilic attack. Then, MD frames are further filtered out for extended poses of Impranil DLN based on maximising internal distance and angles measurements of the ligand structure. In the end, k-means frames clustering is performed to obtain trajectory of ten representative frames of *Tj*Cut-Impranil DLN complexes.

Applying these criteria, productive frames were filtered from the MD simulations for each system, resulting in a discrete set of productive poses. The number of frames that met these criteria for each system is shown in Table 5.

Table 5. Number of frames selected from MD simulations of *Tj*Cut2 in complex with Impranil DLN repeating units based on productive pose criteria.

	ester P1	ester P2	urethane P1	urethane P2
Hexanediol	220 306	48 835	30 501	40 694
Neopentyl	62 462	142 879	210 312	316 544

Systems with the highest number of productive frames include: hexanediol ester P1 and neopentyl ester P2, urethane P1, and urethane P2, with 220k, 143k, 210k, and 317k frames, respectively. These selected frames, based on distance and angle criteria, were generally distributed evenly throughout the MD simulations (Fig. 28). However, in certain cases, productive frames primarily appeared at the beginning of a given replica, followed by system destabilisation. The discrepancies between the number of productive frames extracted from these MD simulations with Impranil DLN in different poses, may suggest which pose allows for better binding to *Tj*Cut2. For the complexes with low number of frames, it can also indicate a not tightly bound Impranil DLN in the initial complex for MD simulations. For example, for hexanediol ester P2, on the distance plots in Figure 24, it is visible that Impranil DLN disassociates at the beginning each simulation replica.

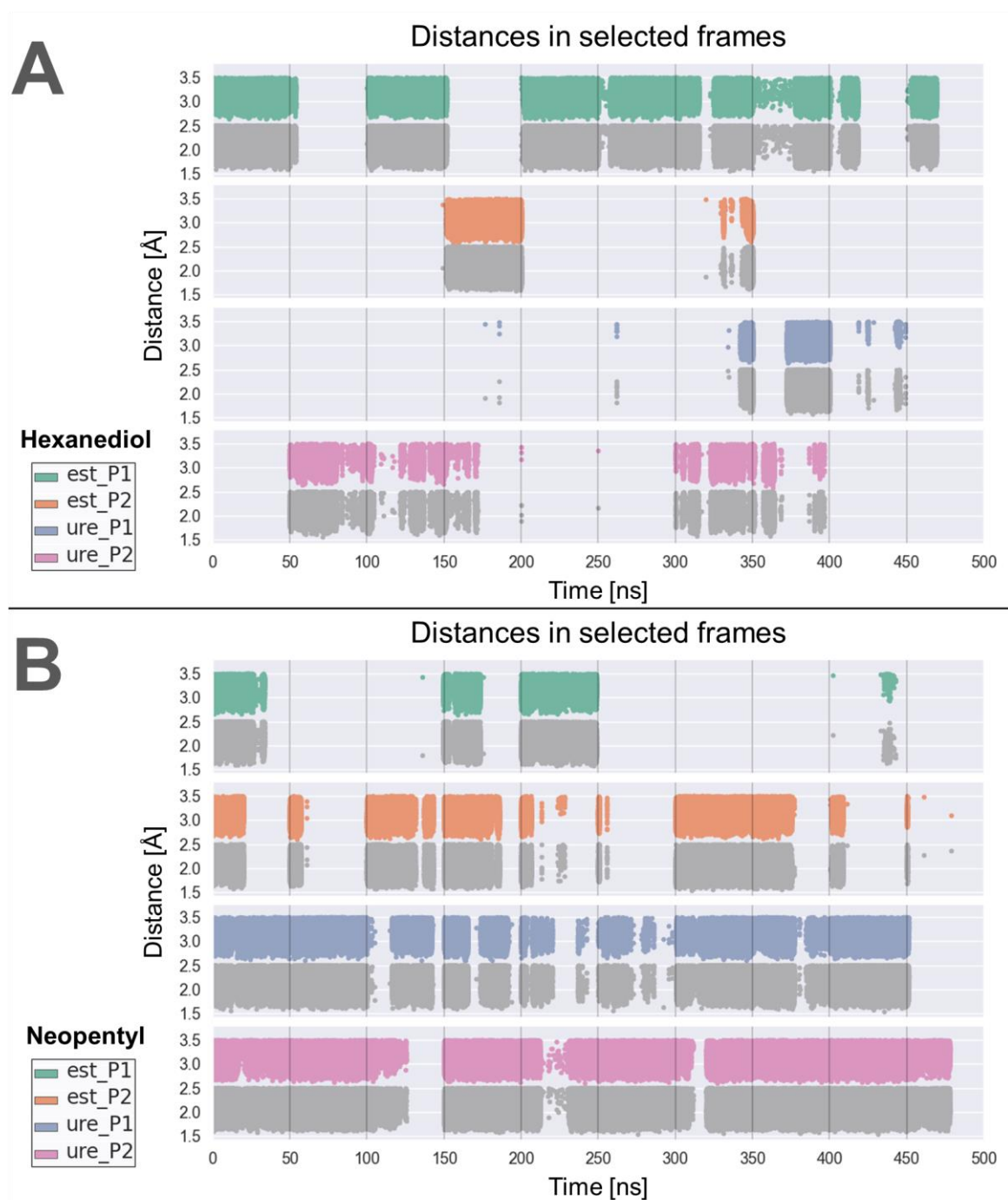


Fig. 28. Measured distances between the γ -oxygen of S130 and the carbonyl carbon of the cleaved group (coloured points), and the distance between the γ -hydrogen of S130 and the ϵ -nitrogen of H208 (grey points) in selected frames from MD simulations. Vertical lines separate ten replicas of MD simulations. **A)** Hexanediol Impranil DLN; **B)** Neopentyl Impranil DLN.

In the docking studies, the angle between S130 O_γ , the carbonyl carbon, and the carbonyl oxygen was constrained to approximately 107° , based on the Bürgi–Dunitz angle for nucleophilic attack [314]. However, none of the docked poses met this angle

requirement. Subsequent productive frames in MD simulations suggested that the angle could be achieved within the range of approximately 70°–90°, as shown in Figure 29.

Interestingly, for the P2 ester involving both hexanediol and neopentyl glycol, the median distance for nucleophilic attack and the S130-H208 proton transfer distance in the productive frames are the shortest among all positions examined (Fig. 29). Additionally, the median angles associated with these interactions are the largest. These observations suggest that the ligand in the P2 ester position may bind more tightly, facilitating closer interaction with the catalytic residues. Such reduced distances and optimised angles could enhance the efficiency of the catalytic process by promoting a more favourable geometry for the reaction.

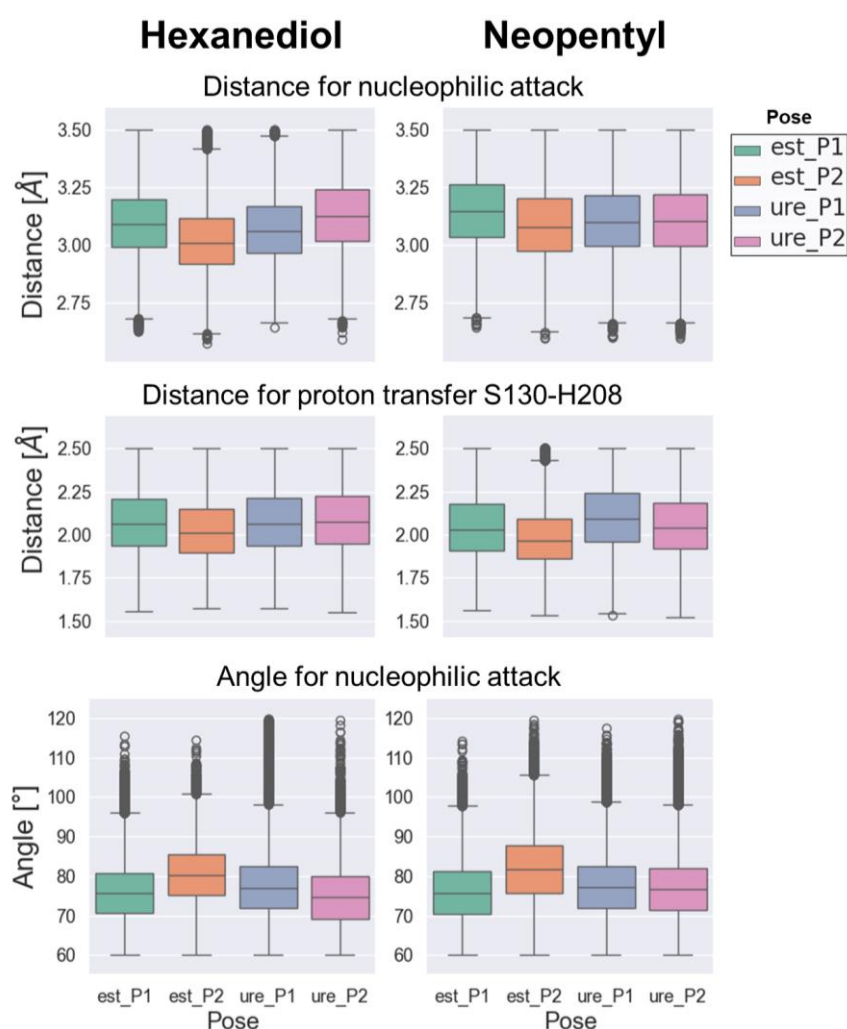


Fig. 29. Boxplots of catalytic distances and angles in the productive frames of MD simulations of *TfCut2* in complex with Impranil DLN (first column: hexanediol, second column: neopentyl). In the first row, boxplots represent the distance between the γ -oxygen of S130 and the carbonyl carbon of the cleaved bond (either ester or urethane); the second row shows the distance between the γ -hydrogen of S130 and the ϵ -nitrogen of H208; and the third row displays the nucleophilic attack angle of S130 toward the cleaved bond in Impranil DLN

(measured as the angle between S130 O γ , the carbonyl carbon, and the carbonyl oxygen) across all poses of Impranil DLN.

Upon further inspection, certain productive poses exhibited tangled Impranil DLN chains, which were not well associated with the surface of *TfCut2*. The modelled ligand is flexible and tends to fold back on itself. To refine the selection, additional criteria were introduced to identify "extended" poses, where the ligand was properly aligned along the enzyme's long and flexible binding groove. Maximising specific distances and angles between the ligand's atoms (detailed in the Methods section) enabled this refined selection. The number of well-bound productive poses for each system is summarised in Table 6.

Table 6. Number of frames selected based on maximising distances and angles to identify extended poses.

	ester P1	ester P2	urethane P1	urethane P2
Hexanediol	3 099	18	615	559
Neopentyl	569	83	1 179	4 041

After this step of filtering frames with Impranil DLN in an extended pose, highly uneven trajectory lengths across different systems were obtained (Table 6). In this step, again, systems with the highest number of productive frames include: hexanediol ester P1 urethane P1, and urethane P2, except for neopentyl ester P2 which has low number of filtered frames (83). In this particular Impranil DLN pose, the ligand structure might have been folding on itself, not giving off many frames in which it would be in an extended pose.

To address the issue of uneven number of frames of the poses and generate evenly representative trajectories, k-means clustering was applied to reduce the data to 10 clusters (i.e., 10 frames) per system. This ensured a more balanced and representative set of frames for further analysis.

As a result of this frame-selection workflow, 10 frames of *TfCut2* and Impranil DLN complexes were obtained for each of the eight systems. Each frame featured Impranil DLN well-bound within *TfCut2*'s binding groove and in a productive pose consistent with the first step of *TfCut2*'s catalytic hydrolysis mechanism (Fig. 30).

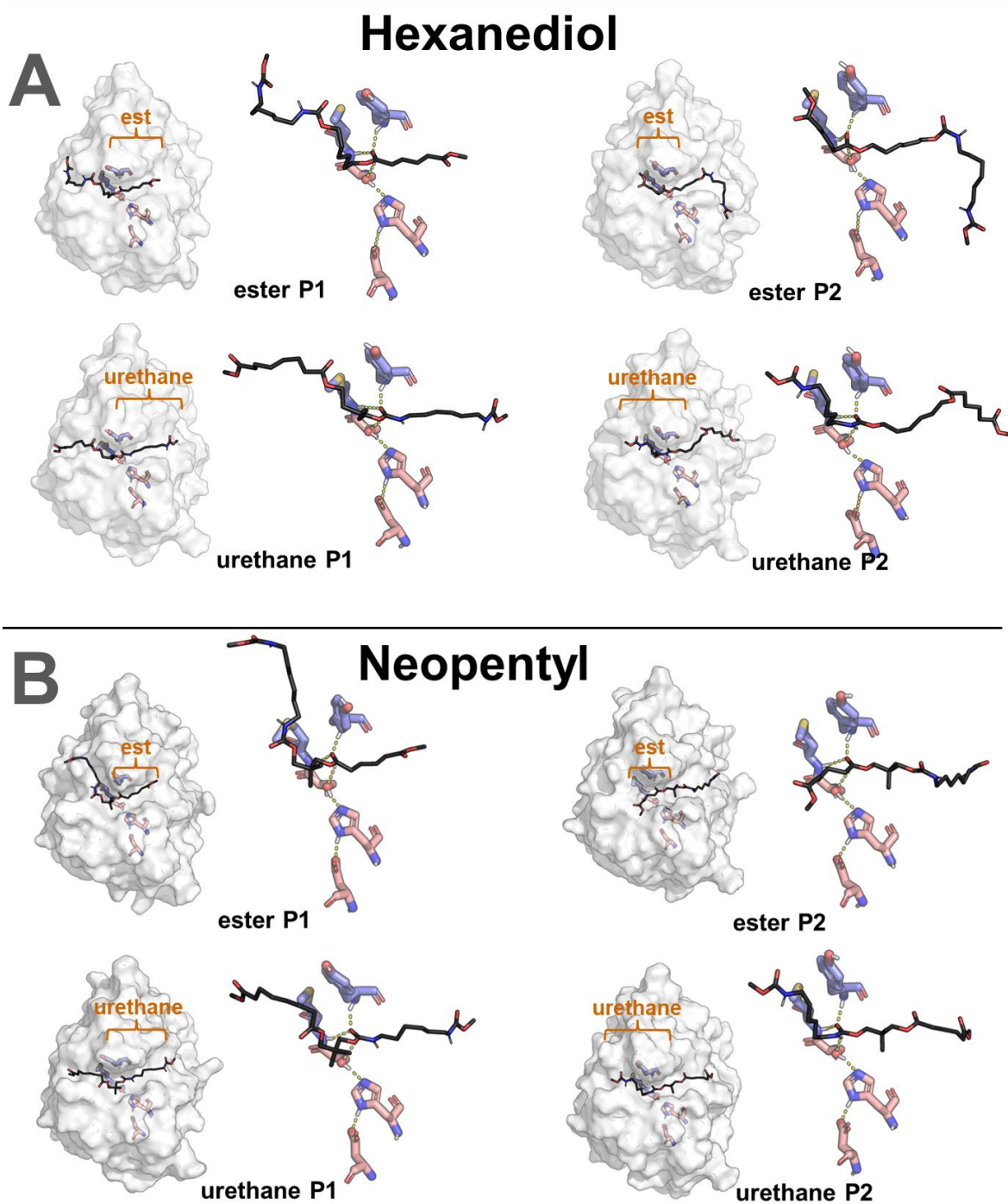


Fig. 30. Representative first frames of the artificial 10-frame trajectories generated using the workflow presented in Figure 27, shown for each of the eight *TfCut2*-Impranil DLN repeating unit systems. The Impranil DLN repeating unit is depicted as black sticks, with the initially docked ester and urethane moieties highlighted by an orange brace. The catalytic triad residues (S130, D176, H208) are displayed as salmon-colored sticks, while the oxanion hole residues (Y60, M131) are shown as purple sticks. Key catalytic and stabilisation distances are indicated by yellow dashed lines. **A)** Hexanediol Impranil DLN; **B)** Neopentyl Impranil DLN.

During the writing of this thesis manuscript, Świderek et al. published a study docking two orientations of an Impranil DLN repeating unit into the active site of lipase A from *Pseudomonas chlororaphis* (PueA), an enzyme with potential for synthetic polymer degradation [161]. These orientations, referred to as RC1 and RC2, correspond to the ester P1 and ester P2 poses identified in the *TfCut2* study. Both orientations position the cleaved ester bond near the catalytic triad, indicating similarities in the binding modes of Impranil DLN to PueA and *TfCut2*, despite structural differences between the enzymes (Fig. 31B). This observation suggests that, while originating from different organisms, these enzymes may share structural features that facilitate polymer substrate binding in an extended conformation.

In that study, the authors showed that RC2 pose represents superior-protein-ligand interactions decomposed by ligand and activation free energy of the acylation step, which is around 10 kcal/mol lower than for RC1 starting structure. At the same time, the kinetics of activation of the catalytic serine is basically equivalent for both poses. This energetical difference may stem from the fact, that in pose RC2 the leaving alcohol group of the tetrahedral intermediate is better stabilised by deprotonated nitrogen of the catalytic histidine [107]. It seems, that in RC2 the catalytic histidine is closer to the leaving group oxygen and able to donate a proton to it more freely (Fig. 31B). What is more, in that study, the authors used a similar approach of measuring distance of terminal atoms in a model of Impranil DLN, to assess the extended poses (Fig. 31B).

Further, the binding pose of a PET trimer within the active site of LCC reported by Tournier et al. [48] was examined (data not shown due to copyright issues). LCC cutinase shares 55.7% identity with *TfCut2*. The bound pose of the PET trimer to LCC strongly resembles in shape the binding mode of the Impranil DLN repeating unit in the hexanediol ester P2 pose within *TfCut2*. It is visible, that the bulky residues in LCC that are responsible for the binding: F243 and “aromatic clamp” formed by Y95 and W190 in LCC are mirrored by F209, and Y60 with W155, respectively, in *TfCut2*.

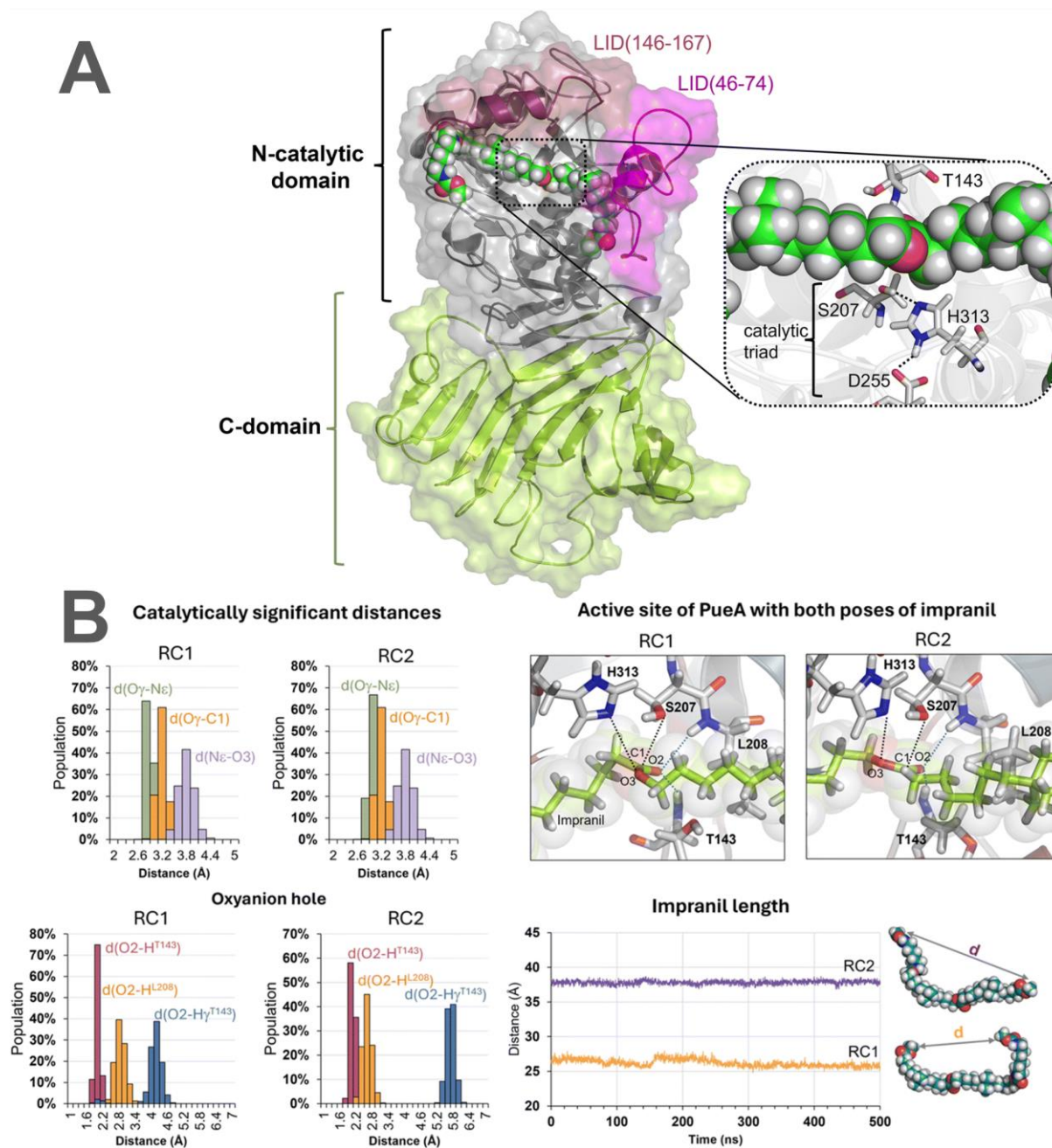


Fig. 31. **A)** Structure of PueA generated by AlphaFold2 with the Impranil DLN repeating unit docked in the active site in an extended conformation (RC1). Adapted from Świderek et al. [161] under a Creative Commons Attribution-NonCommercial 3.0 Unported Licence. **B)** Two modelled orientations of the Impranil DLN repeating unit bound to PueA, with ester as the cleaved group, referred to as RC1 and RC2. The RC1 and RC2 poses correspond to the ester P1 and ester P2 poses, respectively. Adapted from Świderek et al. [161] under a Creative Commons Attribution-NonCommercial 3.0 Unported Licence.

When the productive poses of Impranil DLN are overlaid, they show a clear alignment around the active site (highlighted by a green circle in Fig. 32A). As expected, these poses position the carbonyl group of the cleaved bond near S130 and the oxanyon hole residues, Y60 and M131, ensuring productive interactions. Additionally, alignment occurs within

the "aromatic clamp" region formed by residues Y60 and W155 (Fig. 32B). These two bulky amino acid residues enforce a specific arrangement of the polymer chain within the binding groove, stabilising it close to the active site. Outside of these regions, the polymer chain adopts various conformations, binding flexibly across different areas of the binding surface.

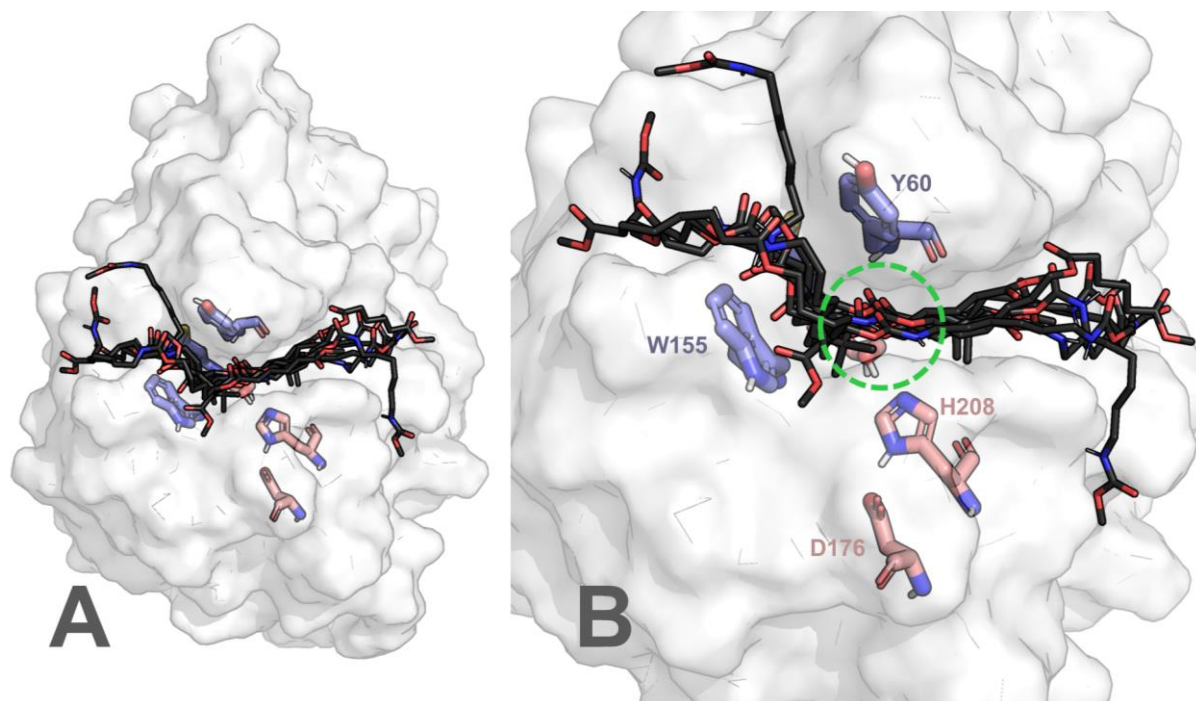


Fig. 32. Overlay of Impranil DLN poses from the first frames of representative artificial 10-frame trajectories shown in Figure 30. The protein structure from hexanediol ester P2 is shown as a white surface for reference. The catalytic triad is shown as salmon sticks, and the aromatic clamp and oxyanion hole residues are depicted as blue sticks. **A)** Overview of the aligned poses. **B)** Zoomed view.

The purpose of this workflow was to identify and analyse events when the ligand was tightly and specifically bound to *TfCut2*. This computational approach enabled the identification of key residues responsible for binding the polymer chain during enzymatic degradation. These amino acid contributions were critical for proposing substitutions to improve polymer chain binding, potentially addressing the rate-limiting step of the reaction. Similar approaches have been applied to model the productive pose of the first step of synthetic polymer degradation in an extended conformation, although different computational methods and enzyme-polymer systems were used [48,161]. The similarity indicates that polymer-binding enzymes, such as *TfCut2*, may adopt common strategies for substrate positioning and stabilisation across different polyester-degrading enzymes.

4.3.4. Analysis of *TfCut2*-Impranil DLN interactions in productive poses

The interactions between *TfCut2* and Impranil DLN were investigated using the ProLIF Python library [299]. The analysis focused on ten representative productive frames for each system, which were identified in the previous step. ProLIF enables the generation and visualisation of interaction fingerprints, detailing the specific amino acid residues that interact with particular ligand atoms. These interactions are visualised as dashed lines, colour-coded according to the type of interaction, with the width of the lines reflecting the frequency of occurrence across the ten frames (with a maximum of 10 observations, as because of 10 frames). The results for Impranil DLN hexanediol and neopentyl poses are presented in Figures 33 and 34, respectively.

The analysis highlights the strongest interactions occurring near the cleaved bond of the ligand, specifically between the carbonyl oxygen and the oxyanion hole residues Y60 and M131, as well as between the carbonyl carbon and the catalytic residue S130. Additionally, frequent hydrophobic interactions are observed between the aromatic residues W155 and Y60 and the polymer backbone carbons adjacent to the cleaved bond. Together, Y60 and W155 form an "aromatic clamp" [149] that plays a crucial role in stabilising the ligand within the active site. Notably, Y60 also frequently engages in van der Waals interactions with the carbonyl carbon of the cleaved ester group (Fig. 33, 34).

Further hydrophobic interactions are detected between the carbon atoms of the polymer chain and residues such as F209, I178, H129, and the catalytic residue H208. Other interactions are more variable, depending on the specific ligand pose and the location of the chain's distal end. However, most of the interactions involving the ligand's backbone carbons are hydrophobic in nature. Hydrogen bond donor/acceptor interactions are primarily observed for the atoms near the other ester and urethane bonds or for hydrogen atoms within the polymer backbone. Van der Waals interactions are also frequently observed throughout the ligand (Fig. 33, 34).

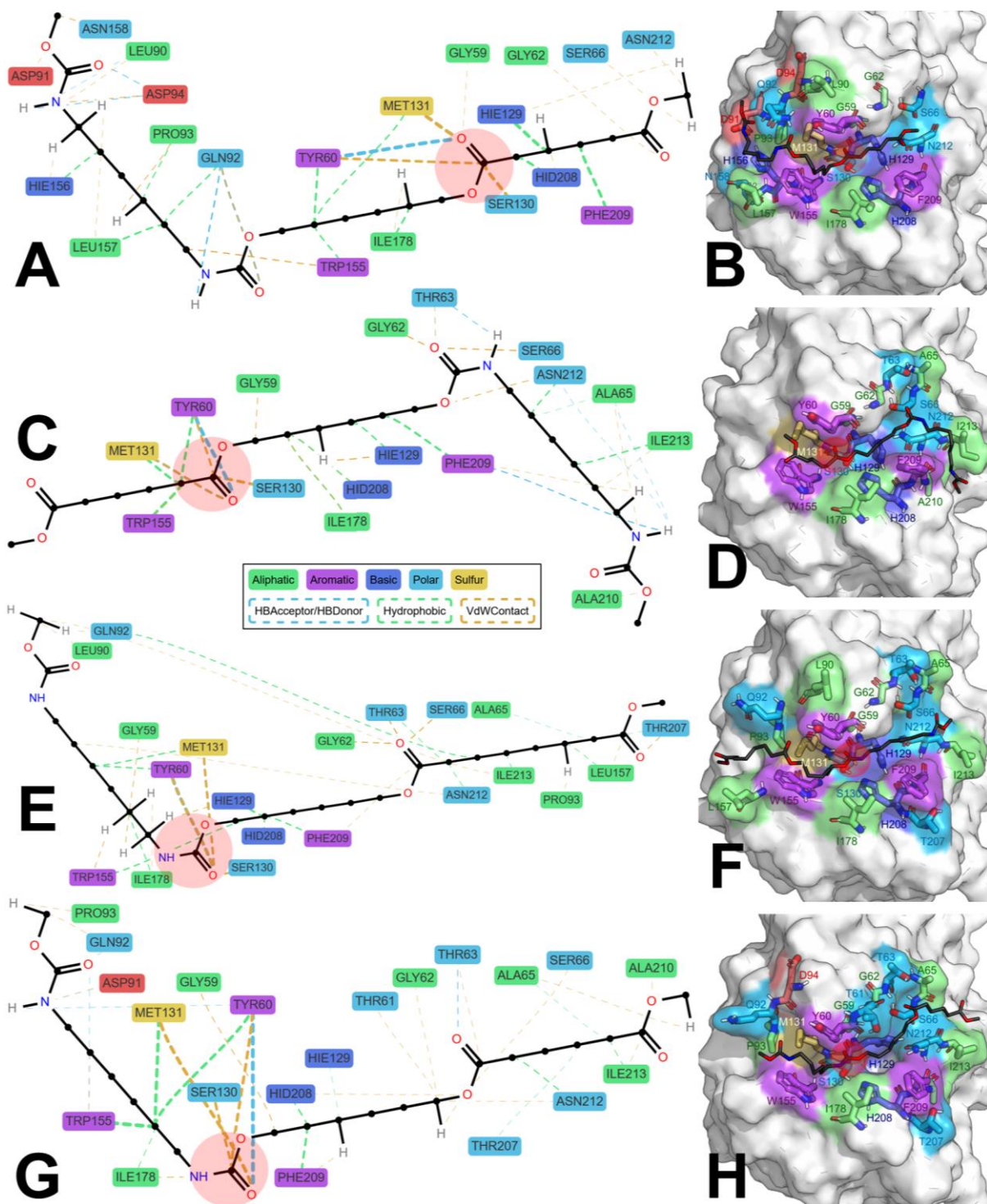


Fig. 33. Interaction fingerprints and visualisations of the binding site and Impranil DLN poses, with key residues from *TfCut2* highlighted. Amino acids are colour-coded according to the legend, and interactions are represented by dashed lines, with width proportional to the frequency of interaction. The cleaved bond is indicated by a transparent red circle. **A)** Ester P1 hexanediol Impranil DLN fingerprint. **B)** Ester P1 hexanediol Impranil DLN snapshot visualisation. **C)** Ester P2 hexanediol Impranil DLN fingerprint. **D)** Ester P2 hexanediol Impranil DLN snapshot visualisation. **E)** Urethane P1 hexanediol Impranil DLN fingerprint. **F)** Urethane P1 hexanediol Impranil DLN snapshot visualisation. **G)** Urethane P2 hexanediol Impranil DLN fingerprint. **H)** Urethane P2 hexanediol Impranil DLN snapshot visualisation.

In contrast, the interactions involving the terminal regions of the Impranil DLN chain are less consistent, engaging variably with different amino acids in the binding site (Fig. 33, 34). This suggests that Impranil DLN (or similar polymer chains) can adopt multiple conformations when bound within *TfCut2*'s active site. The binding of the aliphatic polymer chain to the binding site surface appears relatively unrestricted, with no strong preference for specific conformation.

When comparing the catalytic interactions of H208 between ester P1 and P2 poses, distinct patterns emerge. In the P1 pose of both hexanediol and neopentyl esters, H208 primarily interacts with the α -carbon adjacent to the carbonyl group (Fig. 33A, 34A). In contrast, for the hexanediol ester P2 pose, H208 interacts with the β -carbon adjacent to the leaving oxygen (Fig. 33C), while in the neopentyl ester P2 pose, it interacts with the CH₃ group of neopentyl glycol (Fig. 34C).

In the catalytic mechanism's second step, H208 typically donates a proton from its ϵ -nitrogen to the leaving oxygen of the cleaved bond after forming the tetrahedral intermediate. However, this study models the first step of the reaction, where histidine in the δ -protonated state cannot directly interact with the leaving oxygen. Consequently, due to the hydrophobic nature of its side chain, H208 instead interacts with carbons in the ligand. Notably, in the P2 ester poses, H208 engages with atoms closer to the leaving oxygen than in the P1 poses. In line with the findings of Świderek et al. [161], such proximity in P2 poses may favour more efficient proton transfer, suggesting a potential preference for P2 over P1 in catalytic efficiency.

This pattern implies that for urethane bonds, the P2 pose could similarly be more favourable than the P1 pose, provided urethane bonds are cleavable. In the urethane P1 pose, where the NH group replaces the leaving oxygen, no interaction with H208 in the δ -protonated state is observed, despite the spatial proximity of H208's free ϵ -nitrogen to the NH group (Fig. 33E and 34E). This lack of interaction may indicate that the urethane P1 pose does not position the NH group optimally for proton transfer by H208.

4.3.5. Estimated binding free energies via MM-GBSA approach

To estimate the binding free energy of the *TfCut2*-Impranil DLN complex, MM-GBSA calculations were performed on a set of ten representative frames selected from molecular dynamics simulations for each ligand pose. By using multiple frames rather than a single

snapshot, the analysis captures a range of protein-ligand interactions across different conformational states, providing a more comprehensive view of the binding landscape and accounting for some of the dynamic fluctuations in the enzyme-ligand complex. It is crucial to note that MM-GBSA primarily reflects the enthalpic contribution to binding free energy. The MM component estimates interactions such as electrostatic forces and van der Waals contacts between the protein and ligand whereas the GBSA accounts for solvation free energy. Of note, it does not fully account for the entropic penalty associated with binding—namely, the reduction in flexibility or disorder of both the ligand and protein upon complex formation. This entropic cost, often significant in flexible binding sites like that of *TfCut2*, can compensate the actual binding affinity. Therefore, without including the entropic component, the "total binding free energy" estimated by MM-GBSA may overestimate the true binding affinity, as it omits the energetic cost of the loss in flexibility. The presented results, therefore, represent an enthalpy-driven estimate of binding affinity rather than the full Gibbs free energy of binding. While it is possible to estimate the entropic contribution to binding using Normal Mode Analysis or Quasi-Harmonic analysis, such calculations are computationally expensive. Given the multiple modelled poses of Impranil DLN with *TfCut2*, these entropic estimations were omitted in this study to balance computational feasibility with the scope of the analysis.

Estimation of total binding free energy of the complexes

To assess the binding affinity of Impranil DLN to *TfCut2*, the MM-GBSA method was utilised. The total binding free energy, ΔG , was calculated as the energy difference between the complex, receptor, and ligand, according to the expression:

$$\Delta G_{bind} = \Delta G_{complex} - (\Delta G_{protein} + \Delta G_{ligand})$$

The analysis indicated that the binding affinities of the complexes varied depending on the orientation of the ligand and the specific moieties within the Impranil DLN repeating unit. Complexes with the hexanediol moiety of Impranil DLN generally exhibited lower binding free energies, likely influenced by the slightly larger size or molecular weight of the ligand compared to neopentyl. However, the differences between the respective poses were minimal, with the lowest binding free energy calculated for hexanediol urethane P1, -49.23 ± 5.23 kcal/mol, and the highest for neopentyl ester P2, -41.12 ± 3.05 kcal/mol. Table 7 summarises the average binding free energy for each ligand pose of Impranil DLN, along with the corresponding standard deviation. The similar values of binding free energy suggest that the *TfCut2* binding site accommodates the polymer chain in various configurations without

a strong preference for a particular pose. However, if ester P2 were truly the preferred pose for catalysis, the ΔG_{total} values indicate suboptimal binding. Specifically, neopentyl ester P2 exhibits the highest ΔG_{total} of all poses, contradicting the idea of its preferential role in catalysis. In contrast, hexanediol ester P2 has the second-lowest ΔG_{total} (after hexanediol urethane P2), which might support its binding preference despite not being the absolute lowest.

Table 7. Calculated mean binding free energy differences of *TfCut2*-Impranil DLN complexes using the MM-GBSA method. The binding energy values represent the average $\Delta G_{\text{total}} \pm$ standard deviation across ten frames for each ligand pose. The energy difference was calculated as $\Delta G = (\text{Complex} - \text{Receptor} - \text{Ligand})$ for each pose.

Pose	MM-GBSA ΔG_{total} [kcal/mol]	
	Hexanediol	Neopentyl
Ester P1	-45.83 \pm 3.04	-44.59 \pm 2.40
Ester P2	-46.23 \pm 2.92	-41.12 \pm 3.05
Urethane P1	-49.23 \pm 5.23	-45.01 \pm 2.91
Urethane P2	-43.12 \pm 2.81	-44.53 \pm 2.09

Estimation of per-residue binding free energy of the complexes

In addition to calculating the total binding free energies of the *TfCut2*-Impranil DLN complexes, per-residue binding energy contributions were also evaluated to gain insights into the individual energy contributions of specific residues within the binding site of *TfCut2*. The binding site is composed of several loops and two helices, as illustrated in Fig. 35. This section provides an overview of the binding site architecture and composition, with details derived from the per-residue binding free energy results of the MM-GBSA analysis, which will be discussed in detail later.

The binding site includes the following structural elements:

- **Loops:** Residues 58–62, 129–131, 153–157, and 174–180
- **Helices:** Residues 63–66 and 208–213
- **Strand:** Residues 91–97

This architecture, primarily composed of loops, provides the flexibility required to accommodate bulky substrates, such as polymer chains. Located on the surface of *TfCut2*, the binding site offers easy access to large substrate molecules. Furthermore, the exposed nature of the active site likely contributes to *TfCut2*'s substrate promiscuity, allowing interactions with diverse substrates without the constraints associated with internal protein cavities.

However, it is important to note that MM-GBSA calculations do not explicitly consider entropic contributions, which can be a significant limitation, particularly for flexible regions

like loops. These regions often exhibit substantial conformational dynamics that can influence binding energetics, and neglecting entropy may lead to an incomplete representation of their role in substrate accommodation and stability. Addressing this limitation in future analyses could involve methods that incorporate entropic effects, such as quasi-harmonic analysis or advanced free energy simulations, to provide a more comprehensive view of the binding energetics.

Compartment	TfCut2 sequence
Loop 58-62	P58, G59, Y60, T61, G62
Helix 63-66	T63, E64, A65, S66
Strand 91-97	D91, Q92, P93, D94, S95, R96, A97
Loop 129-131	H129, S130, M131
Loop 153-157	T153, P154, W155, H156, L157
Loop 174-180	D174, L175, D176, T177, I178, A179, P180
208, Helix 209-213	H208, F209, A210, P211, N211, I213

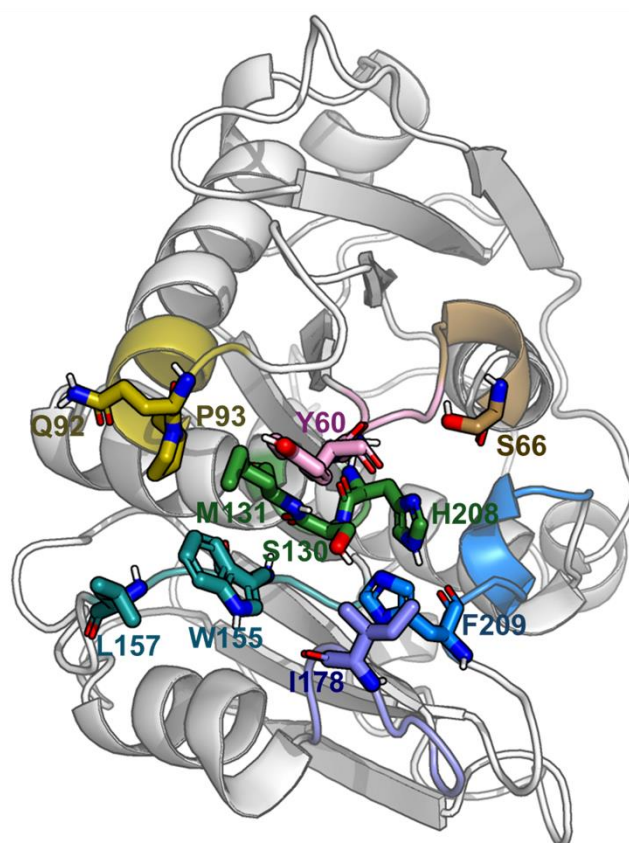


Fig. 35. Amino acid residues composing the binding site of *TfCut2*. Residues were identified based on per-residue binding free energy results from MM-GBSA calculations. Loops and helices are colour-coded, and the strongest binding residues are represented as sticks.

The estimated per-residue binding free energies of the *TfCut2*–Impranil DLN complexes were derived from MM-GBSA calculations and structural information about binding regions within the sequence was integrated from the *TfCut2* PDB structure 4CG1. Although several residues outside the defined binding site slightly contribute to ligand interactions, only those within the core binding site were considered here. The strongest binding residues were all located within the defined binding site.

Figure 36 and 37 present the per-residue binding free energies ($\Delta\Delta G$ in kcal/mol) for each residue in the *TfCut2* binding site, with separate plots for the hexanediol (Fig. 36) and neopentyl (Fig. 37) moieties of Impranil DLN. The contributions of individual residues

to binding were generally consistent across different ligand poses, as indicated by the similar bar lengths. Moreover, amino acid residues interacting with either hexanediol or neopentyl moieties followed similar binding trends. Notably, the residues constituting the binding site were distinguishable in these plots due to their strong binding free energy contributions. Most residues exhibit negative $\Delta\Delta G$ values, indicating that they strengthen ligand binding.

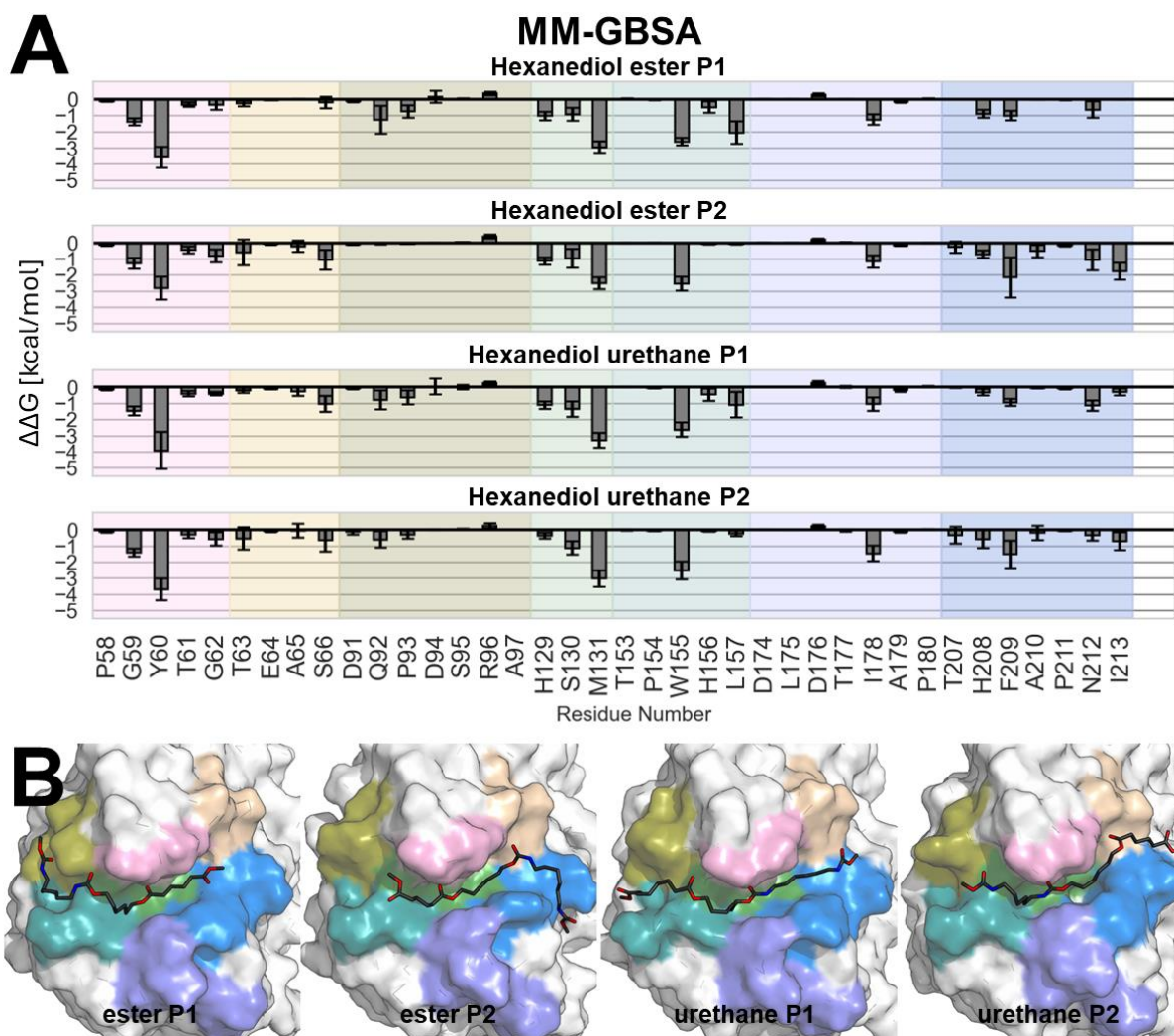


Fig. 36. **A)** Mean per-residue binding free energies ($\Delta\Delta G$ in kcal/mol) for residues within the *TjCut2* binding site, shown for hexanediol poses of Impranil DLN. Coloured blocks correspond to binding site compartments listed in Figure 35. **B)** Representative *TjCut2*-Impranil DLN complexes, highlighting hexanediol poses. The protein is shown as a surface, with residues coloured by binding site compartment.

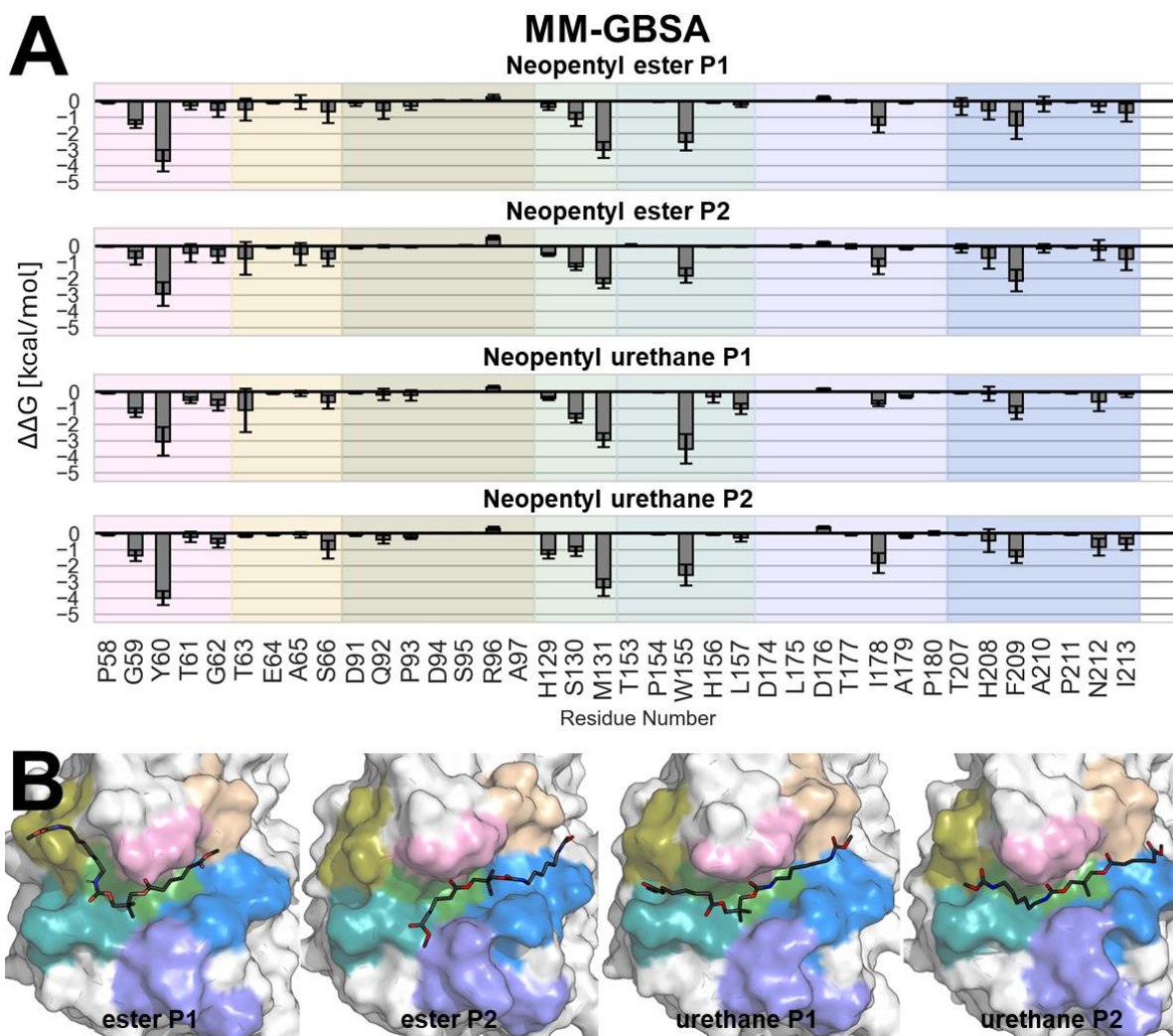


Fig. 37. **A)** Mean per-residue binding free energies ($\Delta\Delta G$ in kcal/mol) for residues within the *TfCut2* binding site, shown for neopentyl poses of Impranil DLN. Coloured blocks correspond to binding site compartments listed in Figure 35. **B)** Representative *TfCut2*-Impranil DLN complexes, highlighting neopentyl poses, shown as in fig. 36B.

The specific binding site compartments for each Impranil DLN pose are examined in more detail below:

- **Loop 58–62 and Helix 63–66:** This upper P1 region showed the strongest binding contributions from Y60 (oxyanion hole residue, from -2 up to -4.5 kcal/mol) and G59 (from -1 up to -1.8 kcal/mol). Other residues in this region bind weakly. Mutagenesis of residues 61–66 could improve binding of Impranil DLN.
- **β -strand 91–97:** In the upper P2 region, Q92 and P93 contribute the most to binding, but overall, none of the residues of this region contribute significantly. Q92, being solvent-exposed, may be a good candidate for mutagenesis to enhance polymer chain interactions. R96 shows a positive $\Delta\Delta G$, which suggests its destabilising role in the binding

of Impranil DLN. However, R96 is likely important for structural stability, as it forms salt bridges with the backbone carbonyl groups of neighbouring residues P58, T89, D91, and a crystal water molecule, as observed in the 4CG1 structure of *TfCut2* (data not shown).

- **Loop 129–131:** This central binding groove region is crucial, with S130 (catalytic residue) and M131 (oxyanion hole residue, from -2 up to -4.5 kcal/mol) showing strong binding contributions. H129 also binds relatively strongly.
- **Loop 153–157:** The lower P2 region showed strong binding from W155 (“aromatic clamp” residue, from -2 up to -4.5 kcal/mol) and L157 with lower $\Delta\Delta G$ than W155. These hydrophobic residues leave limited room for improvement through mutagenesis, as they are already binding strongly.
- **Loop 174–180:** Located centrally, this loop contains catalytic D176. I178 binds strongly (from -1 up to -1.8 kcal/mol) and is located in vicinity of the catalytic residues S130 and H208 (Fig. 35). Other residues contribute less to the binding due to their distance from the active site and binding site groove.
- **Helix 209–213:** This lower P1 region includes catalytic H208, which shows relatively strong binding contributions. F209, N212 and I213 also bind strongly and could be mutagenesis targets.

Overall, the per-residue $\Delta\Delta G$ values were rather consistent across ligand poses, indicating that the Impranil DLN polymer chain can bind in various conformations without drastically altering individual residual contributions.

The strongest binding residues—Y60, M131, and W155—play key roles in polymer anchoring. These residues are largely hydrophobic, facilitating interactions through hydrophobic forces. Y60 and W155, in particular, form an “aromatic clamp” that is essential for anchoring the polymer chain near the active site, consistent with previous findings [149]. These essential residues, along with the catalytic triad, were excluded from mutagenesis considerations due to their critical roles in enzyme function.

The MM-GBSA results align with those obtained from ProLIF analysis, further confirming the contributions of key residues to Impranil DLN binding. Details of the protein design and proposed mutations are discussed in the following chapter.

4.4. Conclusions

In this dissertation, Impranil DLN was chosen as a model PUR substrate because of its widespread use in studies on enzymatic PUR degradation. *TfCut2* was selected as a model enzyme for this study based on its previously reported efficacy in polyester PUR degradation, as highlighted by Schmidt et al. [20]. At the time this study began in 2020, *TfCut2* and Impranil DLN were optimal choices for examining polymer degradation mechanisms. Later reports (from 2022 onward) described PUR-degrading fungal cutinases [22–24] and urethanases [19,26]; however, such enzymes were not yet known in 2020 and thus could not be included in this work.

The proprietary nature of Impranil DLN's structure has posed significant challenges for computational modelling. Literature sources report varying structural interpretations [3,4], contributing to uncertainty about its precise composition. To address this, extensive NMR analyses were conducted within this dissertation to characterise the structural features and repeating units of Impranil DLN. These efforts aimed to provide a robust foundation for constructing a reliable computational model to support subsequent studies. *TfCut2*'s ability to degrade Impranil DLN and other polyester-based PURs was confirmed through prior research by Schmidt et al. [20]. However, urethanase activity in *TfCut2* was not reported. Given findings that single mutations can alter esterase activity to favour amidase activity [140], both ester and urethane orientations were examined in this study to assess potential activity across both bonds.

The specific binding orientation of Impranil DLN or similar polymers in enzyme active sites remains unclear. Świderek et al. [161] addressed this question by modelling Impranil DLN's binding in PueA and introduced two binding poses RC1 and RC2, with RC2 being more favourable by $10 \text{ kcal}\cdot\text{mol}^{-1}$ while exhibiting similar activation energy to RC1. Discussions at the 2024 Faraday Discussions conference suggested that RC2's preference might stem from easier stabilisation of the leaving group by catalytic histidine in the tetrahedral intermediate [107].

This dissertation did not investigate tetrahedral intermediate stabilisation or exact orientation effects through QM/MM methods. Instead, MD methods were used. Although MD simulations, Rosetta energy scores, and MM-GBSA calculations showed differences among the binding poses, distinguishing a preferred pose was challenging for the non-aromatic, aliphatic Impranil DLN. However, in line with findings of Świderek et al. [161] on Impranil

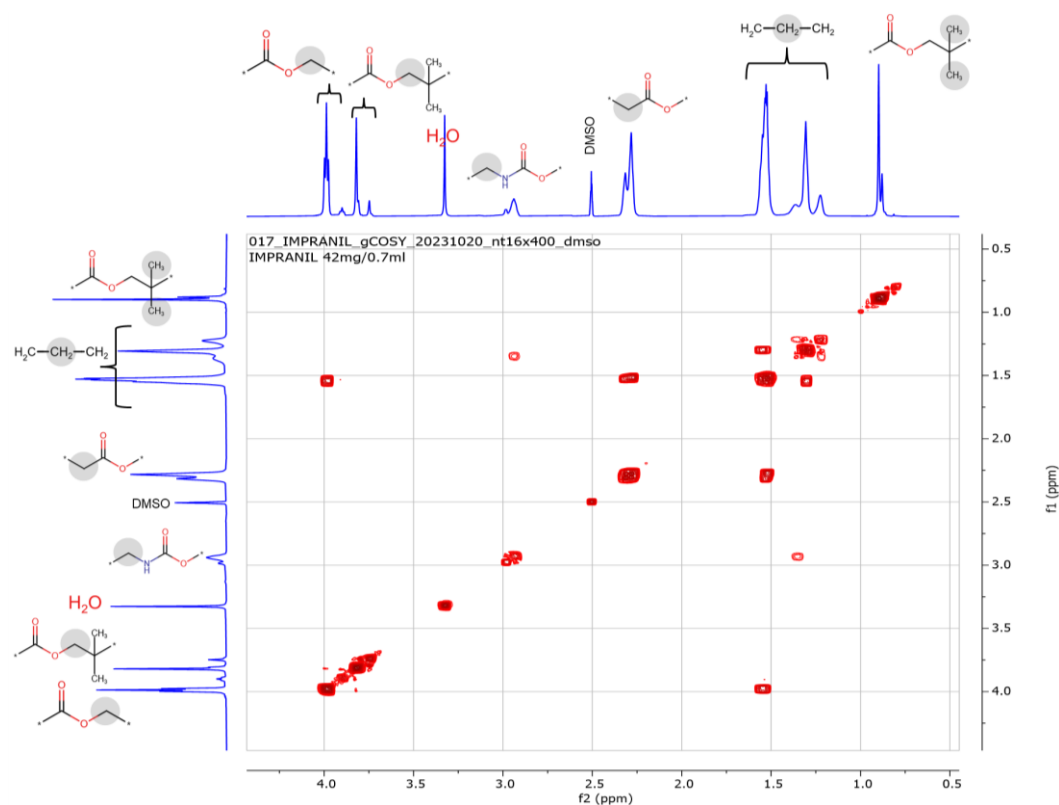
DLN enzymatic hydrolysis, the ester P2 pose could be the most optimal for catalysis, especially in case of hexanediol Impranil DLN moiety. In the hexanediol-based repeating units, orientation appeared less critical for binding. Only in the neopentyl-based repeating unit did the presence of methyl -CH₃ groups cause minor interference due to steric clashes with active site residues, varying by orientation and local conformation.

In general, *TfCut2* likely recognises the polymer chain globally, and the binding orientation of the cleaved bond is crucial for achieving catalytic distances conducive to nucleophilic attack and oxyanion hole stabilisation. Key residues, such as W155 and Y60, form an "aromatic clamp" [149] that stabilises the polymer chain, with other residues (e.g. F209, I178, Q92) also contributing to binding but being less critical. The hydrophobic interactions in *TfCut2*'s groove offer flexibility in binding to the polymer chain, explaining the broad substrate promiscuity of cutinases. Although these enzymes naturally degrade the polyester cutin, they have been applied to Impranil DLN and polyester PURs [20,22–24,128], PET [191,193,315,316], and polyamides [317].

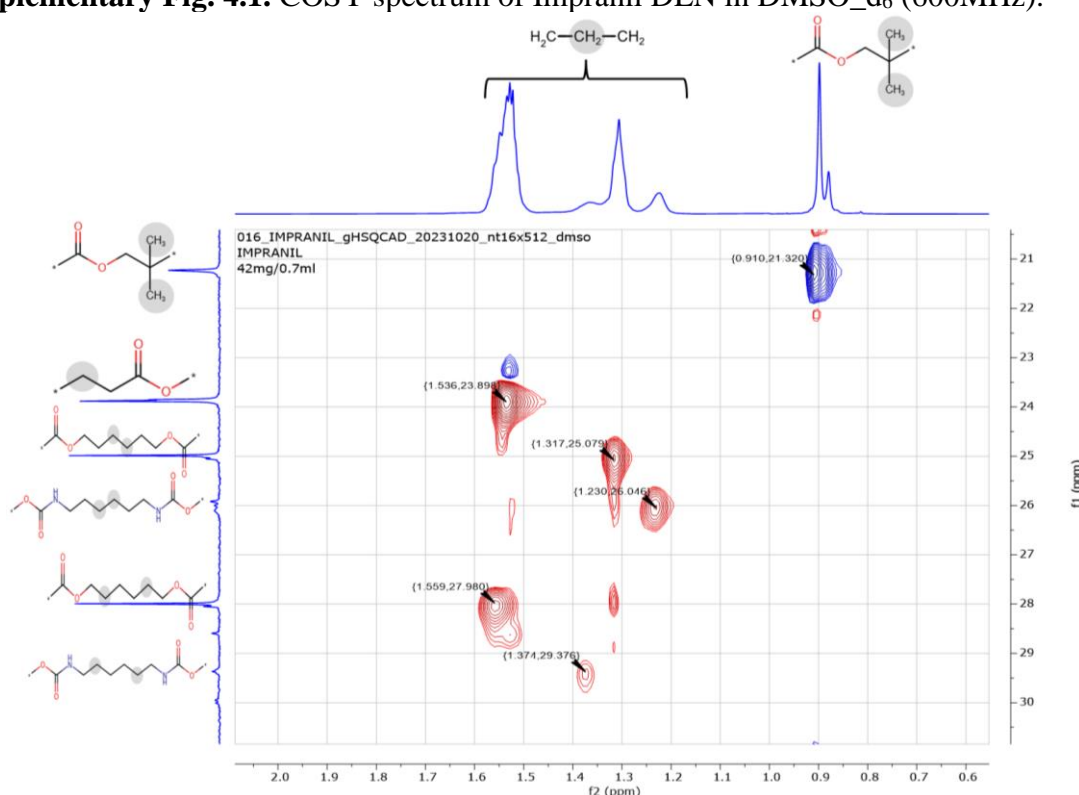
In this study, productive binding poses were selected based on nucleophilic attack distances, proton transfer, and the Bürgi–Dunitz angle, aiming for ~107°. In practice, achieving this angle was difficult; initial inspections suggested a stable angle around 80°, which was used instead. Future work could benefit from additional constraints on oxyanion hole distances and possibly between H208 and D176 to avoid histidine flipping, which sometimes disrupted interactions with other catalytic triad residues.

In this chapter, the first computational studies focused on Impranil DLN recognition by a cutinase has been presented, offering valuable insights into the specific amino acids in the binding site of *TfCut2* and their contributions to effective ligand binding. This work has provided a detailed look into the binding modes of Impranil DLN fragments, demonstrating how *TfCut2*'s structural features accommodate such a complex substrate. These findings establish a strong foundation for future studies aiming to optimise cutinase enzymes for broader applications in polymer degradation.

4.5. Supplementary materials to Chapter 4



Supplementary Fig. 4.1. COSY spectrum of Impranil DLN in DMSO-d₆ (600MHz).



Supplementary Fig. 4.2. Fragment of the phase-sensitive HSQC spectrum of Impranil DLN in DMSO-d₆ (600MHz).

Chapter 5: Description of mutational landscape and design of *TfCut2* mutants

5.1. Introduction

Protein engineering is a highly complex challenge, with 20^N potential solutions, where N represents the protein sequence length or the number of candidate amino acids for substitution, given the 20 naturally occurring amino acids. To manage this vast search space and streamline the design process, researchers often rely on rational or semi-rational design approaches to narrow down possibilities and focus their efforts.

In recent years, computational protein design and computer-aided engineering have transformed the field of catalysis and enzyme-driven processes, providing innovative approaches to tailor enzymes for specific reactions and substrates. These tools allow to analyse complex protein structures, predict interactions with substrates, and identify residues crucial for activity and binding. By using computational methods to design and optimise enzyme functions, scientists have achieved significant advances in the development of biocatalysts, impacting areas such as biotechnology and medicine [318–320].

In enzyme-based processes, computational protein design facilitates the rapid and cost-effective generation of enzyme variants with enhanced catalytic efficiency, stability, and substrate specificity. These methods not only predict how mutations might affect binding affinity, structural stability, and overall reactivity, but also enable systematic sampling of sequence conformational space. Integrating methods like MD simulations, molecular docking, and energy calculations have proven especially powerful, allowing researchers to predict how mutations might affect binding affinity, structural stability, and overall reactivity. This strategic sampling reduces the size of mutant libraries for experimental evaluation, increases hit rates, and facilitates the identification of high-throughput variants. As a result, computational tools play a key role in making enzyme engineering efforts more efficient and focused.

The primary objective of this dissertation is to investigate the molecular determinants involved in enzyme-based degradation of PUR and to optimise the degradation performance of the targeted enzyme, *TfCut2*. Building on insights from Chapter 4, which identified key binding residues involved in *TfCut2*'s interaction with Impranil DLN, this chapter focuses

on the second objective: *Re-designing the substrate binding site of TfCut2* to enhance its recognition and binding of Impranil DLN.

The goal of this study was to propose mutations that would enhance the ΔG of protein-ligand binding, and possibly also enhance rate of polymer degradation, without compromising the structural stability of *TfCut2*, in order to verify if the ligand binding is the rate limiting step in synthetic polymers enzymatic degradation. While improving the stability of the overall protein structure was not a primary objective, it was important to ensure that mutations did not destabilise the enzyme. Therefore, before proposing mutations to improve Impranil DLN binding to *TfCut2*, it was crucial to first investigate the legitimacy and feasibility of introducing mutations into the *TfCut2* sequence, and then to identify functional hot spots whose modification could affect substrate binding and/or the rate of catalysis. The schematic illustration of approaches applied within the second objective of this dissertation, that are described in this chapter, is presented in Figure 38.

The first step reduced the 293 amino acids in *TfCut2* to only the binding site residues (Fig. 38A). Then, essential amino acids, whose substitution could impair *TfCut2*'s enzymatic function, were excluded (Fig. 38B). In the next step, *TfCut2*'s structure and sequence were analysed to obtain information about the possibility of introducing mutations into the remaining amino acids of the binding site, without destabilising the protein's structure and integrity (Fig. 38C).

For this purpose, to evaluate the structural impact of potential mutations on the structure of *TfCut2*, systematic mutations were introduced within *TfCut2*'s binding site and the resulting changes in ΔG were calculated using FoldX [321]. This approach allowed to estimate free energy changes to assess the functional consequences of specific mutations. This analysis generated a substitution matrix, offering insights into the energetic consequences of each single-point mutation and aiding in the prioritisation of potential variants. Additionally, to analyse probability of successfully mutating the binding site residues, the evolutionary variabilities of each of the binding site amino acids were computed by analysing MSA of homologous proteins and mapping conservation and variability scores onto the protein structure to identify mutational targets that could enhance *TfCut2*'s characteristics. Combination of these two approaches provided essential insights for assessing and prioritising potential mutations (Fig. 38C).

To pinpoint residues with the greatest potential to enhance substrate binding, functional hot spots were identified (Fig. 38D). For this, HotSpot Wizard was used, which identifies

functionally relevant residues for mutagenesis via evolutionary and structural analysis by combining sequence and structural analyses [322]. This information about functional hot spots helped to guide the selection of residues for mutation.

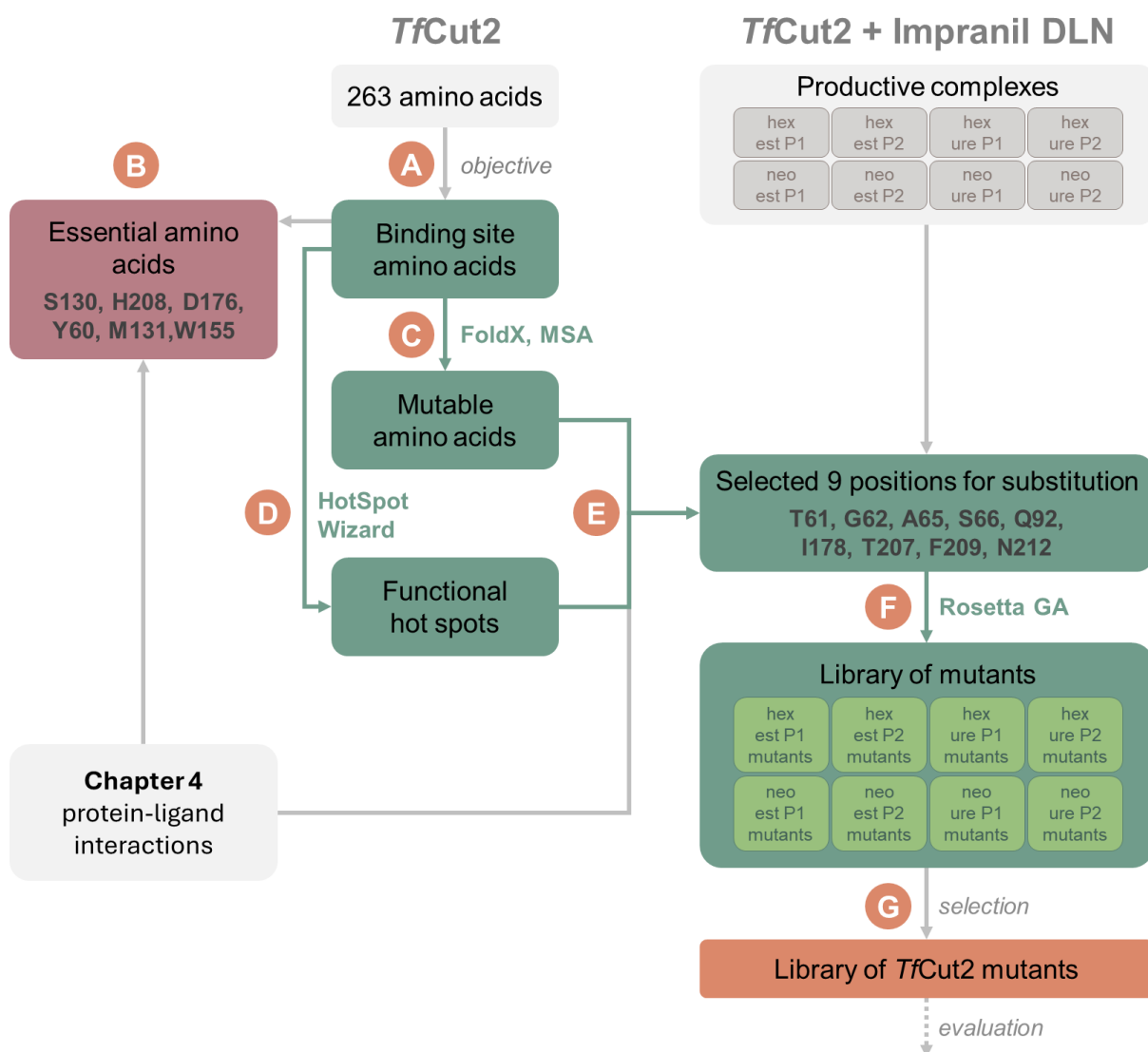


Fig. 38. Schematic of approaches applied to propose mutations to *TfCut2* to enhance its binding affinity and catalytic efficiency for the model PUR substrate Impranil DLN. **A)** Selection of binding site residues for mutagenesis. **B)** Exclusion of essential amino acids from the design process. **C)** Evaluation of mutation feasibility without structural destabilisation. **D)** Identification of functional hot spots likely to impact ligand binding. **E)** Integration of data to select residues for mutation. **F)** Computational protein design using Rosetta with an integrated genetic algorithm (GA) to improve protein-ligand binding; mutant libraries were generated for each Impranil DLN binding pose. **G)** Curation of a library of *TfCut2* mutants for further evaluation.

In the next step, information was integrated from three key areas: 1) protein-ligand interactions and residual binding contributions detailed in Chapter 4, 2) identified residues amenable to mutagenesis, and 3) functional hot spots critical for binding and activity

(Fig. 38E). In the process, nine positions in binding site were selected for mutation: T61, G62, A65, S66, Q92, I178, T207, F209, and N212. These residues were chosen based on the rationale that they could enhance binding to the Impranil DLN chain or they were proximal to the active site, potentially affecting catalytic efficiency.

In the next step, a systematic protein design approach was employed to identify mutations that could enhance the interface ΔG scores and improve the binding of *TfCut2* to Impranil DLN. This approach considered all eight modelled *TfCut2*-Impranil DLN complexes, enabling the identification of pose-specific mutations. For this, a custom methodology incorporating Rosetta protein design and a genetic algorithm was used to substitute the selected nine amino acids (Fig. 38F). For each Impranil DLN pose, a library of mutant complexes was generated, resulting from the subsequent runs of the genetic algorithm. This approach moved beyond classical Rosetta protein design, which typically identifies a limited number of improved mutant complexes, by enabling the generation of diverse mutation sets with improved interface energetics. The sequences and scores of these mutants were then thoroughly analysed to select the most promising candidates for experimental validation. This approach facilitated the proposal of mutations aimed at improving ligand binding by optimising local interactions within each binding mode. The suggested substitutions varied by pose, reflecting differences in local interactions between Impranil DLN and the binding site. Several mutations that were beneficial for specific *TfCut2*-Impranil DLN pose complexes were prioritised for further evaluation.

This integrated approach led to the creation of a library of *TfCut2* mutants (Fig. 38G): 25 single-point mutants and five combined mutants for further evaluation. Experimental validation of these mutants (described in Chapter 6) will help determine which Impranil DLN pose is most relevant in solution, as if a given mutation that interferes with a given pose will cause loss of activity, it may indicate that this particular pose is preferable. This strategy not only optimised enzyme binding but also provided a framework for understanding substrate binding dynamics in enzymatic degradation of synthetic polymers.

5.2. Methodology

Selection of mutational hot spots

To assess the potential for substituting individual amino acids within the *TfCut2* sequence, a comprehensive substitution matrix was generated using the FoldX [321]

programme. In this study, each amino acid in the *TfCut2* sequence was iteratively substituted with the other 19 classical amino acids using FoldX. For each substitution, FoldX calculated the difference in energy ($\Delta\Delta G$) between the mutant and the wild-type enzyme. These energy differences were then compiled into a substitution matrix, where each row corresponds to a specific position in the *TfCut2* sequence, and the 20 columns represented all possible amino acid substitutions at that position.

To identify key residues in *TfCut2* for targeted mutagenesis aimed at improving binding affinity, catalytic activity, or substrate specificity, the HotSpot Wizard webserver [322] was used with default settings, using the PDB structure 4CG1 of *TfCut2* as input.

To further investigate the evolutionary variability and mutability of residues in *TfCut2*, the BALCONY R package [323] was utilised for a detailed analysis of the MSA generated by HotSpot Wizard. This MSA comprised homologous sequences of proteins related to *TfCut2* and was inspected to ensure that it contained appropriate homologous sequences. Schneider entropy [324] was calculated for each MSA position using BALCONY, and then the MSA positions were mapped.

Computational protein design

To enhance binding affinity of Impranil DLN by *TfCut2*, at nine positions: T61, G62, A65, S66, Q92, I178, T207, F209, and N212 a custom genetic algorithm was employed. This algorithm, developed in-house by Dr. Rajendra Sharma (former Post-Doc at Toulouse Biotechnology Institute), but not previously published, was integrated with the Rosetta [266,293] protein design module accessed via PyRosetta [325], and implemented in Python.

The genetic algorithm followed these steps:

1. **Initialisation:** Generation of initial mutant populations using specified seed sequences and the Rosetta protein design tool.
2. **Selection:** Evaluation and selection of the best-performing sequences based on a defined fitness function.
3. **Crossover and Mutation:** Creation of new mutants through crossover and mutation operations.
4. **Evaluation:** Scoring and evaluation of each mutant using Rosetta's *ref2015* [288] all-atom scoring function and the custom genetic algorithm fitness function.
5. **Iteration:** Repeating the crossover, mutation, and evaluation steps for a set number of generations to optimise the mutants.

For each of the eight *TfCut2*-Impranil DLN complexes, the first frame (most representative) of the 10-frames selected after kmeans clustering of MD simulations, was used to run the Rosetta Protein Design with genetic algorithm. For each complex, 50 generations of population size 100 were generated.

The initial generation was generated uniformly. Based on initial test calculation rounds, the crossover probability was set to 0.8. The number of parents next generation was set to 50. The mutation probability was set to 0.5.

5.3. Results and discussion

5.3.1. Assessment of mutational potential and identification of hot spots in *TfCut2*

This section evaluates *TfCut2*'s capacity to accommodate specific amino acid substitutions while maintaining structural integrity and stability. The analysis identifies mutational hot spots within the enzyme, focusing on positions with high potential for introducing beneficial changes. These insights are crucial for guiding modifications aimed at improving PUR degradation efficiency. By exploring mutability and evolutionary conservation, the study sets a foundation for rationally designed mutations that enhance enzyme performance.

Mutation Feasibility of *TfCut2*: estimating free energy changes and evolutionary variability

To estimate the predicted changes in stability ($\Delta\Delta G$) of potential mutants, the systematic mutation within *TfCut2*'s binding site was carried out using FoldX [321]. A substitution matrix was generated, offering insights into the energetic consequences of each single-point mutation and aiding in the prioritisation of potential variants. The substitution matrix for the binding site residues of *TfCut2* is presented in Figure 39. Negative $\Delta\Delta G$ values indicate that a mutation may stabilise the protein, while positive values suggest potential destabilisation. In the original FoldX publication, the authors warn that the empirical standard deviation of FoldX results is 0.46 kcal/mol, as measured between calculated and experimental $\Delta\Delta G$ s [321].

To further refine the analysis from an evolutionary perspective, Schneider entropy [324] was calculated for each residue based on a MSA of homologous proteins, using BALCONY R package [323]. The entropy values were incorporated into the substitution matrix as an additional column (Figure 39). Schneider entropy, ranging from 0 to 1, serves as a metric for evolutionary conservation, where low values indicate conserved positions and high values suggest greater variability. Positions with higher entropy are more likely to tolerate substitutions without significantly destabilising the protein.

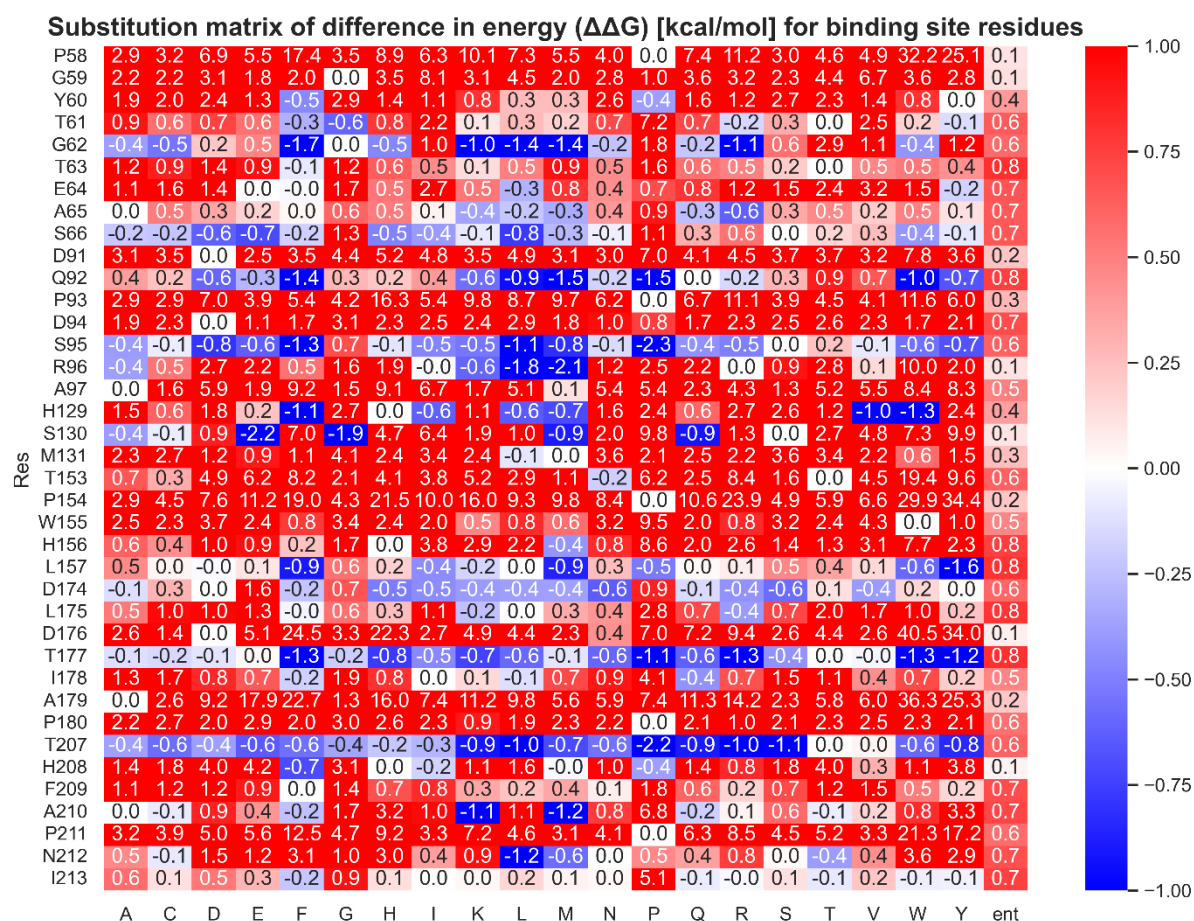


Fig. 39. Substitution matrix of energy differences ($\Delta\Delta G$) between the mutant and wild-type enzyme, calculated using FoldX for the binding site residues. Rows represent specific positions in the *TfCut2* sequence, while the 20 columns represent possible amino acid substitutions. The column labeled ‘ent’ corresponds to the Schneider entropy calculated for each position.

For the catalytic triad residues, S130, H208, and D176, the calculated Schneider entropy value is 0.1, indicating a high degree of conservation. This is consistent with their crucial role in the catalytic function of *TfCut2* and homologous enzymes. Other residues with low entropy values of 0.1 include P58, G59, and R96. FoldX results suggest that P58 and G59 are energetically unfavourable for substitution. Regarding R96, as noted in Chapter 4.3.5 (per-residue MM-GBSA results), this residue is relatively buried, and forms salt bridges

with backbone carbonyl groups of neighbouring residues P58, T89 and D91. Thus, substituting R96 could destabilise the protein, despite FoldX indicating that it could be replaced by leucine or methionine with $\Delta\Delta G$ values of -1.8 and -2.1 kcal/mol, respectively.

The oxyanion residues Y60 and M131 also exhibit low entropy values (0.4 and 0.3, respectively), despite their side chains not being essential for catalysis. These residues stabilise the carbonyl oxygen of the cleaved bond via hydrogen bonds formed by their backbone NH groups. According to FoldX, favourable substitutions for these residues are limited. Notably, Y60 could potentially be replaced by phenylalanine with a $\Delta\Delta G$ of -0.5 kcal/mol, a plausible substitution given the structural similarity between tyrosine and phenylalanine, differing only by the hydroxyl group of tyrosine. A phenylalanine is also present at equivalent position in homologous cutinases *Tcur1278* and *Tcur0390*, as mentioned in Chapter 4.3.2.

Another critical residue involved in ligand binding, W155, has an entropy value of 0.5. However, FoldX results suggest that this residue cannot be favourably substituted.

For other binding site residues, many positions show relatively high entropy values (>0.5), and several are predicted to tolerate multiple favourable substitutions according to FoldX $\Delta\Delta G$ results. These include residues such as T61, G62, A65, S66, Q92, S95, L157, D174, L175, T177, T207 and N212.

In summary, the substitution matrix combined with evolution-based entropy values enabled the identification of positions within the *TfCut2* sequence that are likely to tolerate substitutions without destabilising the protein structure. Furthermore, the matrix highlighted positions where multiple substitutions resulted in negative $\Delta\Delta G$ values, suggesting a higher tolerance for mutation and a greater likelihood of maintaining protein stability. This analysis not only helps identify possible sites for mutation but also specifies which amino acids could be introduced without compromising the structural integrity of *TfCut2*. The substitution matrix provides a valuable guide for future protein engineering efforts aimed at enhancing or altering enzyme function.

Functional hot spots analysis using HotSpot Wizard

To identify mutational hot spots within the *TfCut2* sequence, the HotSpot Wizard web server [322] was utilised. After importing the *TfCut2* structure from the PDB (PDB ID: 4CG1), HotSpot Wizard integrated information from SwissProt to identify essential amino acid residues for *TfCut2* functionality: Y60, S130, M131, W155, D176, D204, and H208. These are the essential residues that form the catalytic triad (S130, D176, H208), the oxyanion hole

(Y60, M131), the "aromatic clamp" (Y60, W155), and the divalent metal-binding site (D204) [188].

HotSpot Wizard results highlighted several types of amino acid hot spots: functional hot spots, correlating hot spots, stability hot spots based on protein flexibility, and stability hot spots derived from sequence consensus.

- **Functional hot spots:** The residues T61, G62, T63, A65, S66, F209, and N212 were identified, all of which are located in the binding site of *TfCut2*.
- **Correlating hotspots:** Pairs of co-evolving residues identified as correlating hotspots were E64-T83, Q92-K159, L104-L124, N105-R143, R138-H156, L159-W161, and K186-E254.
- **Stability hotspots based on protein flexibility:** The following residues were indicated: A1, L14, R18, R110, K216, R245, G247, L248, F249, and P263.
- **Stability hotspots based on sequence consensus:** Residues L14, S19, R46, N48, N49, Y51, A65, E72, I72, I87, N101, N105, H106, M107, I108, A111, L139, N145, K216, and I217 were identified.

Of particular interest for this project were the functional hot spots located within the binding site and especially in vicinity to the active site, as they can be critical for the protein's performance. Mutating these residues could potentially improve or disrupt various functional properties, such as catalytic efficiency or substrate specificity. Additionally, HotSpot Wizard can provide predictions on the likelihood of preserving function for all amino acids in *TfCut2*, considering any of the 19 possible substitutions. Since the tool integrates methods such as MSA analysis, FoldX, and Rosetta calculations [322], that were also individually applied within this dissertation, the results of the webserver were not directly used for proposing substitutions. This decision ensures greater transparency and control over the mutation design process, as HotSpot Wizard operates as a somewhat opaque "black box," limiting detailed insight into the origins of its predictions

5.3.2. Selection of residues for mutation

The next step involved selecting the most promising residues for mutation. The catalytic triad was excluded from consideration, as modifications to these residues could disrupt the enzyme's core catalytic mechanism, or even result in a complete loss of enzymatic activity.

Key residues critical for polymer chain binding, located in the P2 region of the binding site, were also excluded from the mutational analysis. These included Y60 and M131,

which form the oxyanion hole, as well as the bulky hydrophobic W155. The proximity of these hydrophobic residues to the catalytic serine enables *TfCut2* to stabilise the polymer chain in a conformation suitable for hydrolysis. Specifically, the NH backbone groups of Y60 and M131 stabilise the carbonyl carbon of the hydrolysed groups, while Y60, M131, and W155 collectively stabilise the aliphatic polymer chain via hydrophobic side-chain interactions. Previous studies have shown that substituting these residues often results in a significant loss of enzymatic activity. For example, the W155F variant of *TfCut2*, despite replacing tryptophan with another aromatic and hydrophobic residue, led to a complete loss of activity against PET [191]. Similarly, the M131A variant exhibited reduced hydrolytic activity on *para*-nitrophenyl butyrate (*p*NPB), highlighting M131's importance for catalytic efficiency. Interestingly, in the same study, the Y60A variant showed slightly enhanced relative activity on *p*NPB hydrolysis, with a neutral effect on tomato cutin degradation [192].

The final selection of residues for mutations was based on the following criteria:

1. Contribution to substrate binding estimated using MM-GBSA calculations (Chapter 4.3.5).
2. Possibility of introducing given substitutions without destabilising the overall structure, evaluated through FoldX ΔG calculations and positional entropy values derived from MSA.
3. Identification of functional hot spots by the HotSpot Wizard webserver through structural and sequential analyses.

Additionally, the residues were selected based on their location within the binding site, to provide feedback on their relevance for catalysis in case of residues in vicinity of the active site or provide verification of hypothesis of importance of P1 and P2 sites for binding.

The region of *TfCut2*'s binding site with the greatest potential for optimisation lies predominantly in the P1 region. Aside from F209, this area lacks bulky hydrophobic residues that could facilitate strong interactions with the polymer chain. HotSpot Wizard further identified several residues within the P1 region as potential functional hot spots, including T61, G62, T63, A65, S66, F209, and N212. Consequently, the following residues within the P1 region were selected for mutation: T61, G62, A65, S66, F209, and N212.

In the P2 region, only Q92 was selected due to its quite significant role in binding according to MM-GBSA and ProLIF results, that could be ameliorated via substitution. This residue is highly solvent-exposed, and ΔG calculations, along with its high entropy value (0.8), suggest that it can be mutated without destabilising the overall structure.

Additionally, two residues closely related to the active site, I178 and T207, were selected (Fig. 40B). I178, a hydrophobic residue, plays a significant role in binding the polymer

chain but may also restrict substrate and water access to the active site. Meanwhile, T207, a small polar residue, is directly linked to catalytic H208 via the backbone, and its mutation could influence catalysis, potentially improving flexibility through substitution to a smaller amino acid.

In summary, residues contributing weakly to binding (such as the small and/or polar T61, G62, A65, S66, Q92, and N212) were selected for mutation, with the aim of enhancing binding via substitution to larger, more hydrophobic amino acids. Additionally, residues with strong binding contributions near the active site (I178 and F209) were selected to explore how different amino acids might impact enzyme performance. Lastly, residues near the catalytic triad, particularly near H208, were targeted for mutation: T207, I178, and F209, to modulate the chemical environment of the active site. Some residues were chosen based on multiple factors. The selected residues and the essential amino acids for *Tf*Cut2 functionality are visualised in Figure 40B, together with estimated per-residue MM-GBSA scores for each Impranil DLN pose (Fig. 40A).

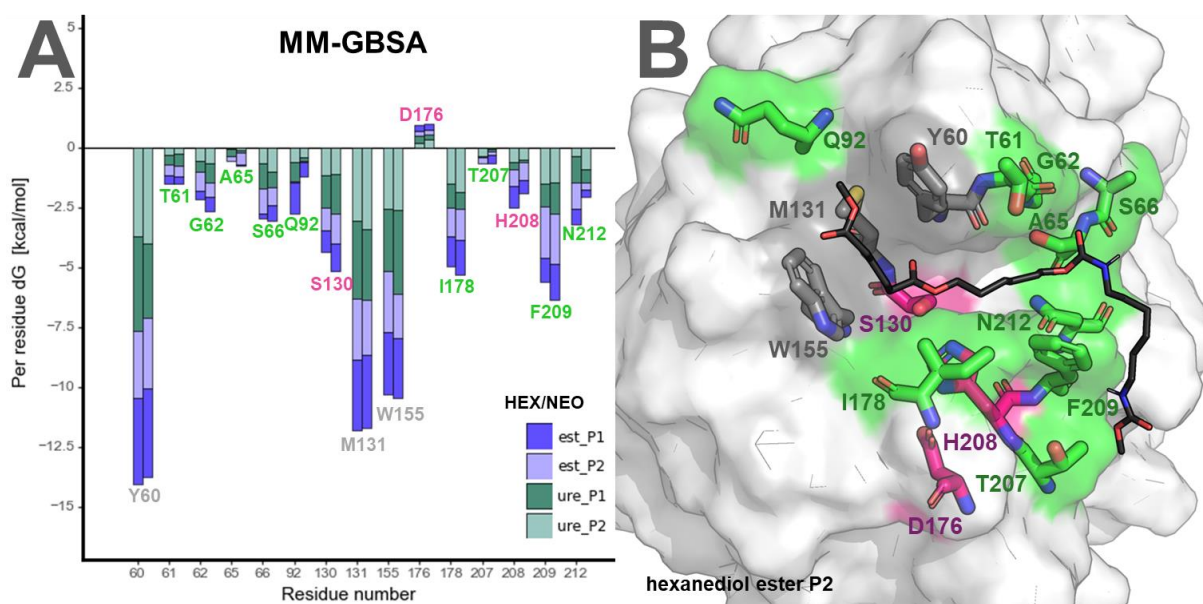


Fig. 40. **A**) Mean per-residue ΔG [kcal/mol] values for selected *Tf*Cut2 residues in complexes with hexanediol (first column) and neopentyl (second column) moieties of Impranil DLN. **B**) Snapshot from an MD simulation frame showing the *Tf*Cut2 complex with hexanediol Impranil DLN in the ester P2 pose, highlighting the location of key residues. Residues are colour-coded as follows: oxanyon hole and aromatic clamp (grey), catalytic triad residues (pink), and binding site residues selected for substitution (green).

5.3.3. Computational protein design of *TfCut2* using a genetic algorithm

The primary objective of this study was to propose mutations that enhance the binding of Impranil DLN to *TfCut2*. To achieve this, Rosetta suite [266,293], with its all-atom ref2015 scoring function [288], was employed to evaluate both total and interface scores of *TfCut2*-Impranil DLN complexes. To systematically explore potential mutations in the *TfCut2* binding site and optimise its interaction with Impranil DLN, a custom genetic algorithm was applied. This algorithm was integrated with Rosetta's protein design module via PyRosetta [325], a Python-based implementation of Rosetta functionalities. The selected in previous step nine residues of the *TfCut2* binding site—T61, G62, A65, S66, Q92, I178, T207, F209, and N212, were targeted for mutation using this algorithm.

In this approach, each mutant sequence was encoded as a “chromosome” within the genetic algorithm population, enabling systematic exploration of substitutions at these residues. The genetic algorithm was initialised with the wild-type *TfCut2* sequence at these positions and incorporated sequences from a MSA to account for evolutionary favoured substitutions as input seed. Protein design was performed on eight different *TfCut2*-Impranil DLN models, each representing a single repeating unit of the polymer, enabling tailored optimisation for specific ligand poses. This strategy facilitated the identification of mutations aimed at improving the enzyme's binding affinity and catalytic efficiency, demonstrating a robust method for rational enzyme design using computational tools.

The fitness function of the genetic algorithm was designed to optimise the binding affinity of *TfCut2* for Impranil DLN. The function was defined as:

$$Fitness = -1 \times (Total_{mut} - Total_{WT}) - 50 \times (I_{mut} - I_{WT})$$

Where:

- $Total_{mut}$ - total score of the mutant protein-ligand complex
- $Total_{WT}$ - total score of the wild-type complex
- I_{mut} - interface score between the mutant protein and ligand
- I_{WT} - interface score of the wild-type complex

The coefficient (50) in the fitness function highlights the significance of the interface score in evaluating the fitness of each mutant, as the function prioritised mutants with improved interface score. For each of the eight poses of Impranil DLN, the genetic algorithm ran for 50

generations with a population size of 100, yielding 5000 mutant complexes per pose. Each mutant complex was evaluated using both total and interface scores, as presented in Figure 41, which shows the generated mutants across each Impranil DLN pose. This genetic algorithm framework enabled an extensive exploration of the energetic landscape surrounding initial *Tf*Cut2-Impranil DLN poses, introducing mutations and repacking sidechains. Black stars in Figure 41 represent the initial wild-type complex poses as reference points; mutants positioned below these stars have lower interface scores, making them promising candidates for further analysis. The results from Rosetta protein design required evaluation based on both interface and total scores of the variants and prediction of structural adjustments that could improve polymer binding. Given that the primary goal of these mutations was to enhance *Tf*Cut2's binding affinity to the polymer chain, the genetic algorithm prioritised lower interface scores, even with a slight compromise in total score. This approach supports the identification of variants with potentially improved catalytic interactions with Impranil DLN.

The distribution of data points in Fig. 41 reveals two clusters across all poses. The clusters on the right contain mutants with significantly higher total scores than the wild-type, making them less favourable due to potential destabilisation. Consequently, mutations were selected from the clusters with lower total score and the lowest interface scores.

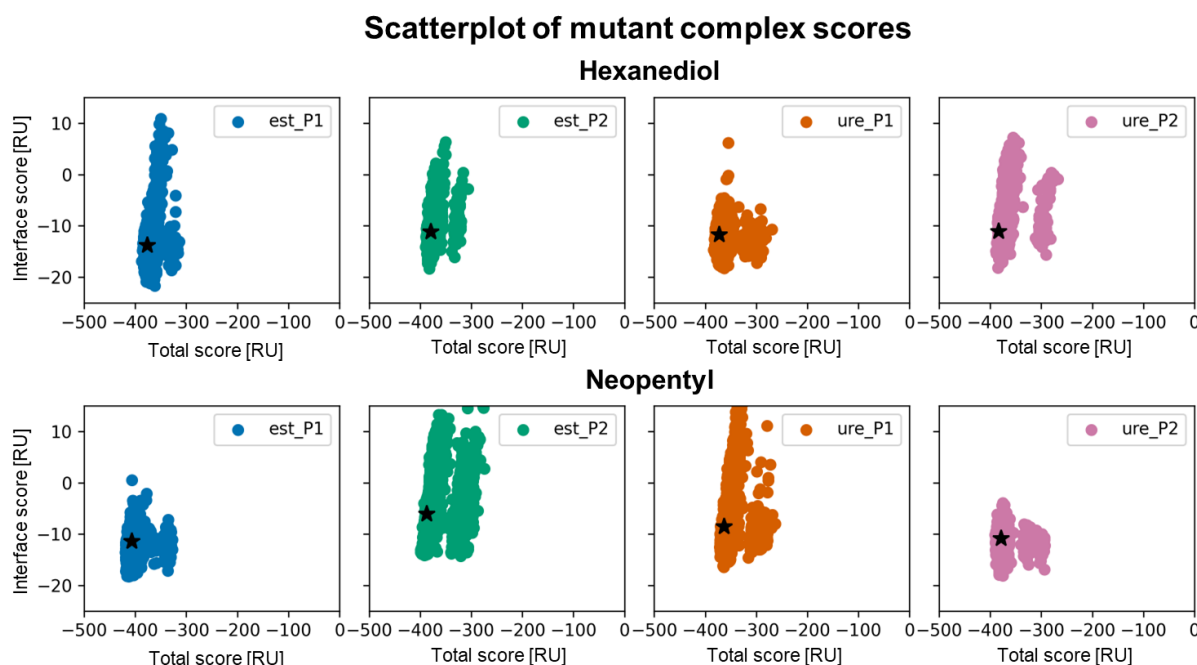


Fig. 41. Scatter plot of scores (interface vs total) of generated mutant *Tf*Cut2-Impranil DLN complexes in the Rosetta combined with genetic algorithm approach. Each graph displays 5000 mutants for a specific Impranil DLN pose. Black stars indicate the initial *Tf*Cut2 wild-type complex with Impranil DLN in the corresponding pose. The calculated scores are in Rosetta Units (RU).

To understand the bifurcation of data points, the 50 mutants with the lowest interface score from the high-total-score clusters (in the right clusters in plots Figure 41) were examined. These complexes, shown in Figure 42A, were identified as containing the T61P substitution, which contributed to the observed bifurcation in scores. Figure 42B presents a logo plot displaying the relative frequency of each amino acid substitution across these mutants, underscoring that the T61P mutation resulted in unfavourable total scores of the *Tf*Cut2-Impranil DLN mutant complexes, despite low interface scores. According to FoldX calculations (Chapter 5.3.1), the ΔG of T61P mutant is 7.2 kcal/mol, indicating strongly destabilising effect. These findings suggest that T61P is not a favourable mutation and should be discarded.

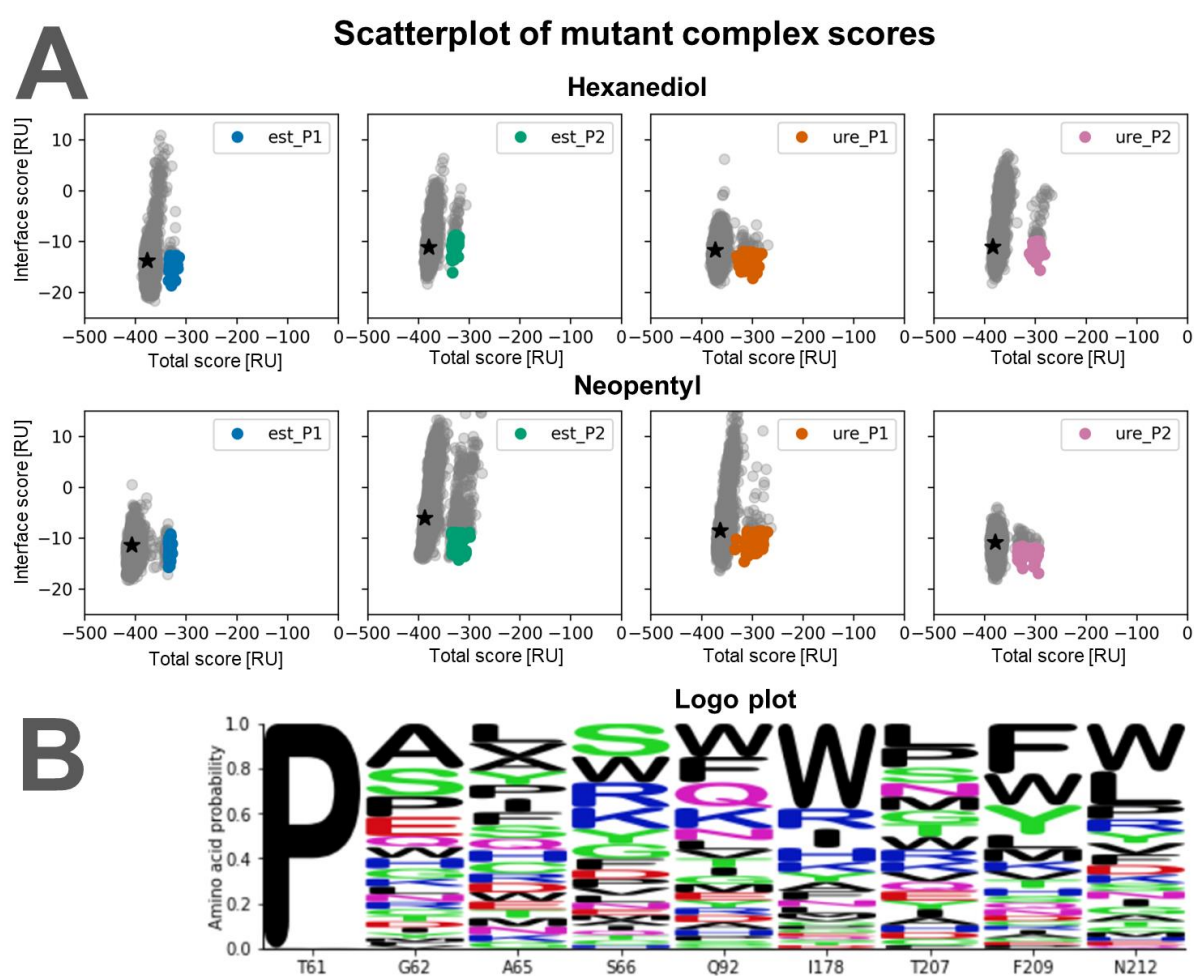


Fig. 42. **A)** Scatter plot of scores (interface vs total) of generated mutant *Tf*Cut2-Impranil DLN complexes in the Rosetta combined with genetic algorithm approach, displaying 5000 mutants for each Impranil DLN pose (grey points) with black stars representing the initial *Tf*Cut2 wild-type complex in each pose. Colourful points indicate the 50 lowest interface-score mutants from the higher-total-score clusters. **B)** Logo plot of selected mutants from each pose, showing amino acid frequency at each position.

To identify promising substitutions, the 50 mutants with the lowest interface scores (and lowest total scores) were selected for each pose of Impranil DLN (Fig. 43). These 400 complexes (50 mutants across 8 poses) represent the best candidates for further analysis based on their sequences.

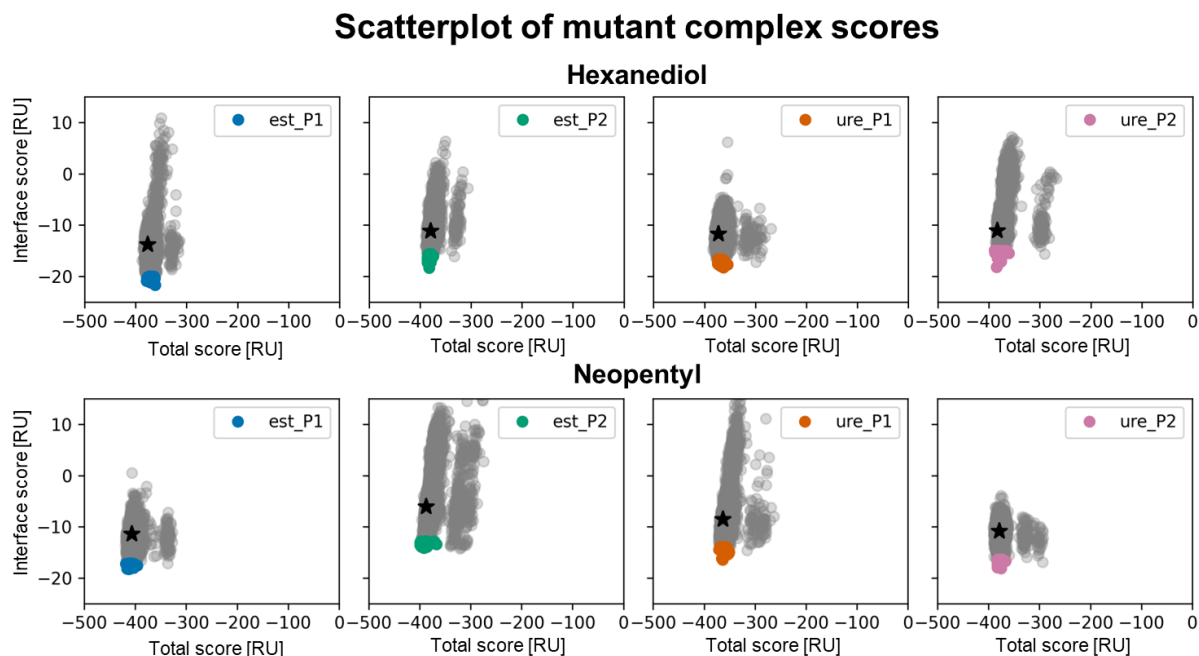


Fig. 43. Scatter plot of scores (interface vs total) of generated mutant *TfCut2*-Impranil DLN complexes in the Rosetta combined with genetic algorithm approach. Each graph displays 5000 mutants per Impranil DLN pose (grey points). Black stars represent the initial wild-type complex, and colourful points highlight the 50 mutants with the lowest interface scores from the clusters with lower total scores.

Logo plots were generated to visualise the frequency of each amino acid substitution. Figure 43A presents a logo plot compiled from all 400 selected mutants, and Figure 43B provides logo plots for each pose individually.

Rosetta frequently suggests introducing tryptophan to residues at positions G62, S66, Q92, I178, F209, and N212 (Fig. 44). At F209, the substitution to tryptophan (F209W) might not significantly impact enzyme properties, as it involves replacing one aromatic, hydrophobic, bulky amino acid with another of similar nature, though slightly larger. However, tryptophan substitutions at other positions could potentially destabilise the enzyme, restrict substrate access to the active site, or even reduce enzymatic activity. Such substitutions should be approached with caution, as Rosetta's recommendations arise from its tendency to tightly fit amino acid side chains around the ligand to enhance binding [326], potentially at the expense of overall stability or accessibility. Selecting mutations from these data proved challenging, especially given that eight different Impranil DLN binding poses were considered, with Rosetta

genetic algorithm run for each complex separately. This workflow optimised mutants to best accommodate each specific pose of Impranil DLN. As a result, there is limited sequence consistency across poses and no consensus sequence can be selected. However, the results of experimental evaluation may indicate which pose of Impranil DLN is more probable in solution, as if a given mutation that interferes with a given pose will cause loss of activity, it may indicate that this particular pose is preferable.

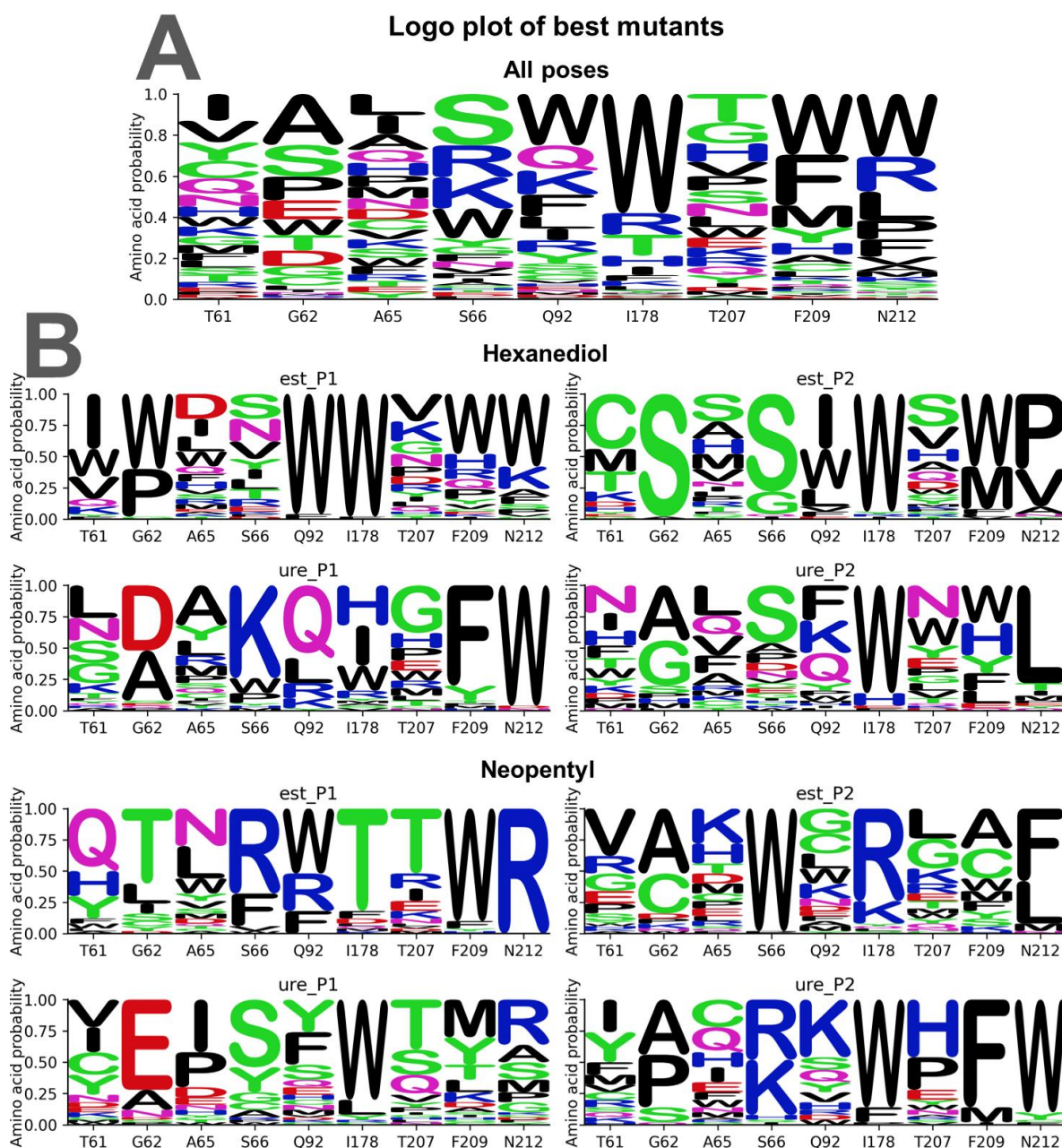


Fig. 44. Logo plots for the best mutant complexes: A) combined for all poses; B) individually per pose.

A more straightforward design workflow would ideally involve a single complex, allowing the binding site to be optimised specifically for one substrate pose. Impranil DLN binding exhibits a high degree of positional flexibility across the *TfCut2* binding site, with the exception of regions near the catalytic residues and the aromatic clamp (Y60–W155). In these areas, the ligand consistently adopts specific binding poses, indicating a strong preference for these positions. However, beyond these regions, the polymer chain interacts variably with different residues in the binding site, adopting diverse conformations.

The following chapter outlines the final selection of single-point mutants, integrating Rosetta results with additional software analysis.

5.3.4. Rationale for proposed mutations and expected influence on *TfCut2* performance

Rosetta protein design with implemented genetic algorithm played a pivotal role in guiding the mutation selection process by identifying substitutions that could enhance ligand binding. Due to the variability among poses, identifying a single consensus sequence proved challenging. However, several promising mutations were identified for individual poses of the ligand. Since the fitness function of the genetic algorithm was focused on favouring mutants with improved interface scores, rather than total scores, to avoid proposing destabilising mutations, the information about ΔG calculated by FoldX in previous steps, was also incorporated.

Additionally, occurrences of specific amino acids at target positions in the MSA were considered to prioritise evolutionarily viable substitutions (Fig. 45). For instance, mutations such as G62A, A65S, Q92Y, I178V, I178T, T207D, T207G, T207S, F209L, F209S, and N212M, which appear in the MSA, were deemed worth exploring. Many of these substitutions were also supported by Rosetta predictions, underscoring their potential to enhance binding affinity without compromising protein integrity.

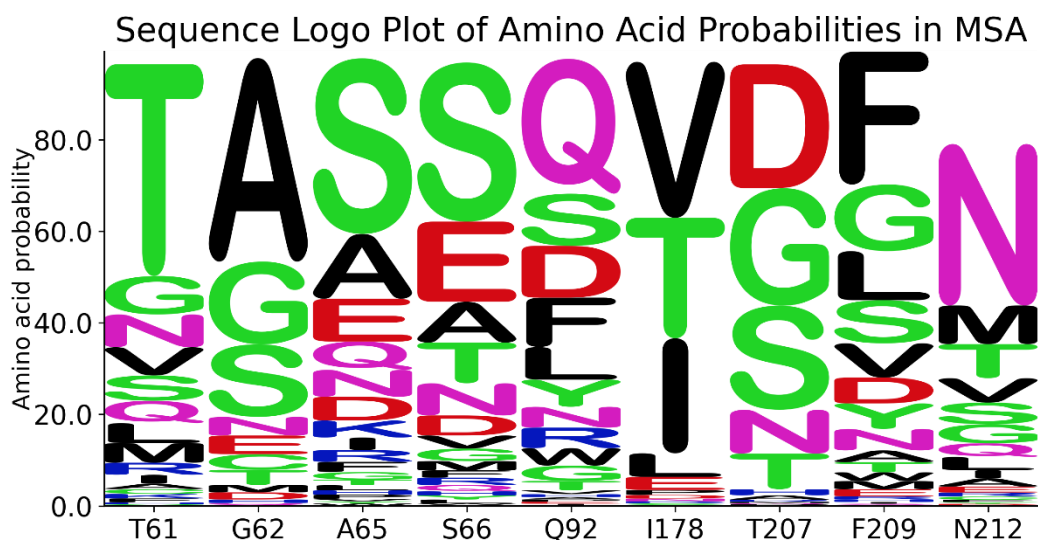


Fig. 45. Sequence Logo Plot of amino acid probabilities in MSA positions mapped to the selected positions in *TfCut2* sequence, generated by analysis with BALCONY R library.

The selection process for identifying suitable mutations was complex and iterative, involving multiple computational evaluations. While it is challenging to provide a detailed step-by-step description within the scope of this dissertation, the key findings and the rationale behind the selected mutations are presented.

The detailed summary of the rationale behind each substitution is listed in Table 8:

Table 8. Detailed rationale behind each selected single-point mutation. The column “Proposed by Rosetta” indicates if a given mutation was proposed via Rosetta with genetic algorithm and for which Impranil DLN poses. Column “Observed in MSA” indicates if a given mutation could be found on this position within MSA within probability of at least 5%.

Residue	Mutation	Rationale	Proposed by Rosetta	Observed in MSA
T61	T61V	Hydrophobic substitution for stronger substrate binding	Hex: eP1 Neo: eP2, uP1, uP2	Yes
G62	G62A	Enhances binding with slightly larger residue	Hex: uP1, uP2 Neo: eP2, uP1, uP2	Yes
	G62Y	Strengthens hydrophobic interactions	No	No
A65	A65L	Improves hydrophobic binding	Hex: eP1, eP2, uP1 Neo: eP1	No
	A65S	Adds polar interactions along the binding groove	Hex: eP2	Yes
	A65Y	Larger residue with dual hydrophobic/polar properties	Hex: eP1, uP1	No

S66	S66F	Larger hydrophobic residue for stronger binding	Neo: eP1	No
	S66V	Small hydrophobic substitution for enhanced interaction	Hex: eP1	No
	S66Y	Larger residue with dual hydrophobic/polar properties	Hex: eP1 Neo: uP1	No
Q92	Q92Y	Enhances substrate binding with hydrophobic property	Neo: uP1	Yes, rare
	Q92W	Bulky hydrophobic residue for strong interactions	Hex: eP1, eP2 Neo: eP1, eP2	Yes, rare
I178	I178A	Small residue to improve flexibility near the active site and access to it	No	No
	I178L	Similar size for hydrophobic interactions	Neo: uP1	Yes
	I178V	Smaller hydrophobic residue for slight interaction shift	No	Yes
	I178T	Polar residue to balance water access and binding	Neo: eP1	Yes
T207	T207G	Increases flexibility around H208	Hex: uP1, uP2 Neo: eP2	Yes
	T207D	Larger, acidic substitution for altered interactions	Hex: eP2	Yes
	T207S	Conserves existing interactions near catalytic histidine	Hex: eP2 Neo: uP1	Yes
F209	F209L	Reduces bulk while maintaining hydrophobicity	Hex: uP2	Yes
	F209S	Introduces polar element to facilitate product release	No	Yes
	F209W	Bulkier aromatic for stronger binding	Hex: eP1, eP2, uP2 Neo: eP1, eP2	No
N212	N212A	Small hydrophobic residue for stable binding	Neo: uP1	No
	N212M	Larger residue to strengthen binding	Hex: uP2 Neo: eP2, uP1	Yes

	N212F	Bulky hydrophobic residue for enhanced substrate binding	Neo: eP2	No
--	--------------	--	----------	----

The 24 single-point mutations are strategically designed to enhance various aspects of *TfCut2*'s interaction with Impranil DLN. These selected mutations target specific functional goals to improve binding, stability, or catalytic efficiency. Below is a breakdown of each category along with individual mutations:

- **Enhancing Hydrophobic Interactions:** Substitutions introducing larger or more hydrophobic residues are intended to strengthen contacts with the hydrophobic polymer chain of Impranil DLN. Notable mutations include G62Y, A65L, A65Y, S66V, and N212F, all of which aim to reinforce hydrophobic binding interactions.
- **Increasing Flexibility and Water Access:** Smaller residues, such as I178A and T207G, are introduced near the active site to improve flexibility and potentially allow better water accessibility, which may facilitate substrate processing and product release.
- **Optimising Catalytic Efficiency:** Mutations near catalytic residues, like F209L and T207S, were selected to either maintain or subtly modify binding interactions, potentially influencing the enzyme's catalytic rate.

In addition to the single-point mutants, several multi-point mutants were proposed based on favourable combinations of single substitutions that were identified in Rosetta's mutant sets. These combined mutants include:

- G62A/A65L/S66F/Q92W
- G62A/A65L/S66F/Q92Y
- G62A/A65L/S66Y
- G62A/A65S/S66Y
- I178T/T207G

5.4. Conclusions

This dissertation aimed to re-design the substrate binding site of *TfCut2* to enhance its interaction with Impranil DLN. Achieving this objective involved first modelling, investigating, and analysing protein-ligand interactions, as detailed in Chapter 4. Building on these insights, Chapter 5 focused on proposing specific mutations to improve ligand binding and catalytic efficiency.

The mutability and suitability of introducing substitutions to *TfCut2* were systematically evaluated using several computational tools. The impact of single mutations on protein stability was assessed using FoldX, evolutionary variability of each residue was verified by analysing MSA, and functional hot spots were identified using HotSpot Wizard. These analyses helped prioritise nine key positions in the binding site: T61, G62, A65, S66, Q92, I178, T207, F209, and N212. These residues were chosen for their potential to improve binding mainly through enhanced hydrophobic interactions or steric complementarity with the polymer chain, or their potential to ameliorate the catalytic efficiency of *TfCut2* in Impranil DLN degradation. Subsequently, protein design focusing on improving the ligand binding was performed using Rosetta combined with genetic algorithm. Lastly, findings of all these approaches were analysed to propose a library of *TfCut2* mutants.

The mutation-selection process combined computational analyses with visual inspection to ensure the rational design of variants. As a result, 24 single-point mutants and 10 multiple mutants were proposed for further evaluation. These mutants represent promising candidates for improving the enzyme's affinity for Impranil DLN and catalytic performance. The detailed evaluation of these mutants is presented in Chapter 6.

Chapter 6: Evaluation of proposed *TfCut2* mutants

6.1. Introduction

Combining experimental validation with computational evaluation offers a comprehensive understanding of how specific mutations influence enzyme function. In this chapter, the focus is on evaluating *TfCut2* mutants proposed in the previous chapter, addressing the third objective of this dissertation: *Computational and experimental evaluation of TfCut2 mutants*.

The proposed mutations are strategically located in the binding site of *TfCut2*, with the aim of improving ligand binding affinity and potentially enhancing catalytic efficiency. These mutations were selected based on their potential to optimise interactions between the enzyme and Impranil DLN, either by strengthening binding interactions or by influencing key residues involved in catalysis. By focusing on the enzyme's binding site, we aim to achieve more efficient degradation of the polymer substrate. Additionally, characterising these modifications will deepen our understanding of how targeted mutations influence enzyme activity and stability, providing valuable insights for advancing enzymatic polymer degradation strategies.

This evaluation seeks to address the broader challenge of enhancing enzymatic efficiency and stability for the degradation of complex polymers like Impranil DLN. This substrate presents unique difficulties due to its heterogeneous composition, mixed bond types (ester and urethane), and undefined structural properties. Effective degradation requires not only strong binding and catalytic activity but also a balance between structural stability and flexibility to accommodate large, dynamic polymer chains. Understanding how specific mutations affect these factors is crucial for designing more efficient polymer-degrading enzymes. To comprehensively evaluate the proposed mutations, this dissertation employs a combination of computational and experimental approaches to assess their effects on both enzyme structure and function.

Additionally, the structure of Impranil DLN after hydrolysis by wild-type *TfCut2* was analysed using NMR studies. This analysis complemented the structural study of Impranil DLN itself and helped confirm which bonds were hydrolysed by *TfCut2*.

To computationally assess the impact of mutations on the enzyme structure, the energetic effects of each mutation were evaluated by computing ΔG using Rosetta's all-atom scoring function. To complement the structural analysis, MD simulations were conducted to evaluate the structural stability and flexibility of *TfCut2* mutants in their ligand-free forms. These simulations focused on identifying any disruptions to the enzyme's tertiary structure or increased structural fluctuations introduced by the mutations.

While improving thermal stability was not the primary objective of this study, experimentally verifying the structural integrity of the mutants was crucial. To ensure that the mutations did not destabilise the structure of the *TfCut2* mutants, the melting temperature (T_m) was measured using nanoDSF, a differential scanning fluorimetry (DSF) technique. T_m value provides key insights into a protein's structural stability and rigidity. A higher T_m value typically indicates a well-organised core with strong hydrogen bonds, hydrophobic interactions, and ionic forces, helping the protein maintain its folded, functional state at elevated temperatures [235,327]. Lower T_m values, on the other hand, suggest a protein is more prone to denaturation when temperature increases, which could compromise its function. Given that even few mutations can impact thermal stability [236], T_m value serves as an important indicator of whether proposed mutations affect structural integrity of the enzyme. Thermally stable proteins are valuable for several reasons, including their potential to enhance the efficiency of industrial processes and to provide insights into the mechanisms of protein folding and stabilisation [328]. However, in case of the polymer-degrading cutinases, increasing rigidity is not always beneficial, as loss of flexibility in the binding site region could impede the incorporation and binding of large polymer substrates, a process that typically requires a dynamic binding site [235].

Subsequently, it was important to assess information about influence of the mutations on the binding of Impranil DLN in different poses. To evaluate the influence of mutations on the binding of Impranil DLN, mutations were inserted into all eight modelled *TfCut2*-Impranil DLN complexes containing different ligand poses that were selected through the pipeline described in Chapter 4. For this, Rosetta was used, which allowed to simultaneously score these constructs in terms of total and interface scores. The scores of the mutant-ligand complexes revealed information about both the ΔG of the total complex and the ΔG of the protein-polymer interface. The interface score specifically reflects the protein-ligand interaction energies, highlighting how each mutation may influence binding affinity and interaction quality.

For the experimental evaluation of Impranil DLN degradation by *TfCut2* and its mutants, degradation was tracked by monitoring the reduction in turbidity, a simple and measurable indicator of enzymatic degradation progress. Schmidt et al. [20] utilised this property to compare the degradation efficiency of Impranil DLN by several cutinases (namely *TfCut2*, LCC, *Tcur1278* and *Tcur0390*), applying a kinetic model proposed by Mukai et al. [195]. While this model provides a valuable framework for heterogeneous substrates, its applicability to Impranil DLN is limited due to significant differences in substrate composition and behaviour. The P[(R)-3HB] films studied by Mukai et al. consisted of uniform monomeric units, enabling assumptions like a constant absorption coefficient independent of chain length. In contrast, Impranil DLN poses several challenges [107] such as: 1) undefined composition: the precise chemical structure, proportions of structural units, and presence of additives (e.g., chain extenders or plasticisers) in Impranil DLN are not known; 2) mixed bond types: Impranil DLN contains both ester and urethane bonds, complicating the interpretation of degradation rates and spectrophotometric changes; and 3) uncertain absorption changes: it is unclear which specific bonds are cleaved during degradation and to what extent these cleavages influence the observed spectrophotometric changes.

Given these limitations, the Mukai et al. [195] model cannot be directly applied to Impranil DLN. Instead, enzymatic activity in this study was evaluated using initial degradation rates to compare the activity of different *TfCut2* variants. Although this approach does not yield kinetic constants like k_{cat} and K_m , it provides a practical means to assess relative enzymatic efficiencies under the constraints of an undefined and heterogeneous substrate. The initial degradation rates of *TfCut2* mutants, relative to the wild-type enzyme, can provide insights into whether the mutations enhance or diminish catalytic efficiency. Turbidity reduction was monitored by measuring optical density at 400 nm (OD_{400}) at regular time intervals. The hydrolysis rates were determined from the linear portion of the OD_{400} decrease over time. It is crucial to assess only the initial degradation rates, as enzyme activity may decline over time, potentially skewing the results.

While this turbidimetric method is not ideal, it was chosen because of the challenges associated with the heterogeneity of the Impranil DLN structure. Hydrolysis of ester bonds alone can produce several products, including 1,6-hexanediol, neopentyl glycol, adipic acid, and partially degraded polymer fragments. Even if every ester and urethane bond were hydrolysed, the resulting mixture would still consist of four distinct product molecules: 1,6-hexanediol, neopentyl glycol, adipic acid, and hexamethylene diamine. Despite its

limitations, the turbidimetric assay is used in this dissertation as an effective indicator of initial degradation rates, which in turn serves as a comparable measure of the catalytic efficiency of *TfCut2* mutants in Impranil DLN degradation. Lastly, this chapter summarises the effect of mutations on protein dynamics, stability, and binding to Impranil DLN, as assessed through computational and experimental approaches. By integrating these complementary methods, the study provides a holistic understanding of the molecular mechanisms at play. Although direct measurements of catalytic mechanisms were not performed, indirect insights into enzymatic efficiency were inferred from degradation rate comparisons. These findings highlight the value of combining predictive computational tools with experimental validation to evaluate *TfCut2* mutants, particularly for improving the enzymatic degradation of synthetic polymers like Impranil DLN.

6.2. Methodology

6.2.1. Computational methods

Generation of mutant structures and complexes with Impranil DLN

To investigate the structural ligand binding impact of specific mutations on *TfCut2*, 3D structures models of mutants were generated using PyRosetta [325], Python-based implementation of the functions from Rosetta [266,293]. For the mutants without the ligand, the native *TfCut2* structure (prepared as described in Chapter 4.2.: Proteins preparation) served as a template, and mutations were introduced sequentially based on a predefined list. For the systems of *TfCut2* in complex with Impranil DLN, the first of the 10-frames selected after k-means clustering of MD simulations, as described in previous subsections, were used as *TfCut2* wild-type with Impranil DLN in initial complexes.

For each mutation, side-chain conformations were optimised using a *TaskFactory* paired with *PackRotamersMover*, maintaining the backbone configuration while accommodating new side-chain orientations. Following mutation introduction, the structures were refined using the *FastRelax* protocol, a PyRosetta method that minimises structural strain and optimises interatomic interactions within the modified regions. This relaxation step provided a stable conformation for each mutant by exploring local conformational space and minimising energy. The all-atom energy scoring function *ref2015* [288] was applied to evaluate the structures throughout the protocol. Monte Carlo minimisation was incorporated

to further refine the structures, enhancing stability by sampling various low-energy conformations. For mutants with anticipated interaction interfaces, such as those involving ligand binding, the *InterfaceAnalyzerMover* assessed changes in interaction energy, highlighting mutations' potential effects on binding properties. The finalised mutant structures were saved as PDB files. This protocol allowed for the systematic generation of a library of mutant structures, preserving the structural integrity of *TfCut2* while capturing the effects of targeted substitutions.

MD simulations of unbound TfCut2 mutants

The wild-type *TfCut2* and mutant structures were prepared using a custom PyRosetta script [325] to insert mutations, as described in the previous subsection. Crystallographic water molecules from the 4CG1 structure were retained, ensuring that there were no atomic clashes due to slight conformational differences resulting from the packing and Rosetta *FastRelax* process. This also accounted for a potential overlap between substituted residues and the original placement of crystal water molecules. Additionally, two Ca^{2+} ions were incorporated at each divalent-metal binding site within the structure.

To prepare the system for simulation, the *LeaP* tool from AmberTools18 [286] was employed. *LeaP* was used to add the necessary counterions to neutralise the system and to solvate the model in a 20 Å octahedral box of TIP3P water molecules.

MD simulations of apo *TfCut2* mutants were conducted following the same protocol outlined in Chapter 4.2: MD simulations. Each *TfCut2* mutant and wild-type were simulated in 10 replicas for 50 ns.

6.2.2. Experimental methods

NMR spectra analysis of Impranil DLN samples after TfCut2 wild-type and HCl acidic hydrolysis

Enzymatic hydrolysis was performed in 10 mL of M9 minimal salts (30 g/L Na_2HPO_4 , 15 g/L KH_2PO_4 , 2.5 g/L NaCl , 5 g/L NH_4Cl .) containing *TfCut2* at a concentration of 4 µg/mL. Impranil concentration in the reaction mixture was 1%. The solution was incubated at 37 °C and 150 rpm for 24 hours, cooled and stored at 4°C until used for hydrolysis product extraction.

For hydrolysis in acidic environment, 1ml of Impranil DLN suspensions were exposed to 3ml of 0.1 M HCl. The reaction was heated to 65 °C for 24 h and then allowed to cool

to room temperature. The reactions were centrifuged (14,000 rpm, 45 min) and the supernatants were separated from the Impranil pellets and used for further analytical characterisation.

To confirm the structure of the Impranil DLN, NMR spectroscopy was used: ^1H and ^{13}C NMR. ^1H and ^{13}C NMR spectra were recorded on a Varian 600 MHz spectrometer, using the following deuterated DMSO.

The spectra of Impranil DLN before hydrolysis were prepared as described in Chapter 4.2.2.

Cloning of TfCut2 into pET-20b(+) for protein production

The *TfCut2.KW3* sequence (PDB: 4CG1_A) without the secretion signal peptide was converted to gene encoding sequence and adapted to the codon bias of *E.coli* using EMBOSS Backtranseq (<https://www.ebi.ac.uk/jdispatcher>). The resulting gene sequence was synthesised and ligated into the expression vector pET-20b(+) between *NcoI* and *XhoI* restriction sites by GenScript. The final pET-20b(+) construct containing the *TfCut2.KW3* gene, the pelB leader sequence, a 6xHis tag, and the TEV protease cleavage site sequence was cloned into *E.coli* BL21(DE3).

Mutagenesis of TfCut2-containing plasmid

Site-directed mutagenesis of the *TfCut2* was performed with Q5® Site-Directed Mutagenesis Kit (New England Biolabs) following manufacturer's recommendations. I178T/T207G mutant was obtained using NEBuilder HiFi DNA Assembly Kit (New England Biolabs). The mutagenic primers were designed using NEBaseChanger®. The sequences of mutated plasmids were confirmed by DNA sequencing.

Production of TfCut2 and mutants

The cells containing the desired plasmids were grown individually in 50-100 mL of Lysogeny broth supplemented with 100 $\mu\text{g}/\text{mL}$ ampicillin. When the absorbance of the culture at 600 nm reached 0.5-0.7, the protein production was induced by the addition of isopropyl-1-thio- β -D-galactopyranoside (IPTG) at a final concentration of 0.4 mM. After induction, the culture was grown at 37 °C for 2.5-3.5 hours, and cells were harvested by centrifugation and washed with phosphate-buffered saline.

TfCut2 was purified from the periplasmic cell fraction separated by exploring the osmotic shock treatment. The periplasmic fraction was obtained as follows. The washed cell pellet was resuspended in the hypertonic solution (20 mM Tris-HCl buffer, pH 8.0, 25%

(w/v) sucrose and 1 mM ethylenediaminetetraacetic acid (EDTA)) and incubated on ice for 30 min. Then, cells were centrifuged, resuspended in cold deionised water and incubated on ice for 30 min. After incubation, cells were harvested by centrifugation. The supernatant obtained was the periplasmic fraction. 1M Tris-HCl, pH 8.0, was added to the periplasmic fraction to a final concentration of 20 mM, and the resulting TfCut2-containing solution was kept at -20 °C until use.

Purification of TfCut2 and mutants

Purification of TfCut2 variants was performed by immobilised metal ion affinity chromatography (IMAC) using Protino® Ni-NTA slurry (Macherey-Nagel). The periplasmic cell fractions were thawed and supplemented with NaCl and imidazole to final concentrations of 300 mM and 5 mM, respectively. Then, 75 µL of pre-equilibrated Ni-NTA slurry were mixed with the protein solution at room temperature for 1-2 hours with gentle rotation.

After binding, the resin was transferred to spin columns and washed four times with 750 µL of binding buffer to remove nonspecifically bound contaminants. Proteins were then eluted with 30 µL of elution buffer (20 mM Tris-HCl, pH 8.0, 300 mM NaCl, 250 mM imidazole).

An aliquot of 100 µL of the eluate was used for imidazole removal and buffer exchange to 10 mM Tris-HCl, pH 7.4 using Bio-Spin® 6 columns (Bio-Rad). The purified proteins were analysed for activity in Impranil degradation assays and by SDS-PAGE to confirm purity. Protein concentrations were determined by Bradford assay. Purified proteins were aliquoted and stored at -20 °C until use.

Primary screening for Impranil DLN hydrolysis activity

To assess the Impranil DLN-degrading activity of TfCut2 and its mutants during protein extraction and purification, a primary screening was performed using agarose plates containing 0.5% Impranil DLN in M9 minimal salts.

Aliquots taken at different steps of the protein purification were spotted onto agarose gel and incubated at 37°C. Zones of clearance appeared at the applied fractions indicated enzymatic activity against Impranil DLN. This method enabled a rapid, qualitative assessment of hydrolytic activity under standard conditions.

Thermostability assessment using nanoDSF technology

Tfcut2 variants were tested for thermostability in 20 mM Tris-HCl buffer at pH 7.5 using Prometheus NT.48 (Nano Temper Technologies). The total protein concentration

in the sample was 100 $\mu\text{g}/\text{mL}$. Each *TfCut2* variant was tested in duplicate. The temperature change ranged from 20 to 95 C with a 1°C step. The thermal unfolding transition midpoint T_m (°C) was calculated from the ratio of tryptophan emission at 330 and 350 nm.

Measurement of initial degradation rates of Impranil DLN

TfCut2 variants were screened for activity in Impranil hydrolysis using a turbidimetric assay. The samples with a final volume of 200 μL were prepared in 96-well plates containing M9 minimal salts as a buffer and partially purified *Tfcut2* at a concentration of 1.5 $\mu\text{g}/\text{mL}$. The reaction was started by the addition of Impranil at a final concentration of 0.1%. The decrease of the turbidity was monitored for 30 min by measuring the optical density at 400 nm at constant time intervals of 30 s at room temperature. The hydrolysis rates were determined from the linear part of the graphs of the decreasing OD₄₀₀ over time. All determinations were performed in at least two independent experiments.

6.3. Results and discussion

6.3.1. *TfCut2* mutants structure and stability

This section evaluates the stability, structure and dynamics of the proposed mutants and presents the findings from the computational and experimental approaches. The analysis includes: 1) computational assessments, comprising $\Delta\Delta G$ calculations of the mutants in their free form and MD simulations to evaluate dynamics and flexibility; and 2) experimental determination of T_m to assess structural stability.

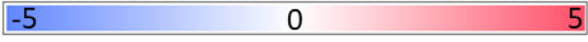
Unbound TfCut2 mutants ΔG

To construct and evaluate the ΔG of 24 single-point and five combined mutants, a custom PyRosetta [266,293,325] script was employed. This script not only facilitated the creation and scoring of mutant structures but also generated initial structures for MD simulations, described in the subsequent section. Specifically, the script processed the wild-type *TfCut2* structure by performing an initial relaxation step, introducing the specified mutations, relaxing the mutants again, and finally scoring and saving the resulting structures.

While single-point mutants were previously constructed and scored using FoldX (Chapter 5.3.1) to generate a substitution matrix, the mutants in this analysis were generated using Rosetta to ensure consistency with the Rosetta combined with genetic algorithm protein design process employed throughout this dissertation. The results, summarised in Table 9, reveal that many of the constructed mutants exhibited higher total scores than the wild-type *TfCut2*. This outcome aligns with the design objective of optimising the interface score and improving ligand interactions, occasionally at the expense of a slight decrease in overall structural stability (as indicated by higher total scores). Among the single-point mutants, the most favourable total scores were observed for A65S, T207D, and N212F, with relative energy differences of -1.14 RU, -1.11 RU, and -1.42 RU, respectively, compared to the wild-type. Conversely, the least favourable ΔG was calculated for the T61V mutant, with a relative total energy difference of +8.59 RU. All five combined mutants showed positive ΔG values, indicating reduced overall stability compared to the wild-type.

Table 9. Rosetta-calculated total energies of *TfCut2* mutants generated using a custom PyRosetta script, along with the relative total energies compared to the wild-type *TfCut2* ($\text{total}_{\text{WT}} - \text{total}_{\text{mutant}}$), expressed in Rosetta Units (RU).

Mutant	ΔG Rosetta score [RU]	$\Delta\Delta G$ Rosetta Score [RU]
wild-type	-841.55	0
T61V	-832.95	8.59
G62A	-841.42	0.13
G62Y	-837.36	4.18
A65S	-842.69	-1.14
A65L	-842.31	-0.76
A65Y	-838.32	3.23
S66V	-838.5	3.04
S66F	-838.8	2.75
S66Y	-841.16	0.38
Q92Y	-838.89	2.65
Q92W	-837.91	3.63
I178V	-840.7	0.85
I178A	-838.98	2.57
I178T	-837.83	3.72
I178L	-841.65	-0.1
T207S	-841.03	0.52
T207D	-842.66	-1.11
T207G	-839.59	1.96
F209L	-840.89	0.65
F209S	-842.1	-0.56

F209W	-839.35	2.19
N212A	-840.4	1.15
N212M	-839.8	1.75
N212F	-842.96	-1.42
G62A/A65L/S66F/Q92W	-837.36	4.19
G62A/A65L/S66F/Q92Y	-837.17	4.38
G62A/A65L/S66Y	-835.89	5.66
G62A/A65S/S66Y	-840.07	1.47
I178T/T207G	-836.62	4.92
Legend: 		

Evaluation of mutants dynamics through MD simulations

To evaluate the structural integrity, flexibility and dynamics of the proposed *Tf*Cut2 mutants, MD simulations were performed with the structures constructed in the previous subsection. The analysis of RMSD for the molecular dynamics (MD) simulations demonstrates that *Tf*Cut2 and its mutants generally maintain structural stability, with most systems exhibiting deviations below 2 Å (Fig. 46).

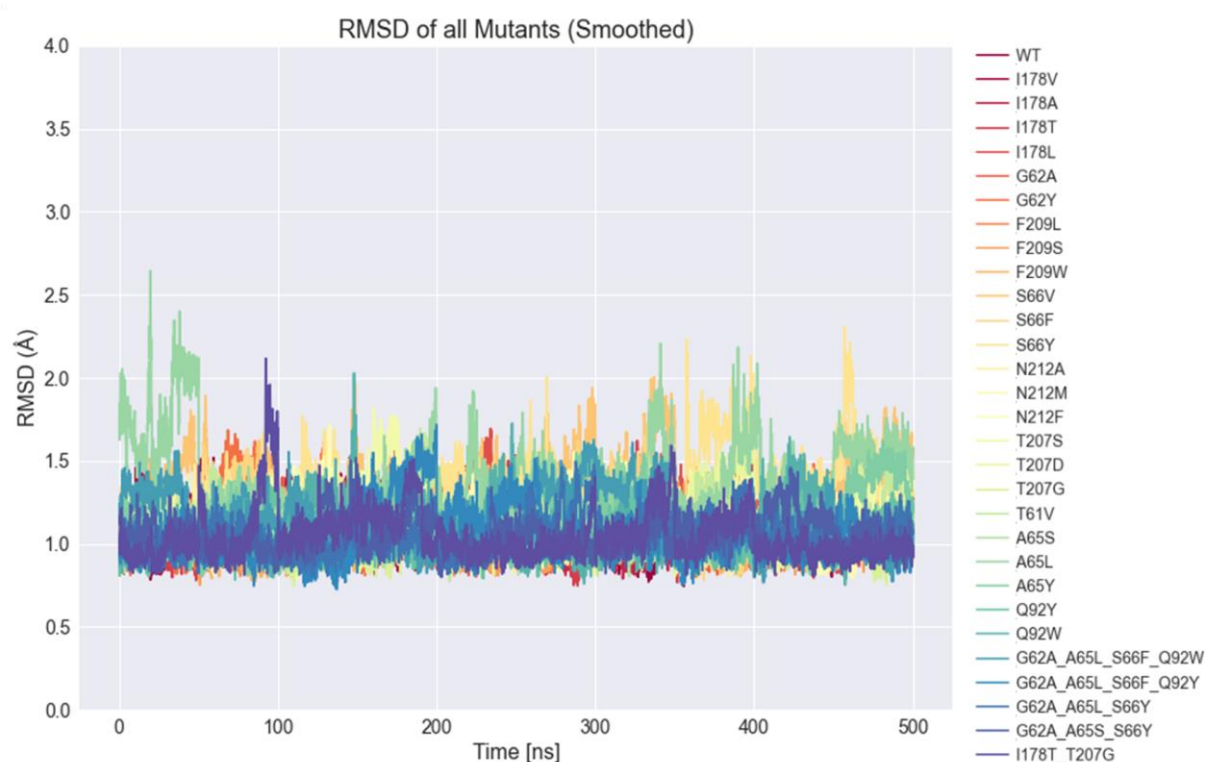


Fig. 46. Superimposed RMSD plots calculated for the C-alpha, C, and N atoms of *Tf*Cut2 and mutants during MD simulations of apo structures. To enhance readability, a moving window average was applied with a window size of 100 frames.

For the wild-type *Tf*Cut2 and most of its mutants, RMSD values remain below 2 Å throughout the MD simulations (Fig. 46). However, certain mutants, including S66V, S66Y,

A65L, exhibit less stable behaviour, with RMSD values occasionally exceeding 2 Å. These observations suggest that specific mutants may exhibit increased structural flexibility and/or reduced stability.

Overall, the fluctuations in mutant structures largely follow patterns observed for the wild-type enzyme. However, when examining the RMSF plots (Fig. 47), it is evident that the regions of *Tj*Cut2, in both the wild-type and mutant structures, exhibiting the greatest variability in RMSF values are: the N-terminal region, binding site regions including loops 58-62, 63-66, 174-180, and helix 209-213, as well as loop 85-92, loop 205-210, and loop 241-251. Higher fluctuations, particularly in loop regions, suggest increased flexibility, which typically arises from weaker stabilising interactions (such as hydrogen bonds and hydrophobic contacts). This flexibility allows these regions to explore a broader range of conformations during the simulations. Consequently, the higher RMSD fluctuations in the binding site of certain mutants may indicate decreased structural stability but increased flexibility, which could potentially enhance their ability to accommodate larger substrates, such as polymer chains.

The loop spanning residues 241-251 exhibits the highest flexibility in the wild-type, apart from the N- and C-terminal regions. Notably, residue D246 is absent in the crystal structure, supporting the observed flexibility in this region [149]. Interestingly, mutant S66Y shows reduced flexibility in the 241-251 region compared to the wild-type, while S66F exhibits increased flexibility in that region. This suggests that substitutions at residue S66 could influence the flexibility of loop 241-251. Additionally, A65L shows increased RMSF values, particularly in binding site regions, including loops 58-62 and 63-66.

Binding site region 58-66 is where high variability in fluctuations can be found, especially in case of the mutants with substitutions at positions: G62, A65 and S66, with A65L exhibiting the strongest fluctuations in that region (Fig. 47). Interestingly, residues 58-66 are in the P1 region, where several functional hot spots have been identified by HotSpot Wizard.

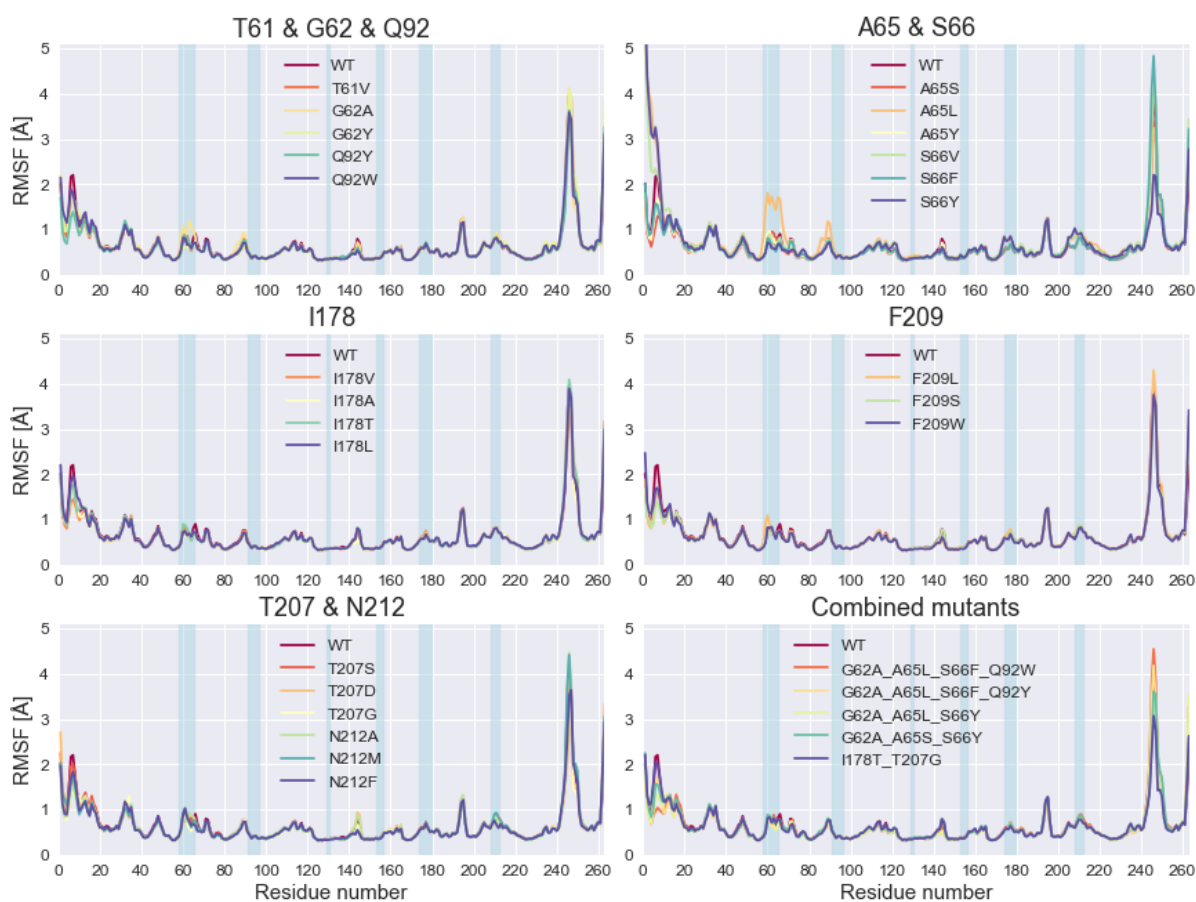


Fig. 47. RMSF plots for C-alpha, C, and N atoms of *TfCut2* and its mutants across 10 replicas of MD simulations. Mutants are grouped according to the substituted residue. Binding site regions are indicated in light blue.

Protein variant production and yield analysis

Protein yield and concentration can provide preliminary insights into the structural and solubility characteristics of the protein variants. Variants with higher yields are often indicative of properly folded and stable proteins during production, while lower yields may reflect challenges such as aggregation, improper folding, or instability during expression and purification. The details of variants' expression, production yield, concentrations and purity are presented in Table 10.

Among the proposed *TfCut2* variants, three could not be successfully produced: S66Y, Q92W, and I178L. For S66Y and I178L, the elution fractions demonstrated very low yields, and protein concentrations were undetectable after desalting, as determined by the Bradford assay. In the case of Q92W, negligible expression was observed even under optimised conditions. Interestingly, freshly transformed cells expressing Q92W produced faint halos on Impranil agar plates, but induction in larger volumes (50 mL cultures) failed to produce detectable protein. Despite these challenges, Q92W was successfully expressed as part

of the combined mutant G62A/A65L/S66F/Q92W, suggesting potential stabilisation effects from other mutations in the combined construct (Table 10).

Interestingly, computational stability predictions (e.g., ΔG values) did not consistently correlate with production outcomes. For instance, S66Y, which failed to be produced, did not show unfavourable computed ΔG values. The highest production yields were observed for T207D, followed by T207G. Notably, these were the only variants with yields exceeding that of the wild-type.

Table 10. Characteristics of the *TfCut2* mutants production process.

<i>TfCut2</i>	Expression	Culture volume [mL]	Protein yield [μ g]	Total protein concentration in the sample (Bradford assay) [μ g/mL]	Protein purity (SDS-PAGE)
wild-type	High	60	123	1230	High
T61V	High	50	26.8	268	High
G62A	High	50	8.3	83	High
G62Y	Moderate	100	33.5	335	Moderate
A65L	High	50	23.7	237	High
A65S	Moderate	100	13.1	131	Moderate
A65Y	High	50	32.0	320	Moderate
S66F	High	50	16.1	161	Moderate
S66V	High	50	7.2	72	Moderate
S66Y	Moderate	50	Elution fraction demonstrates low yield, but after desalting, the protein concentration was not detectable by Bradford assay		
Q92Y	High	50	19.2	192	Moderate
Q92W	Expression of the mutant is negligible (if any). Only freshly transformed cells demonstrated faint halos on Impranil plates. Being induced in 50 mL of medium, cells did not demonstrate Q92W expression, and periplasmic proteins did not show halos on Impranil plates.				
I178A	High	50	39.7	397	High
I178L	Moderate	100	Elution fraction demonstrates low yield, but after desalting, the protein concentration was not detectable by Bradford assay		
I178T	Moderate	50	34.9	349	High
I178V	High	50	15.7	157	Moderate
T207D	High	50	146.2	1462	The highest among all <i>TfCut2</i> variants
T207G	High	50	143.3	1433	High
T207S	High	50	20	200	Low

F209L	Moderate	50	1.7	17	Low
N212A	High	50	31.1	311	Moderate
N212F	High	50	16.8	168	Moderate
N212M	High	50	45.4	454	High
G662A/A65L/S66F/Q92Y	Moderate	100	22	220	Low
G62A/A65L/S66F/Q92Y	Moderate	50	22.5	225	Low
G62A/A65L/S66Y	High	50	16.8	168	High
G62A/A65S/S66Y	High	50	20.2	202	Moderate
I178T/T207G	High	50	35.2	352	High

Sustained enzymatic activity of TfCut2 variants on Impranil DLN plates

Leveraging the property of Impranil DLN to become translucent as degradation progresses, 0.5% Impranil DLN agarose plates with M9 minimal salts were used for activity screening during protein production and purification. This assay provides qualitative rather than quantitative insights into enzymatic activity.

Most mutants formed halos of similar sizes, indicating the presence of active *TfCut2* variants in the corresponding fractions (data not shown). The proteins were purified using His-tag affinity chromatography, and activity was tested on fractions collected during elution. However, the T207D variant exhibited unexpected behaviour. Initially, its halo size was comparable to other variants after one day at 37 °C. Yet, unlike the others, the T207D halo continued to expand significantly over time. Remarkably, even after being left at room temperature for over 20 days, the halo around the T207D sample showed consistent growth, suggesting exceptional stability and prolonged activity for this variant (Fig. 48).

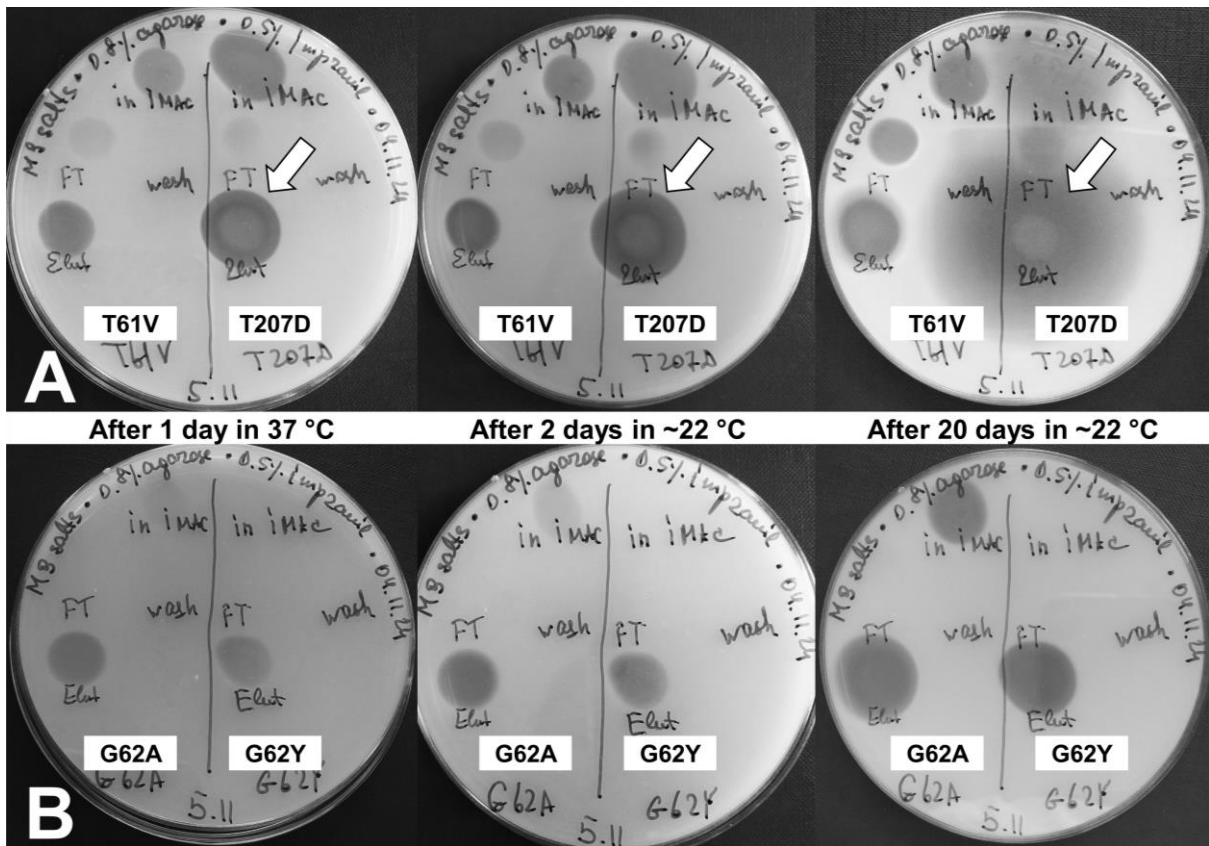


Fig. 48. Photos of 0.5% Impranal DLN agarose plates showing halos formed by the flow-through fraction collected during elution (“FT Elut”) of *TjCut2* mutants purified using His-tag affinity chromatography. **A)** T61V and T207D variants. **B)** G62A and G62Y variants. The flow-through fraction of the T207D variant is indicated by a white arrow, demonstrating its sustained enzymatic activity over time.

Evaluation of the thermal stability of mutants

To evaluate how the proposed mutations affect the stability of *TjCut2*, nanoDSF technique was used. This method measures conformational protein stability by monitoring the intrinsic fluorescence of tryptophan or tyrosine residues, rather than relying on extrinsic fluorogenic dyes typically detected via qPCR instruments [329]. NanoDSF provides a precise and label-free approach to assess protein stability under thermal stress, offering insights into the relationship between structural changes and stability.


To evaluate the thermostability of the proposed mutants, a nanoDSF experiment was conducted. NanoDSF leverages the intrinsic fluorescence of aromatic amino acids; as the protein unfolds with increasing temperature, the local environment surrounding these residues changes, resulting in alterations to their fluorescence emission. These changes are recorded, allowing for the determination of the protein's thermal stability through the measurement of the thermal unfolding transition midpoint (T_m), which is the temperature

at which half of the protein is unfolded. Supplementary figures 6.4 and 5.5 present the thermal unfolding curves of the wild-type *TfCut2* and its mutants.

The T_m value of wild-type *TfCut2* was determined to be 71.31 °C, which corresponds to the melting temperature of 70°C reported in literature [149]. NanoDSF analysis of the S66Y, F209S, G62A/A65L/S66F/Q92W, and G62A/A65L/S66F/Q92Y mutants revealed two maxima in the first derivative of fluorescence. This suggests a two-step unfolding mechanism or the presence of impurities, such as residual *E. coli* proteins (Supplementary figs. 6.4, 6.5). Otherwise, the mutants demonstrated relatively high thermostability, with T_m values ranging from -6.39 to 3.33 °C compared to the wild-type. This indicates that, for most of the mutants, structural integrity was largely preserved. The measure T_m values for the *TfCut2* mutants are presented in Table 11.

Table 11. Determination of T_m values of *TfCut2* and its mutants by nanoDSF.

Mutant	T_m	relative $T_m \Delta$ ($T_{mMUT} - T_{mWT}$)
WT	71.31	0
T61V	71.08	-0.23
G62A	72.18	0.87
G62Y	71.18	-0.13
A65S	71.54	0.23
A65L	71.03	-0.28
A65Y	70.75	-0.56
S66V	68.26	-3.05
S66F	64.92	-6.39
S66Y	52.25, 66.7	-4.61
Q92Y	71.5	0.19
I178A	65.83	-5.48
I178V	70.8	-0.51
I178T	67.24	-4.07
T207S	70.07	-1.24
T207D	73.13	1.82
T207G	70.80	-0.51
F209S	53.43, 64.7	-6.61
F209W	71.43	0.12
N212A	72.58	1.27
N212M	74.64	3.33
N212F	71.83	0.52
G62A/A65L/S66F/Q92W	52.72, 71.5	0.19
G62A/A65L/S66F/Q92Y	53.16, 68.2	-3.11
G62A/A65L/S66Y	68.95	-2.36

G62A/A65S/S66Y	68.90	-2.41
I178T/T207G	67.31	-4.00
Legend:		

The computational ΔG values from FoldX and Rosetta do not show a significant correlation with the experimentally determined T_m values of the mutants, as indicated by a non-parametric Spearman correlation test for non-normally distributed data (data not shown). This lack of correlation is expected, given that the introduced mutations were primarily located in flexible loop regions within the binding site, resulting in a dataset with limited structural variability. Nevertheless, it is notable that the use of FoldX and Rosetta as guides during protein design enabled the selection of mutations that, for most mutants, did not significantly destabilise the *TfCut2* structure.

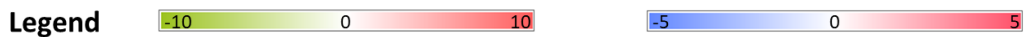
6.3.2. Binding evaluation of *TfCut2* mutants with Impranil DLN

In this subsection, the impact of mutations on the binding of Impranil DLN to *TfCut2* is evaluated computationally. The goal is to identify which poses of Impranil DLN show improvements or declines in total and interface ΔG upon mutation. Many of the *TfCut2* mutants were previously proposed using a genetic algorithm combined with Rosetta, to specifically enhance binding for particular poses of Impranil DLN.

To directly assess the effects of the proposed mutations on all of the Impranil DLN poses, they were introduced into the eight productive complexes of wild-type protein-ligand identified in Chapter 4. Using Rosetta, the mutated complexes were constructed and scored to determine both total and interface ΔG . These scores provide insights into the overall stability of the complexes and the strength of protein-ligand interactions. Notably, most mutants demonstrated negative $\Delta\Delta G$ values for both total and interface scores, indicating potential improvements in binding stability (Table 9).

Table 12. Results of the $\Delta\Delta G$ (Score_{WT} - Score_{mut}) total and interface scores of the mutated *TfCut2* in complex with Impranil DLN in Rosetta Units (RU).

Mutant	Total score								Interface score							
	Hexanediol				Neopentyl				Hexanediol				Neopentyl			
	est P1	est P2	ure P1	ure P2	est P1	est P2	ure P1	ure P2	est P1	est P2	ure P1	ure P2	est P1	est P2	ure P1	ure P2
WT	-788.09	-781.51	-805.29	-795.55	-770.67	-806.28	-785.22	-779.10	-34.02	-34.20	-32.63	-29.77	-34.15	-26.95	-26.74	-35.77
T61V	2.91	5.14	6.55	7.56	2.89	1.51	9.70	11.12	-1.24	-1.67	-1.09	-1.96	0.01	-1.05	-0.11	-0.24
G62A	-6.76	-3.79	0.01	-0.42	-2.33	-3.08	-2.29	-5.24	-1.32	-1.58	-0.53	-1.57	0.18	-2.23	-2.08	-0.46
G62Y	-3.25	3.50	22.15	-4.31	-0.07	10.48	-0.52	4.53	-2.80	3.05	-0.35	-5.50	2.52	-2.35	-5.33	0.75
A65L	-7.84	-3.38	-1.37	1.20	-2.55	0.10	-1.96	-4.34	-0.71	-0.99	-0.07	-1.35	-0.10	0.96	-1.32	-0.35
A65S	-10.57	-6.61	-0.37	-0.70	-2.47	-2.36	-0.48	-4.53	-0.30	-2.00	-0.02	-0.07	-0.06	0.97	-1.89	-0.04
A65Y	-6.19	-2.60	1.56	0.43	-0.23	-4.38	2.36	-1.28	-0.68	-1.22	-0.15	-1.95	-0.04	-4.19	-1.35	0.08
S66F	-7.18	2.06	-1.78	4.98	-2.22	-7.45	8.30	-5.06	-0.22	3.50	-1.55	-6.00	-0.23	-3.33	-3.24	-2.50
S66V	-9.37	0.58	1.98	-3.50	-1.87	-0.21	1.66	-2.47	-0.58	0.72	-1.39	-2.16	0.75	-0.80	-1.60	-1.46
S66Y	-10.54	-0.30	-3.18	8.82	0.30	-4.84	8.22	-6.01	-0.84	1.81	-1.74	-5.95	0.15	-5.27	-1.06	-2.57
Q92Y	-8.87	-2.18	-0.25	0.79	-5.20	3.22	1.07	-1.76	-1.89	-2.23	-2.54	-3.91	0.40	0.01	-0.46	0.15
Q92W	-9.60	-1.90	2.48	2.79	-5.92	1.79	-4.39	-0.73	-2.65	-2.64	-3.29	-1.89	-2.02	-0.11	-1.62	-0.45
I178A	-8.43	-0.24	4.47	-3.29	1.20	-1.44	-5.37	-6.71	0.18	-0.62	0.34	-1.36	0.19	-0.25	-1.47	1.37
I178L	-9.52	-5.31	1.37	-5.21	-2.08	-4.31	-3.87	-2.68	-0.66	-1.05	-3.05	-1.08	-1.88	-1.49	-2.25	1.15
I178V	-13.06	-6.96	-0.36	-10.10	-2.94	-3.19	-1.34	-5.00	1.42	-1.64	-0.27	-2.67	0.54	0.04	-1.02	0.25
I178T	-8.42	-3.30	-11.26	-5.36	-2.16	-0.99	-5.68	-1.69	0.78	-1.33	-0.31	-0.43	0.50	0.65	-0.79	1.64
F209L	-12.47	-3.94	0.30	-0.80	-3.52	-6.39	-6.75	-5.92	0.92	-1.51	-2.99	0.30	1.02	-1.65	-0.79	0.92
F209S	-11.00	-1.13	1.92	-1.57	0.17	-9.08	-3.32	-2.44	0.75	-1.22	-0.73	-1.26	2.26	-0.66	0.15	3.89
F209W	-8.12	-4.22	-1.10	-1.09	0.95	-0.60	1.82	-1.10	2.15	-0.88	0.12	-1.43	0.11	0.04	-0.05	0.88
T207D	-8.00	-5.94	-2.80	-0.99	-2.99	-4.57	-3.25	-2.67	-0.87	-1.00	-0.06	-1.35	0.74	0.10	-1.78	0.16
T207G	-8.76	-2.91	0.41	1.39	2.47	-2.21	0.40	-2.49	-0.97	-1.20	-1.81	-1.19	-0.05	0.42	0.71	-0.16
T207S	-8.24	-4.00	-1.08	-1.35	-0.02	-6.45	-1.85	-4.69	-0.65	-1.94	-0.57	-1.22	-0.14	-0.21	-0.54	-0.12
N212A	-9.00	-6.04	0.42	-7.83	-2.58	-7.71	-3.47	0.54	-1.89	-2.29	0.09	-4.77	0.92	-1.30	-3.32	-0.50
N212F	-10.44	-5.63	-1.68	-4.49	0.46	-6.00	-6.98	-9.98	-2.67	-1.09	-1.52	-3.19	0.94	-1.69	-4.22	-1.51
N212M	-8.56	-2.36	-1.61	-2.87	3.31	-0.52	0.81	-7.50	-3.05	-3.31	-0.83	-5.21	1.19	-2.46	-2.67	-2.13
G62A,A65L,S66F,Q92W	-3.83	0.86	2.21	5.92	-4.73	-2.02	1.74	-1.92	-1.66	-1.33	-5.58	-8.89	-0.72	-4.79	-3.88	-3.07
G62A,A65L,S66F,Q92Y	-8.31	9.93	-2.95	4.58	-5.15	-1.05	4.90	-7.16	-1.95	4.33	-4.45	-8.84	0.73	-4.31	-2.52	-2.64
G62A,A65L,S66Y	-10.35	-1.52	-1.44	10.36	-2.69	-6.86	4.72	-5.64	-1.44	-1.27	-1.85	-6.39	-0.24	-3.76	-1.75	-1.51
G62A,A65S,S66Y	-8.79	-2.72	-2.62	5.63	2.03	-4.73	4.65	-6.17	-1.30	-1.16	-2.67	-5.61	0.12	-4.34	0.47	-2.57
I178T,T207G	-6.34	-0.16	2.70	2.75	3.02	1.91	-3.98	-2.44	-2.14	-0.67	-1.60	1.55	0.67	0.76	0.21	1.49



Interestingly, the *TfCut2* mutants in complex with Impranil DLN exhibit, in most cases, negative $\Delta\Delta G$ total scores (indicating improved stability or lower energy) as opposed to the Rosetta mutants in free form, presented in Chapter 6.3.1. This difference likely arises from the influence of the protein-ligand interface on the overall energy of the system, as the mutations were designed to enhance binding interactions with Impranil DLN, particularly by improving the interface score. These effects become apparent in the context of the complex, where favourable interactions such as hydrogen bonding, van der Waals forces, or hydrophobic packing stabilise the interface, leading to a more negative total $\Delta\Delta G$ score. In contrast, these mutations may destabilise the protein in the free form, as they were not optimised for standalone stability.

Additionally, the energetic contributions of the interface play a significant role in the bound state. Mutations that improve interface interactions can offset destabilising effects observed in the free form, thereby enhancing the stability of the complex. The Rosetta scoring function accounts for these interactions, explaining why the mutants generally perform better energetically when evaluated in the presence of the ligand.

The results indicate that the T61V mutation worsens the total score but improves the interface score. The I178V mutation consistently resulted in better total scores across all Impranil poses compared to the corresponding wild-type complexes. Some mutations, such as S66F, S66Y, N212A, and N212M, enhanced the interface score for specific poses, notably for the hexanediol urethane P2 pose.

Overall, the results demonstrate that each mutant managed to improve either the total or interface scores for at least some of the complexes with Impranil DLN poses. This outcome is in agreement with the predictions made during the design process, as Rosetta identified different mutations optimised for distinct poses of the substrate. Such diversity among the mutants reflects the potential adaptability of *TfCut2* and provides valuable insights into its binding preferences for specific sites or bond types within Impranil DLN. By evaluating these different mutants, this study contributes to a better understanding of how *TfCut2* interacts with complex polymer substrates like Impranil DLN.

6.3.3. Degradation of Impranil DLN by *TfCut2* and mutants

This section evaluates the degradation of Impranil DLN by *TfCut2* wild-type and its mutants through experimental methods. Two main aspects are addressed: 1) identifying the specific bonds in Impranil DLN hydrolysed by *TfCut2*, using NMR analysis of the substrate before and after hydrolysis by the wild-type enzyme and under acidic conditions (HCl hydrolysis); and 2) assessing the efficiency of the proposed mutants by measuring their initial degradation rates in a kinetic loop.

Evaluation of hydrolysed bonds in Impranil DLN by *TfCut2* wild-type

To identify the primary bonds hydrolysed by *TfCut2* wild-type in Impranil DLN, NMR in deuterated DMSO analysis was performed on the hydrolysed sample. The hydrolysis reaction was conducted in M9 minimal salts with *TfCut2* at a concentration of 4 µg/mL and 1% Impranil DLN. The mixture was incubated at 37°C, with shaking at 150 rpm for 24 hours, then cooled and stored at 4°C until extraction.

For comparison, an acidic hydrolysis control was prepared by incubating Impranil DLN with 0.1 M HCl at 65°C for 24 hours, following the procedure outlined by Biffinger et al. [3].

NMR spectra of Impranil DLN of the hydrolysed samples showed the expected ester and urethane functional groups in the polymer chain, but also, additional signals indicating products of ester bond hydrolysis, such as alcohol groups and carboxylic acids (Fig. 49).

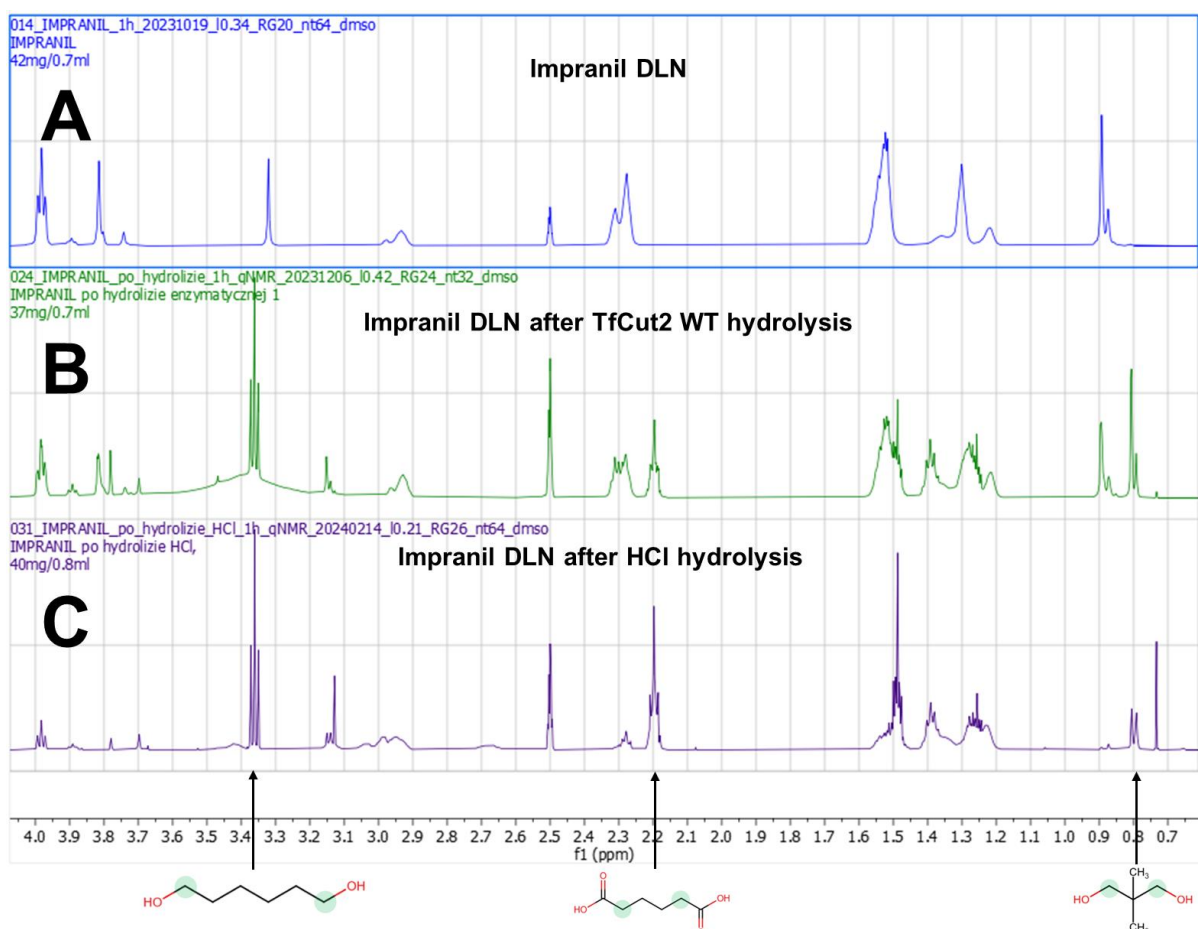


Fig. 49. ^1H NMR spectra of **A)** Impranil DLN, **B)** Impranil DLN after enzymatic hydrolysis by *TfCut2* wild-type, and **C)** Impranil DLN after enzymatic hydrolysis in HCl; in DMSO_d_6 (600MHz), range 0.7-4.0 ppm. Below the picks, chemical structures containing proton groups responsible for signals in degradation products are proposed (in green).

The ^1H NMR spectrum of Impranil DLN (Fig. 49), recorded in deuterated DMSO, shows characteristic signals corresponding to structural fragments in the polymer. In the range of 3.7–4.1 ppm, signals from ester fragments are observed, specifically the CH_2 group of the alcohol residue in 1,6-hexanediol and neopentyl glycol. These signals decrease following hydrolysis by *TfCut2* (Fig. 49B) and are even smaller after HCl hydrolysis (Fig. 49C). A new triplet at 3.4 ppm, absent in the unhydrolysed Impranil DLN (Fig. 49A), indicates the presence of 1,6-hexanediol, a product of ester bond hydrolysis.

The signal at 3.0 ppm corresponds to CH_2 groups adjacent to nitrogen in the urethane structure, while a multiplet at 2.3 ppm represents CH_2 protons in the α -position relative to the ester carbonyl group. This signal is reduced in the spectra after hydrolysis. Additionally,

at 2.2 ppm, a triplet indicates adipic acid, a product of ester bond hydrolysis, which becomes more prominent after enzymatic (Fig. 49B) and acidic hydrolysis (Fig. 49C).

The signals in the 1.2–1.6 ppm range originate from CH₂ groups in the β- and γ-positions of the 1,6-hexanediol chain, the β-position of adipic acid, and the β- and γ-positions in hexamethylene diisocyanate. A singlet at 0.9 ppm corresponds to isolated CH₃ groups in the aliphatic structure of neopentyl glycol, which disappears almost completely after HCl hydrolysis (Fig. 49C). After hydrolysis, new signals at 0.8 and 0.7 ppm correspond to isolated CH₃ groups, indicating further degradation of ester bonds near neopentyl glycol in the HCl-treated sample.

The signal at 7.0 ppm corresponds to NH group in urethane bond. This signals' integral values increase following the hydrolysis by *TfCut2* and HCl (Supplementary figs. 6.1-6.3). The absence of amine signals (-NH₂), after urethane bonds hydrolysis, in the spectra is likely due to overlapping chemical shifts with other components and potential reactions between amines and carboxylic acids formed during hydrolysis, leading to amide bond formation [330,331]. These interactions form a clathrate, which precipitates out of the solution as salts, making it difficult to detect amines. While it remains unclear whether *TfCut2* hydrolyses urethane bonds, urethane bonds should hydrolyse at least in HCl, however, it is challenging to assess the hydrolysis of urethane bonds in the HCl sample as well.

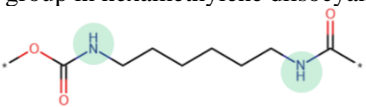
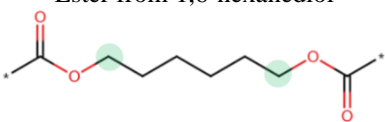
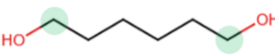

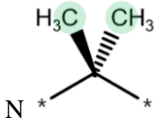
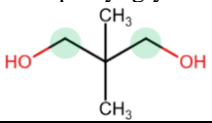
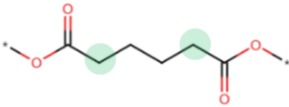
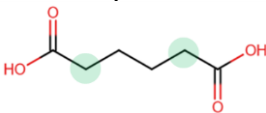
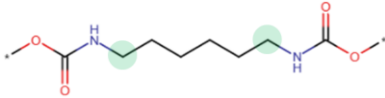
The NMR spectra reveal that *TfCut2* does not fully degrade Impranil DLN within 24 hours, unlike HCl hydrolysis, which shows a greater extent of degradation. This is evident in the signal at 0.9 ppm, corresponding to CH₃ groups in neopentyl glycol within the polymer chain. In the spectrum after HCl hydrolysis, this signal is nearly absent, indicating extensive degradation, whereas it remains present, albeit reduced, in the spectrum following *TfCut2* hydrolysis (Fig. 49B, C).

Additionally, the signal at 2.2 ppm, indicative of adipic acid as a hydrolysis product, is notably smaller after *TfCut2* hydrolysis compared to HCl hydrolysis, further supporting the higher efficiency of HCl. Interestingly, the signal at 3.4 ppm, representing free 1,6-hexanediol, appears comparable between the two hydrolysis conditions. This suggests that *TfCut2* preferentially hydrolyses ester bonds adjacent to 1,6-hexanediol over those adjacent to neopentyl glycol (Fig. 49B, C). These findings highlight a selective catalytic activity of *TfCut2* and its limited overall degradation efficiency under the experimental conditions.

Quantitative comparison of the degradation extent between *TfCut2* and HCl is difficult due to the unknown polymer chain lengths and the lack of a consistent reference signal,

as all signals shift upon degradation, including those from $-\text{CH}_3$ groups. A summary of the characteristic structures identified in Impranil DLN based on the ^1H NMR spectrum is presented in Table 10. The values of integrals of the signals are shown in Supplementary figures 6.1-6.3.

Table 13. ^1H NMR results of Impranil DLN before and after hydrolysis with HCl and enzyme *TfCut2*, in DMSO- d_6 . Products are marked in gray.

Name of compound and chemical structure	Chemical shifts (ppm)	Impranil DLN	Impranil DLN after <i>TfCut2</i> hydrolysis	Impranil DLN after HCl hydrolysis
NH group in hexamethylene diisocyanate 	7.0	0.92	2.21	4.0
Ester from 1,6-hexanediol 	4.0	10.00	10.00	10.00
	3.9	1.04	2.58	3.23
1,6-hexanediol 	3.4	0.37	18.29	29.68
Ester from neopentyl glycol 	3.82	5.08	6.01	1.61
	3.75	1.02	1.88	3.5
Methyl group 	0.9	9.38	10.14	3.15
Neopentyl glycol 	0.8	0	9.70	15.33
Ester from adipic acid 	2.3	15.39	17.46	12.80
Adipic acid 	2.2	0	10.82	54.28
Urethane from hexamethylene diisocyanate 	2.95	4.04	9.75	33.25

The analysis of Impranil DLN NMR spectra before and after hydrolysis allowed to confirm ester bonds degradation by *TfCut2* and release of 1,6-hexanediol, neopentyl glycol and adipic acid by *TfCut2*. However, the degradation of urethane bonds by *TfCut2* could not be confirmed by this method.

Degradation rate - kinetic loop

To measure and compare the hydrolytic activity of *TfCut2* and its mutants on Impranil DLN, initial degradation rates were determined using a kinetic loop experiment. Impranil DLN degradation was monitored over a 30-minute period by measuring spectrophotometric absorbance at 400 nm (Fig. 50A, B). A linear fit to the data enabled calculation of the initial degradation rate (v_0), with the slope representing the degradation velocity (Fig. 50C, D). The mean and standard deviation of the degradation rates were calculated from three independent experiments (each performed in duplicate) for the *TfCut2* wild-type and its mutants (Fig. 50C, D). Additionally, a statistical t-test was performed to assess the significance of differences between the mutants and WT (Table 14). In the case of some mutants with very low activity, such as N212F and S66V, it was not possible to obtain all three repetitions of the experiments.

Due to the large number of proposed mutants, testing all of them simultaneously was not feasible. Mutants that were easier to produce were prioritised and tested first, while additional mutants were tested in a second batch. Because the two experimental batches were conducted at different times, with wild-type enzymes stored for varying durations, the initial degradation rates (v_0) are not directly comparable between the two batches. While testing the first batch, a gradual decline in enzymatic activity was observed in experiments 1-3 (Table 14), likely due to repeated freeze-thaw cycles. To address this issue, the experimental design was adjusted for the second batch. Instead of spreading the experiments across multiple days, all assays for the second batch were conducted on a single day using fresh aliquots of all variants (including wild-type). Enzyme aliquots were kept on ice between experiments to minimise activity loss. This revised approach aimed to ensure greater consistency and reliability in the measured degradation rates.

Despite the differences in experimental conditions, meaningful comparisons were made within each batch, using the wild-type results from the same batch as internal controls. Mutants from the first batch included T61V, G62A, G62Y, A65L, A65S, A65Y, I178A, I178T, I178V, T207D, T207S, N212A, N212F, and N212M. The second batch included S66F, S66V, Q92Y,

T207G, T207D, F209S, F209W, G62A/A65L/S66F/Q92W, G62A/A65L/S66F/Q92Y, G62A/A65L/S66Y, G62A/A65S/S66Y, and I178T/T207G. Although the activity of wild-type enzyme from the first batch was reduced due to prolonged storage, comparative analysis within each batch still provided reliable insights into the effects of the mutations on hydrolytic activity. For clarity, the results of the two experiments are presented separately in Figure 50. It is important to note that these were preliminary *screening* experiments, designed primarily to evaluate the computationally proposed mutants and their relative activities. Screening procedures inherently exhibit variability, and the measured values should be interpreted as indicative rather than definitive. For mutants showing promising results, subsequent rounds of experiments involving scaled-up protein purification and more detailed characterisation would be necessary to obtain accurate enzymatic parameters. Nonetheless, this screening approach was well-suited to the primary aim of this study: providing experimental validation of computational predictions. In the context of this computationally focused dissertation, these results offer valuable insights into the relative performance of the proposed mutants and guide future directions for experimental optimisation.

From the proposed set of 29 mutants (24 single-point and five combined mutants), 25 mutants were deemed active. Unfortunately, most mutants (19 out of 25 tested) exhibited lower initial degradation rates (v_0) of Impranil DLN compared to wild-type *TjCut2*, while three showed similar initial activity (G62Y, A65Y and I178T) and three demonstrated an increased v_0 : T61V, G62A, and T207D (but only in first batch, in the second it was similar to wild-type). Notably, the G62A mutant displayed more than a twofold increase in v_0 compared to wild-type, suggesting that the addition of a -CH₃ group at this position substantially enhances catalytic efficiency. The G62A had been previously reported as beneficial by relieving inhibition of reaction products by adding steric hindrance caused by the side chain of A62 [316], though tested on different substrates like PET and BHET [191,316]. The other two beneficial mutations, T61V and T207D have not been reported. Mutation T207D not only improved v_0 but also facilitated the highest production yields.

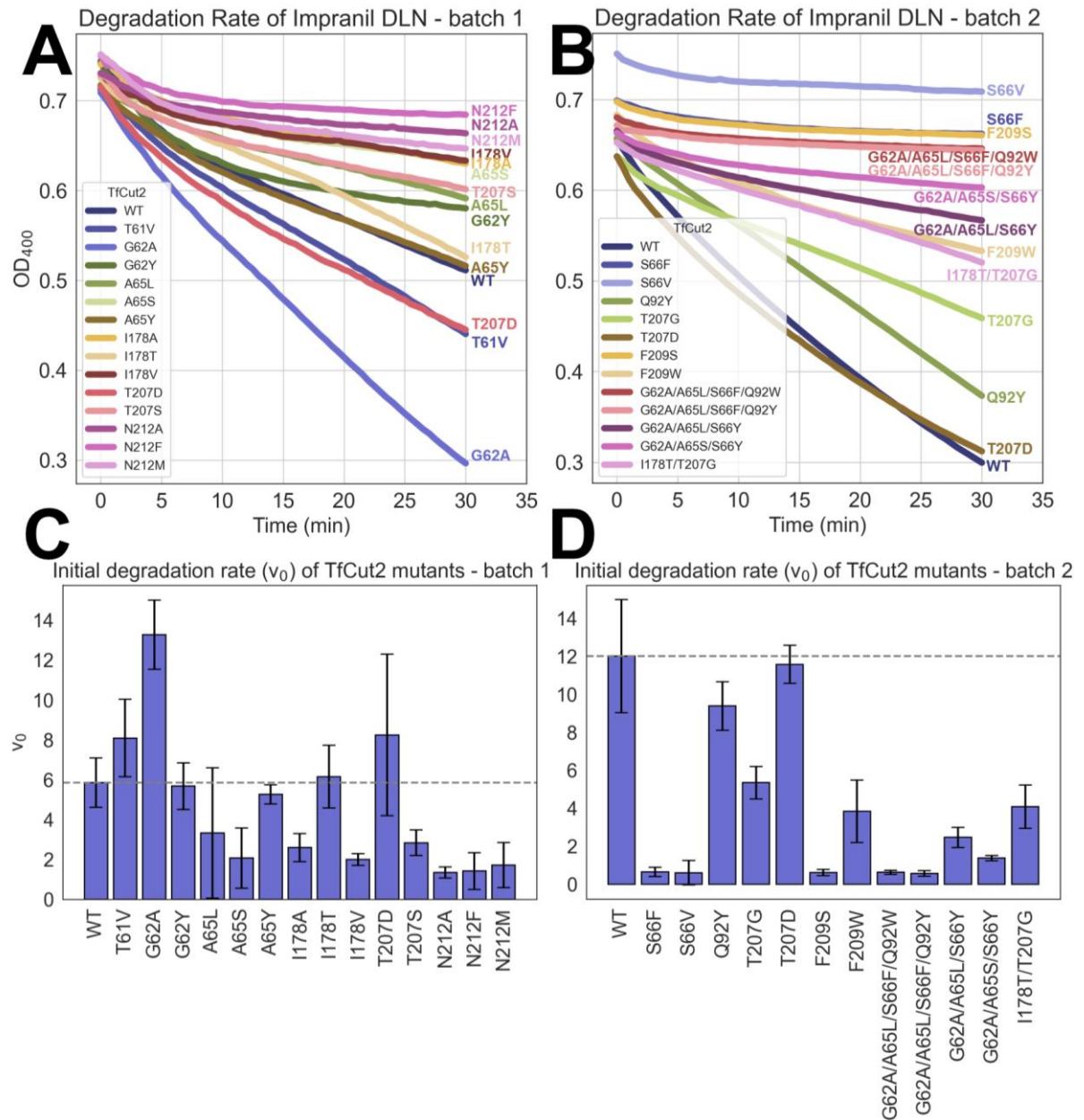


Fig. 50. **A)** Degradation rate of *TfCut2* wild-type and mutants during the first 30 minutes. Data presented as the mean \pm SD of three independent experiments, each performed in duplicate. **B)** Initial rate of Impranil DLN hydrolysis for *TfCut2* variants. WT stands for wild-type.

Due to its interesting properties such as prolonged activity and high production yield, the T207D mutant was evaluated in both experiments. Interestingly, in batch 1, it showed a higher degradation rate than the wild-type, whereas in the second batch experiment, its initial degradation rate was very similar to that of the wild-type, though slightly higher according to the calculated value of statistical t-test (Table 14). This discrepancy could stem from the unique stability of the T207D mutant, as demonstrated by its extended halo formation on Impranil DLN agarose plates, presented in Chapter 6.3.1: Sustained enzymatic activity

of *TjCut2* variants on Impranil DLN plates. In batch 1, where proteins were stored frozen for a longer time before the degradation experiment, the activity of all proteins, including the wild-type, decreased. However, the activity of T207D might have decreased to a lesser extent, resulting in a higher observed degradation rate compared to the wild-type. This highlights a key feature of the T207D mutant: while its efficiency is comparable to the wild-type under standard conditions, it exhibits greater stability, maintaining its activity for a longer duration. This result aligns with the structural implications of the T207D mutation. Although this mutation is unlikely to directly enhance Impranil DLN binding due to its position not in direct contact with the ligand, it may influence catalytic efficiency. T207D is located adjacent to the catalytic residue H208, and the substitution of threonine with aspartic acid introduces a negatively charged residue in this region. This change could reduce inhibition by reaction products via electrostatic repulsion, while also altering the local protein surface properties, potentially facilitating more efficient catalysis under certain conditions.

Three mutations—G62Y, A65Y, and I178T—had minimal impact on activity despite significantly altering residue properties, such as introducing bulkier or more polar amino acids. Additionally, A65Y exhibited OD₄₀₀ readings comparable to wild-type, indicating a likely lack of significant difference in activity for this mutant (t-test p-value = 0.49). Mutations with a negative effect on v_0 included A65L, A65S, S66F, S66V, Q92Y, I178A, I178V, T207G, T207S, F209S, F209W, N212A, N212F and N212M, and all the combined mutants: G62A/A65L/S66F/Q92W, G62A/A65L/S66F/Q92Y, G62A/A65L/S66Y, G62A/A65S/S66Y, and I178T/T207G.

Especially mutations S66F, S66V, F209S, and the two combined mutants (G62A/A65L/S66F/Q92W and G62A/A65L/S66F/Q92Y) resulted in a significant loss of activity, with $(v_0^{mut}/v_0^{WT}=0.05)$. These findings suggest that S66 may not be an ideal candidate for mutation, or that the specific substitutions made were particularly detrimental. Notably, the combined mutants also include the S66F mutation, which likely contributed to their reduced activity. These results are surprising, as S66 is a solvent-exposed residue with high mutational potential, as indicated by FoldX predictions and entropy analysis (0.7). However, S66 forms part of a short helix 63–66, and substitutions at this position may disrupt the secondary structure of this region, leading to loss of activity.

For F209S, the detrimental effect is also unexpected, as a serine is present at this position in *IsPETase* and in homologous sequences. The lack of a bulky hydrophobic residue at this position (in the P1 region) might destabilise the binding of Impranil DLN,

especially given that the P1 region is already less hydrophobic than the P2 region. This destabilisation could explain the observed decrease in degradation rates.

As for the combined mutants, in addition to S66F, they also contain A65L, a mutation previously shown in RMSD and RMSF analyses to have destabilising effects on protein dynamics. These combined destabilising effects likely contribute to the significant loss of activity observed for these mutants.

The detailed values of the assessed initial degradation rates, along with the results of the t-test statistics, are presented in Table 14. The t-test was conducted on the datasets of OD₄₀₀ measurements over time. In some cases, such as T207D in batch 2, the calculated initial degradation rate appeared slightly lower than that of the wild-type ($v_0^{mut}/v_0^{WT}=0.96$), yet the t-test indicated a significantly higher activity. This discrepancy arises because the t-test considers all data points in the time series, which may exhibit curvature. In contrast, the v_0 calculation relies on a linear fit to the initial phase of the data, potentially introducing bias when the data are non-linear. Such inconsistencies were observed only for mutants with activities close to that of the wild-type. Interestingly, for I178T, the opposite trend was observed. This reflects the subtle differences in how these statistical and analytical methods interpret the same dataset, particularly for mutants with marginally altered degradation rates.

Table 14. Initial degradation rates (v_0) of Impranil DLN for *TfCut2* wild-type and its mutants. ‘Exp1’, 2, 3 indicate measured OD400 in separate experiments; ‘Mean’ and ‘Std’ indicate the mean of the measurements and standard deviation, respectively. ‘Statistic t-test’ shows the calculated t-test values (conducted after verifying data normality and variance similarity), and ‘p-val’ represents the corresponding p-values. P-value < 0.05 denotes statistical significance.

Batch 1	<i>TfCut2</i>	Exp 1	Exp 2	Exp 3	Mean	Std	v_0^{mut}/v_0^{WT}	Statistic t-test	p-val
	WT	7.12	5.82	4.63	5.86	1.25	1.00		
	T61V	9.83	6.00	8.45	8.09	1.94	1.38	4.83	0.00
	G62A	12.17	15.28	12.38	13.28	1.74	2.27	11.36	0.00
	G62Y	6.84	5.71	4.50	5.68	1.17	0.97	-3.64	0.00
	A65L	7.00	2.24	0.74	3.33	3.27	0.57	-6.39	0.00
	A65S	3.69	1.82	0.69	2.07	1.52	0.35	-11.32	0.00
	A65Y	5.36	5.69	4.75	5.27	0.48	0.90	0.69	0.49
	I178A	3.36	2.44	1.98	2.59	0.70	0.44	-12.61	0.00
	I178T	7.95	5.49	5.02	6.15	1.57	1.05	-2.91	0.00
	I178V	2.23	2.10	1.67	2.00	0.29	0.34	-11.94	0.00
	T207D	12.87	6.54	5.33	8.25	4.05	1.41	6.10	0.00
	T207S	3.54	2.70	2.27	2.84	0.65	0.48	-7.94	0.00
N212A	1.46	1.54	1.03	1.34	0.27	0.23	-15.90	0.00	

	N212F	2.07	0.76	-	1.42	0.93	0.24	-18.24	0.00
	N212M	3.02	1.13	1.00	1.72	1.13	0.29	-13.36	0.00
Batch 2	WT	8.79	10.91	12.54	12.02	2.98	1.00		
	S66F	0.57	0.70	0.37	0.65	0.24	0.05	-26.25	0.00
	S66V	0.15	-	-	0.61	0.64	0.05	-35.53	0.00
	Q92Y	8.14	10.12	10.80	9.39	1.28	0.78	-5.82	0.00
	T207G	6.23	4.53	5.29	5.35	0.85	0.45	-10.28	0.00
	T207D	0.12	10.09	12.27	11.58	1.00	0.96	1.03	0.00
	F209S	0.38	0.66	0.76	0.62	0.16	0.05	-26.30	0.00
	F209W	3.44	6.34	3.37	3.84	1.65	0.32	-14.95	0.00
	G62A/A65L/S66F/Q92W	0.51	0.66	0.73	0.63	0.11	0.05	-25.99	0.00
	G62A/A65L/S66F/Q92Y	0.42	0.71	0.59	0.57	0.15	0.05	-25.51	0.00
	G62A/A65L/S66Y	1.88	2.61	2.91	2.47	0.53	0.21	-18.52	0.00
G62A/A65S/S66Y	1.29	1.54	1.31	1.38	0.14	0.11	-21.85	0.00	
I178T/T207G	4.02	5.27	2.99	4.09	1.14	0.34	-16.28	0.00	

In summary, most of the tested mutants (19 out of 25) exhibited lower initial degradation rates compared to wild-type (*TfCut2*), while three had similar rates and three showed improved performance. Overall, this is not a highly successful outcome. The mutations were primarily designed to enhance ligand binding; however, these results suggest that ligand binding may not be the rate-limiting step, and other factors, such as stability or catalytic efficiency, could play more significant roles.

Improved binding of the hydrophobic polymer chain often involves introducing larger hydrophobic residues (such as in case of essential for activity Y60, M131, W155 in the wild-type structure), but such substitutions may destabilise the enzyme's structure or negatively alter its surface properties. Modest changes, such as G62A and T61V, improved activity, while more disruptive mutations, such as A65L, F209W, and Q92Y, reduced efficiency. Similarly, although some stronger substitutions, like G62Y and A65Y, did not significantly impair activity, they also failed to enhance it.

These findings suggest that while the expansive binding site of *TfCut2* can tolerate certain structural changes, substitutions involving bulky hydrophobic residues may not be ideal. On the other hand, reducing bulk, as seen with mutations like I178A, I178V, and F209S, can disrupt critical interactions with the ligand. In some cases however, a substitution

of a hydrophobic amino acid to a smaller polar one, like in I178T, activity similar to the wild-type can be maintained.

A potentially promising strategy might involve introducing negatively charged residues near the active site, as demonstrated by T207D, which not only preserves activity but could also enhance catalytic rates by facilitating release of products of the ester hydrolysis (e.g. hydrolysed acids) from the binding site.

In the next chapter, a more detailed structural analysis of selected mutants is presented.

6.3.4 Selected *TfCut2* mutants with improved properties for in-depth analysis

This section provides a detailed analysis of the successful mutants T61V, G62A and T207D, focusing on the molecular factors that contribute to their improvements in degradation rates or stability.

T61V

Although the $\Delta\Delta G$ values predicted by FoldX and Rosetta for the T61V mutation are positive, suggesting a potential destabilisation, the experimental results do not fully support this conclusion. The marginal reduction in T_m observed for the T61V mutant does not indicate significant destabilisation. It is worth noting that although the production yield of T61V is lower than that of wild-type, this does not necessarily correlate with a significant decrease in functional stability or activity. The reduction in yield could be attributed to other factors, such as differences in solubility or expression efficiency, but it does not undermine the mutant's improved binding and activity.

The improved interface $\Delta\Delta G$ scores suggests that the mutation enhances ligand binding and observed increase in the rate of Impranil DLN degradation ($v_o^{mut}/v_o^{WT} = 1.38$) could suggest that in this case, the improvement of ligand binding truly improved the degradation.

The positive $\Delta\Delta G$ from the computational models likely reflects the disruption of a hydrogen bond between the hydroxyl of T61 and the carbonyl of Y60 (Fig. 51 A). This bond disruption, while it could suggest destabilisation, does not appear to substantially affect the protein's overall stability or catalytic activity. On the contrary, replacing T61 with valine introduces a more hydrophobic environment in the binding region, which seems to favour better interactions with the hydrophobic sections of Impranil DLN (Fig. 51 B). In all poses

of Impranil DLN, residue 61 interacts with these hydrophobic areas, as it is located near the cleaved bond. The “next” hydrolysable bond is further away, so the bound Impranil molecule is always positioned with its polymer chain (1,6-hexanediol or adipic acid) or, in the case of neopentyl glycol, CH₃ groups.

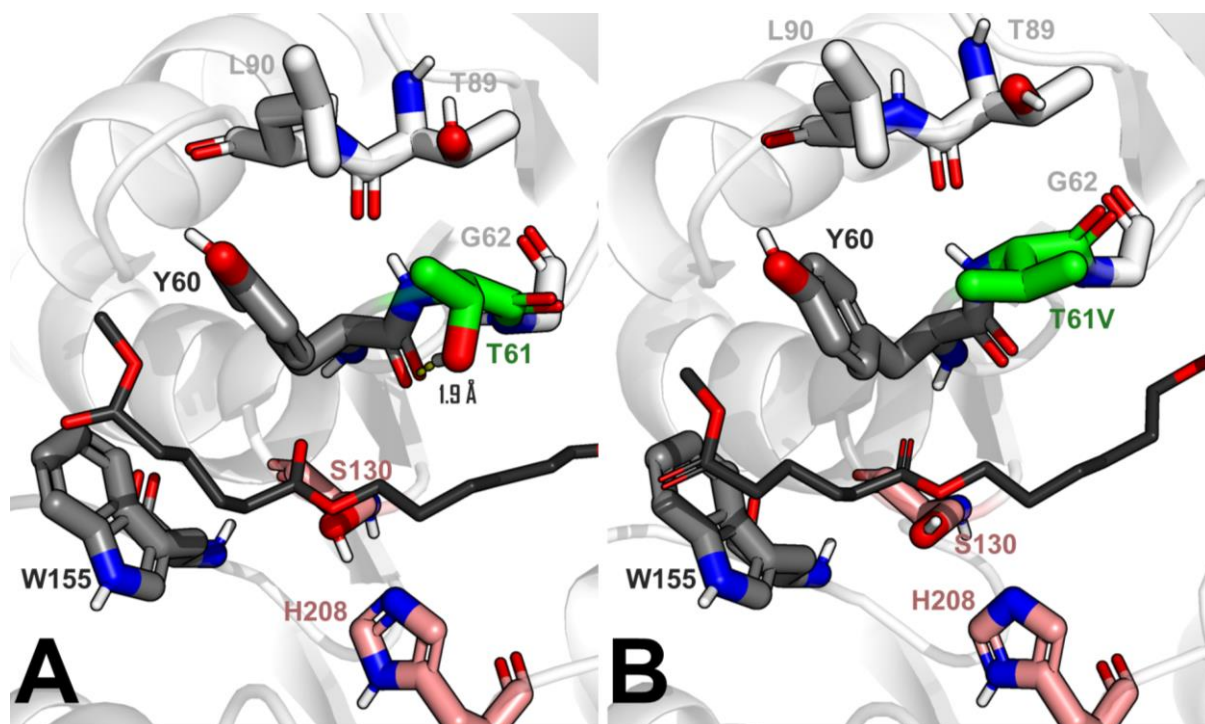


Fig. 51. **A)** First representative frame from selected productive MD simulation frames showing wild-type *Tfcut2* in complex with the hexanediol ester P2. Catalytic residues are depicted as salmon-coloured sticks, aromatic clamp residues (Y60 and W155) as grey sticks, the substituted residue T61 as green sticks, and nearby residues within a 3 Å radius are shown in white sticks. A likely hydrogen bond between T61 and Y60 is indicated by a yellow dashed line. **B)** The same complex as in panel A, now with the T61V mutation introduced using Rosetta. Residues are represented similarly to panel A, with the Impranil DLN in the hexanediol ester P2 pose shown in black sticks.

G62A

Computational $\Delta\Delta G$ show very marginal destabilisation, in line with the slightly higher T_m of +0.87 °C compared to wild-type *Tfcut2*, suggesting that the mutant maintains similar stability. Rosetta scores for the G62A mutant indicate comparable or improved energy scores across all ligand poses, and the rate of Impranil DLN degradation is over two-fold higher than the wild-type. Notably, G62A is an evolutionarily conserved mutation at this position, with a probability of over 30%. This highlights the importance of considering evolutionary acceptable substitutions even when designing catalysts for non-natural substrates.

Overall, G62A enhances Impranil DLN degradation by improving ligand binding through hydrophobic interactions, without compromising the enzyme's structural integrity.

This mutation has also been shown to increase activity on PET and Bis(2-Hydroxyethyl) terephthalate (BHET), likely by relieving product inhibition through steric hindrance from the alanine side chain [191,316]. While the substitution was primarily designed to enhance polymer chain binding, the improved product release could also be a contributing factor. Additionally, glycine-to-alanine substitutions often improve protein stability by reducing chain entropy in the unfolded state, stabilising the folded structure [332].

T207D

The T207D mutant demonstrates slight stabilisation, as evidenced by a T_m increase of +1.82°C and favourable computational $\Delta\Delta G$ predictions. This mutant also exhibits a modestly improved degradation rate for Impranil DLN and the highest production yield among all proposed mutants, even surpassing that of the wild-type. These findings suggest beneficial structural and functional effects resulting from this mutation.

Residue T207 is not directly involved in ligand binding but is positioned adjacent to the catalytic H208, implying that its substitution could influence local stability, flexibility, and catalytic efficiency. In the wild-type structure, the hydroxyl group of T207 points towards the backbone carbonyl oxygen of L175 on a neighbouring loop (Fig. 52A). While the distance (2.8 Å) is too large for direct hydrogen bonding, this interaction may be mediated by a water molecule, contributing to local stabilisation.

The T207D mutation replaces the threonine side chain with the negatively charged carboxyl group (-COO⁻) of aspartate. In the mutant structure, the carboxyl group forms a hydrogen bond with the backbone NH group of F209 (1.9 Å) (Fig. 52B), while disrupting interactions with L175 from the neighbouring loop. This alteration could increase local flexibility, particularly near catalytic residues D176 and H208, enhancing their mobility and interactions, which are essential for catalysis.

Moreover, the introduction of aspartate's negative charge modifies the local electrostatic environment, potentially influencing the protonation state and nucleophilicity of H208. This adjustment may optimise substrate interaction or stabilise reaction intermediates, indirectly enhancing catalytic efficiency.

Additionally, the negatively charged carboxyl group of aspartate may promote faster product release by repelling carboxylate groups of hydrolysis products, particularly carboxylic acid. This electrostatic repulsion could facilitate product expulsion from the active site, improving turnover rates.

Overall, the T207D mutation likely enhances active site dynamics, increases catalytic flexibility, and accelerates product release, contributing to its observed improvements in activity and stability.

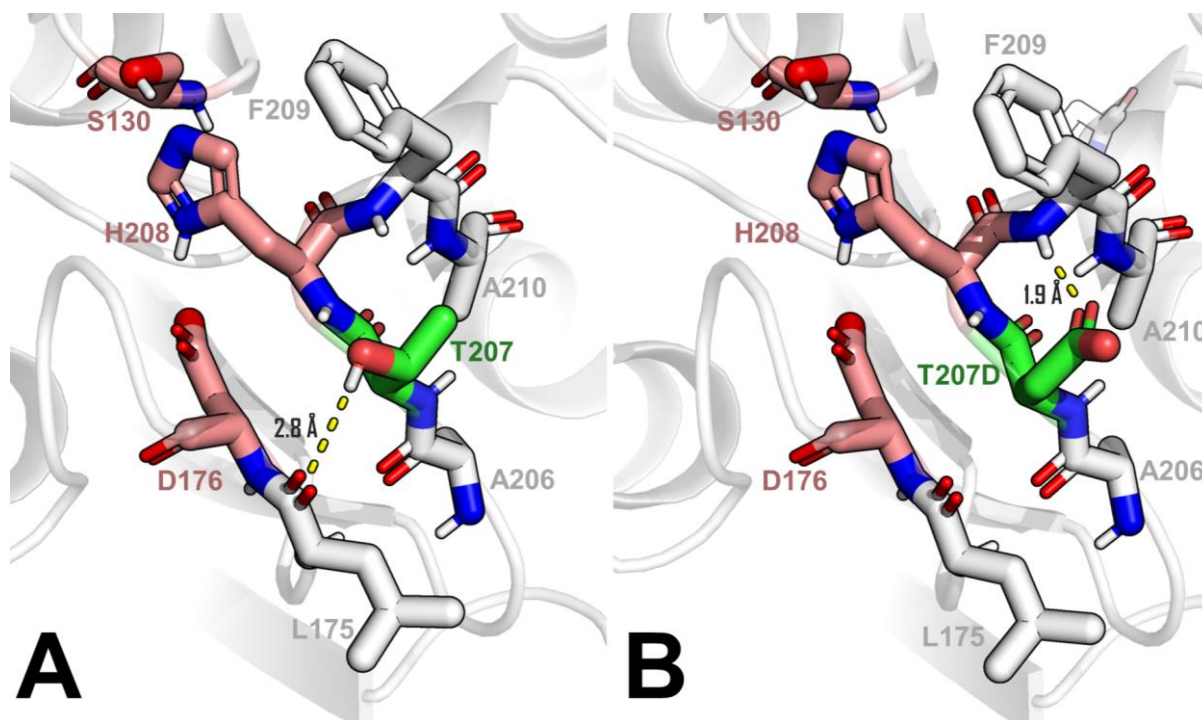


Fig. 52. **A)** Structure of wild-type *TjCut2* (PDB id: 4CG1). Catalytic residues are shown in salmon, T207 in green, and neighbouring residues in white. The measured distance is indicated by a yellow dashed line. **B)** Structure of *TjCut2* T207D mutant, with a similar representation as in Fig. 52A, generated by introducing T207D mutation to 4CG1 wild-type *TjCut2* structure.

6.4. Conclusions

This chapter presented the computational and experimental evaluation of the proposed *TjCut2* mutants, addressing the third and final objective of this dissertation.

All proposed mutants appeared to exhibit reasonable stability, with most showing only modest increases in $\Delta\Delta G$ as calculated by Rosetta. Additionally, the changes in flexibility by single-point mutations were generally minimal. Identifying the precise reasons behind the unsuccessful production of some variants would require a more in-depth and time-intensive analysis. Potential factors could include altered charge distribution, misfolding, or suboptimal heterologous expression levels.

Overall, 24 single-point mutants and five multiple mutants were proposed. Among these, 20 single-point mutants and five combined mutants were successfully produced

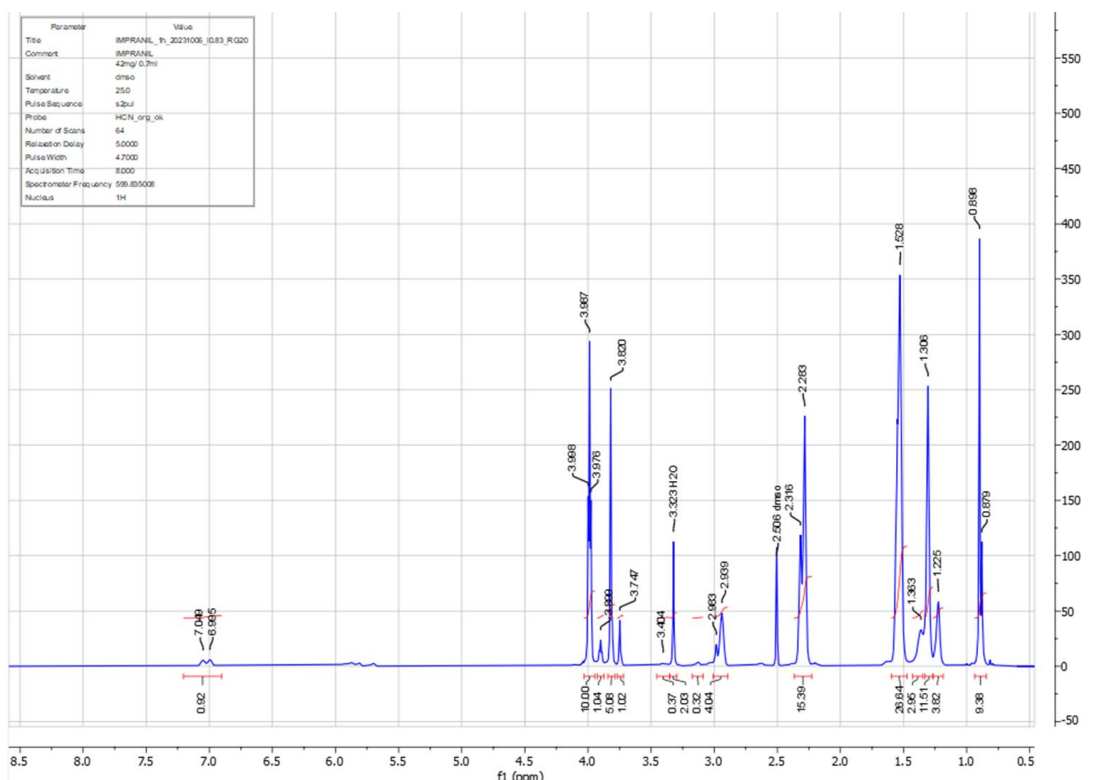
and tested for thermostability and activity measurements. The evaluation prioritised successfully produced mutants, providing a detailed rationale for how each mutation influenced the variants' T_m and activity towards Impranil DLN degradation. The produced and evaluated mutants generally exhibited thermostability comparable to the wild-type, indicating that the applied mutations avoided destabilising the protein while aiming to enhance Impranil DLN affinity or catalytic efficiency.

In general, three successful mutations that render *TjCut2* more efficient for Impranil DLN degradation were proposed: T61V, G62A and T207D. While G62A mutation to *TjCut2* was previously reported to be beneficial, albeit tested on different substrates, such as PET and BHET [191,316], the other two mutations, T61V and T207D have not been previously reported. Mutation T207D, apart from slightly improving the degradation rate of Impranil DLN, also helps to produce the mutant in much higher concentrations. Three other mutations did not alter the activity much: G62Y, A65Y and I178T and most of the mutations had negative effect on the degradation rates of Impranil DLN, namely: A65L, A65S, S66F, S66V, Q92Y, I178A, I178V, T207G, T207S, F209S, F209W, N212A, N212F and N212M, and all the combined mutants: G62A/A65L/S66F/Q92W, G62A/A65L/S66F/Q92Y, G62A/A65L/S66Y, G62A/A65S/S66Y, and I178T/T207G.

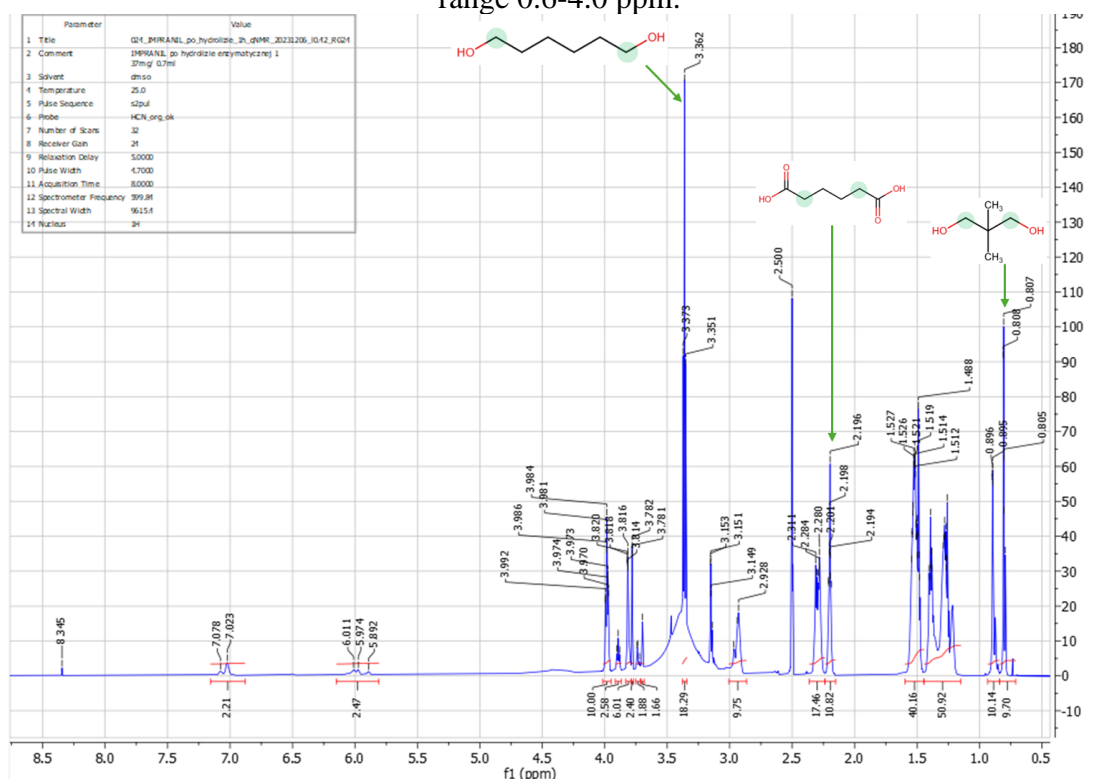
Direct comparisons between computational predictions and experimental results were feasible only in terms of thermostability, using FoldX $\Delta\Delta G$ or Rosetta total score $\Delta\Delta G$. However, no clear correlation between these computational metrics and experimental thermostability was observed, reflecting the inherent complexity of stability changes introduced by mutations. While degradation rates for Impranil DLN could not be directly compared to computational predictions, the analysis highlighted that many mutations designed to improve binding did not lead to increased catalytic efficiency. This suggests that ligand binding is not the rate-limiting step for Impranil DLN degradation. Instead, other factors, such as structural stability, surface properties, or the dynamics of the active site, may play more critical roles in determining enzyme efficiency. These findings underscore the importance of considering the broader context of enzymatic function when interpreting computational predictions and designing future experiments.

Future work could focus on combining successful mutants to guide iterative rounds of enzyme engineering, progressively enhancing PUR degradation efficiency. Additionally, degradation experiments at higher temperatures could be conducted to assess the interplay between thermostability and catalytic performance under industrially relevant conditions.

6.5. Supplementary materials to Chapter 6

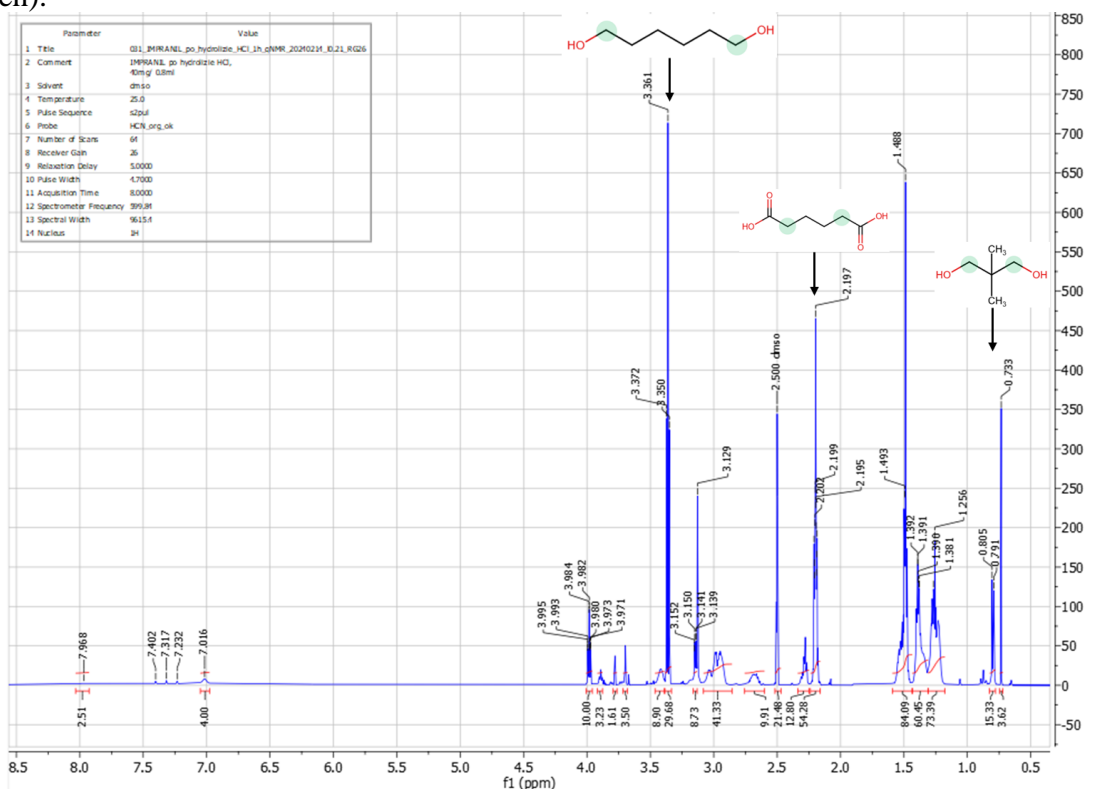


Supplementary figure. 6.1. ¹H NMR spectrum of Impranil DLN in DMSO-d₆ (600MHz), range 0.6-4.0 ppm.

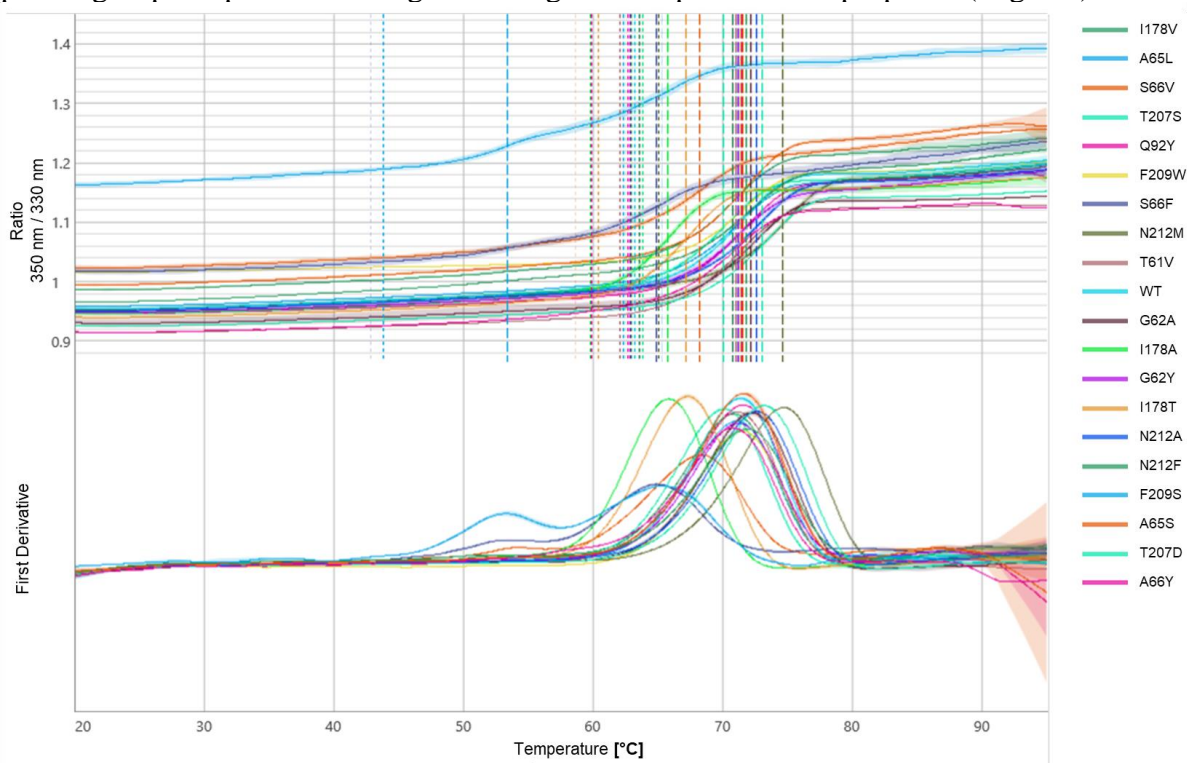


Supplementary figure. 6.2. ¹H NMR spectrum of Impranil DLN after enzymatic hydrolysis by *TfCut2*, in DMSO-d₆ (600MHz), range 0.7-4.8 ppm. Above the picks, chemical structures

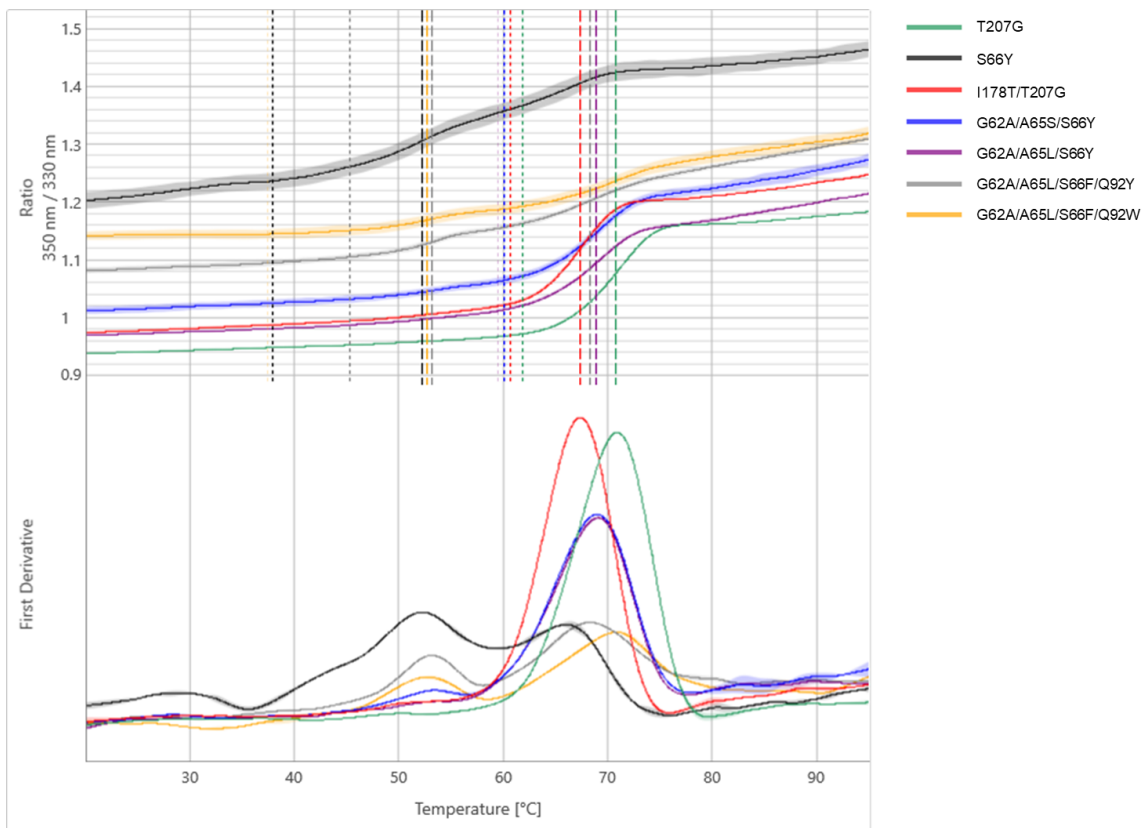
containing proton groups responsible for signals in degradation products are proposed (in green).



Supplementary figure. 6.3. ^1H NMR spectrum of Impranil DLN after hydrolysis in HCl, in DMSO_{d6} (600MHz), range 0.7-4.0 ppm. Above the picks, chemical structures containing proton groups responsible for signals in degradation products are proposed (in green).



Supplementary figure. 6.4. Results of thermostability as measured by nanoDSF: thermal unfolding curves and first derivative.



Supplementary figure. 6.5. Results of thermostability as measured by nanoDSF: thermal unfolding curves and first derivative.

Chapter 7: Conclusions and perspectives

7.1. Summary of key findings

This dissertation addresses the urgent need for effective enzymatic solutions to recycle synthetic polymers, focusing on PUR, one of the primary contributors to plastic waste. Despite significant advances in enzymatic degradation for other synthetic polymers, especially PET, research on PUR degradation remains in the lag phase, representing a substantial knowledge gap. This work is the first computational studies to explore the interaction between a model PUR, Impranil DLN, and *Thermobifida fusca* cutinase (*TfCut2*) and to introduce mutations aimed at enhancing enzymatic degradation of PUR.

This dissertation is a comprehensive study, involving both computational analysis and experimental validation, to investigate the process of enzymatic degradation of PUR. First, NMR studies helped to shed light on the obscure chemical structure of Impranil DLN, a polyester PUR which was a model study in most of the PUR enzymatic degradation studies conducted so far. This approach allowed to model single repeating units of Impranil DLN computationally with more confidence. Subsequently, through a combination of computational chemistry tools, key molecular determinants responsible for PUR recognition and binding by *TfCut2* were identified. The workflow enabled the reconstruction of *TfCut2*-Impranil DLN complex in productive modes, and evaluation of Impranil DLN binding to *TfCut2*'s surface active site. In the process, both ester and urethane bond cleavage sites were considered. By analysing protein-ligand interactions, the dissertation identified residues critical for substrate binding and catalysis, laying the groundwork for *TfCut2* engineering.

A combination of computational tools and evolutionary information was used to propose variants of *TfCut2*. These mutations were designed mainly to enhance Impranil DLN binding through hydrophobic interactions or stabilise binding poses or favour catalytic turnover. Experimental validation of proposed mutants provided valuable insights and revealed that most mutants retained thermostability comparable to the wild-type enzyme, suggesting that the mutations did not significantly disrupt the enzyme's structure. Activity assays revealed that while eight out of fourteen mutants exhibited reduced degradation rates, three showed comparable activity, and three mutations—T61V, T207D, and G62A—demonstrated enhanced Impranil DLN degradation rates. In particular, the G62A mutant exhibited a more than twofold

increase in initial degradation rate, while T207D also facilitated higher protein production yields and long-lasting stability, underscoring its practical value.

These findings underscore the complexity of optimising enzymatic degradation of polymers. While hydrophobic interactions at the binding site play a pivotal role in accommodating large polymer substrates, this study highlights that binding affinity alone may not be the rate-limiting step in polymer degradation. Additional factors, such as substrate positioning, active site accessibility, flexibility, and catalytic turnover, likely contribute to PUR degradation efficiency. This insight aligns with emerging research suggesting that enhancing enzyme performance for synthetic polymer degradation requires a multifaceted approach.

7.2. Limitations of the study

PUR present challenging substrates for enzymatic degradation due to their structural diversity and the variety of hydrolysable bonds they contain. Unlike unified synthetic polymers such as PET, where degradation can be monitored by quantifying specific degradation products like terephthalic acid (TPA), PUR are heterogeneous and lack coherent, standardised degradation markers. Even in cases where PUR are completely degraded, the resulting mixtures contain diverse products that must be further separated and analysed to assess degradation efficiency accurately. Likewise, this problem also severely limits the possibilities of recovering structural units in the recycling process. Consequently, it is inherently difficult to precisely evaluate an enzyme's ability to degrade PUR substrates.

Challenges with the model substrate, Impranil DLN

Impranil DLN was chosen as a model PUR substrate because it becomes translucent upon degradation, providing a convenient method for initial activity testing. However, significant limitations are associated with its use. Its exact composition is proprietary, and reported initial attempts to characterise its structure were found to be incorrect. Even if its primary structural units could be described within this dissertation and confirmed by literature, it remains unclear whether the substrate contains chain extenders, plasticizers, or other additives, and to what extent these components influence degradation.

Additionally, no standard methods exist to directly correlate the observed change in Impranil DLN's translucency with the cleavage of specific bond types (e.g., ester or urethane) or the extent of bond cleavage. For instance, it is uncertain whether complete

translucency indicates the degradation of polymer chains into smaller polymer chain units or if only single monomeric units must remain in the reaction mixture. Furthermore, hydrolysis products are often not fully solubilised, complicating quantitative analysis of the extent of Impranil degradation.

These uncertainties make it difficult to define standard kinetic parameters such as K_M and k_{cat} . The lack of solubility and visibility into reaction intermediates precludes techniques like stop-flow kinetics or measuring initial bursts of activity. This is because stop-flow methods require accurate tracking of substrate and product concentrations over time, which is unfeasible for Impranil DLN due to the heterogeneous and poorly characterised nature of its degradation products. Consequently, the only viable approach was to measure initial degradation rates, which allowed for comparative evaluation between designed *TjCut2* variants.

Limitations in computational modelling

The computational modelling of PUR substrates also presented challenges. Even though the study modelled only a fragment of the PUR polymer (three structural units), the large number of rotatable bonds in these fragments made it computationally infeasible to generate a full set of conformers. As a result, only single structural units of Impranil DLN could be docked using flexible docking protocols, and the rest of the chain had to be reconstructed later. This approach in modelling only a small part of a polymer chain limits the representation of the true behaviour of PUR polymers, as full polymer chains likely exhibit lower flexibility, even in amorphous regions.

The binding of a polymer ligand to the enzyme surface is also rather not specific, complicating the identification of preferential binding poses. Although several binding modes of Impranil DLN to *TjCut2* were modelled, computational methods could not definitely distinguish which pose was most favourable. For example, binding energies for urethane bonds were often lower than those for ester bonds, despite the known preference of *TjCut2* for hydrolysing ester bonds. This limitation underscores the difficulty of accurately modelling and predicting polymer-enzyme interactions computationally.

Challenges in enzyme engineering for PUR degradation

The inability to determine the exact binding pose of the polymer substrate also complicates enzyme engineering. Without a clear understanding of the substrate's binding

mode, it is challenging to design mutations that would optimise specific interactions or catalytic efficiency. Furthermore, the rate-limiting step in enzymatic degradation of PURs remains unclear. While substrate binding likely plays a significant role, the process involves complex dynamics. For instance, plastic-degrading enzymes need to balance thermostability with flexibility to accommodate large, amorphous substrates like PURs.

These challenges are intrinsic to enzymatic catalysis, but the structure and composition of PURs present additional difficulties. The high energy of urethane bonds, which are inherently more resistant to cleavage, makes enzymatic hydrolysis difficult. Moreover, the crystallinity of the hard segments in PURs can limit enzyme accessibility. Most commercially produced PURs are thermosets with covalently crosslinked chains, which further hinder degradation due to their structural rigidity and reduced solubility. While Impranil DLN serves as a convenient model substrate for studying enzymatic degradation, it does not fully capture the complexity of real-world PURs, where these structural challenges significantly impact degradation potential.

The inherent complexity of PURs, with their varied and incoherent structures, further complicates the development of universal enzymes for their degradation. Designing enzymes that are effective across different PUR formulations remains a significant challenge, requiring further investigation into substrate-specific binding and degradation mechanisms.

General limitations

This dissertation faced numerous challenges due to the lack of established knowledge and methodologies in the field of enzymatic PUR degradation. The structural and compositional complexity of PURs, coupled with the proprietary and poorly characterised nature of Impranil DLN, posed significant hurdles. Computational approaches were limited by the size and flexibility of the polymer fragments, while experimental methods struggled with the lack of standardised techniques for assessing degradation efficiency and kinetics.

Nevertheless, within these constraints, the study successfully developed and applied innovative approaches to shed light on the enzymatic degradation of PURs. It provided new insights into the proprietary structure of Impranil DLN and identified promising mutations that enhance degradation efficiency. These findings lay the groundwork for future studies aimed at addressing the significant knowledge gaps in this field.

7.3. Future directions

PUR degradation by enzymes remains an underexplored area, and this dissertation highlights the potential of computational and experimental approaches to address this critical gap. Immediate next steps should include combining the successful single-point mutations (G62A, T61V, T207D) to evaluate potential synergistic effects on catalytic efficiency and stability. Testing these mutants under diverse conditions, such as elevated temperatures or with alternative polymer substrates, could provide deeper insights into their performance and versatility. Furthermore, individual *TfCut2* variants may exhibit distinct specificities for different bond types in PUR, suggesting that a combination or cocktail of enzymes might outperform a single enzyme. However, to achieve this, it is essential to determine which bonds in Impranil DLN (or other PUR substrates) are specifically targeted by each variant.

Future computational studies should also investigate the interactions of enzymes with the surface of solid polymer matrices—a largely unexplored area, as most studies assume direct access to polymer chains. Expanding this work to other classes of PURs, as well as related synthetic polymers, is a promising avenue. The observed similarities in Impranil DLN and PET binding modes, along with the G62A variant's enhanced activity for both substrates [191,316], suggest that findings from cutinase studies on one polymer type can potentially be applied to others. This raises the exciting possibility of engineering enzymes with promiscuous activity, capable of degrading polymer mixtures commonly found in plastic waste. Such enzymes could be invaluable for addressing the heterogeneous nature of real-world polymer waste streams.

Future experimental work should also aim to refine the assessment of enzymatic activity by incorporating small model compounds that mimic PUR structural units. For example, a library of short compounds containing ester, urethane, and amide bonds could help evaluate substrate specificity of variants and provide mechanistic insights into *TfCut2*'s catalytic activity. A similar approach was effectively employed in studies on *HiC* cutinase [22], where enzymatic activity was assessed on substrates like *pNPB*, *pNPC*, *pNPBC*, and *pNPA*. Adopting such protocols could bridge the gap between simplified laboratory assays and the complex nature of polymer degradation.

Another crucial direction is the development of standardised and cohesive protocols for assessing PUR degradation efficiency. Model substrates like Impranil DLN, while useful for initial testing, suffer from proprietary composition and lack of clear degradation metrics.

For PET, compounds like BHET correlate well with the degradation of PET films and provide a reliable estimate of enzymatic hydrolysis [333]. Establishing similar standards for PUR substrates would enable more consistent comparisons across studies and advance the field.

In the long term, this research lays the groundwork for tailoring cutinases to degrade a broader range of synthetic polymers, addressing industrial needs for polymer recycling and environmental remediation. By improving enzyme efficiency and stability, this work contributes to the ongoing development of sustainable solutions for managing polymer waste.

7.4. Broader impact

The degradation of synthetic polymers represents one of the most pressing environmental challenges of our time. Enzymatic biodegradation offers a sustainable and eco-friendly alternative to conventional methods like recycling or incineration. This work underscores the potential of computational and experimental protein engineering to develop enzymes with enhanced catalytic efficiencies and substrate specificities, enabling significant advances in tackling plastic waste.

This research offers a framework for tailoring cutinases to degrade a broader range of synthetic polymers, with implications for industrial polymer recycling and environmental remediation. By enhancing enzyme efficiency and production yield, this work contributes to the development of sustainable solutions for polymer waste management. Overall, this work contributes valuable insights into the rational design of cutinases for polymer degradation, paving the way for future iterative enzyme engineering efforts. In the long run, this research can inform the development of integrated degradation pipelines, incorporating pretreatment processes, optimised reaction conditions, and tailored enzyme formulations for efficient PUR degradation. Furthermore, understanding the molecular mechanisms of polymer degradation could guide the design and production of polymer-based materials that are more easily biodegradable, fostering innovation in sustainable packaging.

Overall, this work highlights the transformative potential of enzymatic solutions to address the global plastic recycling challenge. It provides a stepping stone for future research efforts aimed at creating a circular economy for plastics, particularly PUR, thereby contributing to a more sustainable and environmentally resilient future.

References

- [1] Joo S, Cho JJ, Seo H, Son HF, Sagong HY, Shin TJ, et al. Structural insight into molecular mechanism of poly(ethylene terephthalate) degradation. *Nat Commun* 2018;9. <https://doi.org/10.1038/s41467-018-02881-1>.
- [2] Danso D, Chow J, Streita WR. Plastics: Environmental and biotechnological perspectives on microbial degradation. *Appl Environ Microbiol* 2019;85:1–14. <https://doi.org/10.1128/AEM.01095-19>.
- [3] Biffinger JC, Barlow DE, Cockrell AL, Cusick KD, Hervey WJ, Fitzgerald LA, et al. The applicability of Impranil® DLN for gauging the biodegradation of polyurethanes. *Polym Degrad Stab* 2015;120:178–85. <https://doi.org/10.1016/j.polymdegradstab.2015.06.020>.
- [4] Fuentes-Jaime J, Vargas-Suárez M, Cruz-Gómez MJ, Loza-Tavera H. Concerted action of extracellular and cytoplasmic esterase and urethane-cleaving activities during Impranil biodegradation by *Alicyclophilus denitrificans* BQ1. *Biodegradation* 2022;33:389–406. <https://doi.org/10.1007/s10532-022-09989-8>.
- [5] Praet E. Plastic pollution: archaeological perspective on an Anthropocene climate emergency. *World Archaeol* 2024;1–19. <https://doi.org/10.1080/00438243.2024.2320123>.
- [6] Jayasekara R, Harding I, Bowater I, Loneragan G. Biodegradability of a Selected Range of Polymers and Polymer Blends and Standard Methods for Assessment of Biodegradation. *J Polym Environ* 2005;13:231–51. <https://doi.org/10.1007/s10924-005-4758-2>.
- [7] Kalali EN, Lotfian S, Entezar Shabestari M, Khayatzaadeh S, Zhao C, Yazdani Nezhad H. A critical review of the current progress of plastic waste recycling technology in structural materials. *Curr Opin Green Sustain Chem* 2023;40:100763. <https://doi.org/10.1016/j.cogsc.2023.100763>.
- [8] Tolkien JRR. *The Return of the King*. 1955.
- [9] Lehner R, Weder C, Petri-Fink A, Rothen-Rutishauser B. Emergence of Nanoplastic in the Environment and Possible Impact on Human Health. *Environ Sci Technol* 2019;53:1748–65. <https://doi.org/10.1021/acs.est.8b05512>.
- [10] Pedler K, Davis G. *Mutant 59: The Plastic-Eaters*. 1971.
- [11] Latour B. *Down to Earth: Politics in the New Climatic Regime*. Polity Press; 2018.
- [12] Sagan C. *Pale Blue Dot: A Vision of the Human Future in Space*. 1994.
- [13] Raczynska A, Góra A, André I. An overview on polyurethane degrading enzymes. *Biotechnol Adv* 2024;77:108439. <https://doi.org/10.1016/j.biotechadv.2024.108439>.
- [14] Puetz H, Janknecht C, Contreras F, Vorobii M, Kurkina T, Schwaneberg U. Validated High-Throughput Screening System for Directed Evolution of Nylon-Depolymerizing Enzymes. *ACS Sustain Chem Eng* 2023. <https://doi.org/10.1021/acssuschemeng.3c01575>.
- [15] Polo Fonseca L, Duval A, Luna E, Ximenis M, De Meester S, Avérous L, et al. Reducing the carbon footprint of polyurethanes by chemical and biological depolymerization: Fact or fiction? *Curr Opin Green Sustain Chem* 2023;41:100802. <https://doi.org/10.1016/j.cogsc.2023.100802>.
- [16] Akindoyo JO, Beg MDH, Ghazali S, Islam MR, Jeyaratnam N, Yuvaraj AR. Polyurethane types, synthesis and applications-a review. *RSC Adv* 2016;6:114453–82. <https://doi.org/10.1039/c6ra14525f>.
- [17] Zia KM, Anjum S, Zuber M, Mujahid M, Jamil T. Synthesis and molecular characterization of chitosan based polyurethane elastomers using aromatic diisocyanate. *Int J Biol Macromol* 2014;66:26–32. <https://doi.org/10.1016/j.ijbiomac.2014.01.073>.
- [18] Chattopadhyay DK, Webster DC. Thermal stability and flame retardancy of polyurethanes. *Prog Polym Sci* 2009;34:1068–133. <https://doi.org/10.1016/j.progpolymsci.2009.06.002>.
- [19] Bayer T, Palm GJ, Berndt L, Meinert H, Branson Y, Schmidt L, et al. Structural Elucidation of a Metagenomic Urethanase and Its Engineering Towards Enhanced Hydrolysis Profiles. *Angew Chemie Int Ed* 2024:e202404492. <https://doi.org/10.1002/anie.202404492>.
- [20] Schmidt J, Wei R, Oeser T, Silva LAD e. S, Breite D, Schulze A, et al. Degradation of polyester polyurethane by bacterial polyester hydrolases. *Polymers (Basel)* 2017;9:65. <https://doi.org/10.3390/polym9020065>.
- [21] Hung C-S, Zingarelli S, Nadeau LJ, Biffinger JC, Drake CA, Crouch AL, et al. Carbon Catabolite Repression and Impranil Polyurethane Degradation in *Pseudomonas protegens* Strain Pf-5. *Appl Environ Microbiol* 2016;82:6080–90. <https://doi.org/10.1128/AEM.01448-16>.
- [22] Di Bisceglie F, Quartinello F, Vielnascher R, Guebitz GM, Pellis A. Cutinase-Catalyzed Polyester-Polyurethane Degradation: Elucidation of the Hydrolysis Mechanism. *Polymers (Basel)* 2022;14. <https://doi.org/10.3390/polym14030411>.
- [23] Jiang Z, Chen X, Xue H, Li Z, Lei J, Yu M, et al. Novel polyurethane-degrading cutinase BaCut1 from

- Blastobotrys sp. G-9 with potential role in plastic bio-recycling. *J Hazard Mater* 2024;472:134493. <https://doi.org/10.1016/j.jhazmat.2024.134493>.
- [24] Liu J, Xin K, Zhang T, Wen Y, Li D, Wei R, et al. Identification and characterization of a fungal cutinase-like enzyme CpCut1 from *Cladosporium* sp. P7 for polyurethane degradation. *Appl Environ Microbiol* 2024;90. <https://doi.org/10.1128/aem.01477-23>.
- [25] Ruiz C, Main T, Hilliard NP, Howard GT. Purification and characterization of two polyurethanase enzymes from *Pseudomonas chlororaphis*. *Int Biodeterior Biodegradation* 1999;43:43–7. [https://doi.org/10.1016/S0964-8305\(98\)00067-5](https://doi.org/10.1016/S0964-8305(98)00067-5).
- [26] Branson Y, Sötl S, Buchmann C, Wei R, Schaffert L, Badenhorst CPS, et al. Urethanasases for the Enzymatic Hydrolysis of Low Molecular Weight Carbamates and the Recycling of Polyurethanes. *Angew Chem Int Ed Engl* 2023;62:e202216220. <https://doi.org/10.1002/anie.202216220>.
- [27] Gamerith C, Herrero Acero E, Pellis A, Ortner A, Vielnascher R, Luschnig D, et al. Improving enzymatic polyurethane hydrolysis by tuning enzyme sorption. *Polym Degrad Stab* 2016;132:69–77. <https://doi.org/10.1016/j.polymdegradstab.2016.02.025>.
- [28] Nakajima-Kambe T, Onuma F, Kimpara N, Nakahara T. Isolation and characterization of a bacterium which utilizes polyester polyurethane as a sole carbon and nitrogen source. *FEMS Microbiol Lett* 1995;129:39–42. [https://doi.org/10.1016/0378-1097\(95\)00131-N](https://doi.org/10.1016/0378-1097(95)00131-N).
- [29] Nomura N, Shigeno-Akutsu Y, Nakajima-Kambe T, Nakahara T. Cloning and sequence analysis of a polyurethane esterase of *Comamonas acidovorans* TB-35. *J Ferment Bioeng* 1998;86:339–45. [https://doi.org/10.1016/S0922-338X\(99\)89001-1](https://doi.org/10.1016/S0922-338X(99)89001-1).
- [30] Shigeno-Akutsu Y, Nakajima-Kambe T, Nomura N, Nakahara T. Purification and properties of culture-broth-secreted esterase from the polyurethane degrader *Comamonas acidovorans* TB-35. *J Biosci Bioeng* 1999;88:484–7. [https://doi.org/10.1016/s1389-1723\(00\)87663-x](https://doi.org/10.1016/s1389-1723(00)87663-x).
- [31] Gautam R, Bassi AS, Yanful EK. *Candida rugosa* lipase-catalyzed polyurethane degradation in aqueous medium. *Biotechnol Lett* 2007;29:1081–6. <https://doi.org/10.1007/s10529-007-9354-1>.
- [32] Ufarté L, Laville E, Duquesne S, Morgavi D, Robe P, Klopp C, et al. Discovery of carbamate degrading enzymes by functional metagenomics. *PLoS One* 2017;12:e0189201.
- [33] Howard GT, Ruiz C, Hilliard NP. Growth of *Pseudomonas chlororaphis* on a polyester–polyurethane and the purification and characterization of a polyurethanase–esterase enzyme. *Int Biodeterior Biodegradation* 1999;43:7–12. [https://doi.org/10.1016/S0964-8305\(98\)00057-2](https://doi.org/10.1016/S0964-8305(98)00057-2).
- [34] Howard GT, Crother B, Vicknair J. Cloning, nucleotide sequencing and characterization of a polyurethanase gene (pueB) from *Pseudomonas chlororaphis*. *Int Biodeterior Biodegradation* 2001;47:141–9. [https://doi.org/10.1016/S0964-8305\(01\)00042-7](https://doi.org/10.1016/S0964-8305(01)00042-7).
- [35] Howard GT, Mackie RI, Cann IKO, Ohene-Adjei S, Aboudehen KS, Duos BG, et al. Effect of insertional mutations in the pueA and pueB genes encoding two polyurethanasases in *Pseudomonas chlororaphis* contained within a gene cluster. *J Appl Microbiol* 2007;103:2074–83. <https://doi.org/10.1111/j.1365-2672.2007.03447.x>.
- [36] Stern R V, Howard GT. The polyester polyurethanase gene (pueA) from *Pseudomonas chlororaphis* encodes a lipase. *FEMS Microbiol Lett* 2000;185:163–8. <https://doi.org/10.1111/j.1574-6968.2000.tb09056.x>.
- [37] Hung C-S, Zingarelli S, Nadeau LJ, Biffinger JC, Drake CA, Crouch AL, et al. Carbon Catabolite Repression and Impranil Polyurethane Degradation in *Pseudomonas protegens* Strain Pf-5. *Appl Environ Microbiol* 2016;82:6080–90. <https://doi.org/10.1128/AEM.01448-16>.
- [38] Howard GT, Blake RC. Growth of *Pseudomonas fluorescens* on a polyester–polyurethane and the purification and characterization of a polyurethanase–protease enzyme. *Int Biodeterior Biodegradation* 1998;42:213–20. [https://doi.org/10.1016/S0964-8305\(98\)00051-1](https://doi.org/10.1016/S0964-8305(98)00051-1).
- [39] Vega RE, Main T, Howard GT. Cloning and expression in *Escherichia coli* of apolyurethane-degrading enzyme from *Pseudomonas fluorescens*. *Int Biodeterior Biodegradation* 1999;43:49–55. [https://doi.org/10.1016/S0964-8305\(98\)00068-7](https://doi.org/10.1016/S0964-8305(98)00068-7).
- [40] Plastics – the fast Facts 2023. *Plast Eur* 2023;2023.
- [41] Pu M, Fang C, Zhou X, Wang D, Lin Y, Lei W, et al. Recent Advances in Environment-Friendly Polyurethanes from Polyols Recovered from the Recycling and Renewable Resources: A Review. *Polymers (Basel)* 2024;16. <https://doi.org/10.3390/polym16131889>.
- [42] Furtwengler P, Avérous L. Renewable polyols for advanced polyurethane foams from diverse biomass resources. *Polym Chem* 2018;9:4258–87. <https://doi.org/10.1039/C8PY00827B>.
- [43] Straits Research. *Global Polyurethane Mark Size, Share Trends Anal Rep By Prod (Flexible Foam Rigid Foam By Appl (Furniture Bedding, Automotive, Electron By Reg Segm Forecast 2023 - 2031* 2023.
- [44] Vollmer I, Jenks MJF, Roelands MCP, White RJ, van Harmelen T, de Wild P, et al. Beyond Mechanical Recycling: Giving New Life to Plastic Waste. *Angew Chemie - Int Ed* 2020;59:15402–23.

- <https://doi.org/10.1002/anie.201915651>.
- [45] Ellis LD, Rorrer NA, Sullivan KP, Otto M, McGeehan JE, Román-Leshkov Y, et al. Chemical and biological catalysis for plastics recycling and upcycling. *Nat Catal* 2021;4:539–56. <https://doi.org/10.1038/s41929-021-00648-4>.
- [46] Wei R, Tiso T, Bertling J, O'Connor K, Blank LM, Bornscheuer UT. Possibilities and limitations of biotechnological plastic degradation and recycling. *Nat Catal* 2020;3:867–71. <https://doi.org/10.1038/s41929-020-00521-w>.
- [47] Jönsson C, Wei R, Biundo A, Landberg J, Schwarz Bour L, Pezzotti F, et al. Biocatalysis in the Recycling Landscape for Synthetic Polymers and Plastics towards Circular Textiles. *ChemSusChem* 2021;14:4028–40. <https://doi.org/10.1002/cssc.202002666>.
- [48] Tournier V, Topham CM, Gilles A, David B, Folgoas C, Moya-Leclair E, et al. An engineered PET depolymerase to break down and recycle plastic bottles. *Nature* 2020;580:216–9. <https://doi.org/10.1038/s41586-020-2149-4>.
- [49] Yoshida S, Hiraga K, Takehana T, Taniguchi I, Yamaji H, Maeda Y, et al. A bacterium that degrades and assimilates poly(ethylene terephthalate). *Science* (80-) 2016.
- [50] Lopez-Lorenzo X, Huetting D, Bosshard E, Syrén P-O. Degradation of PET microplastic particles to monomers in human serum by PETase. *Faraday Discuss* 2024. <https://doi.org/10.1039/D4FD00014E>.
- [51] Sevilla ME, Garcia MD, Perez-Castillo Y, Armijos-Jaramillo V, Casado S, Vizuete K, et al. Degradation of PET Bottles by an Engineered Ideonella sakaiensis PETase. *Polymers (Basel)* 2023;15. <https://doi.org/10.3390/polym15071779>.
- [52] Taniguchi I, Yoshida S, Hiraga K, Miyamoto K, Kimura Y, Oda K. Biodegradation of PET: Current Status and Application Aspects. *ACS Catal* 2019;9:4089–105. <https://doi.org/10.1021/acscatal.8b05171>.
- [53] Kushwaha A, Goswami L, Singhvi M, Kim BS. Biodegradation of poly(ethylene terephthalate): Mechanistic insights, advances, and future innovative strategies. *Chem Eng J* 2023;457:141230. <https://doi.org/10.1016/j.cej.2022.141230>.
- [54] Tournier V, Duquesne S, Guillaumot F, Cramail H, Taton D, Marty A, et al. Enzymes' Power for Plastics Degradation. *Chem Rev* 2023. <https://doi.org/10.1021/acs.chemrev.2c00644>.
- [55] Qiu J, Chen Y, Zhang L, Wu J, Zeng X, Shi X, et al. A comprehensive review on enzymatic biodegradation of polyethylene terephthalate. *Environ Res* 2024;240:117427. <https://doi.org/10.1016/j.envres.2023.117427>.
- [56] Skleničková K, Abbrent S, Halecký M, Kočí V, Beneš H. Biodegradability and ecotoxicity of polyurethane foams: A review. *Crit Rev Environ Sci Technol* 2022;52:157–202. <https://doi.org/10.1080/10643389.2020.1818496>.
- [57] Magnin A, Pollet E, Phalip V, Avérous L. Evaluation of biological degradation of polyurethanes. *Biotechnol Adv* 2020;39:107457. <https://doi.org/10.1016/j.biotechadv.2019.107457>.
- [58] Liu J, He J, Xue R, Xu B, Qian X, Xin F, et al. Biodegradation and up-cycling of polyurethanes: Progress, challenges, and prospects. *Biotechnol Adv* 2021;48:107730. <https://doi.org/10.1016/j.biotechadv.2021.107730>.
- [59] Huang S, Podgórski M, Han X, Bowman CN. Chemical recycling of poly(thiourethane) thermosets enabled by dynamic thiourethane bonds. *Polym Chem* 2020;11:6879–83. <https://doi.org/10.1039/D0PY01050B>.
- [60] Sheppard DT, Jin K, Hamachi LS, Dean W, Fortman DJ, Ellison CJ, et al. Reprocessing Postconsumer Polyurethane Foam Using Carbamate Exchange Catalysis and Twin-Screw Extrusion. *ACS Cent Sci* 2020;6:921–7. <https://doi.org/10.1021/acscentsci.0c00083>.
- [61] Ding H, Zhao B, Mei H, Li L, Zheng S. Transformation of Commodity Poly(hydroxyether of bisphenol A) into Vitrimers *via* Post Crosslinking with Hindered Urea Bonds. *Chinese J Polym Sci* 2020;38:915–20. <https://doi.org/10.1007/s10118-020-2457-z>.
- [62] Fortman DJ, Sheppard DT, Dichtel WR. Reprocessing Cross-Linked Polyurethanes by Catalyzing Carbamate Exchange. *Macromolecules* 2019;52:6330–5. <https://doi.org/10.1021/acs.macromol.9b01134>.
- [63] Wang S, Yang Y, Ying H, Jing X, Wang B, Zhang Y, et al. Recyclable, Self-Healable, and Highly Malleable Poly(urethane-urea)s with Improved Thermal and Mechanical Performances. *ACS Appl Mater Interfaces* 2020;12:35403–14. <https://doi.org/10.1021/acsami.0c07553>.
- [64] Gamardella F, Guerrero F, De la Flor S, Ramis X, Serra A. A new class of vitrimers based on aliphatic poly(thiourethane) networks with shape memory and permanent shape reconfiguration. *Eur Polym J* 2020;122:109361. <https://doi.org/10.1016/j.eurpolymj.2019.109361>.
- [65] Gamardella F, Muñoz S, De la Flor S, Ramis X, Serra A. Recyclable Organocatalyzed Poly(Thiourethane) Covalent Adaptable Networks. *Polymers (Basel)* 2020;12. <https://doi.org/10.3390/polym12122913>.
- [66] Jia Y, Ying H, Zhang Y, He H, Cheng J. Reconfigurable Poly(urea-urethane) Thermoset Based on Hindered Urea Bonds with Triple-Shape-Memory Performance. *Macromol Chem Phys*

- 2019;220:1900148. <https://doi.org/10.1002/macp.201900148>.
- [67] Zhang K, Hu J, Yang S, Xu W, Wang Z, Zhuang P, et al. Biodegradation of polyester polyurethane by the marine fungus *Cladosporium halotolerans* 6UPA1. *J Hazard Mater* 2022;437:129406. <https://doi.org/10.1016/j.jhazmat.2022.129406>.
- [68] Puiggené Ò, Espinosa MJC, Schlosser D, Thies S, Jehmlich N, Kappelmeier U, et al. Extracellular degradation of a polyurethane oligomer involving outer membrane vesicles and further insights on the degradation of 2,4-diaminotoluene in *Pseudomonas capeferrum* TDA1. *Sci Rep* 2022;12:2666. <https://doi.org/10.1038/s41598-022-06558-0>.
- [69] Álvarez-Barragán J, Domínguez-Malfavón L, Vargas-Suárez M, González-Hernández R, Aguilar-Osorio G, Loza-Tavera H. Biodegradative activities of selected environmental fungi on a polyester polyurethane varnish and polyether polyurethane foams. *Appl Environ Microbiol* 2016;82:5225–35. <https://doi.org/10.1128/AEM.01344-16>.
- [70] Magnin A, Entzmann L, Pollet E, Avérous L. Breakthrough in polyurethane bio-recycling: An efficient laccase-mediated system for the degradation of different types of polyurethanes. *Waste Manag* 2021;132:23–30. <https://doi.org/10.1016/j.wasman.2021.07.011>.
- [71] Santerre JP, Labow RS, Duguay DG, Erfle D, Adams GA. Biodegradation evaluation of polyether and polyester-urethanes with oxidative and hydrolytic enzymes. *J Biomed Mater Res* 1994;28:1187–99. <https://doi.org/10.1002/jbm.820281009>.
- [72] Nakajima-Kambe T, Onuma F, Akutsu Y, Nakahara T. Determination of the polyester polyurethane breakdown products and distribution of the polyurethane degrading enzyme of *Comamonas acidovorans* strain TB-35. *J Ferment Bioeng* 1997;83:456–60. [https://doi.org/10.1016/S0922-338X\(97\)83000-0](https://doi.org/10.1016/S0922-338X(97)83000-0).
- [73] Labow RS, Erfle DJ, Santerre JP. Elastase-induced hydrolysis of synthetic solid substrates: poly(ester-urea-urethane) and poly(ether-urea-urethane). *Biomaterials* 1996;17:2381–8. [https://doi.org/10.1016/S0142-9612\(96\)00088-9](https://doi.org/10.1016/S0142-9612(96)00088-9).
- [74] Yamamoto N, Nakayama A, Oshima M, Kawasaki N, Aiba S. Enzymatic hydrolysis of lysine diisocyanate based polyurethanes and segmented polyurethane ureas by various proteases. *React Funct Polym* 2007;67:1338–45. <https://doi.org/10.1016/j.reactfunctpolym.2007.08.011>.
- [75] Campiñez M, Aguilar-de-Leyva Á, Ferris C, De Paz MV, Galbis J, Caraballo I. Study of the properties of the new biodegradable polyurethane PU (TEG-HMDI) as matrix forming excipient for controlled drug delivery. *Drug Dev Ind Pharm* 2013;39:1758–64. <https://doi.org/10.3109/03639045.2012.736516>.
- [76] Liu J, Zeng Q, Lei H, Xin K, Xu A, Wei R, et al. Biodegradation of polyester polyurethane by *Cladosporium* sp. P7: Evaluating its degradation capacity and metabolic pathways. *J Hazard Mater* 2023;448:130776. <https://doi.org/10.1016/j.jhazmat.2023.130776>.
- [77] Magnin A, Entzmann L, Bazin A, Pollet E, Avérous L. Green Recycling Process for Polyurethane Foams by a Chem-Biotech Approach. *ChemSusChem* 2021;14:4234–41. <https://doi.org/10.1002/cssc.202100243>.
- [78] Jin X, Dong J, Guo X, Ding M, Bao R, Luo Y. Current advances in polyurethane biodegradation. *Polym Int* 2022;71:1384–92. <https://doi.org/10.1002/pi.6360>.
- [79] Akutsu-Shigeno Y, Adachi Y, Yamada C, Toyoshima K, Nomura N, Uchiyama H, et al. Isolation of a bacterium that degrades urethane compounds and characterization of its urethane hydrolase. *Appl Microbiol Biotechnol* 2006;70:422–9. <https://doi.org/10.1007/s00253-005-0071-1>.
- [80] Russell JR, Huang J, Anand P, Kucera K, Sandoval AG, Dantzer KW, et al. Biodegradation of polyester polyurethane by endophytic fungi. *Appl Environ Microbiol* 2011;77:6076–84. <https://doi.org/10.1128/AEM.00521-11>.
- [81] Masaki K, Fujihara K, Kakizono D, Mizukure T, Okuda M, Mukai N. *Aspergillus oryzae* acetamidase catalyzes degradation of ethyl carbamate. *J Biosci Bioeng* 2020;130:577–81. <https://doi.org/10.1016/j.jbiosc.2020.07.015>.
- [82] Jia Y, Zhou J, Du G, Chen J, Fang F. Identification of an urethanase from *Lysinibacillus fusiformis* for degrading ethyl carbamate in fermented foods. *Food Biosci* 2020;36:100666. <https://doi.org/10.1016/j.fbio.2020.100666>.
- [83] Kang T, Lin J, Yang L, Wu M. Expression, isolation, and identification of an ethanol-resistant ethyl carbamate-degrading amidase from *Agrobacterium tumefaciens* d3. *J Biosci Bioeng* 2021;132:220–5. <https://doi.org/10.1016/j.jbiosc.2021.05.003>.
- [84] Czeiszperger R. Hydrolytic stability of PU elastomers -A comprehensive review. *GAK Gummi Fasern Kunststoffe* 2012;66:772–8.
- [85] De Souza FM, Kahol PK, Gupta RK. Introduction to Polyurethane Chemistry. *ACS Symp Ser* 2021;1380:1–24. <https://doi.org/10.1021/bk-2021-1380.ch001>.
- [86] Atiqah A, Mastura TM, Ali AAB, Jawaid M, Sapuan MS. A Review on Polyurethane and its Polymer Composites. *Curr Org Synth* 2017;14:233–48. <https://doi.org/10.2174/1570179413666160831124749>.

- [87] Dutta AS. 2 - Polyurethane Foam Chemistry. *Plast Des Libr* 2018;17–27. <https://doi.org/10.1016/B978-0-323-51133-9.00002-4>.
- [88] Maurya AK, de Souza FM, Gupta RK. Polyurethane and Its Composites: Synthesis to Application. *Polyurethanes Prep Prop Appl Vol 1 Fundam* 2023;1452:1. <https://doi.org/doi:10.1021/bk-2023-1452.ch001>.
- [89] Jiang R, Zheng X, Zhu S, Li W, Zhang H, Liu Z, et al. Recent Advances in Functional Polyurethane Chemistry: From Structural Design to Applications. *ChemistrySelect* 2023;8:e202204132. <https://doi.org/10.1002/slct.202204132>.
- [90] Soto M, Sebastián RM, Marquet J. Photochemical activation of extremely weak nucleophiles: highly fluorinated urethanes and polyurethanes from polyfluoro alcohols. *J Org Chem* 2014;79:5019–27. <https://doi.org/10.1021/jo5005789>.
- [91] Ristić I, Cakić S, Vukić N, Teofilović V, Tanasić J, Pilić B. The Influence of Soft Segment Structure on the Properties of Polyurethanes. *Polymers (Basel)* 2023;15. <https://doi.org/10.3390/polym15183755>.
- [92] Sadeghi MMG, Sayaf M. From PET Waste to Novel Polyurethanes. *Mater. Recycl. - Trends Perspect.*, 2012. <https://doi.org/10.5772/31642>.
- [93] Lu X, Wang Y, Wu X. Study of hydrogen bonds in polyester-polyurethanes by solution n.m.r. *Polymer (Guildf)* 1994;35:2315–20. [https://doi.org/10.1016/0032-3861\(94\)90767-6](https://doi.org/10.1016/0032-3861(94)90767-6).
- [94] Tang Y, Labow R, Santerre J. Enzyme-induced biodegradation of polycarbonate-polyurethanes: Dependence on hard-segment chemistry. *J Biomed Mater Res* 2001;57:597–611. [https://doi.org/10.1002/1097-4636\(20011215\)57:43.3.CO;2-K](https://doi.org/10.1002/1097-4636(20011215)57:43.3.CO;2-K).
- [95] Tang YW, Labow R, Santerre J. Enzyme-induced biodegradation of polycarbonate polyurethanes: Dependence on hard-segment concentration. *J Biomed Mater Res* 2001;56:516–28. [https://doi.org/10.1002/1097-4636\(20010915\)56:4<516::AID-JBM1123>3.0.CO;2-B](https://doi.org/10.1002/1097-4636(20010915)56:4<516::AID-JBM1123>3.0.CO;2-B).
- [96] Zhao X, Liu X, Feng K, An W-L, Tian F, Du R, et al. Multicycling of Epoxy Thermoset Through a Two-Step Strategy of Alcoholysis and Hydrolysis using a Self-Separating Catalysis System. *ChemSusChem* 2022;15:e202101607. <https://doi.org/10.1002/cssc.202101607>.
- [97] Oertel G. *Polyurethane handbook*. Hanser Publ 1985.
- [98] Jayakumar R, Nanjundan S, Prabaharan M. Metal-containing polyurethanes, poly(urethane–urea)s and poly(urethane–ether)s: A review. *React Funct Polym* 2006;66:299–314. <https://doi.org/10.1016/j.reactfunctpolym.2004.12.008>.
- [99] Loredó-Treviño A, Gutiérrez-Sánchez G, Rodríguez-Herrera R, Aguilar CN. Microbial Enzymes Involved in Polyurethane Biodegradation: A Review. *J Polym Environ* 2012;20:258–65. <https://doi.org/10.1007/s10924-011-0390-5>.
- [100] Magnin A, Pollet E, Avérous L. Chapter Fifteen - Characterization of the enzymatic degradation of polyurethanes. *Enzym Plast Degrad* 2021;648:317–36. <https://doi.org/10.1016/bs.mie.2020.12.011>.
- [101] Du Y, Liu X, Shah N, Liu S, Zhang J, Zhou B. ChemSpace: Interpretable and Interactive Chemical Space Exploration. *ChemRxiv* 2022. <https://doi.org/10.26434/chemrxiv-2022-x49mh-v3>.
- [102] Jones, Frank N., Nichols, Mark E., Pappas SP. *Organic coatings : science and technology*, Fourth Edition. 2017.
- [103] Crabbe JR, Campbell JR, Thompson L, Walz SL, Schultz WW. Biodegradation of a colloidal ester-based polyurethane by soil fungi. *Int Biodeterior Biodegradation* 1994;33:103–13. [https://doi.org/10.1016/0964-8305\(94\)90030-2](https://doi.org/10.1016/0964-8305(94)90030-2).
- [104] Brunner I, Fischer M, Rüthi J, Stierli B, Frey B. Ability of fungi isolated from plastic debris floating in the shoreline of a lake to degrade plastics. *PLoS One* 2018;13:e0202047.
- [105] Howard GT, Vicknair J, Mackie RI. Sensitive plate assay for screening and detection of bacterial polyurethanase activity. *Lett Appl Microbiol* 2001;32:211–4.
- [106] Molitor R, Bollinger A, Kubicki S, Loeschke A, Jaeger K-E, Thies S. Agar plate-based screening methods for the identification of polyester hydrolysis by *Pseudomonas* species. *Microb Biotechnol* 2020;13:274–84. <https://doi.org/10.1111/1751-7915.13418>.
- [107] Acevedo-rocha C, Bakshi A, Bornscheuer UT, Campopiano DJ, Civi J, Ehinger FJ, et al. Artificial, biomimetic and hybrid enzymes: general discussion. *Faraday Discuss* 2024. <https://doi.org/10.1039/d4fd90024c>.
- [108] Ciuffi B, Fratini E, Rosi L. Plastic pretreatment: The key for efficient enzymatic and biodegradation processes. *Polym Degrad Stab* 2024;222:110698. <https://doi.org/10.1016/j.polymdegradstab.2024.110698>.
- [109] Bhardwaj H, Gupta R, Tiwari A. Communities of Microbial Enzymes Associated with Biodegradation of Plastics. *J Polym Environ* 2013;21:575–9. <https://doi.org/10.1007/s10924-012-0456-z>.
- [110] Dai Z, Hatano B, Kadokawa J, Tagaya H. Effect of diaminotoluene on the decomposition of polyurethane foam waste in superheated water. *Polym Degrad Stab* 2002;76:179–84. <https://doi.org/10.1016/S0141->

- 3910(02)00010-1.
- [111] Paciorek-Sadowska J, Czupryński B, Liszkowska J. Glycolysis of rigid polyurethane–polyisocyanurate foams with reduced flammability. *J Elastomers Plast* 2015;48:340–53. <https://doi.org/10.1177/0095244315576244>.
- [112] Beneš H, Rösner J, Holler P, Synková H, Kotek J, Horák Z. Glycolysis of flexible polyurethane foam in recycling of car seats. *Polym Adv Technol* 2007;18:149–56. <https://doi.org/10.1002/pat.810>.
- [113] Mitova V, Grancharov G, Molero C, Borreguero AM, Troev K, Rodriguez JF. Chemical Degradation of Polymers (Polyurethanes, Polycarbonate and Polyamide) by Esters of H-phosphonic and Phosphoric Acids. *J Macromol Sci Part A* 2013;50:774–95. <https://doi.org/10.1080/10601325.2013.792667>.
- [114] Nikje MMA, Nikrah M, Mohammadi FHA. Microwave-assisted Polyurethane Bond Cleavage via Hydroglycolysis Process at Atmospheric Pressure. *J Cell Plast* 2008;44:367–80. <https://doi.org/10.1177/0021955X08090279>.
- [115] Gallorini R, Ciuffi B, Real Fernández F, Carozzini C, Ravera E, Papini AM, et al. Subcritical Hydrothermal Liquefaction as a Pretreatment for Enzymatic Degradation of Polyurethane. *ACS Omega* 2022;7:37757–63. <https://doi.org/10.1021/acsomega.2c04734>.
- [116] Lattuati-Derieux A, Thao-Heu S, Lavédrine B. Assessment of the degradation of polyurethane foams after artificial and natural ageing by using pyrolysis-gas chromatography/mass spectrometry and headspace-solid phase microextraction-gas chromatography/mass spectrometry. *J Chromatogr A* 2011;1218:4498–508. <https://doi.org/10.1016/j.chroma.2011.05.013>.
- [117] Yarahmadi N, Vega A, Jakubowicz I. Accelerated ageing and degradation characteristics of rigid polyurethane foam. *Polym Degrad Stab* 2017;138. <https://doi.org/10.1016/j.polymdegradstab.2017.03.012>.
- [118] Davies P, Evrard G. Accelerated ageing of polyurethanes for marine applications. *Polym Degrad Stab* 2007;92:1455–64. <https://doi.org/10.1016/j.polymdegradstab.2007.05.016>.
- [119] Magnin A, Pollet E, Perrin R, Ullmann C, Persillon C, Phalip V, et al. Enzymatic recycling of thermoplastic polyurethanes: Synergistic effect of an esterase and an amidase and recovery of building blocks. *Waste Manag* 2019;85:141–50. <https://doi.org/10.1016/j.wasman.2018.12.024>.
- [120] Ozsagioglu E, Iyisan B, Guvenilir Y. Biodegradation and Characterization Studies of Different Kinds of Polyurethanes with Several Enzyme Solutions. *Polish J Environ Stud* 2013;21:1777–82.
- [121] Marson A, Masiero M, Modesti M, Scipioni A, Manzardo A. Life Cycle Assessment of Polyurethane Foams from Polyols Obtained through Chemical Recycling. *ACS Omega* 2021;6:1718–24. <https://doi.org/10.1021/acsomega.0c05844>.
- [122] Wiatrowski M, Tan ECD, Davis R. Chapter 6 - TEA and LCA of bio-based polyurethanes. In: Pomeroy RSBT-RPP, editor. *Emerg. Issues Anal. Chem.*, Elsevier; 2023, p. 153–76. <https://doi.org/10.1016/B978-0-323-99982-3.00004-3>.
- [123] Dong C-D, Tiwari A, Anisha GS, Chen C-W, Singh A, Haldar D, et al. Laccase: A potential biocatalyst for pollutant degradation. *Environ Pollut* 2023;319:120999. <https://doi.org/10.1016/j.envpol.2023.120999>.
- [124] Alcántara AR, Hernaiz M-J, Sinisterra J-V. 3.28 - Biocatalyzed Production of Fine Chemicals. In: Moo-Young MBT-CB (Second E, editor. *Compr. Biotechnol.*, Burlington: Academic Press; 2011, p. 309–31. <https://doi.org/10.1016/B978-0-08-088504-9.00225-7>.
- [125] Akutsu Y, Nakajima-Kambe T, Nomura N, Nakahara T. Purification and Properties of a Polyester Polyurethane-Degrading Enzyme from *Comamonas acidovorans* TB-35. *Appl Environ Microbiol* 1998;64:62–7. <https://doi.org/10.1128/AEM.64.1.62-67.1998>.
- [126] Shah Z, Hasan F, Krumholz L, Aktas DF, Shah AA. Degradation of polyester polyurethane by newly isolated *Pseudomonas aeruginosa* strain MZA-85 and analysis of degradation products by GC–MS. *Int Biodeterior Biodegradation* 2013;77:114–22. <https://doi.org/10.1016/j.ibiod.2012.11.009>.
- [127] Buchholz PCF, Feuerriegel G, Zhang H, Perez-Garcia P, Nover L-L, Chow J, et al. Plastics degradation by hydrolytic enzymes: The plastics-active enzymes database—PAZy. *Proteins Struct Funct Bioinforma* 2022;90:1443–56. <https://doi.org/10.1002/prot.26325>.
- [128] de Witt J, Molitor R, Gätgens J, Ortmann de Percin Northumberland C, Kruse L, Polen T, et al. Biodegradation of poly(ester-urethane) coatings by *Halopseudomonas formosensis*. *Microb Biotechnol* 2023;1–15. <https://doi.org/10.1111/1751-7915.14362>.
- [129] Masaki K, Mizukure T, Kakizono D, Fujihara K, Fujii T, Mukai N. New urethanase from the yeast *Candida parapsilosis*. *J Biosci Bioeng* 2020;130:115–20. <https://doi.org/10.1016/j.jbiosc.2020.03.005>.
- [130] Trott S, Bauer R, Knackmuss HJ, Stolz A. Genetic and biochemical characterization of an enantioselective amidase from *Agrobacterium tumefaciens* strain d3. *Microbiology* 2001;147:1815–24. <https://doi.org/10.1099/00221287-147-7-1815>.
- [131] UniProt: the Universal Protein Knowledgebase in 2023. *Nucleic Acids Res* 2023;51:D523–31.

- <https://doi.org/10.1093/nar/gkac1052>.
- [132] Wheeler DL, Barrett T, Benson DA, Bryant SH, Canese K, Chetvernin V, et al. Database resources of the national center for biotechnology information. *Nucleic Acids Res* 2006;35:D5–D12.
- [133] Katoh K, Rozewicki J, Yamada KD. MAFFT online service: multiple sequence alignment, interactive sequence choice and visualization. *Brief Bioinform* 2019;20:1160–6. <https://doi.org/10.1093/bib/bbx108>.
- [134] Stothard P. The sequence manipulation suite: JavaScript programs for analyzing and formatting protein and DNA sequences. *Biotechniques* 2000;28:1102,1104. <https://doi.org/10.2144/00286ir01>.
- [135] McKinney W, others. Data structures for statistical computing in python. *Proc. 9th Python Sci. Conf.*, vol. 445, 2010, p. 51–6.
- [136] Waskom M, Botvinnik O, O’Kane D, Hobson P, Lukauskas S, Gemperline DC, et al. *mwaskom/seaborn: v0.8.1 (September 2017)* 2017. <https://doi.org/10.5281/zenodo.883859>.
- [137] Galmés MÁ, Nödling AR, He K, Luk LYP, Świderek K, Moliner V. Computational design of an amidase by combining the best electrostatic features of two promiscuous hydrolases. *Chem Sci* 2022;13:4779–87. <https://doi.org/10.1039/D2SC00778A>.
- [138] Galmés MÁ, García-Junceda E, Świderek K, Moliner V. Exploring the Origin of Amidase Substrate Promiscuity in CALB by a Computational Approach. *ACS Catal* 2020;10:1938–46. <https://doi.org/10.1021/acscatal.9b04002>.
- [139] Biundo A, Subagia R, Maurer M, Ribitsch D, Syrén P-O, Guebitz GM. Switched reaction specificity in polyesterses towards amide bond hydrolysis by enzyme engineering. *RSC Adv* 2019;9:36217–26. <https://doi.org/10.1039/C9RA07519D>.
- [140] Syrén PO, Hendil-Forsell P, Aumailley L, Besenmatter W, Gounine F, Svendsen A, et al. Esterases with an Introduced Amidase-Like Hydrogen Bond in the Transition State Have Increased Amidase Specificity. *ChemBioChem* 2012;13:645–8. <https://doi.org/10.1002/cbic.201100779>.
- [141] Hackenschmidt S, Moldenhauer EJ, Behrens GA, Gand M, Pavlidis I V, Bornscheuer UT. Enhancement of Promiscuous Amidase Activity of a *Bacillus subtilis* Esterase by Formation of a π - π Network. *ChemCatChem* 2014;6:1015–20. <https://doi.org/10.1002/cctc.201300837>.
- [142] Kourist R, Bartsch S, Fransson L, Hult K, Bornscheuer UT. Understanding Promiscuous Amidase Activity of an Esterase from *Bacillus subtilis*. *ChemBioChem* 2008;9:67–9. <https://doi.org/10.1002/cbic.200700521>.
- [143] Jung S, Kim J, Park S. Rational design for enhancing promiscuous activity of *Candida antarctica* lipase B: a clue for the molecular basis of dissimilar activities between lipase and serine-protease. *RSC Adv* 2013;3:2590–4. <https://doi.org/10.1039/C2RA23333A>.
- [144] Kürten C, Carlberg B, Syrén P-O. Mechanism-Guided Discovery of an Esterase Scaffold with Promiscuous Amidase Activity. *Catalysts* 2016;6. <https://doi.org/10.3390/catal6060090>.
- [145] Berman HM. The Protein Data Bank. *Nucleic Acids Res* 2000;28:235–42. <https://doi.org/10.1093/nar/28.1.235>.
- [146] Jumper J, Evans R, Pritzel A, Green T, Figurnov M, Ronneberger O, et al. Highly accurate protein structure prediction with AlphaFold. *Nature* 2021;596:583–9. <https://doi.org/10.1038/s41586-021-03819-2>.
- [147] Varadi M, Bertoni D, Magana P, Paramval U, Pidruchna I, Radhakrishnan M, et al. AlphaFold Protein Structure Database in 2024: providing structure coverage for over 214 million protein sequences. *Nucleic Acids Res* 2024;52:D368–75. <https://doi.org/10.1093/nar/gkad1011>.
- [148] Varadi M, Anyango S, Deshpande M, Nair S, Natassia C, Yordanova G, et al. AlphaFold Protein Structure Database: massively expanding the structural coverage of protein-sequence space with high-accuracy models. *Nucleic Acids Res* 2022;50:D439–44. <https://doi.org/10.1093/nar/gkab1061>.
- [149] Roth C, Wei R, Oeser T, Then J, Föllner C, Zimmermann W, et al. Structural and functional studies on a thermostable polyethylene terephthalate degrading hydrolase from *Thermobifida fusca*. *Appl Microbiol Biotechnol* 2014;98:7815–23. <https://doi.org/10.1007/s00253-014-5672-0>.
- [150] Kold D, Dauter Z, Laustsen AK, Brzozowski AM, Turkenburg JP, Nielsen AD, et al. Thermodynamic and structural investigation of the specific SDS binding of *Humicola insolens* cutinase. *Protein Sci* 2014;23:1023–35. <https://doi.org/10.1002/pro.2489>.
- [151] Grochulski P, Li Y, Schrag JD, Bouthillier F, Smith P, Harrison D, et al. Insights into interfacial activation from an open structure of *Candida rugosa* lipase. *J Biol Chem* 1993;268:12843–7.
- [152] Schrödinger LLC, DeLano W. PyMOL n.d.
- [153] Heredia A. Biophysical and biochemical characteristics of cutin, a plant barrier biopolymer. *Biochim Biophys Acta - Gen Subj* 2003;1620:1–7. [https://doi.org/10.1016/S0304-4165\(02\)00510-X](https://doi.org/10.1016/S0304-4165(02)00510-X).
- [154] Wei R, Oeser T, Then J, Kühn N, Barth M, Schmidt J, et al. Functional characterization and structural modeling of synthetic polyester-degrading hydrolases from *Thermomonospora curvata*. *AMB Express* 2014;4:44. <https://doi.org/10.1186/s13568-014-0044-9>.

- [155] Ronkvist ÅM, Xie W, Lu W, Gross RA. Cutinase-Catalyzed Hydrolysis of Poly(ethylene terephthalate). *Macromolecules* 2009;42:5128–38. <https://doi.org/10.1021/ma9005318>.
- [156] Acero EH, Ribitsch D, Steinkellner G, Gruber K, Greimel K, Eiteljoerg I, et al. Enzymatic surface hydrolysis of PET: Effect of structural diversity on kinetic properties of 385 cutinases from *Thermobifida*. *Macromolecules* n.d.;44:4632–40. <https://doi.org/10.1021/ma200949p>.
- [157] Sulaiman S, Yamato S, Kanaya E, Kim JJ, Koga Y, Takano K, et al. Isolation of a novel cutinase homolog with polyethylene terephthalate-degrading activity from leaf-branch compost by using a metagenomic approach. *Appl Environ Microbiol* 2012;78:1556–62. <https://doi.org/10.1128/AEM.06725-11>.
- [158] Eisner H, Riegler-Berket L, Gamez CFR, Sagmeister T, Chalhoub G, Darnhofer B, et al. The Crystal Structure of Mouse Ces2c, a Potential Ortholog of Human CES2, Shows Structural Similarities in Substrate Regulation and Product Release to Human CES1. *Int J Mol Sci* 2022;23. <https://doi.org/10.3390/ijms232113101>.
- [159] Mohamed YM, Ghazy MA, Sayed A, Ouf A, El-Dorry H, Siam R. Isolation and characterization of a heavy metal-resistant, thermophilic esterase from a Red Sea brine pool. *Sci Rep* 2013;3:3358. <https://doi.org/10.1038/srep03358>.
- [160] Albayati S, Masomian M, Ishak SNH, Ali M, Thean A, Mohd Shariff F, et al. Main Structural Targets for Engineering Lipase Substrate Specificity. *Catalysts* 2020;10:747. <https://doi.org/10.3390/catal10070747>.
- [161] Świderek K, Marti S, Arafet K, Moliner V. Computational study of the Mechanism of a polyurethane esterase A (PueA) from *Pseudomonas chlororaphis*. *Faraday Discuss* 2024. <https://doi.org/10.1039/D4FD00022F>.
- [162] Mohapatra BR, Bapuji M. Characterization of urethanase from *Micrococcus* species associated with the marine sponge (*Spirasfrella* species). *Lett Appl Microbiol* 1997;25:393–6. <https://doi.org/10.1111/j.1472-765X.1997.tb00003.x>.
- [163] Syrén PO, Hult K. Amidases Have a Hydrogen Bond that Facilitates Nitrogen Inversion, but Esterases Have Not. *ChemCatChem* 2011;3:853–60. <https://doi.org/10.1002/cctc.201000448>.
- [164] Cerqueira NMFA, Moorthy H, Fernandes PA, Ramos MJ. The mechanism of the Ser-(cis)Ser-Lys catalytic triad of peptide amidases. *Phys Chem Chem Phys* 2017;19:12343–54. <https://doi.org/10.1039/C7CP00277G>.
- [165] Martinez C, Nicolas A, van Tilbeurgh H, Egloff MP, Cudrey C, Verger R, et al. Cutinase, a lipolytic enzyme with a preformed oxyanion hole. *Biochemistry* 1994;33:83–9. <https://doi.org/10.1021/bi00167a011>.
- [166] Nyon MP, Rice DW, Berrisford JM, Hounslow AM, Moir AJG, Huang H, et al. Catalysis by *Glomerella cingulata* cutinase requires conformational cycling between the active and inactive states of its catalytic triad. *J Mol Biol* 2009;385:226–35. <https://doi.org/10.1016/j.jmb.2008.10.050>.
- [167] Martinez C, De Geus P, Lauwereys M, Matthyssens G, Cambillau C. *Fusarium solani* cutinase is a lipolytic enzyme with a catalytic serine accessible to solvent. *Nature* 1992;356:615–8. <https://doi.org/10.1038/356615a0>.
- [168] Elmi F, Lee H-T, Huang J-Y, Hsieh Y-C, Wang Y-L, Chen Y-J, et al. Stereoselective esterase from *Pseudomonas putida* IFO12996 reveals alpha/beta hydrolase folds for D-beta-acetylthioisobutyric acid synthesis. *J Bacteriol* 2005;187:8470–6. <https://doi.org/10.1128/jb.187.24.8470-8476.2005>.
- [169] Derewenda ZS, Derewenda U, Kobos PM. (His)C ϵ -H \cdots O=C< Hydrogen Bond in the Active Sites of Serine Hydrolases. *J Mol Biol* 1994;241:83–93. <https://doi.org/10.1006/jmbi.1994.1475>.
- [170] Labahn J, Neumann S, Büldt G, Kula M-R, Granzin J. An alternative mechanism for amidase signature enzymes. *J Mol Biol* 2002;322:1053–64. [https://doi.org/10.1016/s0022-2836\(02\)00886-0](https://doi.org/10.1016/s0022-2836(02)00886-0).
- [171] Hedstrom L. Serine protease mechanism and specificity. *Chem Rev* 2002;102:4501–24. <https://doi.org/10.1021/cr000033x>.
- [172] Nakagawa Y, Hasegawa A, Hiratake J, Sakata K. Engineering of *Pseudomonas aeruginosa* lipase by directed evolution for enhanced amidase activity: mechanistic implication for amide hydrolysis by serine hydrolases. *Protein Eng Des Sel* 2007;20:339–46. <https://doi.org/10.1093/protein/gzm025>.
- [173] Belostotskii AM, Aped P, Hassner A. MM3 force field as a tool in mechanistic studies of nitrogen inversion processes for alkylamines. *J Mol Struct THEOCHEM* 1997;398–399:427–34. [https://doi.org/10.1016/S0166-1280\(97\)00081-X](https://doi.org/10.1016/S0166-1280(97)00081-X).
- [174] Cammenberg M, Hult K, Park S. Molecular Basis for the Enhanced Lipase-Catalyzed N-Acylation of 1-Phenylethanamine with Methoxyacetate. *ChemBioChem* 2006;7:1745–9. <https://doi.org/10.1002/cbic.200600245>.
- [175] Alogaidi A, Armstrong F, Bakshi A, Bornscheuer UT, Brown G, Bruton I, et al. Biocatalysis for industry, medicine and the circular economy: general discussion. *Faraday Discuss* 2024. <https://doi.org/10.1039/d4fd90025a>.
- [176] Wei R, Zimmermann W. Microbial enzymes for the recycling of recalcitrant petroleum-based plastics:

- how far are we? *Microb Biotechnol* 2017;10:1308–22. <https://doi.org/10.1111/1751-7915.12710>.
- [177] Novy V, Carneiro LV, Shin JH, Larsbrink J, Olsson L. Phylogenetic analysis and in-depth characterization of functionally and structurally diverse CE5 cutinases. *J Biol Chem* 2021;297:101302. <https://doi.org/10.1016/j.jbc.2021.101302>.
- [178] Fan C-Y, Köller W. Diversity of cutinases from plant pathogenic fungi: differential and sequential expression of cutinolytic esterases by *Alternaria brassicicola*. *FEMS Microbiol Lett* 1998;158:33–8. <https://doi.org/10.1111/j.1574-6968.1998.tb12796.x>.
- [179] Leger RJS, Joshi L, Roberts DW. Adaptation of proteases and carbohydrates of saprophytic, phytopathogenic and entomopathogenic fungi to the requirements of their ecological niches. *Microbiology* 1997;143 (Pt 6:1983–92. <https://doi.org/10.1099/00221287-143-6-1983>.
- [180] Liang X, Zou H. Biotechnological Application of Cutinase: A Powerful Tool in Synthetic Biology. *SynBio* 2023;1:54–64. <https://doi.org/10.3390/synbio1010004>.
- [181] Khan FI, Lan D, Durrani R, Huan W, Zhao Z, Wang Y. The Lid Domain in Lipases: Structural and Functional Determinant of Enzymatic Properties. *Front Bioeng Biotechnol* 2017;5:16. <https://doi.org/10.3389/fbioe.2017.00016>.
- [182] Yang Y, Min J, Xue T, Jiang P, Liu X, Peng R, et al. Complete bio-degradation of poly(butylene adipate-co-terephthalate) via engineered cutinases. *Nat Commun* 2023;14:1645. <https://doi.org/10.1038/s41467-023-37374-3>.
- [183] Pan W, Bai Z, Su T, Wang Z. Enzymatic degradation of poly(butylene succinate) with different molecular weights by cutinase. *Int J Biol Macromol* 2018;111:1040–6. <https://doi.org/10.1016/j.ijbiomac.2018.01.107>.
- [184] Yang S, Xu H, Yan Q, Liu Y, Zhou P, Jiang Z. A low molecular mass cutinase of *Thielavia terrestris* efficiently hydrolyzes poly(esters). *J Ind Microbiol Biotechnol* 2013;40:217–26. <https://doi.org/10.1007/s10295-012-1222-x>.
- [185] Liu J, He J, Xue R, Xu B, Qian X, Xin F, et al. Biodegradation and up-cycling of polyurethanes: Progress, challenges, and prospects. *Biotechnol Adv* 2021;48:107730. <https://doi.org/10.1016/j.biotechadv.2021.107730>.
- [186] do Canto VP, Thompson CE, Netz PA. Polyurethanases: Three-dimensional structures and molecular dynamics simulations of enzymes that degrade polyurethane. *J Mol Graph Model* 2019;89:82–95. <https://doi.org/10.1016/j.jmgm.2019.03.001>.
- [187] Flores-Castañón N, Sarkar S, Banerjee A. Structural, functional, and molecular docking analyses of microbial cutinase enzymes against polyurethane monomers. *J Hazard Mater Lett* 2022;3:100063. <https://doi.org/10.1016/j.hazl.2022.100063>.
- [188] Then J, Wei R, Oeser T, Barth M, Belisário-Ferrari MR, Schmidt J, et al. Ca²⁺ and Mg²⁺ binding site engineering increases the degradation of polyethylene terephthalate films by polyester hydrolases from *Thermobifida fusca*. *Biotechnol J* 2015;10:592–8. <https://doi.org/10.1002/biot.201400620>.
- [189] Furukawa M, Kawakami N, Tomizawa A, Miyamoto K. Efficient Degradation of Poly(ethylene terephthalate) with *Thermobifida fusca* Cutinase Exhibiting Improved Catalytic Activity Generated using Mutagenesis and Additive-based Approaches. *Sci Rep* 2019;9:16038. <https://doi.org/10.1038/s41598-019-52379-z>.
- [190] Wei R, von Haugwitz G, Pfaff L, Mican J, Badenhorst CPS, Liu W, et al. Mechanism-Based Design of Efficient PET Hydrolases. *ACS Catal* 2022.
- [191] Mrigwani A, Pitaliya M, Kaur H, Kasilingam B, Thakur B, Guptasarma P. Rational mutagenesis of *Thermobifida fusca* cutinase to modulate the enzymatic degradation of polyethylene terephthalate. *Biotechnol Bioeng* 2023;120:674–86. <https://doi.org/10.1002/bit.28305>.
- [192] Dong Q, Yuan S, Wu L, Su L, Zhao Q, Wu J, et al. Structure-guided engineering of a *Thermobifida fusca* cutinase for enhanced hydrolysis on natural polyester substrate. *Bioresour Bioprocess* 2020;7:37. <https://doi.org/10.1186/s40643-020-00324-8>.
- [193] Silva C, Da S, Silva N, Matamá T, Araújo R, Martins M, et al. Engineered *Thermobifida fusca* cutinase with increased activity on polyester substrates. *Biotechnol J* 2011;6:1230–9. <https://doi.org/10.1002/biot.201000391>.
- [194] Michaelis L, Menten ML. Die Kinetik der Invertinwirkung. *Biochem Z* 1913;49:333–369.
- [195] Mukai K, Yamada K, Doi Y. Kinetics and mechanism of heterogeneous hydrolysis of poly[(R)-3-hydroxybutyrate] film by PHA depolymerases. *Int J Biol Macromol* 1993;15:361–6. [https://doi.org/10.1016/0141-8130\(93\)90054-P](https://doi.org/10.1016/0141-8130(93)90054-P).
- [196] Meier A, Söding J. Automatic Prediction of Protein 3D Structures by Probabilistic Multi-template Homology Modeling. *PLoS Comput Biol* 2015;11:e1004343. <https://doi.org/10.1371/journal.pcbi.1004343>.
- [197] Skariyachan S, Garka S. Chapter 1 - Exploring the binding potential of carbon nanotubes and fullerene

- towards major drug targets of multidrug resistant bacterial pathogens and their utility as novel therapeutic agents. In: Grumezescu Graphenes and Nanotubes AMBT-F, editor., William Andrew Publishing; 2018, p. 1–29. <https://doi.org/10.1016/B978-0-12-813691-1.00001-4>.
- [198] Šali A, Blundell TL. Comparative Protein Modelling by Satisfaction of Spatial Restraints. *J Mol Biol* 1993;234:779–815. <https://doi.org/10.1006/jmbi.1993.1626>.
- [199] Bordoli L, Kiefer F, Arnold K, Benkert P, Battey J, Schwede T. Protein structure homology modeling using SWISS-MODEL workspace. *Nat Protoc* 2009;4:1–13. <https://doi.org/10.1038/nprot.2008.197>.
- [200] Zhang Y. I-TASSER server for protein 3D structure prediction. *BMC Bioinformatics* 2008;9:1–8. <https://doi.org/10.1186/1471-2105-9-40>.
- [201] Agu PC, Afiukwa CA, Orji OU, Ezech EM, Ofoke IH, Ogbu CO, et al. Molecular docking as a tool for the discovery of molecular targets of nutraceuticals in diseases management. *Sci Rep* 2023;13:13398. <https://doi.org/10.1038/s41598-023-40160-2>.
- [202] Jain AN. Virtual screening in lead discovery and optimization. *Curr Opin Drug Discov Devel* 2004;7:396–403.
- [203] Feng Y, Zhang K, Wu Q, Huang S-Y. NLDock: a Fast Nucleic Acid–Ligand Docking Algorithm for Modeling RNA/DNA–Ligand Complexes. *J Chem Inf Model* 2021;61:4771–82. <https://doi.org/10.1021/acs.jcim.1c00341>.
- [204] Rosell M, Fernández-Recio J. Docking approaches for modeling multi-molecular assemblies. *Curr Opin Struct Biol* 2020;64:59–65. <https://doi.org/10.1016/j.sbi.2020.05.016>.
- [205] He J, Wang J, Tao H, Xiao Y, Huang S-Y. HNADOCK: a nucleic acid docking server for modeling RNA/DNA–RNA/DNA 3D complex structures. *Nucleic Acids Res* 2019;47:W35–42. <https://doi.org/10.1093/nar/gkz412>.
- [206] Kitchen DB, Decornez H, Furr JR, Bajorath J. Docking and scoring in virtual screening for drug discovery: methods and applications. *Nat Rev Drug Discov* 2004;3:935–49. <https://doi.org/10.1038/nrd1549>.
- [207] Das DR, Kumar D, Kumar P, Dash BP. Molecular docking and its application in search of antisickling agent from *Carica papaya*. *J Appl Biol Biotechnol* 2020;8:105–16.
- [208] Lemmon G, Meiler J. Rosetta ligand docking with flexible XML protocols. *Methods Mol Biol* 2012;819:143–55. https://doi.org/10.1007/978-1-61779-465-0_10.
- [209] Kaufmann KW, Lemmon GH, Deluca SL, Sheehan JH, Meiler J. Practically useful: what the Rosetta protein modeling suite can do for you. *Biochemistry* 2010;49:2987–98. <https://doi.org/10.1021/bi902153g>.
- [210] Raman S, Vernon R, Thompson J, Tyka M, Sadreyev R, Pei J, et al. Structure prediction for CASP8 with all-atom refinement using Rosetta. *Proteins* 2009;77 Suppl 9:89–99. <https://doi.org/10.1002/prot.22540>.
- [211] Chaudhury S, Gray JJ. Conformer selection and induced fit in flexible backbone protein-protein docking using computational and NMR ensembles. *J Mol Biol* 2008;381:1068–87. <https://doi.org/10.1016/j.jmb.2008.05.042>.
- [212] Jiang L, Althoff EA, Clemente FR, Doyle L, Röthlisberger D, Zanghellini A, et al. De novo computational design of retro-aldol enzymes. *Science* 2008;319:1387–91. <https://doi.org/10.1126/science.1152692>.
- [213] Bhuiyan A, Needham P, Walker R. Amber PME Molecular Dynamics Optimization, 2015, p. 73–89. <https://doi.org/10.1016/B978-0-12-803819-2.00019-7>.
- [214] Karplus M, Petsko GA. Molecular dynamics simulations in biology. *Nature* 1990;347:631–9. <https://doi.org/10.1038/347631a0>.
- [215] McDowell SE, Spacková N, Sponer J, Walter NG. Molecular dynamics simulations of RNA: an *in silico* single molecule approach. *Biopolymers* 2007;85:169–84. <https://doi.org/10.1002/bip.20620>.
- [216] Tian C, Kasavajhala K, Belfon KAA, Raguette L, Huang H, Miguez AN, et al. ff19SB: Amino-Acid-Specific Protein Backbone Parameters Trained against Quantum Mechanics Energy Surfaces in Solution. *J Chem Theory Comput* 2020;16:528–52. <https://doi.org/10.1021/acs.jctc.9b00591>.
- [217] Ponder JW, Case DA. Force fields for protein simulations. *Adv Protein Chem* 2003;66:27–85. [https://doi.org/10.1016/s0065-3233\(03\)66002-x](https://doi.org/10.1016/s0065-3233(03)66002-x).
- [218] Dickson CJ, Walker RC, Gould IR. Lipid21: Complex Lipid Membrane Simulations with AMBER. *J Chem Theory Comput* 2022;18:1726–36. <https://doi.org/10.1021/acs.jctc.1c01217>.
- [219] Wang J, Wolf RM, Caldwell JW, Kollman PA, Case DA. Development and testing of a general amber force field. *J Comput Chem* 2004;25:1157–74. <https://doi.org/10.1002/jcc.20035>.
- [220] Allinger NL. Conformational analysis. 130. MM2. A hydrocarbon force field utilizing V1 and V2 torsional terms. *J Am Chem Soc* 1977;99:8127–34. <https://doi.org/10.1021/ja00467a001>.
- [221] Lii J-H. Molecular Mechanics (MM4) Studies of Carboxylic Acids, Esters, and Lactones. *J Phys Chem A* 2002;106:8667–79. <https://doi.org/10.1021/jp0142029>.
- [222] Wang J, Wang W, Kollman PA, Case DA. Automatic atom type and bond type perception in molecular

- mechanical calculations. *J Mol Graph Model* 2006;25:247–60. <https://doi.org/10.1016/j.jmgl.2005.12.005>.
- [223] Jakalian A, Jack DB, Bayly CI. Fast, efficient generation of high-quality atomic charges. AM1-BCC model: II. Parameterization and validation. *J Comput Chem* 2002;23:1623–41. <https://doi.org/10.1002/jcc.10128>.
- [224] Genheden S, Ryde U. The MM/PBSA and MM/GBSA methods to estimate ligand-binding affinities. *Expert Opin Drug Discov* 2015;10:449–61. <https://doi.org/10.1517/17460441.2015.1032936>.
- [225] Foloppe N, Hubbard R. Towards predictive ligand design with free-energy based computational methods? *Curr Med Chem* 2006;13:3583–608. <https://doi.org/10.2174/092986706779026165>.
- [226] Homeyer N, Gohlke H. Free Energy Calculations by the Molecular Mechanics Poisson-Boltzmann Surface Area Method. *Mol Inform* 2012;31:114–22. <https://doi.org/10.1002/minf.201100135>.
- [227] Zoete V, Michielin O. Comparison between computational alanine scanning and per-residue binding free energy decomposition for protein–protein association using MM-GBSA: Application to the TCR-p-MHC complex. *Proteins Struct Funct Bioinforma* 2007;67:1026–47. <https://doi.org/10.1002/prot.21395>.
- [228] Massova I, Kollman PA. Computational Alanine Scanning To Probe Protein–Protein Interactions: A Novel Approach To Evaluate Binding Free Energies. *J Am Chem Soc* 1999;121:8133–43. <https://doi.org/10.1021/ja990935j>.
- [229] Srinivasan J, Cheatham TE, Cieplak P, Kollman PA, Case DA. Continuum Solvent Studies of the Stability of DNA, RNA, and Phosphoramidate–DNA Helices. *J Am Chem Soc* 1998;120:9401–9. <https://doi.org/10.1021/ja981844+>.
- [230] Lee MR, Tsai J, Baker D, Kollman PA. Molecular dynamics in the endgame of protein structure prediction. *J Mol Biol* 2001;313:417–30. <https://doi.org/10.1006/jmbi.2001.5032>.
- [231] Godschalk F, Genheden S, Söderhjelm P, Ryde U. Comparison of MM/GBSA calculations based on explicit and implicit solvent simulations. *Phys Chem Chem Phys* 2013;15:7731–9. <https://doi.org/10.1039/C3CP00116D>.
- [232] Goldsmith M, Tawfik DS. Enzyme engineering: reaching the maximal catalytic efficiency peak. *Curr Opin Struct Biol* 2017;47:140–50. <https://doi.org/10.1016/j.sbi.2017.09.002>.
- [233] Xin F, Dong W, Dai Z, Jiang Y, Yan W, Lv Z, et al. Chapter 9 - Biosynthetic Technology and Bioprocess Engineering. In: Singh SP, Pandey A, Du G, Kumar SBT-CD in B and B, editors., Elsevier; 2019, p. 207–32. <https://doi.org/10.1016/B978-0-444-64085-7.00009-5>.
- [234] Rayu S, Karpouzas DG, Singh BK. Emerging technologies in bioremediation: constraints and opportunities. *Biodegradation* 2012;23:917–26. <https://doi.org/10.1007/s10532-012-9576-3>.
- [235] Cea PA, Pérez M, Herrera SM, Muñoz SM, Fuentes-Ugarte N, Coche-Miranda J, et al. Deciphering Structural Traits for Thermal and Kinetic Stability across Protein Family Evolution through Ancestral Sequence Reconstruction. *Mol Biol Evol* 2024;41:msae127. <https://doi.org/10.1093/molbev/msae127>.
- [236] Rahban M, Zolghadri S, Salehi N, Ahmad F, Haertlé T, Rezaei-Ghaleh N, et al. Thermal stability enhancement: Fundamental concepts of protein engineering strategies to manipulate the flexible structure. *Int J Biol Macromol* 2022;214:642–54. <https://doi.org/10.1016/j.ijbiomac.2022.06.154>.
- [237] Chica RA, Doucet N, Pelletier JN. Semi-rational approaches to engineering enzyme activity: combining the benefits of directed evolution and rational design. *Curr Opin Biotechnol* 2005;16:378–84. <https://doi.org/10.1016/j.copbio.2005.06.004>.
- [238] Wang Y, Xue P, Cao M, Yu T, Lane ST, Zhao H. Directed Evolution: Methodologies and Applications. *Chem Rev* 2021;121:12384–444. <https://doi.org/10.1021/acs.chemrev.1c00260>.
- [239] Bornscheuer U, Kazlauskas RJ. Survey of protein engineering strategies. *Curr Protoc Protein Sci* 2011;Chapter 26:26.7.1–26.7.14. <https://doi.org/10.1002/0471140864.ps2607s66>.
- [240] Oroz-Guinea I, Zorn K, Brundiek H. Chapter 2 - Protein engineering of enzymes involved in lipid modification. In: Bornscheuer UTBT-LM by E and EM, editor., AOCs Press; 2018, p. 11–43. <https://doi.org/10.1016/B978-0-12-813167-1.00002-5>.
- [241] Lutz S. Beyond directed evolution—semi-rational protein engineering and design. *Curr Opin Biotechnol* 2010;21:734–43. <https://doi.org/10.1016/j.copbio.2010.08.011>.
- [242] Ferreira P, Fernandes PA, Ramos MJ. Modern computational methods for rational enzyme engineering. *Chem Catal* 2022;2:2481–98. <https://doi.org/10.1016/j.checat.2022.09.036>.
- [243] Chowdhury R, Maranas CD. From directed evolution to computational enzyme engineering—A review. *AIChe J* 2020;66:e16847. <https://doi.org/10.1002/aic.16847>.
- [244] Ebert M, Pelletier JN. Computational tools for enzyme improvement: why everyone can - and should - use them. *Curr Opin Chem Biol* 2017;37:89–96. <https://doi.org/10.1016/j.cbpa.2017.01.021>.
- [245] Sequeiros-Borja CE, Surpeta B, Brezovsky J. Recent advances in user-friendly computational tools to engineer protein function. *Brief Bioinform* 2021;22. <https://doi.org/10.1093/bib/bbaa150>.
- [246] Zhou L, Tao C, Shen X, Sun X, Wang J, Yuan Q. Unlocking the potential of enzyme engineering via

- rational computational design strategies. *Biotechnol Adv* 2024;73:108376. <https://doi.org/10.1016/j.biotechadv.2024.108376>.
- [247] Romero-Rivera A, Garcia-Borrás M, Osuna S. Role of Conformational Dynamics in the Evolution of Retro-Aldolase Activity. *ACS Catal* 2017;7:8524–32. <https://doi.org/10.1021/acscatal.7b02954>.
- [248] Crean RM, Gardner JM, Kamerlin SCL. Harnessing Conformational Plasticity to Generate Designer Enzymes. *J Am Chem Soc* 2020;142:11324–42. <https://doi.org/10.1021/jacs.0c04924>.
- [249] Gardner JM, Biler M, Risso VA, Sanchez-Ruiz JM, Kamerlin SCL. Manipulating Conformational Dynamics To Repurpose Ancient Proteins for Modern Catalytic Functions. *ACS Catal* 2020;10:4863–70. <https://doi.org/10.1021/acscatal.0c00722>.
- [250] James LC, Tawfik DS. Conformational diversity and protein evolution – a 60-year-old hypothesis revisited. *Trends Biochem Sci* 2003;28:361–8. [https://doi.org/10.1016/S0968-0004\(03\)00135-X](https://doi.org/10.1016/S0968-0004(03)00135-X).
- [251] Maria-Solano MA, Serrano-Hervás E, Romero-Rivera A, Iglesias-Fernández J, Osuna S. Role of conformational dynamics in the evolution of novel enzyme function. *Chem Commun* 2018;54:6622–34. <https://doi.org/10.1039/C8CC02426J>.
- [252] Spence MA, Kaczmarek JA, Saunders JW, Jackson CJ. Ancestral sequence reconstruction for protein engineers. *Curr Opin Struct Biol* 2021;69:131–41. <https://doi.org/10.1016/j.sbi.2021.04.001>.
- [253] St-Jacques AD, Rodriguez JM, Eason MG, Foster SM, Khan ST, Damry AM, et al. Computational remodeling of an enzyme conformational landscape for altered substrate selectivity. *Nat Commun* 2023;14:6058. <https://doi.org/10.1038/s41467-023-41762-0>.
- [254] Zamora RA, Ramirez-Sarmiento CA, Castro-Fernández V, Villalobos P, Maturana P, Herrera-Morande A, et al. Tuning of Conformational Dynamics Through Evolution-Based Design Modulates the Catalytic Adaptability of an Extremophilic Kinase. *ACS Catal* 2020;10:10847–57. <https://doi.org/10.1021/acscatal.0c01300>.
- [255] Babkova P, Dunajova Z, Chaloupkova R, Damborsky J, Bednar D, Marek M. Structures of hyperstable ancestral haloalkane dehalogenases show restricted conformational dynamics. *Comput Struct Biotechnol J* 2020;18:1497–508. <https://doi.org/10.1016/j.csbj.2020.06.021>.
- [256] Stephens ZD, Lee SY, Faghri F, Campbell RH, Zhai C, Efron MJ, et al. Big Data: Astronomical or Genomical? *PLOS Biol* 2015;13:e1002195.
- [257] Folkman L, Stantic B, Sattar A, Zhou Y. EASE-MM: Sequence-Based Prediction of Mutation-Induced Stability Changes with Feature-Based Multiple Models. *J Mol Biol* 2016;428:1394–405. <https://doi.org/10.1016/j.jmb.2016.01.012>.
- [258] Teng S, Srivastava AK, Wang L. Sequence feature-based prediction of protein stability changes upon amino acid substitutions. *BMC Genomics* 2010;11:S5. <https://doi.org/10.1186/1471-2164-11-S2-S5>.
- [259] Yang Y, Niroula A, Shen B, Vihinen M. PON-Sol: prediction of effects of amino acid substitutions on protein solubility. *Bioinformatics* 2016;32:2032–4. <https://doi.org/10.1093/bioinformatics/btw066>.
- [260] Falda M, Toppo S, Pescarolo A, Lavezzo E, Di Camillo B, Facchinetti A, et al. Argot2: a large scale function prediction tool relying on semantic similarity of weighted Gene Ontology terms. *BMC Bioinformatics* 2012;13:S14. <https://doi.org/10.1186/1471-2105-13-S4-S14>.
- [261] De Ferrari L, Mitchell JBO. From sequence to enzyme mechanism using multi-label machine learning. *BMC Bioinformatics* 2014;15:150. <https://doi.org/10.1186/1471-2105-15-150>.
- [262] Koskinen P, Törönen P, Nokso-Koivisto J, Holm L. PANNZER: high-throughput functional annotation of uncharacterized proteins in an error-prone environment. *Bioinformatics* 2015;31:1544–52. <https://doi.org/10.1093/bioinformatics/btu851>.
- [263] Cozzetto D, Buchan DWA, Bryson K, Jones DT. Protein function prediction by massive integration of evolutionary analyses and multiple data sources. *BMC Bioinformatics* 2013;14:S1. <https://doi.org/10.1186/1471-2105-14-S3-S1>.
- [264] Scherer M, Fleishman SJ, Jones PR, Dandekar T, Bencurova E. Computational Enzyme Engineering Pipelines for Optimized Production of Renewable Chemicals. *Front Bioeng Biotechnol* 2021;9:673005. <https://doi.org/10.3389/fbioe.2021.673005>.
- [265] Rohl CA, Strauss CEM, Misura KMS, Baker DBT-M in E. Protein Structure Prediction Using Rosetta. *Numer. Comput. Methods, Part D*, vol. 383, Academic Press; 2004, p. 66–93. [https://doi.org/10.1016/S0076-6879\(04\)83004-0](https://doi.org/10.1016/S0076-6879(04)83004-0).
- [266] Leaver-Fay A, Tyka M, Lewis SM, Lange OF, Thompson J, Jacak R, et al. ROSETTA3: an object-oriented software suite for the simulation and design of macromolecules. *Methods Enzymol* 2011;487:545–74. <https://doi.org/10.1016/B978-0-12-381270-4.00019-6>.
- [267] Watson JL, Juergens D, Bennett NR, Trippe BL, Yim J, Eisenach HE, et al. De novo design of protein structure and function with RFdiffusion. *Nature* 2023;620:1089–100. <https://doi.org/10.1038/s41586-023-06415-8>.

- [268] Dauparas J, Anishchenko I, Bennett N, Bai H, Ragotte RJ, Milles LF, et al. Robust deep learning-based protein sequence design using ProteinMPNN. *Science* (80-) 2022;378:49–56. <https://doi.org/10.1126/science.add2187>.
- [269] Buller R, Damborsky J, Hilvert D, Bornscheuer U. Structure Prediction and Computational Protein Design for Efficient Biocatalysts and Bioactive Proteins. *Angew Chemie Int Ed* 2024;n/a:e202421686. <https://doi.org/10.1002/anie.202421686>.
- [270] Chen S, Tong X, Woodard RW, Du G, Wu J, Chen J. Identification and characterization of bacterial cutinase. *J Biol Chem* 2008;283:25854–62. <https://doi.org/10.1074/jbc.M800848200>.
- [271] Herrero Acero E, Ribitsch D, Steinkellner G, Gruber K, Greimel K, Eiteljoerg I, et al. Enzymatic Surface Hydrolysis of PET: Effect of Structural Diversity on Kinetic Properties of Cutinases from *Thermobifida*. *Macromolecules* 2011;44:4632–40. <https://doi.org/10.1021/ma200949p>.
- [272] Chen S, Billig S, Zimmermann W, Chen J. Biochemical characterization of the cutinases from *Thermobifida fusca*. *J Mol Catal B Enzym* 2010;63:121–7. <https://doi.org/10.1016/j.molcatb.2010.01.001>.
- [273] Chen VB, Arendall WB 3rd, Headd JJ, Keedy DA, Immormino RM, Kapral GJ, et al. MolProbity: all-atom structure validation for macromolecular crystallography. *Acta Crystallogr D Biol Crystallogr* 2010;66:12–21. <https://doi.org/10.1107/S0907444909042073>.
- [274] Hegde K, Veeranki VD. Production optimization and characterization of recombinant cutinases from *Thermobifida fusca* sp. NRRL B-8184. *Appl Biochem Biotechnol* 2013;170:654–75. <https://doi.org/10.1007/s12010-013-0219-x>.
- [275] Kleeberg I, Welzel K, Vandenheuvel J, Müller R-J, Deckwer W-D. Characterization of a new extracellular hydrolase from *Thermobifida fusca* degrading aliphatic-aromatic copolyesters. *Biomacromolecules* 2005;6:262–70. <https://doi.org/10.1021/bm049582t>.
- [276] Huang Y-C, Chen G-H, Chen Y-F, Chen W-L, Yang C-H. Heterologous expression of thermostable acetylxyylan esterase gene from *Thermobifida fusca* and its synergistic action with xylanase for the production of xylooligosaccharides. *Biochem Biophys Res Commun* 2010;400:718–23. <https://doi.org/10.1016/j.bbrc.2010.08.136>.
- [277] Sriu J, Zeng Q, Lei H, Xin K, Xu A, Wei R, et al. Biodegradation of polyester polyurethane by *Cladosporium* sp. P7: Evaluating its degradation capacity and metabolic pathway. *J Hazard Mater* 2023;448. <https://doi.org/10.1016/j.jhazmat.2023.130776>.
- [278] Wei R, Oeser T, Zimmermann W. Synthetic polyester-hydrolyzing enzymes from thermophilic actinomycetes. *Adv Appl Microbiol* 2014;89:267–305. <https://doi.org/10.1016/B978-0-12-800259-9.00007-X>.
- [279] Robert X, Gouet P. Deciphering key features in protein structures with the new ENDscript server. *Nucleic Acids Res* 2014;42:W320–4. <https://doi.org/10.1093/nar/gku316>.
- [280] Sulaiman S, You DJ, Eiko K, Koga Y, Kanaya S. Crystal structure of Leaf-branch compost bacterial cutinase homolog n.d. <https://doi.org/10.2210/pdb4EB0/pdb>.
- [281] Waterhouse A, Bertoni M, Bienert S, Studer G, Tauriello G, Gumienny R, et al. SWISS-MODEL: homology modelling of protein structures and complexes. *Nucleic Acids Res* 2018;46:W296–303. <https://doi.org/10.1093/nar/gky427>.
- [282] Guex N, Peitsch MC, Schwede T. Automated comparative protein structure modeling with SWISS-MODEL and Swiss-PdbViewer: a historical perspective. *Electrophoresis* 2009;30 Suppl 1:S162-73. <https://doi.org/10.1002/elps.200900140>.
- [283] Roy A, Kucukural A, Zhang Y. I-TASSER: A unified platform for automated protein structure and function prediction. *Nat Protoc* 2010;5:725–38. <https://doi.org/10.1038/nprot.2010.5>.
- [284] Yang J, Yan R, Roy A, Xu D, Poisson J, Zhang Y. The I-TASSER suite: Protein structure and function prediction. *Nat Methods* 2014;12:7–8. <https://doi.org/10.1038/nmeth.3213>.
- [285] Gordon JC, Myers JB, Folta T, Shoja V, Heath LS, Onufriev A. H++: a server for estimating pKas and adding missing hydrogens to macromolecules. *Nucleic Acids Res* 2005;33:W368-71. <https://doi.org/10.1093/nar/gki464>.
- [286] Case DA, Ben-Shalom IY, Brozell SR, Cerutti DS, Cheatham TE, Cruzeiro VWDI, et al. Amber 2018 Reference Manual. 2018.
- [287] Fecker T, Galaz-Davison P, Engelberger F, Narui Y, Sotomayor M, Parra LP, et al. Active Site Flexibility as a Hallmark for Efficient PET Degradation by *I. sakaiensis* PETase. *Biophys J* 2018;114:1302–12. <https://doi.org/10.1016/j.bpj.2018.02.005>.
- [288] Alford RF, Leaver-Fay A, Jeliakov JR, O’Meara MJ, DiMaio FP, Park H, et al. The Rosetta All-Atom Energy Function for Macromolecular Modeling and Design. *J Chem Theory Comput* 2017;13:3031–48. <https://doi.org/10.1021/acs.jctc.7b00125>.
- [289] Hanwell MD, Curtis DE, Lonie DC, Vandermeersch T, Zurek E, Hutchison GR. Avogadro: an advanced

- semantic chemical editor, visualization, and analysis platform. *J Cheminform* 2012;4:17. <https://doi.org/10.1186/1758-2946-4-17>.
- [290] O'Boyle NM, Banck M, James CA, Morley C, Vandermeersch T, Hutchison GR. Open Babel: An open chemical toolbox. *J Cheminform* 2011;3:33. <https://doi.org/10.1186/1758-2946-3-33>.
- [291] Khatib F, Cooper S, Tyka MD, Xu K, Makedon I, Popovic Z, et al. Algorithm discovery by protein folding game players. *Proc Natl Acad Sci U S A* 2011;108:18949–53. <https://doi.org/10.1073/pnas.1115898108>.
- [292] Maguire JB, Haddox HK, Strickland D, Halabiya SF, Coventry B, Griffin JR, et al. Perturbing the energy landscape for improved packing during computational protein design. *Proteins* 2021;89:436–49. <https://doi.org/10.1002/prot.26030>.
- [293] Fleishman SJ, Leaver-Fay A, Corn JE, Strauch E-M, Khare SD, Koga N, et al. RosettaScripts: a scripting language interface to the Rosetta macromolecular modeling suite. *PLoS One* 2011;6:e20161. <https://doi.org/10.1371/journal.pone.0020161>.
- [294] Cheatham TEIII, Miller JL, Fox T, Darden TA, Kollman PA. Molecular Dynamics Simulations on Solvated Biomolecular Systems: The Particle Mesh Ewald Method Leads to Stable Trajectories of DNA, RNA, and Proteins. *J Am Chem Soc* 1995;117:4193–4. <https://doi.org/10.1021/ja00119a045>.
- [295] Kräutler V, van Gunsteren WF, Hünenberger PH. A fast SHAKE algorithm to solve distance constraint equations for small molecules in molecular dynamics simulations. *J Comput Chem* 2001;22.
- [296] Case DA, Aktulga HM, Belfon K, Ben-Shalom IY, Berryman JT, Brozell SR, et al. *Amber 2022*. University of California, San Francisco: 2022.
- [297] Roe DR, Cheatham TEIII. PTRAJ and CPPTRAJ: Software for Processing and Analysis of Molecular Dynamics Trajectory Data. *J Chem Theory Comput* 2013;9:3084–95. <https://doi.org/10.1021/ct400341p>.
- [298] Gilson MK, Zhou H-X. Calculation of protein-ligand binding affinities. *Annu Rev Biophys Biomol Struct* 2007;36:21–42. <https://doi.org/10.1146/annurev.biophys.36.040306.132550>.
- [299] Bouysset C, Fiorucci S. ProLIF: a library to encode molecular interactions as fingerprints. *J Cheminform* 2021;13:1–9. <https://doi.org/10.1186/s13321-021-00548-6>.
- [300] Van Rossum G, Drake FL. *Python 3 Reference Manual*. Scotts Valley, CA: CreateSpace; 2009.
- [301] McKinney W. *pandas: a Foundational Python Library for Data Analysis and Statistics*. Python High Perform Sci Comput 2011.
- [302] Harris CR, Millman KJ, van der Walt SJ, Gommers R, Virtanen P, Cournapeau D, et al. Array programming with NumPy. *Nature* 2020;585:357–62. <https://doi.org/10.1038/s41586-020-2649-2>.
- [303] Hunter JD. Matplotlib: A 2D Graphics Environment. *Comput Sci Eng* 2007;9:90–5. <https://doi.org/10.1109/MCSE.2007.55>.
- [304] Waskom M. seaborn: statistical data visualization. *J Open Source Softw* 2021;6:3021. <https://doi.org/10.21105/joss.03021>.
- [305] Cock PJA, Antao T, Chang JT, Chapman BA, Cox CJ, Dalke A, et al. Biopython: freely available Python tools for computational molecular biology and bioinformatics. *Bioinformatics* 2009;25:1422–3. <https://doi.org/10.1093/bioinformatics/btp163>.
- [306] Virtanen P, Gommers R, Oliphant TE, Haberland M, Reddy T, Cournapeau D, et al. SciPy 1.0: fundamental algorithms for scientific computing in Python. *Nat Methods* 2020;17:261–72. <https://doi.org/10.1038/s41592-019-0686-2>.
- [307] Ollis DL, Cheah E, Cygler M, Dijkstra B, Frolow F, Franken SM, et al. The α / β hydrolase fold. "Protein Eng Des Sel 1992;5:197–211. <https://doi.org/10.1093/protein/5.3.197>.
- [308] Nikolaivits E, Kanelli M, Dimarogona M, Topakas E. A middle-aged enzyme still in its prime: Recent advances in the field of cutinases. *Catalysts* 2018;8. <https://doi.org/10.3390/catal8120612>.
- [309] Oda M. Structural basis for Ca(2+)-dependent catalysis of a cutinase-like enzyme and its engineering: application to enzymatic PET depolymerization. *Biophys Physicobiology* 2021;18:168–76. <https://doi.org/10.2142/biophysico.bppb-v18.018>.
- [310] Miyakawa T, Mizushima H, Ohtsuka J, Oda M, Kawai F, Tanokura M. Structural basis for the Ca²⁺-enhanced thermostability and activity of PET-degrading cutinase-like enzyme from *Saccharomonospora viridis* AHK190. *Appl Microbiol Biotechnol* 2015;99:4297–307. <https://doi.org/10.1007/s00253-014-6272-8>.
- [311] Nyyssölä A. Which properties of cutinases are important for applications? *Appl Microbiol Biotechnol* 2015;99:4931–42. <https://doi.org/10.1007/s00253-015-6596-z>.
- [312] Lau EY, Bruice TC. Consequences of Breaking the Asp-His Hydrogen Bond of the Catalytic Triad: Effects on the Structure and Dynamics of the Serine Esterase Cutinase. *Biophys J* 1999;77:85–98. [https://doi.org/10.1016/S0006-3495\(99\)76874-8](https://doi.org/10.1016/S0006-3495(99)76874-8).
- [313] Lushchekina S V, Nemukhin A V, Varfolomeev SD, Masson P. Molecular modeling evidence for His438 flip in the mechanism of butyrylcholinesterase hysteretic behavior. *J Mol Neurosci* 2014;52:434–45. <https://doi.org/10.1007/s12031-013-0178-2>.

- [314] Bürgi HB, Dunitz JD, Lehn JM, Wipff G. Stereochemistry of reaction paths at carbonyl centres. *Tetrahedron* 1974;30:1563–72. [https://doi.org/10.1016/S0040-4020\(01\)90678-7](https://doi.org/10.1016/S0040-4020(01)90678-7).
- [315] Chen X-Q, Guo Z-Y, Wang L, Yan Z-F, Jin C-X, Huang Q-S, et al. Directional-path modification strategy enhances PET hydrolase catalysis of plastic degradation. *J Hazard Mater* 2022;433:128816. <https://doi.org/doi.org/10.1016/j.jhazmat.2022.128816>.
- [316] Wei R, Oeser T, Schmidt J, Meier R, Barth M, Then J, et al. Engineered bacterial polyester hydrolases efficiently degrade polyethylene terephthalate due to relieved product inhibition. *Biotechnol Bioeng* 2016;113:1658–65. <https://doi.org/10.1002/bit.25941>.
- [317] Araújo R, Silva C, O'Neill A, Micaelo N, Guebitz G, Soares CM, et al. Tailoring cutinase activity towards polyethylene terephthalate and polyamide 6,6 fibers. *J Biotechnol* 2007;128:849–57. <https://doi.org/10.1016/j.jbiotec.2006.12.028>.
- [318] Park S, Yang X, Saven JG. Advances in computational protein design. *Curr Opin Struct Biol* 2004;14:487–94. <https://doi.org/10.1016/j.sbi.2004.06.002>.
- [319] Gainza-Cirauqui P, Correia BE. Computational protein design—the next generation tool to expand synthetic biology applications. *Curr Opin Biotechnol* 2018;52:145–52. <https://doi.org/10.1016/j.copbio.2018.04.001>.
- [320] Kuhlman B, Bradley P. Advances in protein structure prediction and design. *Nat Rev Mol Cell Biol* 2019;20:681–97. <https://doi.org/10.1038/s41580-019-0163-x>.
- [321] Schymkowitz J, Borg J, Stricher F, Nys R, Rousseau F, Serrano L. The FoldX web server: an online force field. *Nucleic Acids Res* 2005;33:W382–8. <https://doi.org/10.1093/nar/gki387>.
- [322] Sumbalova L, Stourac J, Martinek T, Bednar D, Damborsky J. HotSpot Wizard 3.0: web server for automated design of mutations and smart libraries based on sequence input information. *Nucleic Acids Res* 2018;46:W356–62. <https://doi.org/10.1093/nar/gky417>.
- [323] Pluciennik A, Stolarczyk M, Bzówka M, Raczyńska A, Magdziarz T, Góra A. BALCONY: an R package for MSA and functional compartments of protein variability analysis. *BMC Bioinformatics* 2018;19:300. <https://doi.org/10.1186/s12859-018-2294-z>.
- [324] Sander C, Schneider R. Database of homology-derived protein structures and the structural meaning of sequence alignment. *Proteins Struct Funct Genet* 1991;9:56–68. <https://doi.org/10.1002/prot.340090107>.
- [325] Chaudhury S, Lyskov S, Gray JJ. PyRosetta: A script-based interface for implementing molecular modeling algorithms using Rosetta. *Bioinformatics* 2010;26:689–91. <https://doi.org/10.1093/bioinformatics/btq007>.
- [326] Kuhlman B. Designing protein structures and complexes with the molecular modeling program Rosetta. *J Biol Chem* 2019;294:19436–43. <https://doi.org/10.1074/jbc.AW119.008144>.
- [327] Miotto M, Olimpieri PP, Di Rienzo L, Ambrosetti F, Corsi P, Lepore R, et al. Insights on protein thermal stability: a graph representation of molecular interactions. *Bioinformatics* 2018;35:2569–77. <https://doi.org/10.1093/bioinformatics/bty1011>.
- [328] Vogt G, Argos P. Protein thermal stability: hydrogen bonds or internal packing? *Fold Des* 1997;2:S40–6. [https://doi.org/10.1016/S1359-0278\(97\)00062-X](https://doi.org/10.1016/S1359-0278(97)00062-X).
- [329] Gao K, Oerlemans R, Groves MR. Theory and applications of differential scanning fluorimetry in early-stage drug discovery. *Biophys Rev* 2020;12:85–104. <https://doi.org/10.1007/s12551-020-00619-2>.
- [330] Montalbetti CAGN, Falque V. Amide bond formation and peptide coupling. *Tetrahedron* 2005;61:10827–52. <https://doi.org/10.1016/j.tet.2005.08.031>.
- [331] Valeur E, Bradley M. Amide bond formation: beyond the myth of coupling reagents. *Chem Soc Rev* 2009;38:606–31. <https://doi.org/10.1039/B701677H>.
- [332] Margarit I, Camagnoli S, Frigerio F, Grandi G, Filippis V De, Fontana A. Cumulative stabilizing effects of glycine to alanine substitutions in *Bacillus subtilis* neutral protease. *Protein Eng Des Sel* 1992;5:543–50. <https://doi.org/10.1093/protein/5.6.543>.
- [333] Heumann S, Eberl A, Pobeheim H, Liebminger S, Fischer-Colbrie G, Almansa E, et al. New model substrates for enzymes hydrolysing polyethyleneterephthalate and polyamide fibres. *J Biochem Biophys Methods* 2006;69:89–99. <https://doi.org/10.1016/j.jbbm.2006.02.005>.

Permissions

Permission to use the text of manuscript:

Raczyńska A., Góra A., André I. 2024 *An overview on polyurethane-degrading enzymes*. *Biotechnology Advances* 77, 108439.



An overview on polyurethane-degrading enzymes

Author: Agata Raczyńska, Artur Góra, Isabelle André

Publication: *Biotechnology Advances*

Publisher: Elsevier

Date: December 2024

© 2024 Elsevier Inc. All rights are reserved, including those for text and data mining, AI training, and similar technologies.

Journal Author Rights

Please note that, as the author of this Elsevier article, you retain the right to include it in a thesis or dissertation, provided it is not published commercially. Permission is not required, but please ensure that you reference the journal as the original source. For more information on this and on your other retained rights, please visit: <https://www.elsevier.com/about/our-business/policies/copyright#Author-rights>

BACK

CLOSE WINDOW

© 2024 Copyright - All Rights Reserved | [Copyright Clearance Center, Inc.](#) | [Privacy statement](#) | [Data Security and Privacy](#)
| [For California Residents](#) | [Terms and Conditions](#) Comments? We would like to hear from you. E-mail us at customercare@copyright.com



Silesian
University
of Technology



RESEARCH
UNIVERSITY
EXCELLENCE INITIATIVE
Ministry of Science
and Higher Education

Faculty of Chemistry

mgr inż.
Agata Raczyńska
Doktorant

Gliwice, November 28, 2024

To whom it may concern

CO-AUTHOR CONTRIBUTION STATEMENT

Hereby, I certify that I am a co-author of the following publication: Raczyńska A., Góra A., André I. An overview on polyurethane-degrading enzymes *Biotechnology Advances* (2024) 77, 108439. doi: 10.1016/j.biotechadv.2024.108439

I declare the following contribution to this publication: **90 %**

I was involved in the Conceptualization, Methodology, Formal analysis, Investigation, Writing - Original Draft, Writing - Review & Editing and Visualization.

Agata Raczyńska

Silesian University of Technology
Faculty of Chemistry



HR EXCELLENCE IN RESEARCH

Bolesława Krzywoustego 8, 44-100 Gliwice
+48 32 237 16 59 / +48 690600890
Agata.Raczynska@polsl.pl

NIP 631 020 07 36
ING Bank Śląski S.A. o/Gliwice 60 1050 1230 1000 0002 0211 3056



Gliwice, 19.11.2024

To whom it may concern

CO-AUTHOR CONTRIBUTION STATEMENT

Hereby, I certify that I am a co-author of the following publication: Raczyńska A., Góra A., André I. An overview on polyurethane-degrading enzymes *Biotechnology Advances* (2024) 77, 108439. doi: 10.1016/j.biotechadv.2024.108439

I declare the following contribution to this publication: 5 %

I was involved in the conceptualization, writing - Review & Editing, Supervision.

Artur Góra

Signed by /
Podpisano przez:



Artur Wiktor Góra
Politechnika
Śląska

Date / Data:
2024-11-19 15:19

Silesian University of Technology
Biotechnology Centre

ul. Krzywoustego 8, pok. 010, 44-100 Gliwice
+48 32 237 16 59 / +48 664 768 710
artur.gora@polsl.pl

NIP 631 020 07 36
ING Bank Śląski S.A. o/Gliwice 60 1050 1230 1000 0002 0211 3056



Toulouse, November 19th, 2024

CO-AUTHOR CONTRIBUTION STATEMENT

Hereby, I certify that I am a co-author of the following publication:

Raczyńska A., Góra A., André I.

An overview on polyurethane-degrading enzymes

Biotechnology Advances (2024) 77, 108439.

doi: 10.1016/j.biotechadv.2024.108439

I declare the following contribution to this publication: 5 %

I was involved in the conceptualization, writing - Review & Editing, Supervision.



Dr Isabelle André
Research Director, CNRS
Toulouse Biotechnology Institute
E-mail: Isabelle.andre@insa-toulouse.fr